Synthesis And Characterization Of Nanoscale Alloys And Metal Oxides For Potential Application In Catalysis

Thesis submitted for the degree of

Doctor of Philosophy (Science)

in

Chemistry (Inorganic)

by

Arnab Samanta

Department of Chemistry
University of Calcutta
2021

Dedicated to My Mother…

I would kindly take this pleasant opportunity to acknowledge a lot of nice people who helped and encouraged me during my PhD and without their support this work could not have been completed.

I am wholeheartedly grateful to my supervisors Dr. Subhra Jana and Prof. Samir Kumar Pal for their continuous support, encouragement, valuable discussions, helpful suggestions and perceptive comments throughout my research work.

I would like to convey my gratitude to Dr. Subhra Jana for introducing me to such an interesting and advanced research field and providing me the opportunity to work in her lab and guiding me to achieve my goals. She helped me a lot to grow as a researcher. Besides being a patient guide and excellent teacher, she is a good human being also and possesses a great sense of humours. It is always nourishing for me to talk with her, listen her opinions in various aspects of science and life as well.

I am also very much grateful to Prof. Samir Kumar Pal for his constant support, guidance, encouragement and spending his valuable time towards the academic discussions during my research work. It has been a real privilege for me to work with both of them for five long years. I am really fortunate to have such enthusiastic supervisors.

I am also thankful to all the thesis committee members, faculty members and staffs of S. N. Bose National Centre for Basic Sciences for their genuine cooperation and help.

I would like to express my deep gratitude to Prof. Chittaranjan Sinha, Department of Chemistry, Jadavpur University for his moral support, affection and encouragement from my graduation days.

I would like to thank all of my lab mates for their assistance in my research. I am especially thankful to my senior Sankar Das for his constant encouragement and support to enrich my research work. I am also thankful to Kanika, Sourav Da and Arindam Da for their generous help in every moment. I would like to express my sincere thanks to Shakti Da, Samik Da, Dipayan Da, Amit Da and Urmi Di for their technical support in material characterization during my research work. I would like to thank all of my SNB friends, seniors and juniors for providing a wonderful and friendly environment in campus.

I am grateful to all of my teachers for their inspirational teaching in ethics and discipline in life. Especially, I would like to acknowledge Arup sir and Asish sir who motivated me to study chemistry and carry out research work. I would like to acknowledge Rajkumar Da from IACS for his sincere help in various aspects in my research work. I would like to thank Basudeb Da, Chiranjit Da and Chandana Di for their sincere assistance.

I am thankful to all of my friends particularly Prosenjit, Sourav, Utsav, Kingshuk, Pitambar, Souvik and Uddalok for their memorable, pleasant and perpetual refreshment and support during this journey.

I gratefully acknowledge Department of Science and Technology, Govt. of India and S. N. National Centre for Basic Sciences for providing me fellowship and research facilities.

I would like to thank everybody who helped me for the successful realization of the thesis and express my sincere apology to anyone if I have unintentionally missed him/her.

Last but not the least, I express my deep sense of gratitude to my parents and my sister for their unconditional love, encouragement and mental support in all difficult moments of my life. Without their sacrifices, guidance and blessings, the thesis would not have taken its shape. I am also thankful to all of my family members for their cheerful company and moral support over the years of my study.

Arnab Samanta

Department of Chemical, Biological and Macromolecular Sciences,

S. N. Bose National Centre for Basic Sciences,

Salt Lake, Kolkata 700106, India

List of Publications:

1. **A. Samanta**, S. Das and S. Jana, Doping of Ni in α-Fe_2O_3 Nanoclews to Boost Oxygen Evolution Electrocatalysis. ***ACS Sustainable Chem. Eng.*** 2019, 7, 12117-12124.

2. **A. Samanta**, S. Das and S. Jana, Ultra-Small Intermetallic NiZn Nanoparticles: A Nonprecious Metal Catalyst for Efficient Electrocatalysis. ***Nanoscale Adv.*** 2020, 2, 417-424.

3. **A. Samanta** and S. Jana, Ni, Co and Mn-Doped Fe_2O_3 Nano-Parallelepipeds for Oxygen Evolution. ***ACS Appl. Nano Mater.*** 2021, 4, 5131-5140.

4. **A. Samanta**, S. K. Pal and S. Jana, Synthesis of Template-Free Iron Oxyhydroxide Nanorods for Sunlight-Driven Photo-Fenton Catalysis. ***ACS Omega*** 2021, 6, 27905-27912.

5. **A. Samanta**, S. K. Pal and S. Jana, Exploring Flowery MnO_2/Ag Nanocomposite as an Efficient Solar-Light-Driven Photocatalyst. ***New J. Chem.*** 2022, 46, 4189-4197.

6. **A. Samanta**, S. Das and S. Jana, Exploring β-FeOOH Nanorods as an Efficient Adsorbent for Arsenic and Organic Dyes. ***ChemistrySelect*** 2018, 3, 2467-2473.

7. S. Das, **A. Samanta**, S. Jana, Light-Assisted Synthesis of Hierarchical Flower-Like MnO_2 Nanocomposites with Solar Light Induced Enhanced Photocatalytic Activity. ***ACS Sustainable Chem. Eng.*** 2017, 5, 9086-9094.

8. S. Das, **A. Samanta**, G. Gangopadhyay and S. Jana, Clay-Based Nanocomposites as Recyclable Adsorbent toward Hg(II) Capture: Experimental and Theoretical Understanding. ***ACS Omega*** 2018, 3, 6283-6292.

9. S. Das, **A. Samanta** and S. Jana, Light-Driven Synthesis of Uniform Dandelion-Like Mesoporous Silica Nanoflowers with Tunable Surface Area for Carbon Dioxide Uptake. ***Chem. Eng. J.*** 2019, 374, 1118-1126.

10. A. Modak, S. Das, D. K. Chanda, **A. Samanta** and S. Jana, Thiophene Containing Microporous and Mesoporous Nanoplates for Separation of Mercury from Aqueous Solution. ***New J. Chem.*** 2019, 43, 3341-3349.

11. S. Das, **A. Samanta**, K. Kole, G. Gangopadhyay and S. Jana, MnO_2 Flowery Nanocomposites for Efficient and Fast Removal of Mercury(II) From

Aqueous Solution: A Facile Strategy and Mechanistic Interpretation. ***Dalton Trans.*** 2020, 49, 6790-6800.

12. K. Kole, S. Das, **A. Samanta** and S. Jana, Parametric Study and Detailed Kinetic Understanding of CO_2 Adsorption over High-Surface-Area Flowery Silica Nanomaterials. ***Ind. Eng. Chem. Res.*** 2020, 59, 21393-21402.

13. K. Kole, A. Halder, S. Singh, **A. Samanta**, S. Das, A. K. Kundu, D. Bhattacharyya, S. K. Pal and S. Jana, Chromogenic-Functionalized Silica Nanoflower Composites for the Detection of Carbon Dioxide. ***ACS Appl. Nano Mater.*** 2020, 3, 4321-4328.

14. S. Ghosh, A. Modak, **A. Samanta**, K. Kole and S. Jana, Recent Progresses in Materials Development for CO_2 Conversion: Issues and Challenges. ***Mater. Adv.*** 2021, 2, 3161-3187.

[(1-5) Included in Thesis]

Book Chapter:

1. **A. Samanta** and S. Jana, Nanoscale Alloys and Intermetallics: Recent Progresses in Catalysis, 21st Century Nanoscience-A Handbook: Exotic Nanostructures and Quantum Systems (Volume Five), CRC Press (Taylor & Francis Group), 2020.

List of Patents:

1. S. Das, **A. Samanta** and S. Jana, A Method of Fabricating Monodispersed Silica Nanoflowers for Carbon Dioxide Adsorption. [Patent Granted in 2021; Patent No. 370791; Patent Application No. 201831048458]

2. S. Das, **A. Samanta** and S. Jana, An Improved Method for the Synthesis of δ-MnO_2 Nanocomposites with Enhanced Photocatalytic Activity. [Patent Granted in 2021; Patent No. 377714; Patent Application No. 201731040027]

In this thesis, synthesis and characterization of nanoscale alloys and metal oxides along with their potential application in the field of catalysis have been discussed. The never ending energy demands provoke to the researchers for the production of clean and renewable energy via water splitting as a substitute to the fossil fuels. Over recent years, extensive efforts have been put forward to pursue and design noble-metal-free durable and low-cost electrocatalysts as alternatives to the commonly used state-of-the-art electrocatalysts. Here, NiZn alloys were prepared via thermal decomposition technique through chemical conversion of Ni nanoparticles (NPs) and explored as electrocatalysts for oxygen evolution reaction. The electrocatalytic activity of NiZn alloy was studied by tuning the composition of constituent elements, which demonstrated that the ordered intermetallic NiZn exhibited superior activity compare to the disorder NiZn alloy or only pure Ni NPs. In a step-wise fashion, novel Ni doped iron oxide (Ni-Fe_2O_3) nanoclews were synthesized based on a simple light driven route to boost the electrocatalytic activity of pristine iron oxide (Fe_2O_3) nanoclews for oxygen production. Another interesting finding is the fabrication of Ni-, Co-, and Mn-doped iron oxide nano-parallelepipeds synthesized via a light assisted solution chemistry pathway without employing any template molecule to investigate the role of different dopants on the intrinsic property of the pristine iron oxide parallelepipeds towards oxygen evolution reaction. The other major finding is the design of new low-cost catalysts for the degradation of toxic organic pollutants, since their contamination in water has become a serious environmental and health issues. To address this issue, iron oxyhydroxide nanorods were prepared via a facile route without employment of any template molecule and used as photocatalyst for solar light driven photo-Fenton reaction towards the degradation of organic dyes. Likewise, an efficient and simple approach was developed to fabricate flower-like metal oxide/noble metal nanocomposites to boost the photocatalytic activity of the pristine metal oxide for the degradation of refractory pollutants, which further offered an attractive route in the field of waste water treatment under renewable solar light.

Keywords: Nanoscale alloys and metal oxides, Nanoclews, Nano-parallelepipeds, Nanorods, Nanocomposites, Electrocatalysis, Photocatalysis.

****

Chapter 1

Introduction

1.1 Nanoscience and Nanotechnology

During last few decades, nanoscience and nanotechnology are the fast growing disciplines in the scientific and technological research area. The term "nano" which is a Greek word, means dwarf or extremely small. One nanometer (nm) is one billionth of a meter (10^{-9} m) which is one thousand times smaller than a micron. Historical features of nanoscience and nanotechnology are introduced by Richard Feynman with his famous 1959 lecture. Nanoscience and nanotechnology are the study and application that deal with extremely small sized objects and systems. It is basically an interdisciplinary subject which covers the other science fields, such as chemistry, biology, physics, biotechnology, materials science and engineering etc. It has the potential for modernizing the traditions where materials and products are produced and the variety and type of functionalities can be accessed. It has a substantial commercial impression and importance, which will definitely upsurge in the near future.

1.2 Nanomaterials

Normally, if the size of the particles is in the range of 1-100 nm in any dimensions, they are called nanoparticles or nanomaterials. In nanomaterials, the surface or interface properties dominate over the bulk properties. About 160 years ago, Michael Faraday's legendary discovery illustrated that the opportunity and use of metals could be further extended when they were present in the form of nanomaterials. Nanoparticles (NPs) are comprised of a few hundred up to several thousand of atoms and they are more attractive to a large community of researchers due to their high surface-to-volume ratio and the exciting surface atomic activity. In a finely divided state, as in the form of nanocrystals,

metals exhibit intriguing electronic, optical, magnetic and catalytic properties. Narrow size distribution, stabilization and unique property of nanomaterials make them more attractive compared to the bulk. All these characteristics provoke to the researchers in developing several strategies for improving the synthesis and properties of NPs. The interest in preparation of NPs has increased year after year due to their distinctive electronic, optical, mechanical, magnetic and chemical properties compared to those of the bulk materials. The properties of NPs depend on their external structure (e.g.; size, shape and uniformity) and they can be explored in different valuable applications, ranging from catalysis,[1,2] plasmonics,[3] biosensing,[4] transportation,[5] optics,[6] magnetic application[7] to data storage.[8]

1.3 Classification of Nanomaterials

Nanomaterials can be defined as nanostructure or as nanocomposites material. Depending on the dimension, the nanomaterials can be classified as zero dimensional, one dimensional, two dimensional, three dimensional nanomaterials. Different dimensional nanomaterials are schematically presented in Figure 1.1.

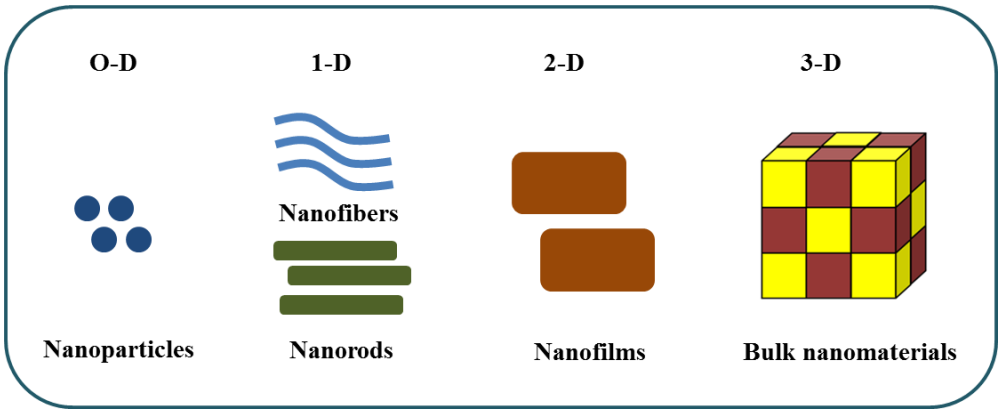

Figure 1.1: Schematic presentation of various dimensional nanomaterials.

1.3.1 Zero Dimensional (0-D)

Zero dimensional (0-D) nanomaterials have nano-dimensions (less than 100 nm) in all the three directions. Most of these zero dimensional nanomaterials are spherical in size. Metallic nanoparticles, such as gold and silver nanoparticles and quantam dots are the ideal examples of the zero dimensional nanomaterials.

1.3.2 One Dimensional (1-D)

In one dimensional (1-D) nanostructures, one of the dimensions is outside the nanometer range. These classes of materials include nanorods, nanowires and nanotubes. These nanostructures are long up to several micrometers in length, but their diameter is in the nanometer scale.

1.3.3 Two Dimensional (2-D)

In two dimensional (2-D) nanostructures, two dimensions are of outside the nanometer range. These nanomaterials include nanofilms, nanolayers and nanocoatings. The area of the nanofilms can be large up to several square micrometers, but the thickness of the nanofilms is always in in the nanometer range.

1.3.4 Three Dimensional (3-D)

In three dimensional (3-D) nanomaterials, all three dimensions are not in the nanoscale region. These structures include bulk materials which are composed of the individual blocks. These individual blocks are in the nanometer scale (1-100 nm).

1.4 Synthetic Strategies of Nanoparticles

Synthesis of nanoparticles and nanostructures are the important aspect of nanoscience and nanotechnology since their properties depend on their size, shape, morphology and stoichiometry. The controllable synthesis of nanoparticles (NPs) is very challenging task

to the researchers. The most commonly used techniques to prepare NPs are broadly categorized into two methods; one is top-down method and another is bottom-up method. A schematic presentation of the 'top-down' and 'bottom-up' methods is shown in Figure 1.2. These two methods are mainly used extensively to achieve NPs having specific size and well-defined surface composition. In the present time, research interest has mainly been focused to develop a reproducible synthetic approach for the preparation of NPs. In this context, top-down methods yield NPs having wide size distribution with relatively larger size and inconsistent catalytic activity. On the other hand, bottom-up methods are the most convenient ways to control the particle size during the synthesis of NPs and thus possess excellent catalytic activity.

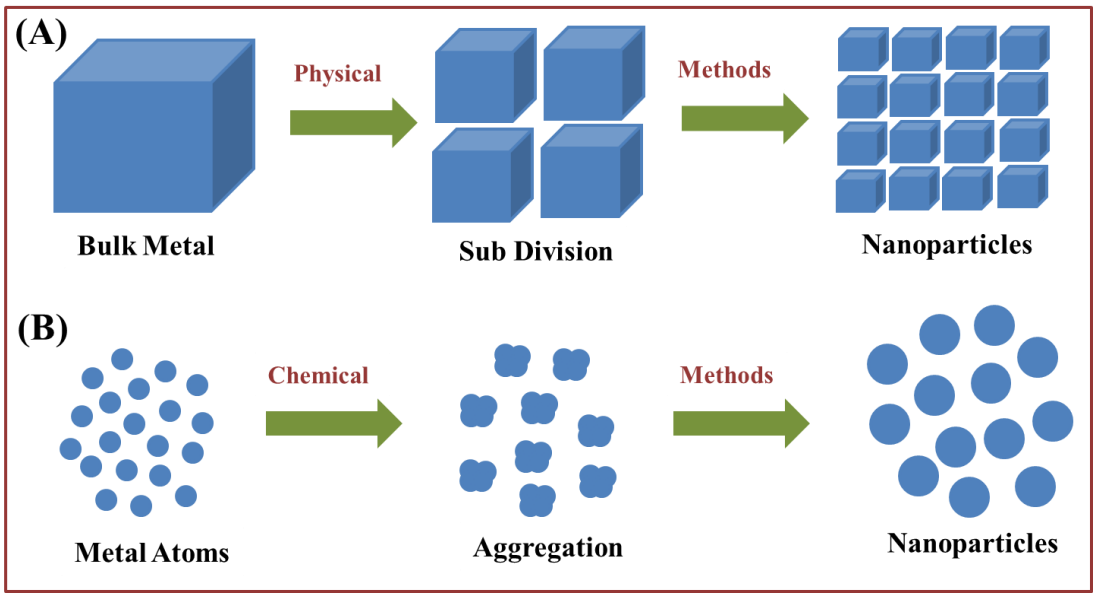

Figure 1.2: Schematic representation of the (A) top-down and (B) bottom-up methods.

1.4.1 Top-Down Methods

Top-down method is basically a physical method, where bulk material is broken down into nanoscale structures or particles. The major disadvantage of this method is the imperfection of surface structure together with wide size distribution. These disadvantages result in extra challenges to fabricate desired nanoparticles. This method actually leads to the bulk preparation of nanomaterials. Various types of lithographic

techniques (such as, photo-, ion beam-, electron-beam or X-ray-lithography), etching, grinding and ball milling processes are the most well-known examples of top-down approaches.[9-13] Among the various techniques, lithography has widely been used for the manufacturing of different electronic components, like computer chips, hard drives, CD and DVD players etc.

1.4.2 Bottom-Up Methods

Bottom-up method is basically a chemical method, where nanostructures are formed due to assemble of several atoms and molecules by carefully controlled chemical reactions. The most universally used synthetic process is the chemical reduction of metal salts. This process is frequently used to prepare most of the metal NPs, because this process leads to the formation of NPs with uniform size, shape and distribution. The capability to assemble nanoscale functional building blocks is useful and effective way for the scientific community to develop valuable materials with specific physical and chemical properties. Wet chemical synthesis, self-assembly, molecular fabrication and electrodeposition are all examples of bottom-up techniques. Generally, in wet chemical synthesis, an aqueous solution of ionic metal salt is reduced to its corresponding atom by using appropriate reducing agents, like sodium borohydride,[14] sodium citrate,[15] hydrazine hydrate,[16] aldehydes,[17] alcohols,[18] di-ketones,[19] sugars[20] etc.

1.5 Important Properties of Nanomaterials

Nanomaterials (NMs) have acquired great interest to the researchers because of the evolution of new phenomena and significant improvement of various properties as compared to their bulk counterpart. Due to large surface area to volume ratio and quantum confinement effect, NMs interact with each other, surrounding substances, light, electric and magnetic field in different way. The properties of NMs are significantly different from their corresponding bulk materials due to large fraction of surface atoms,

high surface energy, reduced imperfections and spatial confinement. Moreover, size, morphology and structure of NPs are not only responsible to govern their properties but also play an important role in controlling their reactivity.

1.5.1 Surface Properties

Surfaces and interfaces play a very significant role for particles or structures as they progress towards smaller dimensions. With decreasing particles size, an enormous percentage of all the atoms in a nanoparticle are exposed to the surfaces, indicating that NP surface and interface effects become more significant. Moreover, when a bulk material is divided into individual NP, surface area increases with the reduction of particle size from the bulk to nano without any change in volume. Thus, there is a substantial increase in the surface area to volume ratio (S/V) with the decrease in particle size. If we consider a spherical particle having radius r, then the surface area (S) and volume (V) of the particle will be $4\pi r^2$ and $(4/3)\pi r^3$ respectively. Therefore, the surface to volume (S/V) ratio of the particle will be (3/r). The surface to volume ratio of a particle is basically inversely proportional to radius of the particles. Hence, with decreasing particle size, surface to volume (S/V) ratio increases. In case of NPs, due to the presence of large percentage of surface atoms along with increased S/V ratio, the surface of NPs is very sensitive compare to their bulk counterparts. For surface chemistry, the chemical environment present at the surface of a NP plays a crucial role in determining the various properties, like chemical reactivity, adhesion, gas storage, catalytic efficacy etc.

1.5.2 Optical Properties

Another most attractive and valuable feature of NPs is their optical property. Application of nanomaterials based on their optical properties includes optical detector, imaging, laser, solar cell, photocatalysis etc. The optical properties of the NPs are influenced by their size, shape, surface characteristics and interaction with the surrounding environment. Generally, NPs have unusual optical properties, such as, colour,

luminescence and non-linear optical properties. For an example, the color of gold NPs depends on their sizes. The color of colloidal suspension of gold NPs changes with the size of the particle. The color of the gold NPs is purple when their size is greater than 20 nm and the color becomes red for 10-20 nm gold NPs. For 2-5 nm gold NPs, the color is yellow. Surface plasmon resonance (SPR) generally found in plasmonic metal NPs. SPR is an optical phenomenon and arises due to the interaction of conduction electrons of metal NPs with the incident photons of specific wavelength, resulting in the collective oscillations of the free conduction band electrons. In SPR, surface electromagnetic waves propagate in parallel to the metal dielectric interfaces. The frequency and width of the surface plasmon absorption depend on the size and shape, dielectric constant and the surrounding medium of the metal NPs.[21,22] Noble metals, like gold, silver and copper NPs exhibit a strong plasmon resonance in visible region, while most of the transition metals display a broad and weakly resolved absorption band in the ultraviolet region.[23,24] For colloidal solution of CdSe-CdS core-shell NPs, the fluorescence can be tuned by regulating their particle size. When the diameter of the NP is 1.7 nm, it exhibits blue fluorescence, whereas red fluorescence is observed for 6 nm particle size.[25]

1.5.3 Electronic Properties

The electronic properties of the NPs are varying and changing significantly from the bulk materials. Generally, in bulk metals, conduction band and valence band are overlapped and they easily conduct electrons due to the availability of continuum of energy levels above the Fermi energy level. However, as the bulk metal is reduced in size, the continuum of the electronic states vanishes and the energy levels become quantized. As a result, a band gap is created or enhanced and now the metal can act as semiconductor. Also semiconductor can behave as insulator when their size is further reduced.[26] In case of bulk semiconductors, Fermi level lies between two bands. Thus, excitation induces the generation of electron and hole that are delocalized over a number of atoms or ions constituting the materials. When the size of the semiconductor materials is smaller than Bohr radius, quantum

size effects arise, in which continuous conduction band becomes discrete. Fundamentally, their unique electronic features have been utilized to develop various types of modules for electronic, optoelectronic and information processing applications. Thus, the electronic properties of the semiconductor nanocrystals are extremely sensitive to the size of the materials.[27,28] Metal nanocrystals can exhibit insulating behavior because of the modification in their electronic structure as their size decreases. This phenomenon is known as size-induced metal-insulator transition. Electrical properties of some nanomaterials are correlated to their unique structures. For example, carbon nanotubes can behave as conductor or semiconductor according to their nanostructure.

1.5.4 Mechanical Properties

Mechanical properties generally depend on the density of dislocations, surface-to-volume ratio, chemical composition and grain size of a solid material. A decrease in grain size drastically changes the strength and hardness. With decreasing the particles size, the elastic strain energy is reduced. Nanoparticles exhibit interesting mechanical properties; like super plasticity, improvement of hardness and strength, fracture ductility etc. Grain boundary diffusion and sliding are the two crucial measures for super plasticity.[29] For example, single wall and multiwall carbon nanotubes (CNTs) are immensely stronger compare to steel because of their smaller size and lighter weight. CNTs have honeycomb-like lattice structure of graphite. Generally, defects or imperfections of a material lead to the decrease in the strength of the materials. Thus, nanomaterials, such as nanorods, nanowires etc. exhibit high mechanical strength due to their small cross section and less numbers of imperfections.[30]

1.5.5 Magnetic Properties

Materials which display some response under applied magnetic field are called magnetic materials. Nanomaterials demonstrate size-dependent magnetic properties that range from

ferromagnetic to paramagnetic to super paramagnetic. Below a critical size, when the size is reduced from bulk to nano, the magnetic particle can exist as a single magnetic domain where all the spins coupled in the alike directions. In this condition, NPs behave like single magnetic dipole. The large surface-to-volume ratio in NPs leads to a considerable fraction of atoms having diverse magnetic coupling with the nearby atoms, resulting to the differing in surface magnetic characteristics. Magnetic domains have dimensions in the range of 10-1000 nm, which are comparable to the size of nanocrystals. So if the crystal size approaches to the single domain dimension upon reduction of the particle size of ferromagnetic material, all the spins get aligned to each other, so the demagnetization becomes difficult. When the particle size becomes smaller than the single domain dimension, the force aligning the spins becomes so weak that it can't overcome thermal randomization in absence of any external magnetic field. This phenomenon is called superparamagnetism. Under an applied magnetic field, they are aligned and the alignment disappears once the external field is removed. Finite size effects and surface effects are the two vital issues that govern the magnetic properties of NPs.[31] It should be noted that magnetic coercivity is very much dependent with particle size. It gradually increases to a maximum value at a particular size and then quickly falls to zero once the particle size further decreases.[32,33] Magnetic nanoparticles are used in a wide range of applications, such as, imaging, bioprocessing, refrigeration, as well as high density magnetic storage media etc.

1.6 Applications of Nanoparticles

Nanoparticles have received enormous importance because of their fundamental scientific significance and many technological applications. Nanoparticles have exceptional catalytic, optical, magnetic and electrical properties owing to their nano-scale dimensions. They are applied in various fields, such as, catalysis,[34,35] sensing,[36,37] environmental remediation,[38,39] supercapacitor,[40] optical imaging,[41] drug delivery,[42] cancer therapy,[43] data storage[44] etc. Recently, S. Abouali et al. demonstrated a facile

electrospinning method with subsequent heat treatments to synthesize carbon nanofibers containing uniformly dispersed Co_3O_4 NPs as electrodes for high-performance supercapacitors.[45] C. A. Martinson et al. reported that cupric oxide NPs showed good adsorption capacity for both As(III) and As(V).[46] Likewise, S. Jana and co-workers reported excellent adsorption efficacy of MnO_2 NPs towards toxic Hg(II) ions over their surfaces.[47] Gold NPs are used for medicinal applications, like treatment of cancer therapy[48] and silver NPs have been used for the sensing application of Alzheimer's disease.[49] R. Demir et al. demonstrated a chemical bath deposition method to prepare CdS NPs for humidity sensing applications.[50] Microfluidically produced Au, Pd and AuPd NPs supported on SnO_2 were used for gas sensing applications.[51] Recently, mesoporous silica materials were used as drug delivery nanocarriers.[52] Amphiphilic polymer-coated hybrid nanoparticles composed of iron oxide and Au NPs were used as potential dual contrast agents for both computed tomography (CT) and magnetic resonance imaging (MRI).[53] A. C. Manna and co-workers demonstrated that zinc oxide NPs exhibit good antibacterial activities toward several microorganisms.[54] Among various types of applications, catalysis is one of the most important areas in which nanomaterials have been extensively used. In the past several years, several researches have explored nanomaterials as catalysts as well as catalyst supports.

1.6.1 Catalytic Application of Nanoparticles

Nanoparticles exhibit attractive catalytic activity compared to bulk materials due to their high surface-to-volume ratio and surface atomic activity. Now, the research activity is more centered towards the nano-catalysts with improved catalytic performances. When nano-catalyst is employed in a reaction, the selectivity of the reaction is enhanced. Generally, catalysis is categorized as either homogeneous catalysis or heterogeneous catalysis. Even though, there is high activity and selectivity in homogeneous catalysis, but a major disadvantage is the separation and recyclability of the catalyst along with agglomeration of the nano-catalyst during the reaction. This issue can be overcome by

using heterogeneous catalysts in which NPs are loaded onto a solid support or synthesized over the support. In heterogeneous catalysis, catalysts exhibit high activity and selectivity as well as it is very easy to recover the catalysts by facile way after the end of the reaction. In materials chemistry, nano-catalyst acts as a bridge between homogeneous and heterogeneous catalysts and it takes part in many challenging catalytic reactions. The features of nano-catalysts can be regulated by varying their morphologies, sizes and facets. Metal NPs are widely used as catalyst for several organic reactions.[55,56] Metal NPs (monometallic or multimetallic) are electronically conducting solids, which facilitate the electron transfer between oxidant and reductant.[57] The catalytic activity of the well-dispersed NPs is very much dependent on their size because of the several factors, such as, increase of the surface area with diminishing the particle size, variation of surface morphology particularly, contribution of different crystallographic planes, modification of the type of surface defects etc. [58,59] These effects are mainly prominent when size of the metal particles becomes in the nanometer range. Gold NPs exhibit good catalytic activity but their catalytic activity completely diminished as the particle size grows into the micrometer length. Several metal oxides NPs, like TiO_2,[60] CoO,[61] Co_3O_4,[62] MnO_2,[63] ZnO,[64] CuO,[65] Fe_2O_3,[66] Fe_3O_4,[67] SnO_2[68] etc. have extensively been used as catalyst in different chemical reactions. To boost the catalytic activity, the surface areas of metal or metal oxides NPs can be regulated by immobilized them over high surface area support material, which in turn produces nanocomposites.[69-71] Nanocomposites are a type of multiphase solid material in which at least one of the phases has dimension in the nanometer range. The method to fabricate nanocomposites seems to be a smart approach as it provides large surface area and high mechanical strength of the catalysts and the catalyst can be recycled easily by simple filtration technique after the completion of the reaction.

1.7 Alloys and Its Importance

Alloys are basically a solid solution of two or more metals or a physical mixture of metals, forming a single solid phase, whereas intermetallic compounds are atomically ordered alloys having well-defined compositions and crystal structures that are different from their constituent elements. It is therefore necessary to make NPs with precisely control over not only their particle size and shape but also their composition at the atomic and macroscopic dimensions to introduce a major effect on their activity. Their properties can be tuned by varying the atomic ordering, composition and size. They also find structural and non-structural applications, as corrosion resistant materials, high temperature gas turbine hardware, heat treatment fixtures, magnetic materials and hydrogen storage materials.[72] Ordered intermetallics provide uniform active sites on the same surface plane because of the better control over structure and electronic effects owing to their compositional and positional order.[73] The catalytic, electronic and optical properties of alloys are different from their corresponding monometallic counterpart due to the electronic effects and ensemble effects of two metals. Their properties depend on their size, shape and composition and have not been utilized in catalytic applications as compared to single-component metal NPs, but they possess enhanced activity and/or selectivity. Alloys and intermetallics have emerged as a class of novel materials with great opportunities towards the development of low-cost and high-performance industrial catalysts and have withdrawn enormous interest as a catalyst as they bring forth excellent catalytic activity in a wide range of inorganic to organic reactions. Their catalytic activity is generally regulated by their particle size, shape, morphology, crystal lattice parameters, specific surface area and modification of the type of surface defects. Well-faceted alloy NPs of Pt_3Ni and Pt_3Co were successfully synthesized by M. M. Tessema and co-workers without using any capping agents and the alloy NPs exhibit much greater activity than that of Pt standard catalyst for oxygen reduction electrocatalysis.[74] A facile approach was demonstrated to prepare composition-controlled monodisperse AgPd NPs, which showed high catalytic activity and durability for the dehydrogenation of formic acid.[75] Composition-dependent

catalytic study demonstrated that $Ag_{42}Pd_{58}$ NPs have the highest activity. Highly dispersed ultrafine NiCo bimetallic alloy NPs supported on porous SiO_2 frameworks have been successfully synthesized by using heteronuclear metal-organic frameworks (MOFs) as metal alloy precursors for furfuryl alcohol hydrogenation.[76] NiCo/SiO_2-MOF exhibits superior catalytic activity than that of Ni/SiO_2-MOF and Co/SiO_2-MOF. A facile one-step route was reported to fabricate carbon-coated FeCo alloy NPs embedded over single-walled carbon nanotubes (FeCo/SWCNTs).[77] The synthesized FeCo/SWCNT catalyst exhibits remarkable oxygen evolution reaction activity. Recently, X. Hao et al. reported a method to prepare Ni3Fe alloy NPs on N-doped porous graphene as a bifunctional electrocatalyst for rechargeable flexible solid zinc-air batteries.[78] However, to date, the preparation of tiny alloys of earth abundant transition metals with tunable composition through low temperature synthesis route remains a challenge.

1.8 Metal Oxides and Its Importance

During the last few decades, metal oxide NPs are gaining increasing scientific and technological importance as catalysts, capacitors, sensors or ceramic materials. Metal oxides represent one of the most important and widely employed catalysts, either as active phases or as support materials. Metal oxides are widely used for their acid-base as well as redox properties and they also establish themselves as the largest family of catalysts in heterogeneous catalysis. Their catalytic performance is extremely dependent on their morphology as well as crystallographic form. Among the various metal oxide catalysts, transition metal oxides have received great attention because of their superb structural flexibility along with their unique chemical and physical properties. They are significantly important to design new functional and smart materials.[79] Particularly, nanoscale transition metal oxides have widely been used in a variety of fundamental research and technological applications because of their exceptional properties as a result of their nanostructures.[80,81] Their unique properties are associated to the presence of

transition metals with mixed valences. As a result, a long-standing effort has been made for the synthesis of monodisperse metal oxide NPs by exploiting them as convenient nanobuilding blocks in constructing ordered superlattice assemblies with advanced functions.[82] In this thesis, mainly the synthesis and catalytic application of nanoscale iron oxide and manganese dioxide were discussed.

Iron is the fourth most abundant element and the second most abundant metal after aluminium in the Earth's crust. Therefore, it stands as the backbone of current infrastructure. In human body, iron is found within erythrocytes as a constituent of heme, which acts as the fundamental porphyrin prosthetic group of hemoglobin that helps O_2 transport.[83] Generally, iron oxides are extensively utilized in many fields due to inexpensiveness and non-toxic nature. They play a very significant role in many biological and geological processes. In view of numerous vital factors (like, abundance, cost, toxicity, environmental compatibility) to use the nanomaterials in the practical application, iron oxide stands out among various materials and has been extensively used in different fields. In nature, iron oxides are available in many forms, like - Fe_2O_3, Fe_3O_4, and FeOOH. It is already established that shape of the nanocrystals has vital role in different catalytic reactions. To demonstrate this, three types of α-Fe_2O_3 oxides with dissimilar micromorphologies were prepared using a simple solvothermal method and the synthesized nanostructures were employed in the oxidation of ethane.[84] Nano sphere-like α-Fe_2O_3 demonstrates better catalytic activity in the oxidation of ethane than that of nanocube-like α-Fe_2O_3 and nanorod-like α-Fe_2O_3 because of the more amounts of oxygen vacancies and lattice defects. Fe_3O_4 magnetic NPs were used as catalyst for the catalytic oxidation of phenol and aniline from aqueous solution.[85] Recently, pristine- and metal-doped β-FeOOH nanorods were prepared via a facile method at ambient temperature and the prepared nanorods were used as catalysts for water oxidation.[86]

Apart from iron oxides, nanoscale manganese oxides are receiving growing potential applications in several areas, such as, catalysis, gas sensors, energy storage, adsorption, lithium-ion batteries, magnetics etc. They exhibit unique properties because of the

multiple valences of manganese (Mn^{2+}, Mn^{3+} and Mn^{4+}) together with strong oxidizing ability. Manganese oxides are widely used as catalysts due to their abundance in nature, acid resistance, low toxicity, narrow bandgap, low cost and high environmental compatibility. Their performance is very much dependent on their morphology as well as crystallographic forms. Manganese dioxides (MnO_2) are available in different forms, such as α-, β-, γ-, δ-, and ε-MnO_2. MnO_2 having structural flexibility along with strong oxidation ability, serves as a promising photocatalyst to degrade the organic pollutants in wastewater. P. Yu et al. reported a low temperature simple hydrothermal method to fabricate sea urchin shaped α-MnO_2 and 3D clew-like ε-MnO_2 nanostructures for electrochemical supercapacitors without employing any template and surfactant molecule.[87] Hierarchical hollow manganese dioxide nanosheets with well-controlled 3D morphologies are prepared by J. B. Fei et al.[88] The as-synthesized MnO_2 nanomaterials demonstrate good adsorbing ability to remove organic dye. F. Cheng et al. reported a facile hydrothermal route to prepare MnO_2 nanomaterials of different crystallographic types and crystal morphologies.[89] These MnO_2 nanomaterials are used as the cathode active materials of primary and rechargeable batteries. However, it still remains a challenging task to design facile and cost-effective methods to prepare nanostructures of metal or metal oxide with high activity.

1.9 Objective of the Thesis

Nanoscale alloys and metal oxides have fascinated to the scientific as well as technological communities not only for their fundamental scientific importance but also for the many technological applications that originate from their unusual and fascinating properties. Additionally, preparation of well-defined monodispersed NPs with controllable size and shape using a low-cost facile technique is the current goal in modern catalysis. Thus, the development of the solution based and morphologically controllable synthesis route to make uniform NPs is the pressing need to explore their potential application mainly in catalysis. Thus, our aim is to design economical and facile methods

for the synthesis of nanoscale uniform alloys and metal oxides for the exploration in electrocatalysis and/or photocatalysis.

The never ending energy demands provoke to the researchers for the production of clean and renewable energy via water splitting as a substitute to the fossil fuels, resulting in a challenging direction to pursue and subsequently design of efficient and renewable energy conversion systems. Over recent years, extensive efforts have been put forward to pursue and design noble-metal-free durable and low-cost electrocatalysts, including transition metals,[90,91] metal oxides,[92,93] phosphides,[94,95] layered double hydroxides,[96,97] metal dichalcogenides,[98] heteroatom-doped carbon matrix,[99] and so on as alternatives to the state-of-the-art expensive electrocatalysts (RuO_2 or IrO_2). Among the numerous catalysts, transition-metal oxides are one of the important classes of materials that possess different oxidation states and coordination environments,[100-103] resulting in tunable electrocatalytic activity together with long-term stability. They have triggered considerable attention from the researchers on account of their intriguing properties, abundance in earth, environmental friendliness, easy preparation, controllable morphology, and superb stability. Apart from transition-metal oxides, nanocrystalline alloys and intermetallics have also emerged as a novel class of materials with high electrocatalytic activity.[104,105] Therefore, the development of cost-effective and high-performance electrocatalysts based on the transition metal oxides and alloys for oxygen production is of immense importance.

Again, in 21st Century, environmental pollution is a great concern to the living systems on the earth. Among various types of environmental pollutions, water pollution is a biggest threat to the aquatic lives as well as human health.[106] The source of water pollution increases with the civilization of the society. This is majorly due to the urban discharges together with industrial effluents mainly organic dyes immensely used in textile and food industries.[107] Organic dyes have very complex structure and they are very harmful due to their toxicity and non-biodegradability.[108,109] Apart from the hazardous effects, they can also hamper the photosynthesis of aquatic plants. Therefore, it

is necessary to degrade the organic dyes to minimize their bad impact on aqueous environment. Hence, it is an urgent need to develop effective and inexpensive wastewater treatment technology. Among the various wastewater treatment technologies, advanced oxidation process has received a great attention due to its strong oxidation ability and high efficacy.[110,111] For advanced oxidation process, designing of a photocatalyst using semiconductor materials with high activity and visible light absorption capability emerges as a promising approach. Moreover, the sun light driven photocatalysis is an ideal and cost-effective way by utilizing the renewable and endless solar energy for the degradation of toxic pollutants via low temperature approach.

1.10 Outline of the Thesis

The present thesis contained total eight chapters as the following.

In the **Chapter 1**, the importance of nanoscience and nanotechnology, synthetic procedures of nanomaterial along with the properties and applications of nanomaterials have been discussed.

In the **Chapter 2**, general outline of the instruments and methods used for the characterization of these nanomaterials have been demonstrated.

In the **Chapter 3**, a general route was developed to achieve ultrasmall Ni and corresponding $Ni_{0.7}Zn_{0.3}$ and NiZn NPs from commercially available reagents via a solution-mediated reaction approach. After characterizing them using various physical methods, their electrocatalytic activities were studied towards oxygen evolution reaction (OER) in detail. It was observed that intermetallic NiZn NPs displayed higher catalytic activity toward OER than that of $Ni_{0.7}Zn_{0.3}$, pure Ni NPs and even the commercial RuO_2. The present study demonstrated that activity of the alloys upsurged from the composition of the constituents which governed their OER performances. Finally, the electrocatalytic efficacy of NiZn was compared with those of the reported Ni-based electrocatalysts.

In the **Chapter 4**, a unique synthesis route was demonstrated to prepare α-Fe_2O_3 nanoclews using a simple light-driven solution chemistry route without using any template molecule and the as-prepared nanoclews were explored as an OER electrocatalyst. To boost the catalytic activity, Ni was doped in α-Fe_2O_3 nanoclews, resulting in the formation of Ni-Fe_2O_3 with analogous morphology. Elemental mapping indicated uniform distribution of Ni with the basic elements (Fe and O) throughout the nanoclews, providing more exposed catalytic active sites as a result of their unique morphology. Outstanding OER activity with enduring structural and morphological stability of the Ni-Fe_2O_3 nanoclews was demonstrated in detail and compared with the present-day OER catalyst.

In the **Chapter 5**, a facile synthesis route was designed to prepare different transition metals doped iron oxide parallelepipeds via a light driven bottom-up chemistry approach deprived of any template molecule. For this purpose, iron oxide (Fe_2O_3), Ni doped iron oxide (Ni-Fe_2O_3), Co doped iron oxide (Co-Fe_2O_3) and Mn doped iron oxide (Mn-Fe_2O_3) nanostructures were successfully prepared. A closer inspection to the morphology clearly authenticated that hierarchical parallelepiped like morphology of M-Fe_2O_3 was evolved due to assembly of several small nanorods. After detailed characterization, they were explored as electrocatalysts in basic medium for OER and their OER activity was compared. Among all the as-prepared catalysts, Ni-Fe_2O_3 showed highest activity and stability during oxygen production owing to owing to the higher electronegativity of Ni and the optimal interaction strength of Ni with hydroxyl ions.

In the **Chapter 6**, a simple route was established to synthesize iron oxyhydroxide nanorods without employing any templating agent via a light driven hydrolysis route. After characterization of the synthesized nanorods by different physical techniques, the photocatalytic activity of as-synthesized β-FeOOH nanorods was explored as a photo-Fenton catalyst under sunlight for the degradation of organic dyes. The effect of pH of the solution, catalyst dosages and concentration of H_2O_2 on their photocatalytic activity has also been demonstrated. The overall dye degradation under solar light irradiation

using β-FeOOH NRs proceeded via photo-generated reactive oxygen species. Our approach thus pointed to an excellent photo-catalytic activity of β-FeOOH nanorods during the photo-Fenton reaction.

In the **chapter 7**, a facile and effective route was developed for the fabrication of hierarchical MnO_2 and MnO_2/Ag nanocomposites (NCs) over the surface of HNTs. The photocatalytic activity of both MnO_2 and MnO_2/Ag NCs was investigated under natural sunlight irradiation for the degradation of organic dye. It was observed that MnO_2/Ag NCs exhibit better photocatalytic activity compare to only MnO_2. Furthermore, repetitive experiments were carried out to establish the reusability and followed by stability of the catalyst. The detail mechanism of the degradation process was illustrated in presence of several scavengers as well as additional supplementary oxygen source, signifying the generation of reactive oxygen species during photocatalysis. Thus, this present approach demonstrated a facile and unique way to fabricate metal oxide/noble metal NCs to boost the photocatalytic activity of the pristine metal oxide.

In the **Chapter 8**, all the research works described in this thesis have been summarized and pointed out the probable avenues for future investigations.

1.11 References

(1) Wittstock, A.; Zielasek, V.; Biener, J.; Friend, C. M.; Bäumer, M. Nanoporous Gold Catalysts for Selective Gas-Phase Oxidative Coupling of Methanol at Low Temperature. *Science* 2**010**, *327*, 319-322.

(2) Jana, S. Advances in Nanoscale Alloys and Intermetallics: Low Temperature Solution Chemistry Synthesis and Application in Catalysis. *Dalton Trans.* **2015**, *44*, 18692-18717.

(3) Cobley, C. M.; Skrabalak, S. E.; Campbell, D. J.; Xia, Y. Shape-Controlled Synthesis of Silver Nanoparticles for Plasmonic and Sensing Applications. *Plasmonics* **2009**, *4*, 171-179.

(4) Bruchez, M.; Moronne, M.; Gin, P.; Weiss, S.; Alivisatos, A. P. Semiconductor Nanocrystals as Fluorescent Biological Labels. *Science* **1998**, *281*, 2013-2016.

(5) Hamedi Shokrlu, Y.; Babadagli, T. In-Situ Upgrading of Heavy Oil/Bitumen During Steam Injection by Use of Metal Nanoparticles: A Study on In-Situ Catalysis and Catalyst Transportation. *SPE Reservoir Eval. Eng.* **2013**, *16*, 333-344.
(6) Wang, J.; Gudiksen, M. S.; Duan, X.; Cui, Y.; Lieber, C. M. Highly Polarized Photoluminescence and Photodetection from Single Indium Phosphide Nanowires. *Science* **2001**, *293*, 1455-1457.
(7) Lu, A. H.; Salabas, E. E.; Schüth, F. Magnetic Nanoparticles: Synthesis, Protection, Functionalization, and Application. *Angew. Chem. Int. Ed.* **2007**, *46*, 1222-1244.
(8) Ahn, E. C.; Wong, H. S. P.; Pop, E. Carbon Nanomaterials for Non-Volatile Memories. *Nat. Rev. Mater.* **2018**, *3*, 18009.
(9) Watt, F.; Bettiol, A. A.; Van Kan, J. A.; Teo, E. J.; Breese, M. B. H. Ion Beam Lithography and Nanofabrication: A Review. *Int. J. Nanosci.* **2005**, *4*, 269-286.
(10) Corbierre, M. K.; Beerens, J.; Lennox, R. B. Gold Nanoparticles Generated by Electron Beam Lithography of Gold(I)-Thiolate Thin Films. *Chem. Mater.* **2005**, *17*, 5774-5779.
(11) Feiertag, G.; Ehrfeld, W.; Freimuth, H.; Kolle, H.; Lehr, H.; Schmidt, M.; Sigalas, M. M.; Soukoulis, C. M.; Kiriakidis, G.; Pedersen, T.; Kuhl, J. Fabrication of Photonic Crystals by Deep X-Ray Lithography. *Appl. Phys. Lett.* **1997**, *71*, 1441-1443.
(12) Cho, K.; Chang, H.; Kil, D. S.; Kim, B.-G.; Jang, H. D. Synthesis of Dispersed $CaCO_3$ Nanoparticles by the Ultrafine Grinding. *J. Ind. Eng. Chem.* **2009**, *15*, 243-246.
(13) Amirkhanlou, S.; Ketabchi, M.; Parvin, N. Nanocrystalline/Nanoparticle ZnO Synthesized by High Energy Ball Milling Process. *Mater. Lett.* **2012**, *86*, 122-124.
(14) Huang, C. C.; Lo, S. L.; Lien, H. L. Zero-Valent Copper Nanoparticles for Effective Dechlorination of Dichloromethane using Sodium Borohydride as a Reductant. *Chem. Eng. J.* **2012**, *203*, 95-100.
(15) Qian, Y.; Wang, C.; Le, Z. G. Decorating Graphene Sheets with Pt Nanoparticles using Sodium Citrate as Reductant. *Appl. Surf. Sci.* **2011**, *257*, 10758-10762.
(16) Wu, X.; Xing, W.; Zhang, L.; Zhuo, S.; Zhou, J.; Wang, G.; Qiao, S. Nickel Nanoparticles Prepared by Hydrazine Hydrate Reduction and Their Application in Supercapacitor. *Powder Technol.* **2012**, *224*, 162-167.
(17) Skrabalak, S. E.; Wiley, B. J.; Kim, M.; Formo, E. V.; Xia, Y. On the Polyol Synthesis of Silver Nanostructures: Glycolaldehyde as a Reducing Agent. *Nano Lett.* **2008**, *8*, 2077-2081.
(18) Ayyappan, S.; Gopalan, R. S.; Subbanna, G. N.; Rao, C. N. R. Nanoparticles of Ag, Au, Pd, and Cu Produced by Alcohol Reduction of the Salts. *J. Mater. Res.* **1997**, *12*, 398-401.

(19) Kundu, S.; Pal, A.; Ghosh, S. K.; Nath, S.; Panigrahi, S.; Praharaj, S.; Pal, T. A New Route to Obtain Shape-Controlled Gold Nanoparticles from Au(III)-β-diketonates. *Inorg. Chem.* **2004**, *43*, 5489-5491.

(20) Nie, T.; Wu, H.; Wong, K. H.; Chen, T. Facile Synthesis of Highly Uniform Selenium Nanoparticles using Glucose as the Reductant and Surface Decorator to Induce Cancer Cell Apoptosis. *J. Mater. Chem. B* **2016**, *4*, 2351-2358.

(21) Kelly, K. L.; Coronado, E.; Zhao, L. L.; Schatz, G. C. The Optical Properties of Metal Nanoparticles: The Influence of Size, Shape, and Dielectric Environment. *J. Phys. Chem. B* **2003**, *107*, 668-677.

(22) Papavassiliou, G. C. Optical Properties of Small Inorganic and Organic Metal Particles. *Prog. Solid State Chem.* **1979**, *12*, 185-271.

(23) García, M. A. Surface Plasmons in Metallic Nanoparticles: Fundamentals and Applications. *J. Phys. D: Appl. Phys.* **2011**, *44*, 283001.

(24) Sá, J.; Tagliabue, G.; Friedli, P.; Szlachetko, J.; Rittmann-Frank, M. H.; Santomauro, F. G.; Milne, C. J.; Sigg, H. Direct Observation of Charge Separation on Au Localized Surface Plasmons. *Energy Environ. Sci.* **2013**, *6*, 3584-3588.

(25) Roduner, E. Size Matters: Why Nanomaterials are Different. *Chem. Soc. Rev.* **2006**, *35*, 583-592.

(26) Alivisatos, A. P. Perspectives on the Physical Chemistry of Semiconductor Nanocrystals. *J. Phys. Chem.* **1996**, *100*, 13226-13239.

(27) Halperin, W. P. Quantum Size Effects in Metal Particles. *Rev. Mod. Phys.* **1986**, *58*, 533-606.

(28) Simon, U. Charge Transport in Nanoparticle Arrangements, *Adv. Mater*. **1998**, *10*, 1487-1492.

(29) Kawasaki, M.; Langdon, T. G. Principles of Superplasticity in Ultrafine-Grained Materials. *J. Mater. Sci.* **2007**, *42*, 1782-1796.

(30) Edelstein, A. S.; Cammarata, R. C. *Nanomaterials: Synthesis, Properties and Applications*, Institute of Physics Publishing: Bristol, U.K., **1996.**

(31) Vazquez-Vazquez, C.; Lopez-Quintela, M. A.; Bujan-Nunez, M. C.; Rivas, J. Finite Size and Surface Effects on the Magnetic Properties of Cobalt Ferrite Nanoparticles. *J. Nanopart. Res.* **2011**, *13*, 1663-1676.

(32) Lee, J. S.; Cha, J. M.; Yoon, H. Y.; Lee, J. K.; Kim, Y. K. Magnetic Multi-Granule Nanoclusters: A Model System That Exhibits Universal Size Effect of Magnetic Coercivity. *Sci. Rep.* **2015**, *5*, 12135-12141.

(33) Kneller, E. F.; Luborsky, F. E. Particle Size Dependence of Coercivity and Remanence of Single-Domain Particles. *J. Appl. Phys.* **1963**, *34*, 656-658.

(34) Xia, Y.; Yang, H.; Campbell, C. T. Nanoparticles for Catalysis. *Acc. Chem. Res.* **2013**, *46*, 1671-1672.
(35) Gao, C.; Lyu, F.; Yin, Y. Encapsulated Metal Nanoparticles for Catalysis. *Chem. Rev.* **2021**, *121*, 834-881.
(36) Saha, K.; Agasti, S. S.; Kim, C.; Li, X.; Rotello, V. M. Gold Nanoparticles in Chemical and Biological Sensing. *Chem. Rev.* **2012**, *112*, 2739-2779.
(37) Gutés, A.; Hsia, B.; Sussman, A.; Mickelson, W.; Zettl, A.; Carraro, C.; Maboudian, R. Graphene Decoration with Metal Nanoparticles: Towards Easy Integration for Sensing Applications. *Nanoscale* **2012**, *4*, 438-440.
(38) Zhang, D.; Wei, S.; Kaila, C.; Su, X.; Wu, J.; Karki, A. B.; Young, D. P.; Guo, Z. Carbon-Stabilized Iron Nanoparticles for Environmental Remediation. *Nanoscale* **2010**, *2*, 917-919.
(39) Khin, M. M.; Nair, A. S.; Babu, V. J.; Murugan, R.; Ramakrishna, S. A Review on Nanomaterials for Environmental Remediation. *Energy Environ. Sci.* **2012**, *5*, 8075-8109.
(40) Zhao, F.; Wang, Y.; Xu, X.; Liu, Y.; Song, R.; Lu, G.; Li, Y. Cobalt Hexacyanoferrate Nanoparticles as a High-Rate and Ultra-Stable Supercapacitor Electrode Material. *ACS Appl. Mater. Interfaces* **2014**, *6*, 11007-11012.
(41) Wu, Y.; Ali, M. R.; Chen, K.; Fang, N.; El-Sayed, M. A. Gold nanoparticles in biological optical imaging. *Nano Today* **2019**, *24*, 120-140.
(42) Chavanpatil, M. D.; Khdair, A.; Panyam, J. Nanoparticles for Cellular Drug Delivery: Mechanisms and Factors Influencing Delivery. *J. Nanosci. Nanotechnol.* **2006**, *6*, 2651-2663.
(43) Sun, T.; Zhang, Y. S.; Pang, B.; Hyun, D. C.; Yang, M.; Xia, Y. Engineered Nanoparticles for Drug Delivery in Cancer Therapy. *Angew. Chem. Int. Ed.* **2014**, *53*, 12320-12364.
(44) Ditlbacher, H.; Krenn, J. R.; Lamprecht, B.; Leitner, A.; Aussenegg, F. R. Spectrally Coded Optical Data Storage by Metal Nanoparticles. *Opt. Lett.* **2000**, *25*, 563-565.
(45) Abouali, S.; Akbari Garakani, M.; Zhang, B.; Xu, Z. L.; Kamali Heidari, E.; Huang, J. Q.; Huang, J.; Kim, J. K. Electrospun Carbon Nanofibers with in Situ Encapsulated Co_3O_4 Nanoparticles as Electrodes for High-Performance Supercapacitors. *ACS Appl. Mater. Interfaces* **2015**, *7*, 13503-13511.
(46) Martinson, C. A.; Reddy, K. J.; Adsorption of arsenic(III) and arsenic(V) by Cupric Oxide Nanoparticles. *J. Colloid Interface Sci.* **2009**, *336*, 406-411.
(47) Das, S.; Samanta, A.; Kole, K.; Gangopadhyay, G.; Jana, S. MnO_2 Flowery Nanocomposites for Efficient and Fast Removal of Mercury(II) from Aqueous Solution: A Facile Strategy and Mechanistic Interpretation. *Dalton Trans.* **2020**, *49*, 6790-6800.

(48) Hirsch, L. R.; Stassord, R. J.; Bankson, J. A.; Sershen, S. R.; Rivera, B.; Price, R. E.; Hazle, J. D.; Halas, N. J.; West, J. L. Nanoshell-mediated Near-infrared Thermal Therapy of Tumors under Magnetic Resonance Guidance. *Proc. Natl. Acad. Sci.* **2003**, *100*, 13549-13554.

(49) Haes, A. J.; Hall, W. P.; Chang, L.; Klein, W. L.; Van Duyne, R. P. A Localized Surface Plasmon Resonance Biosensor: First Steps toward an Assay for Alzheimer's Disease. *Nano Lett.* **2004**, *6*, 1029-1034.

(50) Demir, R.; Okur, S.; Seker, M. Electrical Characterization of CdS Nanoparticles for Humidity Sensing Applications. *Ind. Eng. Chem. Res.* **2012**, *51*, 3309-3313.

(51) Tofighi, G.; Degler, D.; Junker, B.; Müller, S. A.; Lichtenberg, H.; Wang, W.; Weimar, U.; Barsan, N.; Grunwaldt, J.-D. Microfluidically Synthesized Au, Pd and AuPd Nanoparticles Supported on SnO_2 for Gas Sensing Applications. *Sens. Actuators, B* **2019**, *292*, 48-56.

(52) Manzano, M.; Vallet-Regí, M. Mesoporous Silica Nanoparticles for Drug Delivery. *Adv. Funct. Mater.* **2020**, *30*, 1902634.

(53) Kim, D.; Yu, M. K.; Lee, T. S.; Park, J. J.; Jeong, Y. Y.; Jon, S. Amphiphilic Polymer-Coated Hybrid Nanoparticles as CT/MRI Dual Contrast Agents. *Nanotechnology* **2011**, *22*, 155101.

(54) Raghupathi, K. R.; Koodali, R. T.; Manna, A. C. Size-Dependent Bacterial Growth Inhibition and Mechanism of Antibacterial Activity of Zinc Oxide Nanoparticles. *Langmuir* **2011**, *27*, 4020-4028.

(55) Mallampati, R.; Valiyaveettil, S. Eggshell Membrane-Supported Recyclable Catalytic Noble Metal Nanoparticles for Organic Reactions. *ACS Sustainable Chem. Eng.* **2014**, *2*, 855-859.

(56) Yan, N.; Xiao, C.; Kou, Y. Transition Metal Nanoparticle Catalysis in Green Solvents. *Coord. Chem. Rev.* **2010**, *254*, 1179-1218.

(57) Ghosh, S. K.; Mandal, M.; Kundu, S.; Nath, S.; Pal, T. Bimetallic Pt-Ni Nanoparticles Can Catalyze Reduction of Aromatic Nitro Compounds by Sodium Borohydride in Aqueous Solution. *Appl. Catal. A* **2004**, *268*, 61-66.

(58) Augustine, R. L.; O'Leary, S. T. Heterogeneous Catalysis in Organic Chemistry. Part 10. Effect of the Catalyst Support on the Regiochemistry of the Heck Arylation Reaction. *J. Mol. Catal. A: Chem.* **1995**, *95*, 277-285.

(59) Li, Y.; Boone, E.; El-Sayed, M. A. Size Effects of PVP-Pd Nanoparticles on the Catalytic Suzuki Reactions in Aqueous Solution. *Langmuir* **2002**, *18*, 4921-4925.

(60) Xun, S.; Ti, Q.; Jiao, Z.; Wu, L.; He, M.; Chen, L.; Zhu, L.; Zhu, W.; Li, H. Dispersing TiO_2 Nanoparticles on Graphite Carbon for an Enhanced Catalytic Oxidative Desulfurization Performance. *Ind. Eng. Chem. Res.* **2020**, *59*, 18471-18479.

(61) Zhao, Y.; Sun, B.; Huang, X.; Liu, H.; Su, D.; Sun, K.; Wang, G. Porous Graphene Wrapped CoO Nanoparticles for Highly Efficient Oxygen Evolution. *J. Mater. Chem. A* **2015**, *3*, 5402-5408.
(62) Grzelczak, M.; Zhang, J.; Pfrommer, J.; Hartmann, J.; Driess, M.; Antonietti, M.; Wang, X. Electro- and Photochemical Water Oxidation on Ligand-free Co_3O_4 Nanoparticles with Tunable Sizes. *ACS Catal.* **2013**, *3*, 383-388.
(63) Yamaguchi, Y.; Aono, R.; Hayashi, E.; Kamata, K.; Hara, M. Template-Free Synthesis of Mesoporous β-MnO_2 Nanoparticles: Structure, Formation Mechanism, and Catalytic Properties. *ACS Appl. Mater. Interfaces* **2020**, *12*, 36004-36013.
(64) Qamar, M.; Gondal, M. A.; Yamani, Z. H. Laser-Induced Efficient Reduction of Cr (VI) Catalyzed by ZnO Nanoparticles. *J. Hazard. Mater.* **2011**, *187*, 258-263.
(65) Zedan, A. F.; Mohamed, A. T.; El-Shall, M. S.; AlQaradawi, S. Y.; AlJaber, A. S. Tailoring the Reducibility and Catalytic Activity of CuO Nanoparticles for Low Temperature CO Oxidation. *RSC Adv.* **2018**, *8*, 19499-19511.
(66) Zheng, Y. H.; Cheng, Y.; Wang, Y. S.; Bao, F.; Zhou, L. H.; Wei, X. F.; Zhang, Y. Y.; Zheng, Q. Quasicubic α-Fe_2O_3 Nanoparticles with Excellent Catalytic Performance. *J. Phys. Chem. B* **2006**, *110*, 3093-3097.
(67) Veerakumar, P.; Muthuselvam, I. P.; Hung, C. T.; Lin, K. C.; Chou, F. C.; Liu, S. B. Biomass-Derived Activated Carbon Supported Fe_3O_4 Nanoparticles as Recyclable Catalysts for Reduction of Nitroarenes. *ACS Sustainable Chem. Eng.* **2016**, *4*, 6772-6782.
(68) Bhattacharjee, A.; Ahmaruzzaman, M. A Green Approach for the Synthesis of SnO_2 Nanoparticles and Its Application in the Reduction of p-Nitrophenol. *Mater. Lett.* **2015**, *157*, 260-264.
(69) Liao, G.; Fang, J.; Li, Q.; Li, S.; Xu, Z.; Fang, B. Ag-Based Nanocomposites: Synthesis and Applications in Catalysis. *Nanoscale* 2019, 11, 7062-7096.
(70) Chen, S.; Xiang, Y.; Peng, C.; Xu, W.; Banks, M. K.; Wu, R. Synthesis of a Novel Graphene-Based Gold Nanocomposite using PVEIM-*b*-PNIPAM as a Stabilizer And Its Thermosensitivity for the Catalytic Reduction of 4-Nitrophenol. *Inorg. Chem. Front.* **2019**, *6*, 903-913.
(71) Huang, J.; Zhang, L.; Chen, B.; Ji, N.; Chen, F.; Zhang, Y.; Zhang, Z. Nanocomposites of Size-Controlled Gold Nanoparticles and Graphene Oxide: Formation and Applications in SERS and Catalysis. *Nanoscale* **2010**, *2*, 2733-2738.
(72) Stoloff, N. S.; Liu, C. T.; Deevi, S. C. Emerging Applications of Intermetallics. *Intermetallics* **2000**, *8*, 1313-1320.
(73) Casado-Rivera, E.; Volpe, D. J.; Alden, L.; Lind, C.; Downie, C.; Vázquez-Alvarez, T.; Angelo, A. C.; DiSalvo, F. J.; Abruña, H. D. Electrocatalytic Activity of Ordered Intermetallic Phases for Fuel Cell Applications. *J. Am. Chem. Soc.* **2004**, *126*, 4043-4049.

(74) Carpenter, M. K.; Moylan, T. E.; Kukreja, R. S.; Atwan, M. H.; Tessema, M. M. Solvothermal Synthesis of Platinum Alloy Nanoparticles for Oxygen Reduction Electrocatalysis. *J. Am. Chem. Soc.* **2012**, *134*, 8535-8542.
(75) Zhang, S.; Onder, M.; Su, D.; Sun, S. Monodisperse AgPd Alloy Nanoparticles and Their Superior Catalysis for the Dehydrogenation of Formic Acid. Angew. Chem., Int. Ed. **2013**, *52*, 3681-3684.
(76) Wang, H.; Li, X.; Lan, X.; Wang, T. Supported Ultrafine NiCo Bimetallic Alloy Nanoparticles Derived from Bimetal-Organic Frameworks: A Highly Active Catalyst for Furfuryl Alcohol Hydrogenation. *ACS Catal.* **2018**, *8*, 2121-2128.
(77) Xie, D.; Chen, Y.; Yu, D.; Han, S.; Song, J.; Xie, Y.; Hu, F.; Li, L.; Peng, S. Single-Layer Carbon-Coated FeCo Alloy Nanoparticles Embedded in Single-Walled Carbon Nanotubes for High Oxygen Electrocatalysis. *Chem. Commun.* **2020**, *56*, 6842-6845.
(78) Hao, X.; Jiang, Z.; Tian, X.; Song, C.; Chen, S.; Hao, X.; Jiang, Z. J. Synthesis of Ultrasmall, Homogeneously Distributed Ni_3Fe Alloy Nanoparticles on N-Doped Porous Graphene as a Bifunctional Electrocatalyst for Rechargeable Flexible Solid Zinc-Air Batteries. *ACS Appl. Energy Mater.* **2020**, *3*, 12148-12161.
(79) Laurent, S.; Forge, D.; Port, M.; Roch, A.; Robic, C.; Vander Elst, L.; Muller, R. N.; Magnetic Iron Oxide Nanoparticles: Synthesis, Stabilization, Vectorization, Physicochemical Characterizations, and Biological Applications. *Chem. Rev.* **2008**, *108*, 2064-2110.
(80) Sun, S.; Zeng, H. Size-Controlled Synthesis of Magnetite Nanoparticles. *J. Am. Chem. Soc.* **2002**, *124*, 8204-8205.
(81) Ren, T. Z.; Yuan, Z. Y.; Hu, W.; Zou, X. Single Crystal Manganese Oxide Hexagonal Plates with Regulated Mesoporous Structures. *Microporous Mesoporous Mater.* **2008**, *112*, 467-473.
(82) Ge, J.; Hu, Y.; Biasini, M.; Beyermann, W. P.; Yin, Y. Superparamagnetic Magnetite Colloidal Nanocrystal Clusters. *Angew. Chem. Int. Ed.* **2007**, *46*, 4342-4345.
(83) Laurent, S.; Forge, D.; Port, M.; Roch, A.; Robic, C.; Vander Elst, L.; Muller, R. N. Magnetic Iron Oxide Nanoparticles: Synthesis, Stabilization, Vectorization, Physicochemical Characterizations, and Biological Applications. *Chem. Rev.* **2008**, *108*, 2064-2110.
(84) Jian, Y.; Yu, T.; Jiang, Z.; Yu, Y.; Douthwaite, M.; Liu, J.; Albilali, R.; He, C. In-Depth Understanding of the Morphology Effect of α-Fe_2O_3 on Catalytic Ethane Destruction. *ACS Appl. Mater. Interfaces* **2019**, *11*, 11369-11383.
(85) Zhang, S.; Zhao, X.; Niu, H.; Shi, Y.; Cai, Y.; Jiang, G. Superparamagnetic Fe_3O_4 Nanoparticles as Catalysts for the Catalytic Oxidation of Phenolic and Aniline Compounds. *J. Hazard. Mater.* **2009**, *167*, 560-566.

(86) Suzuki, T. M.; Nonaka, T.; Suda, A.; Suzuki, N.; Matsuoka, Y.; Arai, T.; Sato, S.; Morikawa, T. Highly Crystalline β-FeOOH(Cl) Nanorod Catalysts Doped with Transition Metals for Efficient Water Oxidation. *Sustain. Energy Fuels* **2017**, *1*, 636-643.
(87) Yu, P.; Zhang, X.; Wang, D.; Wang, L.; Ma, Y. Shape-Controlled Synthesis of 3D Hierarchical MnO_2 Nanostructures for Electrochemical Supercapacitors. *Cryst. Growth Des.* **2009**, *9*, 528-533.
(88) Fei, J. B.; Cui, Y.; Yan, X. H.; Qi, W.; Yang, Y.; Wang, K. W.; He, Q.; Li, J. B. Controlled Preparation of MnO_2 Hierarchical Hollow Nanostructures and Their Application in Water Treatment. *Adv. Mater.* **2008**, *20*, 452-456.
(89) Cheng, F.; Zhao, J.; Song, W.; Li, C.; Ma, H.; Chen, J.; Shen, P. Facile Controlled Synthesis of MnO_2 Nanostructures of Novel Shapes and Their Application in Batteries. *Inorg. Chem.* **2006**, *45*, 2038-2044.
(90) Wu, L. K.; Wu, W. Y.; Xia, J.; Cao, H. Z.; Hou, G. Y.; Tang, Y. P.; Zheng, G. Q. A Nanostructured Nickel-Cobalt Alloy with an Oxide Layer for an Efficient Oxygen Evolution Reaction. *J. Mater. Chem. A* **2017**, *5*, 10669-10677.
(91) Wang, Y.; Liu, D.; Liu, Z.; Xie, C.; Huo, J.; Wang, S. Porous Cobalt-Iron Nitride Nanowires as Excellent Bifunctional Electrocatalysts for Overall Water Splitting. *Chem. Commun.* **2016**, *52*, 12614-12617.
(92) Lu, Z.; Wang, H.; Kong, D.; Yan, K.; Hsu, P. C.; Zheng, G.; Yao, H.; Liang, Z.; Sun, X.; Cui, Y. Electrochemical Tuning of Layered Lithium Transition Metal Oxides for Improvement of Oxygen Evolution Reaction. *Nat. Commun.* **2014**, *5*, 4345.
(93) Vojvodic, A.; Nørskov, J. K. Optimizing Perovskites for the Water-Splitting Reaction. *Science* **2011**, *334*, 1355-1356.
(94) Kanan, M. W.; Surendranath, Y.; Nocera, D. G. Cobalt–Phosphate Oxygen-Evolving Compound. *Chem. Soc. Rev.* **2009**, *38*, 109-114.
(95) Wasalathanthri, R. N.; Jeffrey, S.; Awni, R. A.; Sun, K.; Giolando, D. M. Electrodeposited Copper-Cobalt-Phosphide: A Stable Bifunctional Catalyst for both Hydrogen and Oxygen Evolution Reactions. *ACS Sustainable Chem. Eng.* **2018**, *7*, 3092-3100.
(96) Qiao, C.; Zhang, Y.; Zhu, Y.; Cao, C.; Bao, X.; Xu, J. One-Step Synthesis of Zinc-Cobalt Layered Double Hydroxide (Zn-Co-LDH) Nanosheets for High-Efficiency Oxygen Evolution Reaction. *J. Mater. Chem. A* **2015**, *3*, 6878-6883.
(97) Song, F.; Hu, X. Exfoliation of Layered Double Hydroxides for Enhanced Oxygen Evolution Catalysis. *Nat. Commun.* **2014**, *5*, 4477.
(98) Zhang, G.; Liu, H.; Qu, J.; Li, J. Two-Dimensional Layered MoS_2: Rational Design, Properties and Electrochemical Applications. *Energy Environ. Sci.* **2016**, *9*, 1190-1209.

(99) Li, R.; Wei, Z.; Gou, X. Nitrogen and Phosphorus Dual-Doped Graphene/Carbon Nanosheets as Bifunctional Electrocatalysts for Oxygen Reduction and Evolution. *ACS Catal.* **2015**, *5*, 4133-4142.
(100) Suen, N. T.; Hung, S. F.; Quan, Q.; Zhang, N.; Xu, Y. J.; Chen, H. M.; Electrocatalysis for the Oxygen Evolution Reaction: Recent Development and Future Perspectives. *Chem. Soc. Rev.* **2017**, *46*, 337-365.
(101) Han, L.; Dong, S.; Wang, E. Transition-Metal (Co, Ni, and Fe)-Based Electrocatalysts for the Water Oxidation Reaction. *Adv. Mater.* **2016**, 28, 9266-9291.
(102) Jana, S.; Rioux, R. M. Seeded Growth Induced Amorphous to Crystalline Transformation of Niobium Oxide Nanostructures. *Nanoscale* **2012**, *4*, 1782-1788.
(103) Grimaud, A.; Carlton, C. E.; Risch, M.; Hong, W. T.; May, K. J.; Shao-Horn, Y. Oxygen Evolution Activity and Stability of $Ba_6Mn_5O_{16}$, $Sr_4Mn_2CoO_9$, and $Sr_6Co_5O_{15}$: the Influence of Transition Metal Coordination. *J. Phys. Chem. C* **2013**, *117*, 25926-25932.
(104) Menezes, P. W.; Panda, C.; Garai, S.; Walter, C.; Guiet, A.; Driess, M. Structurally Ordered Intermetallic Cobalt Stannide Nanocrystals for High-Performance Electrocatalytic Overall Water-Splitting. *Angew. Chem., Int. Ed.* **2018**, *57*, 15237-15242.
(105) Zhu, W.; Zhu, G.; Yao, C.; Chen, H.; Hu, J.; Zhu, Y.; Liang, W. Porous Amorphous FeCo Alloys as Pre-Catalysts for Promoting the Oxygen Evolution Reaction. *J. Alloys Compd.* **2020**, *828*, 154465.
(106) Sirés, I.; Brillas, E. Remediation of Water Pollution Caused by Pharmaceutical Residues Based on Electrochemical Separation and Degradation Technologies: A Review. *Environ. Int.* **2012**, *40*, 212-229.
(107) Mills, A.; Davies, R. H.; Worsley, D. Water Purification by Semiconductor Photocatalysis. *Chem. Soc. Rev.* **1993**, *22*, 417-425.
(108) Grau, P. Textile Industry Wastewaters Treatment. *Water Sci. Technol.* **1991**, *24*, 97-103.
(109) Sanjini, N. S.; Velmathi, S. Photocatalytic Degradation of Rhodamine B by Mesoporous Ti-KIT-6 under UV Light and Solar Light Irradiation. *J. Porous Mater.* **2015**, *22*, 1549-1558.
(110) Yu, C.; Li, G.; Kumar, S.; Yang, K.; Jin, R. Phase Transformation Synthesis of Novel Ag_2O/Ag_2CO_3 Heterostructures with High Visible Light Efficiency in Photocatalytic Degradation of Pollutants. *Adv. Mater.* **2014**, *26*, 892-898.
(111) Tušar, N. N.; Maučec, D.; Rangus, M.; Arčon, I.; Mazaj, M.; Cotman, M.; Pintar, A.; Kaučič, V. Manganese Functionalized Silicate Nanoparticles as a Fenton-Type Catalyst for Water Purification by Advanced Oxidation Processes (AOP). *Adv. Funct. Mater.* **2012**, *22*, 820-826.

****

Chapter 2

Materials, Instrument and Characterization Techniques

2.1 Materials

All the chemicals were of analytical grade and used without further purification. Nickel (II)acetylacetonate (95%), oleylamine (OA, 70%), 1-octadecene (90%), trioctylphosphine (TOP, 90%), diethylzinc (DEZ, 1.0 M in hexane), ruthenium (IV) oxide, nafion, halloysite nanotubes (HNTS), silver nitrate (99.9999%), sodium borohydride ($NaBH_4$), iron (III) chloride, manganese (II) chloride, cobalt (II) chloride and nickel (II) chloride were purchased from Sigma-Aldrich. Toluene, ethanol, potassium permanganate ($KMnO_4$), hydrogen peroxide, carbon black, hydrochloric acid, sulphuric acid and sodium azide were obtained from Merck, India. (3-aminopropyl) triethoxysilane (APTES, 97%) was acquired from Alfa Aesar. Sodium hydroxide (NaOH), potassium hydroxide (KOH), urea, rhodamine B (RhB) and methylene blue (MB) were received from Sisco Research Laboratory, India. Triethanolamine (TEA), tert-butyl alcohol (t-BA) and isopropanol were procured from Spectrochem, India. Millipore water was used during all the experiments.

2.2 Instrument and Characterization Techniques

In order to understand the detailed information of the synthesized nanomaterials, proper characterization of the synthesized nanomaterials is very essential. The properties of the nanomaterials are very important to utilize them in different fields. When the dimension of a material is reduced to nanoscale region, it exhibits different characteristics than that of its bulk component. Hence, it is very significant to carry out the different characterization techniques properly to get the precise and clear information about the

prepared nanomaterials. This chapter demonstrates the various experimental techniques that were used to characterise the prepared nanomaterials. The following characterization techniques were employed for my thesis work.

2.2.1 Scanning Electron Microscopy

Scanning electron microscopy (SEM) is one of the most frequently used techniques for topography and morphological analysis of materials with high resolution and depth of field than optical microscope. This technique is very useful for the micro- and nanostructures analysis. Here, a well-focused beam of electrons is focused on a solid surface of the material and scanned back and forth across the surface of the material. SEM is based on the thermionic emission of electron beam from an electron gun fitted with a tungsten filament or lanthanum hexaboride (LaB_6) cathode or field-emission cathode.[1] First, these electrons pass through a condenser lens and then through an objective lens and finally reach to the sample surfaces. After the bombarding with the sample, the high energy electrons reflect back from the surface of the material and give secondary electrons. The signals from secondary electrons are detected by a detector and amplified. A simplistic schematic diagram of scanning electron microscope is presented in Figure 2.1.

Energy dispersive X-ray spectroscopy (EDS) coupled with SEM helps to detect the elemental composition of the sample. During EDS analysis, the high energy electron beam collides with the atoms of the sample and knocks off an inner shell electron. The vacated position due to the ejection of an inner shell electron is eventually occupied by an outer shell electron. As a result, the transferring outer shell electron must release some of its energy in the form X-ray. The atoms of every element release X-rays with unique amounts of energy, which are characteristic of the elements and can be used to identify the elements present in the sample. The morphology of the material was visualized using field emission scanning electron microscopy (FESEM: FEI QUANTA FEG 250) after drop casting a drop of sample solution on a silicon wafer.

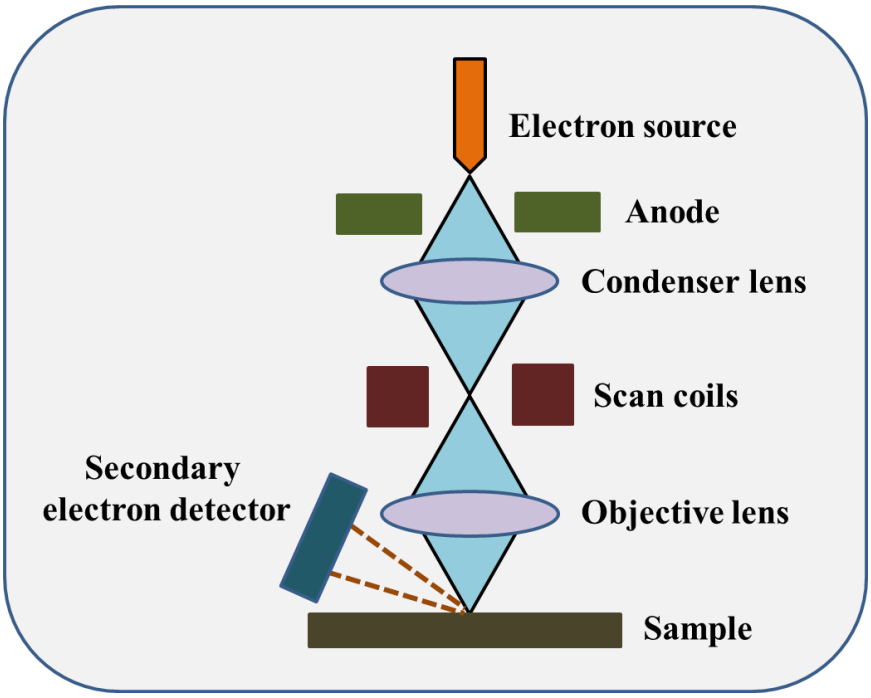

Figure 2.1: Schematic diagram of the scanning electron microscope.

2.2.2 Transmission Electron Microscopy

Transmission electron microscopy (TEM) is one of the most used and adaptable techniques for the characterization of nanomaterials, when the particle size, shape, and internal structure are important.[2] In TEM, a beam of electrons is transmitted through a specimen to construct an image. Generally, three types of electron guns were used in transmission electron microscopes, namely, the tungsten cathode, the lanthanum hexaboride (LaB_6) cathode and the field emission gun. In TEM, the electron beam is well focused using electromagnetic lenses. A simplified diagram of transmission electron microscope is shown in Figure 2.2. A thin specimen is illuminated using uniform and high intensity electrons.[3] The TEM technique is devoted to the analysis of the transmitted beam. The beam is passed through a series of lenses to obtain image, which is magnified and focused by an objective lens onto an imaging device, such as a fluorescent screen or to be detected by a sensor like a CCD camera. In low resolution TEM, the objective

aperture can be adjusted for selection of the central beam (containing the less-scattered electrons) or of a particular diffracted (or scattered in any form) beam to form the bright-field or dark-field image respectively.

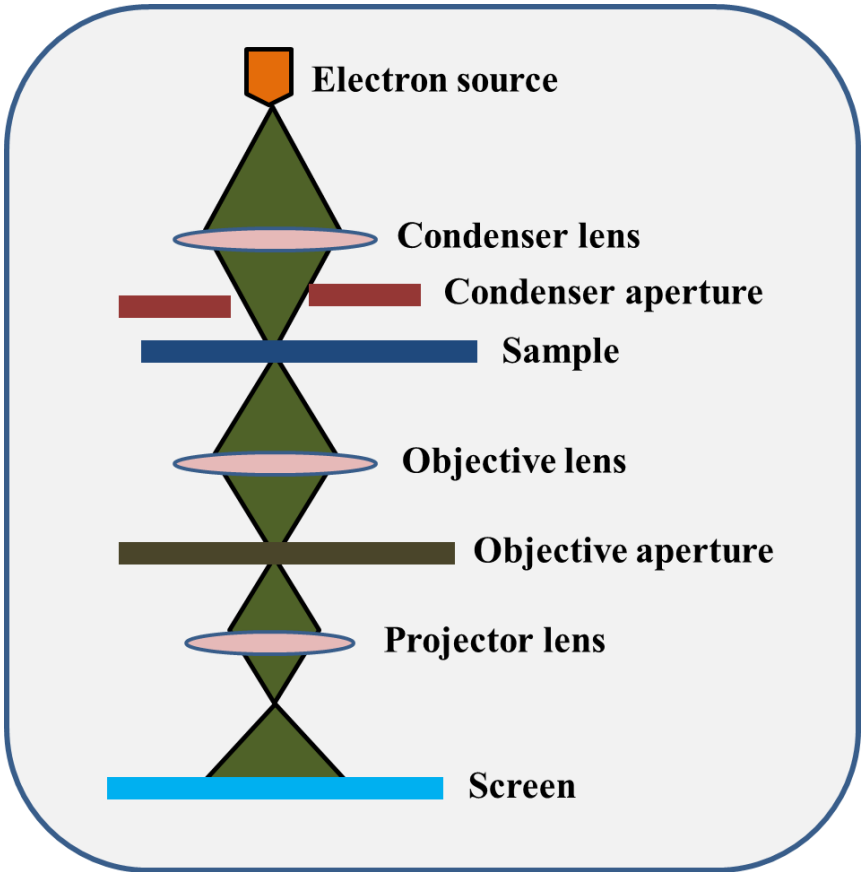

Figure 2.2: A simplified ray diagram of a transmission electron microscope consists of an electron source, condenser lens with aperture, specimen, objective lens with aperture, projector lens and fluorescent screen.

The high-resolution TEM (HRTEM) analysis is very useful to study the faceting, crystallinity and ordering of nanocrystal. By the use of TEM coupled with selected area electron diffraction (SAED), we get important information on the crystallographic direction in the structures. SAED is beneficial to understand the growth kinetics of nanocrystals and it is used for defect analysis in nanocrystals.[4,5] High resolution

transmission electron microscopy (HRTEM) and scanning transmission electron microscopy-energy dispersive spectroscopy (STEM-EDS) elemental mapping analyses were performed in the transmission electron microscope (TEM: FEI TECNAI G2 F20-ST) using an accelerating voltage of 200 kV after drop casting a drop of sample solution on a carbon coated copper grid.

2.2.3 X-ray Photoelectron Spectroscopy (XPS)

X-ray photoelectron spectroscopy (XPS) is a broadly used technique, based on the photoelectric effect for the structural study of solid surfaces to determine the elemental composition of a material as well as valence state of the element.[6,7] When the incident radiation of appropriate energy irradiates on metal surface, electrons are emitted from the surface. The relation between the energy of the excitation radiation, binding energy of the electron (work function) of the metal and the maximum kinetic energy of the emitted electron as proposed by Einstein in 1905 is given below:

$$h\nu = E_b + E_{kin}$$

where, $h\nu$ is the energy of incident radiation, E_b represents the binding energy of the electron to the particular material (i.e., minimum energy required to remove an electron) and E_{kin} denotes the kinetic energy of the ejected electron. In XPS analysis, we can measure the kinetic energy of the inner or valence electron ejected by an incident X-ray photon of known energy ($h\nu$). By knowing these values, it is feasible to evaluate the binding energy (E_b), which is characteristic of the particular material. The chemical environment of the ion can also affect the electron binding energy. For this reason, XPS technique not only used to identify the ion but also provided its oxidation state. Work function of the spectrometer (ϕ_s) should be taken into consideration during the calculation of the kinetic energy of an ejected electron. This work function is an instrument dependent factor (normally derived as part of a calibration procedure) and defines the minimum amount of energy needed to move an electron from the Fermi energy level (at

which E_{kin} = 0) into vacuum. Therefore, the above mentioned equation can be rewritten as:

$$E_{kin} = h\nu - E_b - \phi_s$$

This defines the kinetic energy measured by the analyser. Surface analysis by XPS is accomplished by irradiating a sample with monoenergetic soft X-rays and analysing the energy of the detected electrons. These photons have limited penetrating power in a solid of the order of 1-10 μm. They interact with atoms in the surface region, causing electrons to be emitted by the photoelectric effect.

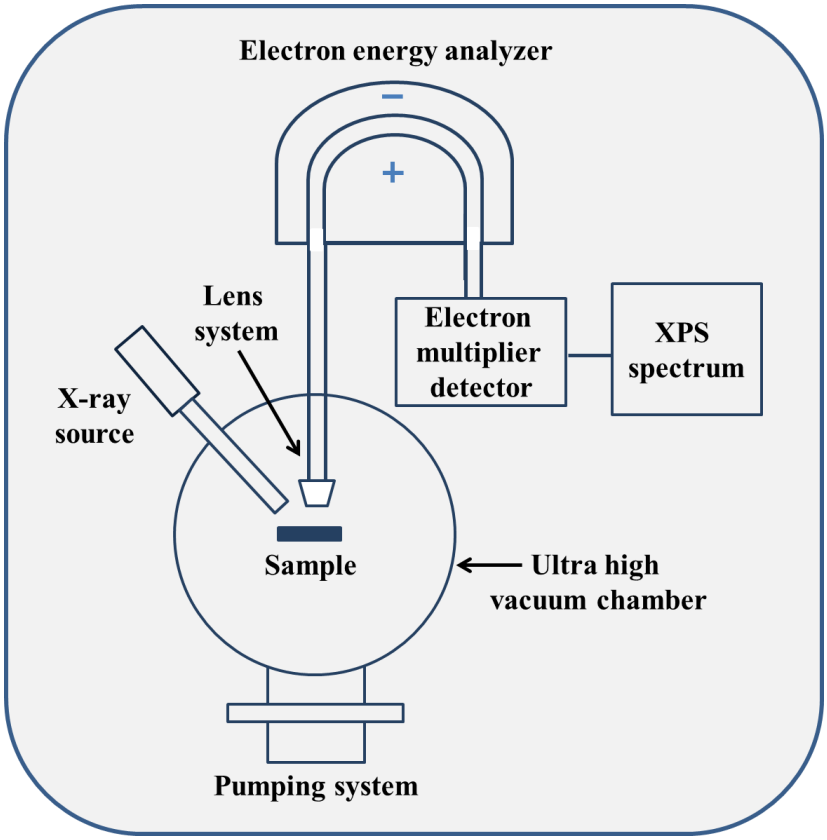

Figure 2.3: Schematic presentation of an XPS instrument. The X-ray radiation interacts with the sample and the emitted electrons are focused onto the analyser, which measures their kinetic energies and indirectly their binding energies.

A simplified schematic presentation of an XPS instrument is shown in Fig. 2.3. In XPS instrument, the main components are the high vacuum pumping system, the ionisation chamber, the X-ray source (ionising radiation), the electron focusing lens, the electron energy analyser, the electron detector and finally the data acquisition system. XPS involves an ultra-high vacuum (UHV) chamber (stainless steel) at 10^{-6}-10^{-10} torr. Conventionally, Mg Kα (1253.6 eV) or Al Kα (1486.6 eV) X-ray source is used in XPS instrument. A specimen can be analysed by placing it in vacuum. The electrons emitted due to the interaction between the X-ray beam with specimen are then focused by a system of lens to reach the electron energy analyser, which allows measurement of the energy of the photoelectrons. A potential difference is established between two electrodes so that only electrons having a certain kinetic energy will reach to the detector (electron multiplier). The data acquisition system helps to observe the XPS spectrum on a screen.

2.2.4 X-ray Diffraction Spectroscopy

X-ray diffraction (XRD) is a fast and nondestructive technique to understand the structural properties of materials and gives information about crystal structure or phase, lattice parameters, crystallite size and orientation of single crystal.[8,9] This technique can be used for thin films, bulk materials or nanomaterials. In XRD, a monochromatic beam of incident X-rays strike on a crystalline sample and these x-rays are scattered elastically by the electrons within the crystal planes. A constructive interference takes place only for certain θ's correlating to those (*hkl*) plane, where path difference is an integral multiple (n) of wavelength. Based on this, the Bragg's equation is simply written as:

$$n\lambda = 2d \sin\theta$$

where, λ is the wavelength of the incident X-ray, d is the interplanar distance, θ is the scattering angle and n is an integer-called order of diffraction. These X-ray can penetrate deep into the material and provide information about the structural arrangement of atoms and molecules. X-rays are diffracted by the oriented crystallites at a particular angle to fulfil the Bragg's condition. As the value of θ and λ is known, one can evaluate the

interplanar spacing. Basically, powder diffractometers are available in two basic varieties: i) *θ-θ* mode in which the X-ray tube and detector move simultaneously and ii) *θ-2θ* mode, where the X-ray tube is fixed, and the specimen moves at half the rate of the detector to maintain the *θ-2θ* geometry. Our used diffractometer is a *θ-2θ* system. The detector motion is coupled with the X-ray source in such a way that detector motion always makes an angle *2θ* with the incident direction of the X-ray beam. The resulting XRD spectrum is a plot against the intensity versus 2θ. A Schematic view of XRD is presented in Figure 2.4.

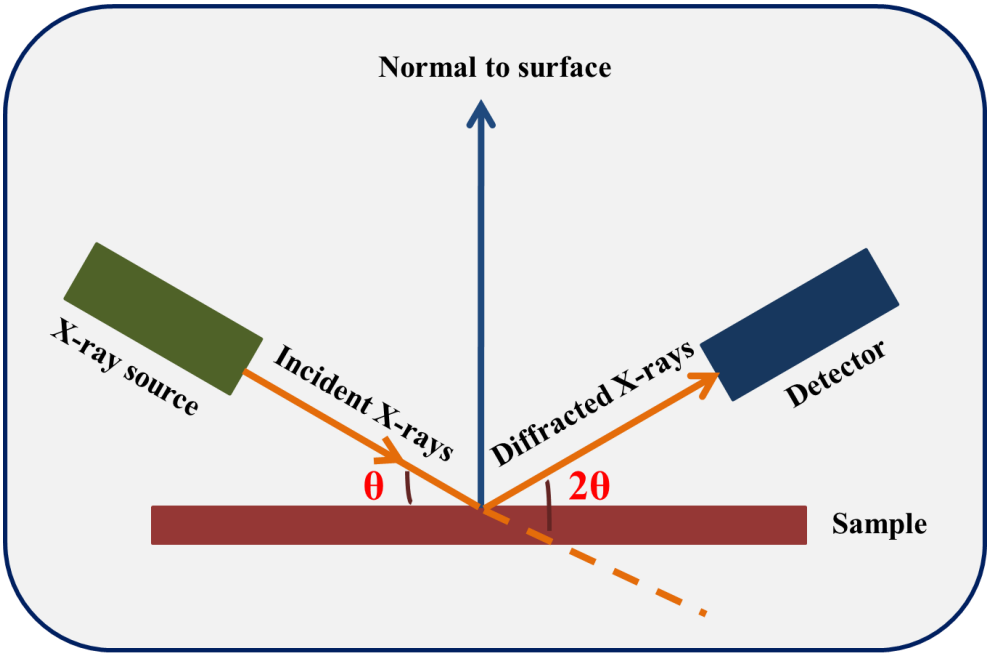

Figure 2.4: Schematic presentation of X-ray diffraction in *θ-2θ* mode.

The crystallinity and particle size of the nanoparticles are also experimentally calculated with the help of X-rays diffraction.[10] The particle size can be calculated from the Scherrer formula:

$$t = \frac{k\lambda}{\beta \cos\theta}$$

where, *k* is the Scherrer's Constant ≈ 0.9, *β* is the intensity at FWHM (Full Width at Half Maximum) in terms of *2θ* and *t* is the thickness (particle size). Powder X-ray diffraction

patterns were recorded on a RIGAKU MiniFlex II powder diffractometer using Cu Kα radiation (λ = 1.5418 Å) with 35 kV beam voltage and 15 mA beam current.

2.2.5 UV-Vis Absorption Spectroscopy

UV-Vis spectroscopy is one of the most commonly used techniques to know the information about the absorption signals of molecules due to the electronic transitions. In this technique, the UV-Vis spectrometer records the transmitted or reflected light from the material. This spectroscopy is also known as electronic spectroscopy. The electronic spectra of molecules are obtained due to the absorption of UV and visible regions of electromagnetic spectrum by the molecules. It provides the information regarding the size, shape and degree of aggregation of nanoparticles.[11,12] Band gap energy of semiconducting material can also be determined by using this technique. The UV-Vis spectrometer can operate in two modes: transmission and reflection mode. In transmission mode, usually the well-dispersed colloidal NPs in solvent are used.

The optical measurements for opaque thin films and those NPs which are not dispersible in solvents are recorded in the diffuse reflectance (DRS) mode. Intensity of spectral lines depends on three main factors: transition probability, population of states and concentration of the material and path length. The concentration of the sample and path length is also very important factor for the energy absorption. Based on this, Beer-Lambert law is often written as:

$$A = \log(I_0/I_t) = \varepsilon c l$$

where, A is the absorbance of the solution, I_0 and I_t are the intensity of the incident and transmitted light respectively at a given wavelength, l represents the path length of the sample and c is the concentration of the absorbing species. ε is the molar absorptivity or extinction coefficient for each species and wavelength. This coefficient is a fundamental molecular property in a given solvent at a particular temperature and pressure. Basically, absorbance is directly proportional to the concentration, where the path length and molar

extinction coefficient are supposed to be constant for the particular measurement. The schematic presentation of UV-vis spectrophotometer in transmission mode is shown in Figure 2.5. The UV-vis absorption spectrophotometer instrument uses a Xenon pulse lamp, which provides a wide wavelength range of 190 to 1100 nm and a dual silicon diode detector. A holographic grating is used to scan the wavelength. The reference radiation beam in the spectrophotometer travels from the light source to the detector without interacting with the sample. On the other hand, the sample radiation beam interacts with the sample when it travels from the light source to the detector. In the present work, UV-visible absorption spectra were recorded at room temperature using a Shimadzu spectrometer (UV-2600) taking the solutions in a 1 cm quartz cuvette. The UV-visible diffuse reflectance absorption spectrum of the nanocomposites was obtained using the same spectrophotometer (Shimadzu, Japan) equipped with a diffuse reflectance accessory.

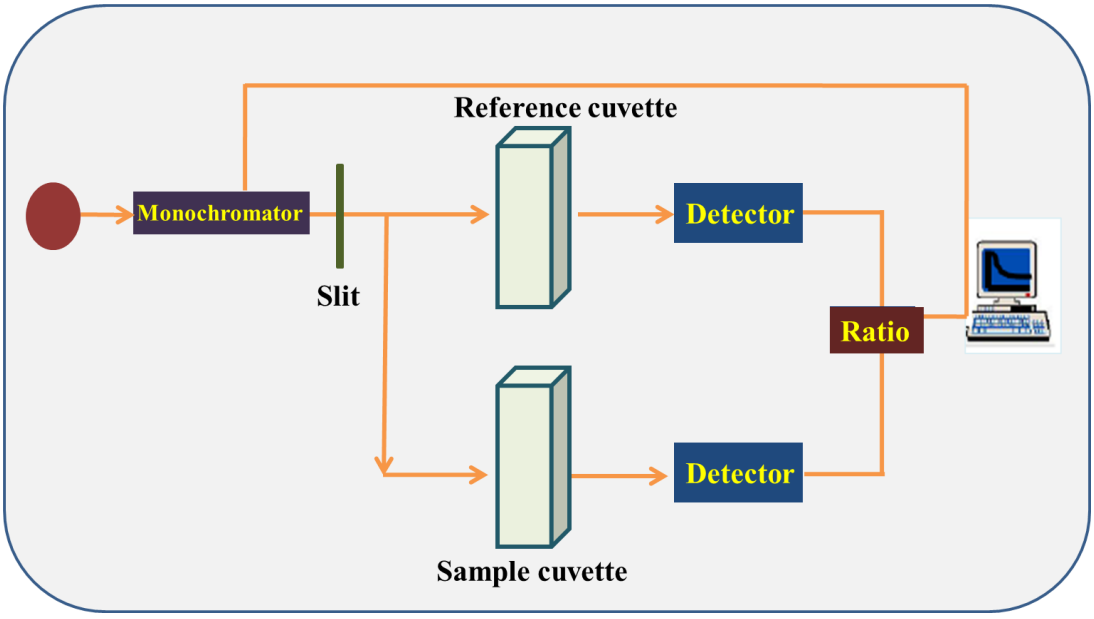

Figure 2.5: Schematic presentations of UV-Vis spectrophotometer in transmission mode.

2.2.6 Fourier Transform Infrared Spectroscopy

Fourier transform infrared (FTIR) spectroscopy is a very effective technique to know the structural information about the chemical bonding or molecular structure of the materials.[13,14] IR spectrophotometer comprises of primarily source, monochromator, beam splitter, mirror and detector. A schematic presentation of a FTIR spectrophotometer is presented in Figure 2.6. In this technique, the materials are exposed with infrared radiation that excites the characteristic vibrational modes in the chemically bonded functional groups present in the material. An IR spectrum demonstrates the fingerprint of a sample having several absorption peaks which relate to the frequencies of vibrations between the bonds of the atoms in the material. Therefore, IR spectrum is considered to be a unique characteristic of the material.

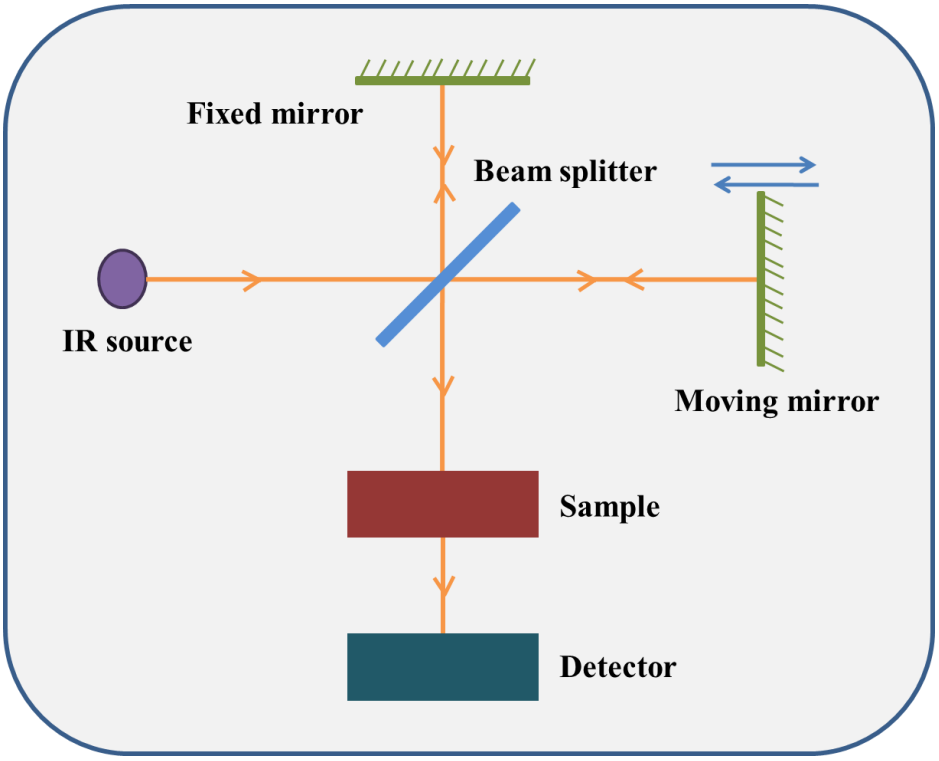

Figure 2.6: Schematic presentations of Fourier transform infrared (FTIR) spectrophotometer.

IR spectrum appears only when the vibrations among bonded atoms generates a change in the permanent electric dipole moment of the molecule. Those molecules which have a permanent electric dipole moment are capable of absorbing IR radiation. Homonuclear or symmetric diatomic molecules (such as H_2, O_2, Cl_2 etc.) are IR inactive as they do not have permanent electric dipole moment, whereas, heteronuclear diatomic molecules (such as CO, HCl, NO etc.) are IR active as they have permanent electric dipole moment. During this measurement, sample was mixed with KBr powder and pelletized. The background correction was made using a reference blank of KBr pellet. In my study, FTIR spectroscopy measurements of the samples were carried out in the range of 500 to 4000 cm^{-1} using JASCO FT/IR 6300. All the FTIR spectra were analyzed using KBr pellets in the transmission mode. No of scans was fixed to 50 with a resolution of 2 cm^{-1}.

2.2.7 Surface Area Measurement

The most common technique to determine the surface area of powders and porous materials is Brunauer-Emmett-Teller (BET) method. In 1938, Stephen Brunauer, Paul Hugh Emmett and Edward Teller published an article about the BET theory in a journal for the first time.[15] Generally, chemically inert probing gas (nitrogen) is employed as adsorbates in BET surface area analyzer so that it does not chemically react with the material surfaces. BET theory points to elucidate the physical adsorption of gas molecules on a solid surface of the materials. The idea of the theory is an expansion of the Langmuir theory, which is a theory for monolayer molecular adsorption to multilayer adsorption with the following assumptions: (a) gas molecules physically adsorb on a solid in layers infinitely; (b) there is no interaction between each adsorption layer; and (c) the Langmuir theory can be applied to each layer. The resulting BET equation is expressed by the following equation:

$$\frac{1}{v[(\frac{p_0}{p})-1]} = \frac{c-1}{v_m c}\left(\frac{p}{p_0}\right) + \frac{1}{v_m c}$$

where, p and p_0 are the equilibrium and the saturation pressure of adsorbates at the temperature of adsorption, v is the adsorbed gas quantity (for example, in volume units)

and v_m is the monolayer adsorbed gas quantity. c is the BET constant. Specific surface area of our synthesized materials was determined by the BET method using nitrogen adsorption/desorption isotherms at 77 K with 3flex Micromeritics analyzer.

2.2.8 Zeta-Potential

The measurement of zeta potential of colloidal dispersions is normally performed by using the technique of micro-electrophoresis. Zeta (ζ) potential measurement process basically indicates an indirect measurement of the net charge on the surface of materials.[16] During the measurement, a voltage gradient is applied across a pair of electrodes at both end of a cell containing the particle dispersion, inducing the movement of charged particles. Charged particles are attracted to the oppositely charged electrode and their velocity is measured. The particle velocity at unit external applied field is expressed as electrophoretic mobility. According to Henry's equation the measured electrophoretic mobility (U_E) is converted into ζ- potential. Henry's equation is -

$$U_E = \frac{2\varepsilon\zeta f(\kappa\alpha)}{3\eta}$$

where, ε and η represent the dielectric constant and viscosity of the medium respectively. $f(k\alpha)$ is the "Henry function", where α denotes hydrodynamic radius and k is the Debye parameter, which signify the thickness of the electrical double layer. Zeta potential measurement was carried out by using Malvern Nano ZS instrument.

2.2.9 Inductively Coupled Plasma Optical Emission Spectrometry

Inductively coupled plasma-optical emission spectrometry (ICP-OES) is a commonly used analytical technique where the composition of elements in samples (mostly dissolved in water) can be measured using plasma and a spectrometer.[17] This technique is also referred to as inductively coupled plasma-atomic emission spectroscopy (ICP-AES). In this spectroscopic method, inductively coupled plasma was used to produce excited atoms and ions, which emit electromagnetic radiation. Each element has its own

distinctive emission spectrum that is measured by a spectrometer. Generally, argon gas is utilized to produce the plasma. The intensity of this emission is correlated with the concentration of the element within the sample. ICP-OES analysis was carried out using the PerkinElmer ICP-OES instrument (PerkinElmer, Inc., Shelton, CT, USA). For ICP-OES analysis, nanomaterials were dissolved in dilute HCl. Then, the supernatant was used for the estimation of the concentration of element present in the nanomaterial.

2.2.10 Electrochemical Analysis

For the electrochemical analysis of different prepared materials, a CHI660E electrochemical workstation (CHI Instruments) was used. All the electrochemical experiments were carried out in alkaline KOH solution at room temperature by using conventional three-electrode system, namely, working electrode, reference electrode and counter electrode. Mainly, cyclic voltammetry (CV), linear sweep voltammetry (LSV), electrochemical impedance spectroscopy (EIS) and chronoamperometry (CA) techniques were used for electrochemical analysis. Cyclic voltammetry is an electrochemical technique to measure the current response of a redox active solution to a linearly cycled potential sweep between two or more set values. In the course of the potential sweep, current response is measured against the applied potential. In CV, the voltage is swept between two potential values (V_1 and V_2) at a fixed scan rate. During CV, when the voltage reaches to V_2 from V_1, the scan is reversed and the voltage is swept back to V_1 from V_2. Linear Sweep Voltammetry (LSV) is equivalent to a one-segment cyclic voltammetry experiment. In LSV, working electrode potential is swept linearly between initial and final values and current response is measured as a function of potential. From LSV plot, we can determine the onset potential and Tafel slope. Electrochemical impedance spectroscopy (EIS) is another vital technique, which uses small amplitude and alternating current (AC) signal to examine the impedance characteristics of an electrochemical cell. The AC signal is scanned over a wide range of frequencies to generate an impedance spectrum for the electrochemical cell. From the EIS study, we get the well-known Nyquist plot, which represents negative of the imaginary versus the real parts of the complex impedance of individual electrodes or electrochemical cells. Charge-

transfer resistance is associated with the semicircle of the Nyquist plot. Chronoamperometry is a time-dependent procedure in which the current response of the electrode was monitored with the time. During this method, a constant potential is applied to the working electrode and current response is observed against time. This technique was used to check the stability of catalysts.

2.3 References

(1) Goldstein, J. I.; Newbury, D. E.; Michael, J. R.; Ritchie, N. W.; Scott, J. H. J.; Joy, D. C. *Scanning Electron Microscopy and X-Ray Microanalysis*; Springer, **2017**.

(2) Wang, Z. L. Transmission Electron Microscopy of Shape-Controlled Nanocrystals and their Assemblies. *J. Phys. Chem. B* **2000**,*104*, 1153-1175.

(3) Carter, C. B.; Williams, D. B. *Transmission Electron Microscopy*; Springer-Verlag US: New York, **2009**.

(4) Duan, J.; Yang, S.; Liu, H.; Gong, J.; Huang, H.; Zhao, X.; Zhang, R.; Du, Y. J. Single Crystal SnO_2 Zigzag Nanobelts. *J. Am. Chem. Soc.* **2005**, *127*, 6180-6181.

(5) Ding,Y.; Wang, Z. L. Structure Analysis of Nanowires and Nanobelts by Transmission Electron Microscopy. *J. Phys. Chem. B.* **2004**, *108*, 12280-12291.

(6) Van der Heide, P. *X-Ray Photoelectron Spectroscopy: An Introduction to Principles and Practices*; John Wiley & Sons, **2011**.

(7) Nefedov, V. I. *X-Ray Photoelectron Spectroscopy on Solid Surfaces*; VSP: Netherlands, **1988**.

(8) Ooi, L. *Principles of X-Ray Crystallography*; Oxford University Press: Oxford, U.K., **2010**.

(9) Poojary, D.M.; Clearfield, A. Application of X-Ray Powder Diffraction Techniques to the Solution of Unknown Crystal Structures. *Acc. Chem. Res.* **1997**, *30*, 414-422.

(10) Holder, C. F.; Schaak, R. E. Tutorial on Powder X-ray Diffraction for Characterizing Nanoscale Materials. *ACS Nano* **2019**, *13*, 7359-7365.

(11) El-Sayed, M. A. Some Interesting Properties of Metals Confined in Time and Nanometer Space of Different Shapes. *Acc. Chem. Res.* **2001**, *34*, 257-264.

(12) Burda, C.; Chen, X.; Narayanan, R.; El-Sayed, M. A. Chemistry and Properties of Nanocrystals of Different Shapes. *Chem. Rev.* **2005**, *105*, 1025-1102.

(13) Stuart, B. H. *Infrared Spectroscopy: Fundamentals and Applications*; John Wiley & Sons, **2004**.

(14) Simonescu, C. M. *Application of FTIR spectroscopy in environmental studies*; INTECH Open Access Publisher, **2012**.
(15) Brunauer, S.; Emmett, P. H.; Teller, E. Adsorption of Gases in Multimolecular layers. *J. Am. Chem. Soc.* **1938**, *60*, 309-319.
(16) Xu, R. Progress in Nanoparticles Characterization: Sizing and Zeta Potential Measurement. *Particuology* **2008**, *6*, 112-115.
(17) Boss, C. B.; Fredeen, K. J. *Concepts, Instrumentation and Techniques in Inductively Coupled Plasma Optical Emission Spectrometry*; Perkin Elmer, **2004**.

****

Chapter 3

Ultra-Small NiZn Intermetallics: A Non-Precious Metal Catalyst for Efficient Electrocatalysis

3.1 Introduction

The renewable energy-driven or electrochemical water splitting via oxygen evolution reaction (OER) represents a perfectly green, sustainable and efficient approach for oxygen production.[1-4] They hold a great promise to supply future oxygen demands due to the enormous source of available water without the emission of any greenhouse gases and thus became advantageous owing to the environmentally benign approach. Moreover, this is believed to be a next generation energy solution as an alternative to the carbon-based energy source, which in turn fascinated to the researchers in developing efficient energy conversion systems apart from the most commonly used state-of-the-art catalysts IrO_2 or RuO_2 for OER,[5,6] as their widespread application would be impeded owing to their low abundance and high cost.[7] In electrochemical water splitting, OER is the anodic reaction and its sluggish kinetics have attracted extensive research attention in pursuing and designing proficient electrocatalysts to expedite the reaction by reducing the overpotential and hence subsequently boost the energy conversion efficacy.

Nanocrystalline alloys and intermetallics have emerged as a novel class of materials which are being explored in the development of green sources of energy in fuel cells,[8-13] Li-ion batteries,[14,15] photocatalysts,[16-18] thermoelectric power generation[19,20] and in diverse applications[21-23] owing to their robust stability and excellent activity. Since the discovery of intermetallic compounds, they demonstrate a prominent prospect by playing a leading role for the fabrication of low-cost high performance potential catalysts.[24-26] Conventionally, intermetallics are synthesized via metallurgical techniques that require high temperature reduction followed by annealing for long period of time[27,28] or through the annealing of nanoparticles (NPs) of a random alloy,[29,30] leading to the sintering of the

particles as well as resulting in the formation of polydisperse particles. Unlike disordered alloys, ordered intermetallics provide uniform active sites on the same surface plane owing to their compositional and positional order as well as possess precise control over the structure accompanied by electronic effects. It is therefore really challenging to get desired monodisperse intermetallics with high surface area, as it is an important criterion interrelated to their physical properties that govern their catalytic activity. Interestingly, tuning of size, structure and composition at the nanoscale dimensions is a key aspect in persuading a significant impact on their catalytic activity, since their chemical and physical properties are associated with the electronic states of the constituent metals. The main objective of the present work is the synthesis of ultra-small intermetallic NPs of earth abundant transition metals using low temperature solution chemistry approach since improving the physical properties by means of controlling the size and composition may lead to the enhanced activity. However, to date, the synthesis of tiny alloys with tunable composition through low temperature route remains a challenge. Additionally, developing cost-effective and high-performance electrocatalysts for oxygen production is of immense importance.

In this chapter, a general route was developed to achieve tiny Ni and corresponding $Ni_{0.7}Zn_{0.3}$ and NiZn NPs from the commercially available reagents via a solution-mediated reaction approach. After characterization by difference physical methods, we have studied their electrocatalytic activity towards OER in details, indicating that intermetallic NiZn NPs possess higher catalytic activity than that of $Ni_{0.7}Zn_{0.3}$, pure Ni NPs and even the commercial RuO_2. Finally, we have compared the electrocatalytic efficacy of NiZn with the reported Ni-based electrocatalysts.

3.2 Experimental Section

3.2.1 Synthesis of Ni, NiZn and $Ni_{0.7}Zn_{0.3}$ Nanoparticles

The nanoscale metal and alloys were synthesized based on the thermal decomposition of subsequent metal salts or organometallic compounds in a hot organoamine solvent. All

reactions were performed under nitrogen atmosphere via standard air-free techniques. First, Ni NPs were synthesized by the following method. Nickel(II) acetylacetonate (0.5 mmol) was taken in a mixture of oleylamine (9.25 mmol), octadecene (9.25 mmol) and trioctylphosphine (9.25 mmol) in a three-necked round-bottom flask. The flask was fitted with a condenser, rubber septum, thermocouple adaptor, and sheath through which a thermocouple was inserted. The reaction mixture was degassed at 100 ºC for 30 min and then heated to 220 ºC using a heating mantle upon which the color of the solution gradually changed from blue to black, signifying the formation of Ni NPs. The black solution was then aged at 220 ºC under nitrogen atmosphere for 90 min. The synthesized particles were collected via centrifugation after addition of acetone-hexane (3:1) mixture. Finally, the collected particles were redispersed in non-polar organic solvents, like hexane or toluene and were stable for couple of months.

For the synthesis of NiZn NPs, first Ni NPs were synthesized following the above mentioned route. Then, the temperature of the reaction mixture containing Ni NPs was increased to 250 ºC. A diethylzinc-oleylamine solution (0.5 mmol) was injected drop-wise into the reaction mixture once the reaction temperature reached to the desired temperature and held at that temperature for 30 min. Then, analogous procedure was followed to collect the NiZn NPs and redispersed in hexane or toluene. For the synthesis of $Ni_{0.7}Zn_{0.3}$ alloy, the amount of diethylzinc solution was changed to 0.18 mmol keeping all other reaction conditions the same. After characterization, all these as-synthesized nanoparticles were explored as electrocatalysts for OER study.

3.2.2 Electrochemical Measurement

A CHI660E electrochemical workstation (CHI Instruments) was used for testing the OER activity of different catalysts. All the electrochemical experiments were carried out at room temperature in a conventional three-electrode system of an electrochemical analyzer using glassy carbon (GC) as the working electrode, Hg/HgO (1.0 M KOH) as the reference electrode and Pt wire as the counter electrode. All potentials were referenced to the reversible hydrogen electrode (RHE) by the equation: *E (vs. RHE) = E*

(vs. Hg/HgO) + 0.098 + 0.059 pH. The GC electrode was polished with 1.0, 0.3 and 0.05 μm alumina slurry successively and washed several times with distilled water before deposition of the catalyst. First, 4.0 mg (30 wt% sample in carbon black) of Ni NPs was dispersed in a solution mixture containing distilled water (250 μL), isopropanol (250 μL) and Nafion® solution (1%, 20 μL). Then, the solution mixture was sonicated for 60 min to make a homogeneous mixture. The working electrode was prepared by drop-casting 15 μL of the sample solution onto the GC electrode (diameter of 3 mm) and dried overnight. The final loading of all the catalysts on the GC electrode is ~ 0.51 mg cm^{-2}. Linear sweep voltammetry (LSV) was performed with scan rate of 5 mV s^{-1} in 1.0 M KOH solution. Cyclic voltammetry (CV) and chronoamperometry (CA) analyses were done to measure the electrochemically active surface area (ECSA) and stability of catalysts. The electrochemical impedance spectroscopy (EIS) was studied in the frequency range of 0.1 Hz - 100 kHz with an AC amplitude of 0.005 V. For the preparation of working electrode using NiZn, $Ni_{0.7}Zn_{0.3}$ and commercial RuO_2 catalysts, similar procedure was followed. The overpotential (η) for each catalyst was calculated using the following equation: $\eta = E(RHE) - 1.23\ V$.

3.3 Results and Discussion

3.3.1. Characterization of the Synthesized Nanoparticles

3.3.1.1 TEM Analysis

Transmission electron microscopy (TEM) was used to characterize the morphology and composition of the NPs (Figure 3.1). TEM images of Ni NPs demonstrate formation of monodispersed spherical morphology having particle size of ~3 nm (Figure 3.1 A,B). After the injection of equimolar diethylzinc (DEZ) to the reaction solution containing Ni NPs at 250ºC, NiZn NPs were formed. TEM micrographs of NiZn NPs shown in Figure 3.1 C,D at different magnifications demonstrated that they retained the spherical morphology of Ni NPs and the estimated particle size is ~ 4.5 nm. The histograms of particle size for Ni and corresponding NiZn NPs are presented in Figure 3.2.

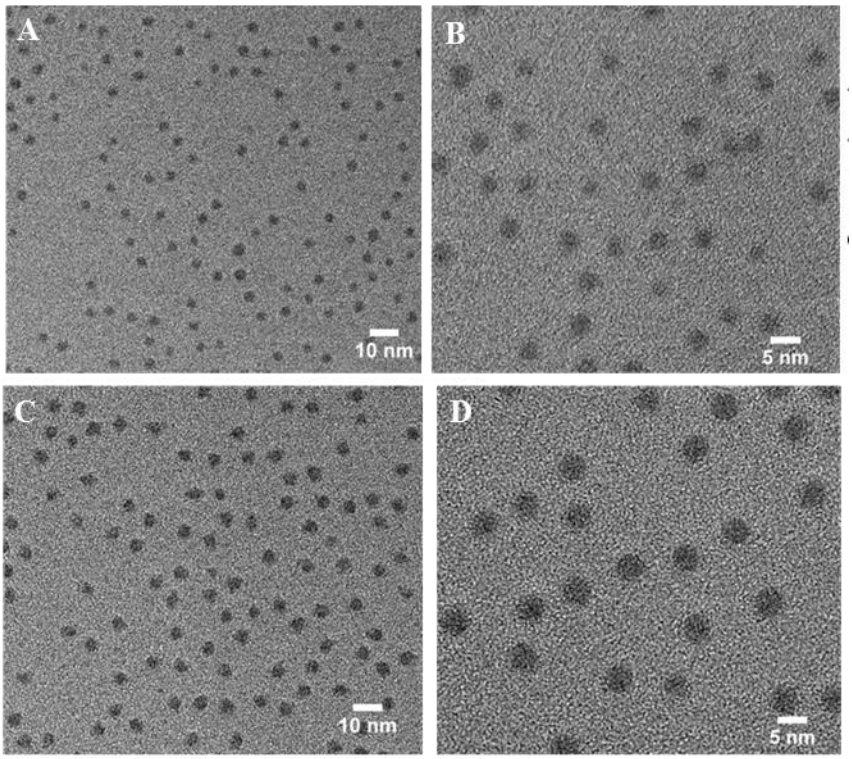

Figure 3.1: TEM micrographs of (A, B) ultra-small Ni NPs and corresponding (C,D) NiZn NPs at different magnifications.

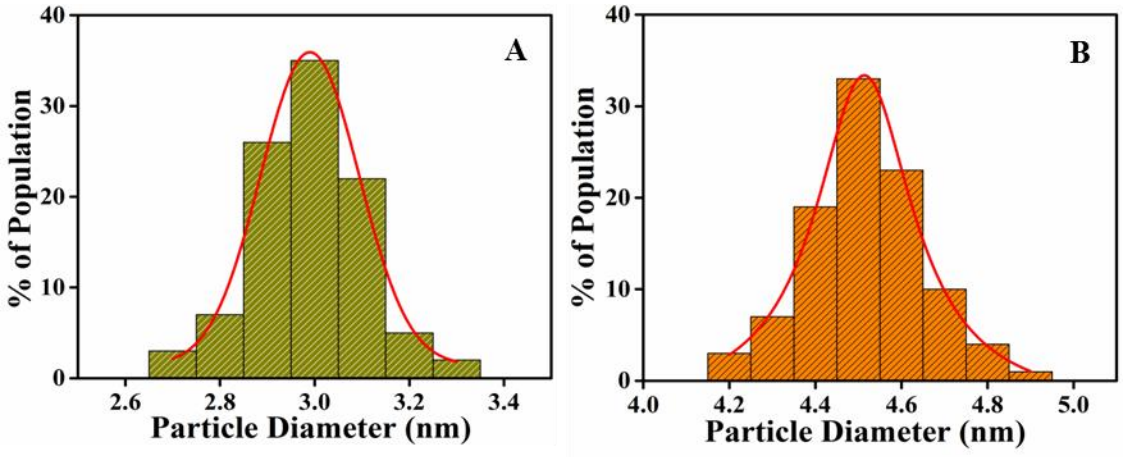

Figure 3.2: Histograms of particle size for (A) Ni NPs and corresponding (B) NiZn alloy.

3.3.1.2 XRD Study

The crystal structure of Ni NPs (Figure 3.3) was examined using powder X-ray diffraction (XRD) that attributes to the formation of face-centered cubic (fcc) Ni NPs (PDF No. 03-065-0380). An extremely broad peak corresponding to (111) plane was observed due to the presence of smaller crystallites and other two peaks corresponding to (200) and (220) planes were suppressed because of the formation of ultra-small Ni NPs. It should be noted that there were no diffraction peaks observed in the XRD pattern for nickel oxides or other phases, indicating the formation of pure fcc Ni NPs. XRD pattern of NiZn NPs displays the formation of the distinct tetragonal structure associated with the ordered alloyed NiZn (PDF No. 01-072-2668) without any crystallographic impurities, obtained with 1:1 of Ni and Zn (Figure 3.3). The observed broad peaks can be assigned to the characteristic (101) and (110) planes of NiZn respectively, whereas other peaks were suppressed owing to their tiny size.

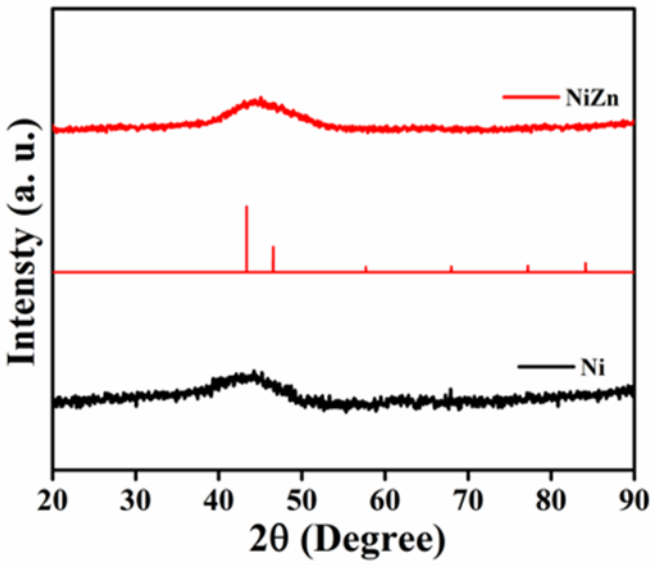

Figure 3.3: XRD patterns of Ni NPs and corresponding NiZn alloy. The simulated XRD pattern of tetragonal NiZn is also provided.

3.3.1.3 Composition and STEM-EDS Elemental Mapping Analyses

We have then performed the compositional analysis in NiZn NPs using TEM energy-dispersive X-ray spectroscopy (TEM-EDS; Figure 3.4.A) and inductively coupled plasma atomic emission spectroscopy (ICP-OES). The overall Ni/Zn composition in NiZn is quantitatively determined to be 0.97/1.0 (49.2 and 50.8 atomic wt% of Ni and Zn respectively). To directly visualize the chemical composition and subsequent distribution of the constituent elements, scanning transmission electron microscopy-energy dispersive spectroscopy (STEM-EDS) elemental mapping was performed. The STEM image of NiZn alloy is illustrated in Figure 3.4.B. The STEM-EDS elemental mapping ascribed

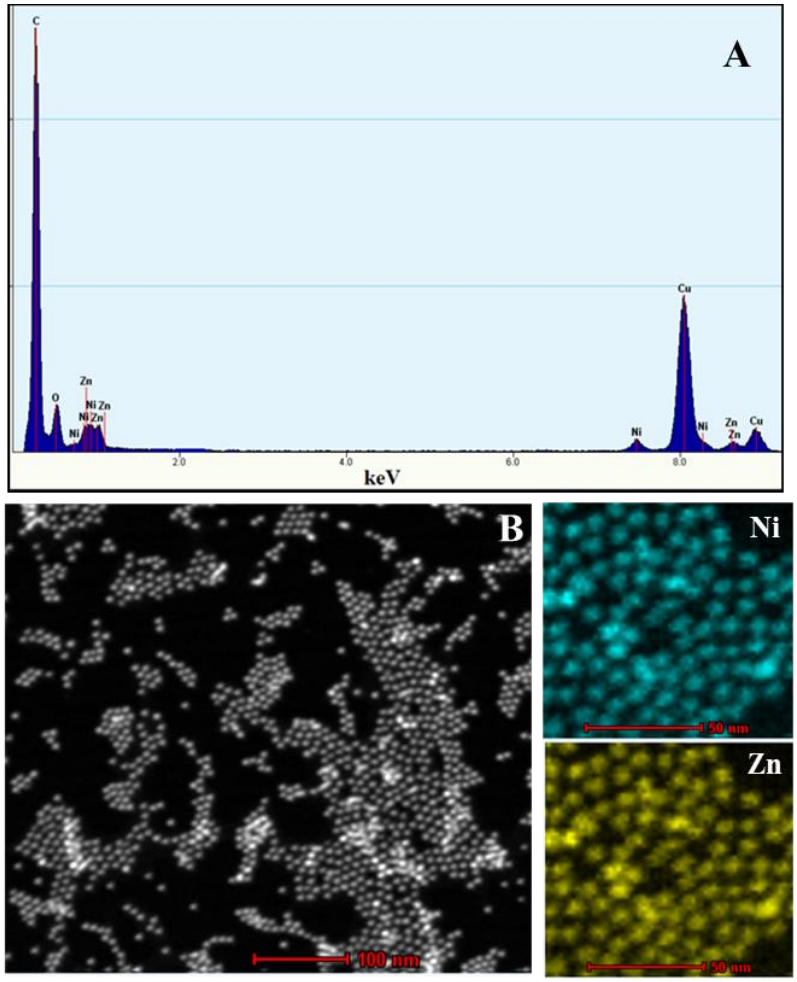

Figure 3.4: (A) EDS spectrum of NiZn represents the presence of both Ni and Zn in the alloy. (B) STEM image of NiZn alloy and the elemental mapping of the Ni (cyan) and Zn (yellow) in the NiZn alloy.

that the distribution of Ni and Zn are even throughout the NiZn, further accrediting to the formation of alloyed structure. Again, the composition of Zn is within the phase boundary of β-phase,[31,32] attributing to the ordered NiZn alloys, i.e.; intermetallic NiZn. No other peaks were observed form the XRD pattern, signifying high purity of the β-NiZn which was produced due to the substitution of Ni atoms via Zn atoms.[33]

3.3.1.4 XPS Analysis

X-ray photoelectron spectroscopy (XPS) was carried out to understand the elemental composition and the electronic interaction between the Ni and Zn atoms in NiZn alloy. The high resolution Ni 2p spectrum (Figure 3.5.A) displays the characteristic spin-orbit peaks for Ni $2p_{3/2}$ and Ni $2p_{1/2}$ with their corresponding shake-up satellites.[34,35] The binding energy (BE) of 852.8 eV for Ni $2p_{3/2}$ and the BE of 870.2 eV for Ni $2p_{1/2}$ are assigned to the metallic Ni^0. Similarly, the fine-scanned Zn 2p spectrum (Figure 3.5.B) attributes to the existence of two peaks for Zn $2p_{3/2}$ and Zn $2p_{1/2}$ at 1021.7 and 1044.7 eV with a BE difference of 23 eV, demonstrating the presence of Zn^0 in the alloy.[36,37] On the basis of their BE, it is established that both Ni and Zn are present in the metallic state in the NiZn alloy. However, a positive shift was noticed for $2p_{3/2}$ and $2p_{1/2}$ peaks for Ni^0 in NiZn compare to the pure Ni NPs (Figure 3.5.C). This indicates the modification of the electronic structure of Ni in NiZn after alloying with Zn.[38] All the experimental analyses and corresponding collective results ascertain the successful synthesis of monodispersed NiZn alloys under the developed reaction route.

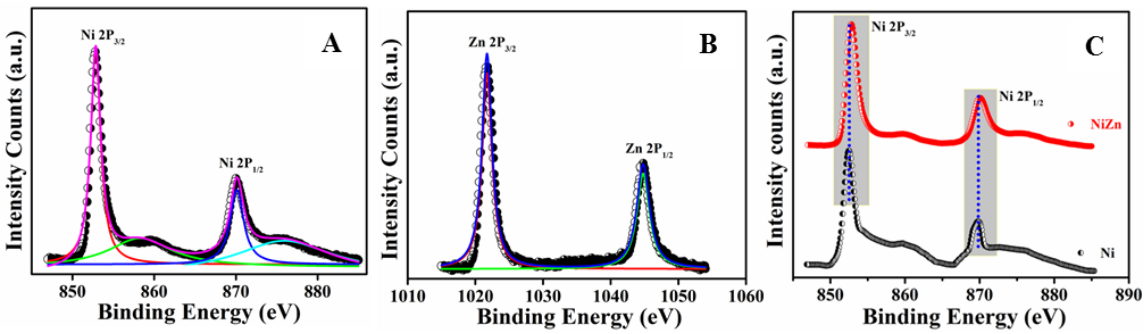

Figure 3.5: High resolution XPS spectra of (A) Ni 2p and (B) Zn 2p in NiZn alloy, indicating the existence of metallic Ni^0 and Zn^0 in the alloy. (C) XPS spectra of Ni 2p in Ni NPs and corresponding NiZn alloy.

3.3.2 Nanoparticle Formation Mechanism

The ultra-small NiZn alloy was synthesized via diffusion-based mechanism which involved two step procedures. First, Ni NPs were formed by the thermolysis or reduction of the corresponding precursors in an organoamine solvent at high temperature and then transformation of that Ni NPs into NiZn intermetallics occurred due to the reaction with diethylzinc, where organoamines act as reducing agent.[39,40] Basically, Zn atoms diffused into the nanocrystalline Ni and produced NiZn alloy. In our present system, the morphology of NiZn alloy was templated by the morphology of the corresponding Ni NPs. Hence, the present synthesis approach provides the formation of uniform spherical NiZn intermetallics, which may have potential application in energy storage and conversion owing to their alloyed structure.

3.3.3 OER Activity

Electrocatalytic performance of the various electrocatalysts was investigated with respect to OER taking 1.0 M KOH aqueous solution ($4OH^- \rightarrow O_2 + 2H_2O + 4e^-$) in a conventional three-electrode configuration.[41] The catalytic properties of the as-synthesized materials were measured after drop casting the ink uniformly onto a GC electrode with a loading of ~0.51 mg cm^{-2}. The ink contains the desired sample and carbon black suspended in a mixture of isopropanol, Nafion and water. To compare the activity of the as-synthesized catalyst, we have also studied the electrocatalytic performance of a standard OER catalyst, namely RuO_2 with a similar amount of loading under similar experimental condition.

3.3.3.1 Linear Sweep Voltammetry Study

The OER activity of the samples was first evaluated by linear sweep voltammetry (LSV) in 1.0 M KOH aqueous solution. Figure 3.6.A demonstrates LSV polarization curves for all the catalysts, where current density is plotted against potential. Interestingly, ultra-small Ni NPs exhibit better electrocatalytic activity compare to the commercial RuO_2.

We have then studied the OER activity of NiZn alloy NPs and found that they possess much higher OER activity than that of RuO_2 or pure Ni NPs. In an electrocatalytic reaction, current density is directly proportional to the OER activity of a catalyst. Thus, the higher current density at a same potential signifies faster OER kinetics. In our system, the current densities at the same potential are always higher for NiZn alloys. To reach the current density of 10 mA cm^{-2}, the required overpotential (η_{10}) was calculated from LSV curve, which is 343, 332 and 283 mV for RuO_2, Ni and NiZn respectively. Hence, the obtained η_{10} for all the catalyst is in the order of RuO_2> Ni> NiZn. To gain further insights into the OER kinetics, Tafel slope was assessed from the following equation;[42] $\eta = b\ log(j/j_0)$, where η indicates overpotential, b represents tafel slope, j and j_0 are the current density and exchange current density respectively. The Tafel slope of NiZn was estimated to be 73 mV dec^{-1}, which is lower than that of Ni (85 mV dec^{-1}) and even RuO_2 (92 mV dec^{-1}) as shown in Figure 3.6.B, indicating much faster OER kinetics of NiZn alloy, demonstrating prominent oxygen evolution activity of NiZn compare to only Ni or RuO_2.

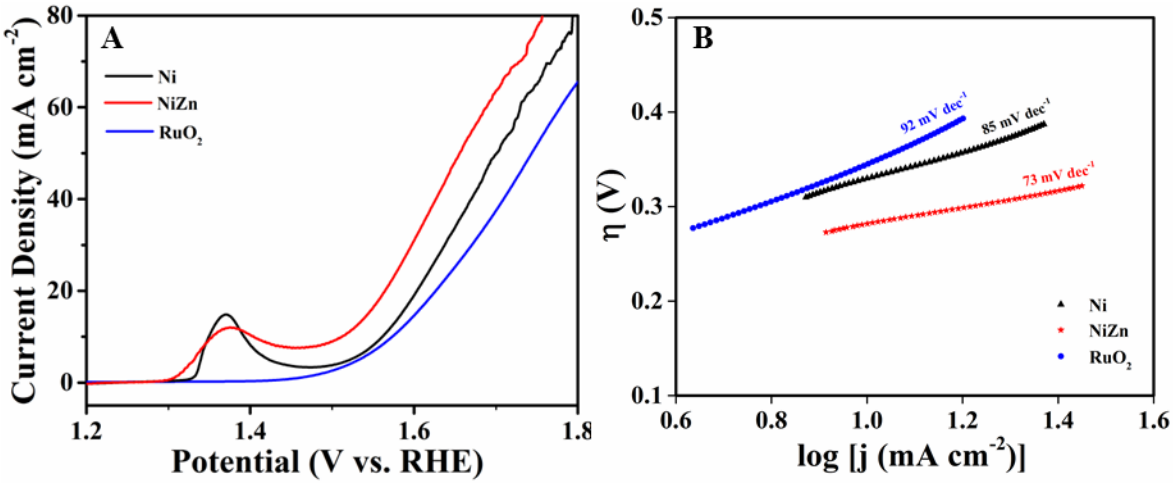

Figure 3.6: OER activity of NiZn alloy, Ni NPs and RuO_2. (A) LSV curves of Ni, NiZn and RuO_2 at a scan rate of 5 mV s^{-1}. (B) Tafel plots of all the catalysts.

3.3.3.2 Electrochemical Impedance Spectroscopy (EIS)

The electrochemical impedance spectroscopy (EIS) was performed at a potential of 10 mA cm^{-2} (η_{10}) for all the catalysts to understand the charge transfer phenomenon between the catalyst and electrolyte as well as to ascribe the OER kinetics of the catalyst. The semicircle of Nyquist plot (Figure 3.7) is associated to the charge-transfer resistance (R_{ct}). The corresponding equivalent circuit diagram was shown in the inset of Figure 3.7, where R_s is solution resistance and R_{ct} is the charge-transfer resistance; CPE represents constant-phase element. It is important to note that lowering of R_{ct} is a crucial parameter for a catalyst from the both scientific and practical viewpoint. The smaller R_{ct} of NiZn (22 Ω) compared to only Ni NPs (51.5 Ω) acquired from Nyquist plot reveals that faster rate of electron transfer occurred in NiZn, which in turn facilitates the OER process. The faster electron transfer is owing to the synergistic effect of Ni and Zn in NiZn alloy, resulting in the excellent electrocatalytic activity of NiZn.

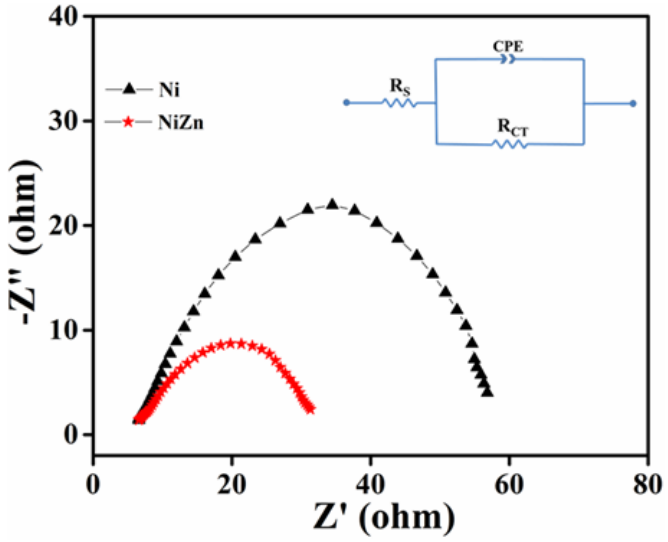

Figure 3.7: Nyquist plots of OER for Ni and NiZn (AC impedance data were acquired at η_{10} potential for both catalysts). Inset of Figure 3C is the corresponding equivalent circuit diagram.

3.3.3.3 Electrochemically Active Surface Area (ECSA)

Electrochemically active surface area (ECSA) is another important factor which regulates the intrinsic activity of an electrocatalyst. The ECSA was calculated from its C_{dl} according to this equation: ECSA = C_{dl}/Cs, where Cs is the specific capacitance for a flat standard with 1 cm2 of real surface area. The common value for Cs is between 20 μF cm^{-2} and 60 μF cm^{-2}. Generally, 40 μF cm^{-2} is considered as the average value of Cs. First, double-layer capacitance (C_{dl}) was measured for the estimation of the ECSA of a catalyst using scan-rate dependent CVs in a non-Faradaic region,[43,44] as they are proportional to each other. The C_{dl} was calculated by performing simple CVs at different scan rates, ranging from 10 to 50 mV s^{-1}, in the non-Faradaic region in a narrow potential window from 1.1 to 1.2 V vs RHE (Figure 3.8). By plotting the half of the capacitive current density differences ($\Delta j = j_{anode} - j_{cathode}$) at 1.15 V i.e.; $\Delta j/2$ against the scan rate and fitting with a linear fit, C_{dl} can be estimated from the slope as shown in Figure 3.9. The C_{dl} value of NiZn and Ni is 1.84 and 0.98 mF cm^{-2} respectively. The larger C_{dl} value of NiZn (1.84 mF cm^{-2}) than that of Ni (0.98 mF cm^{-2}) attributes to the higher ECSA of NiZn, which contributes to an enhanced electrocatalytic activity of NiZn alloy.

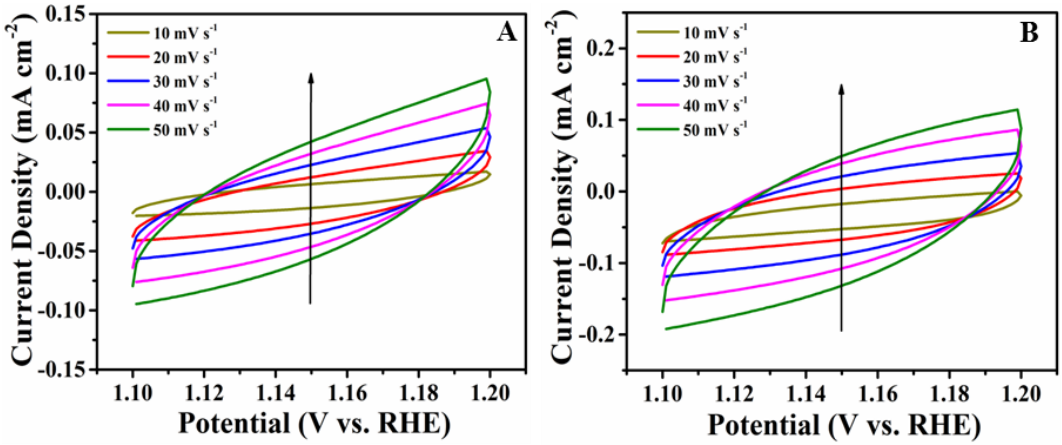

Figure 3.8: Cyclic voltammograms (CVs) of (A) Ni and (B) NiZn measured at different scan rates from 10 to 50 mV s^{-1}.

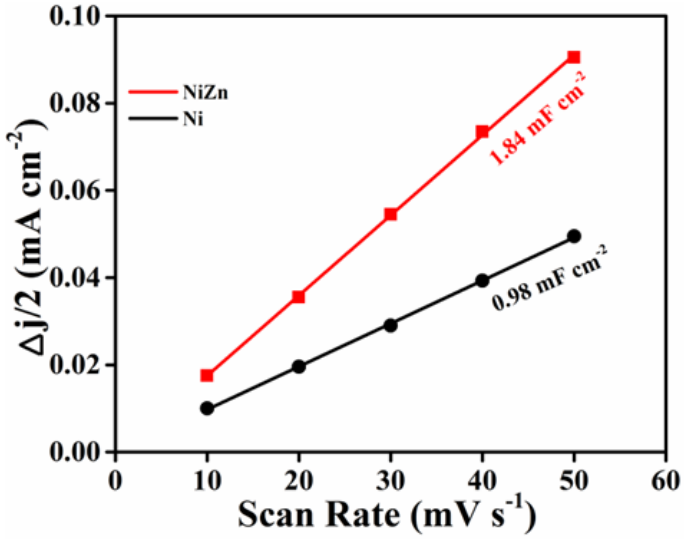

Figure 3.9: Half of the capacitive current density differences (Δj/2) of Ni and NiZn plotted against scan rates, where the double layer capacitance (C_{dl}) is equivalent to the linear slope.

3.3.3.4 Stability Test

Stability and long-standing durability are the pressing necessities for the practical application of any designed electrocatalysts. To demonstrate their stability, potentiostatic analysis of NiZn at an overpotential of η_{10} was carried out for prolonged period of time, indicating almost no change in the current density even after 16 h (Figure 3.10.A). Furthermore, NiZn shows almost unchanged onset potential analogous to the as-deposited fresh catalyst in the LSV curve after continuous OER at η_{10} for a long period of time (Figure 3.10.B). Both the analyses point to the excellent stability as well as durability of NiZn even after repetitive usage.

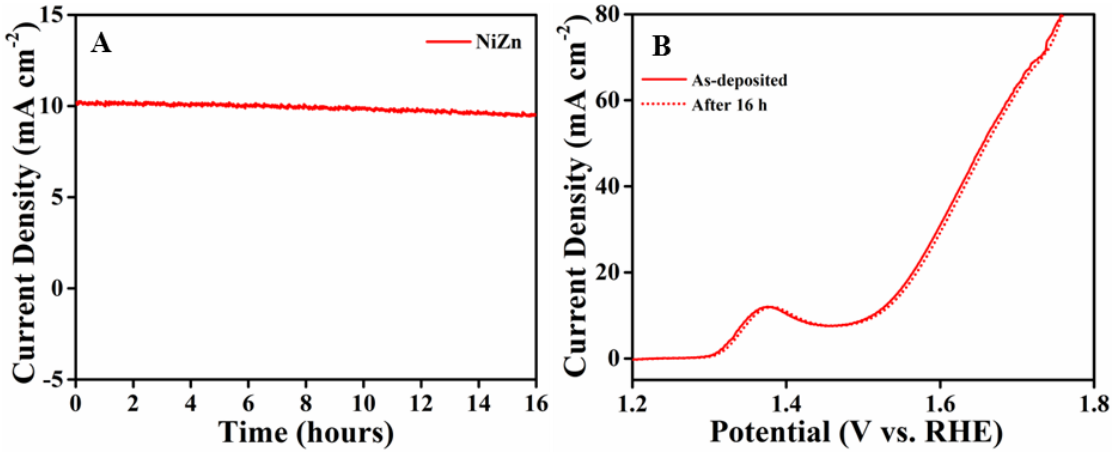

Figure 3.10: (A) i-t curve of NiZn electrocatalyst for OER up to 16 h at η_{10}. (B) NiZn shows almost unchanged LSV curve after continuous OER for 16 h analogous to the as-deposited fresh NiZn catalyst.

3.3.3.5 Post OER Study

Besides electrochemical stability, TEM analysis of NiZn alloy was performed after OER study, which revealed their intact morphology even after the longer chronoamperometry study (Figure 3.11). Then, XPS analysis was performed on NiZn after OER process to demonstrate if there is any chemical change. From the XPS spectra of NiZn alloy, it was noticed that along with the metallic Ni^0 (852.8 eV for Ni $2p_{3/2}$) and Zn^0 (1021.7 eV for Zn $2p_{3/2}$) states, their oxides are also present. The deconvolution of high resolution Ni 2p spectrum (Figure 3.12.A) demonstrates the new peaks for Ni $2p_{3/2}$ at 855.7 eV and for Ni $2p_{1/2}$ at 873.5 eV, suggesting the formation of Ni^{2+} with the metallic Ni^0.[45] Similarly, high resolution Zn 2p spectrum (Figure 3.12.B) indicates the presence of Zn^{2+} along with the metallic Zn^0, as the new peaks are observed at 1022.3 eV and 1045.1 eV for Zn $2p_{3/2}$ and Zn $2p_{1/2}$ respectively.[46] Although TEM analysis demonstrates their unaltered morphology, XPS analysis suggests a slight oxidation of NiZn alloy after prolonged electrochemical study.

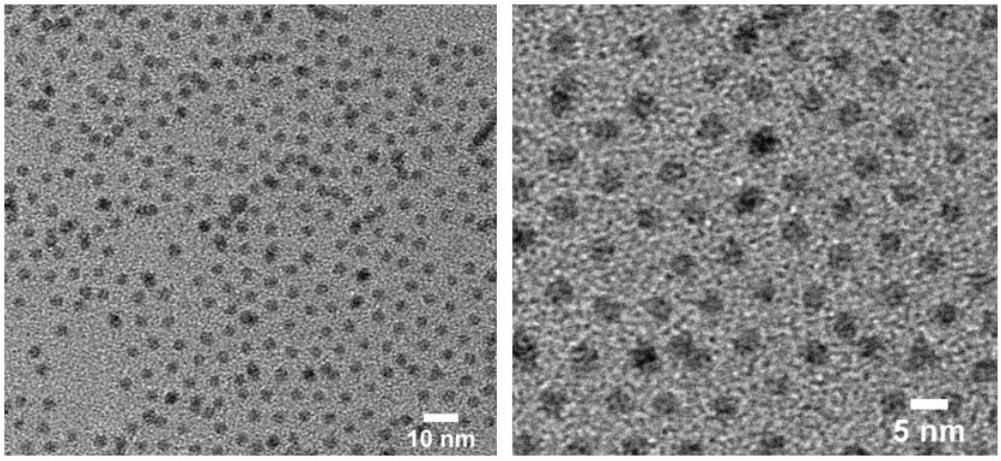

Figure 3.11: TEM micrographs of NiZn intermetallics at two different magnifications after prolonged chronoamperometry analysis.

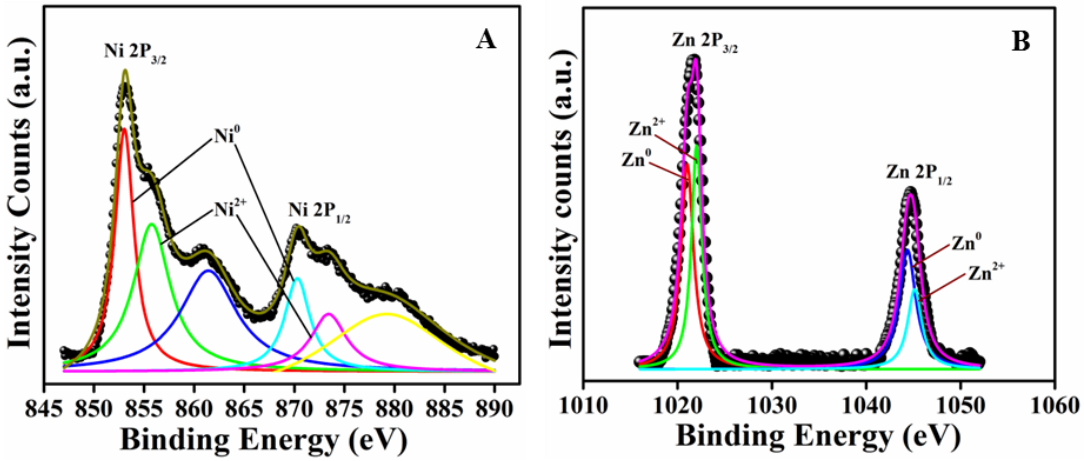

Figure 3.12: XPS spectra of (A) Ni 2p and (B) Zn 2p of NiZn alloy after OER study.

3.3.3.6 Tuning of Composition of the Alloy

It is then interesting to us to study the electrochemical properties of the alloy upon tuning the composition of the constituents. To check this phenomenon, we have prepared nanoscale fcc $Ni_{0.7}Zn_{0.3}$ alloy (PDF No. 01-072-2672) with similar size by changing the reaction condition (Figure 3.13.A, B). The overall composition of Ni and Zn in $Ni_{0.7}Zn_{0.3}$ alloy is quantitatively assessed to be 74.0 and 26.0 atomic wt% of Ni and Zn respectively via ICP-OES analysis. $Ni_{0.7}Zn_{0.3}$ shows an overpotential (η_{10}) of 320 mV which is bit

lower than that of pure Ni NPs but much higher compare to intermetallic NiZn (shown in Figure 3.14.A, B). The estimated overpotential and Tafel slope for all the catalysts are summarized in Table 3.1. All these results signifies that the OER activity is sensitive to the atomic ordering and composition of the alloy, leading to the superior activity of order NiZn intermetallics than that of disorder $Ni_{0.7}Zn_{0.3}$ alloy.

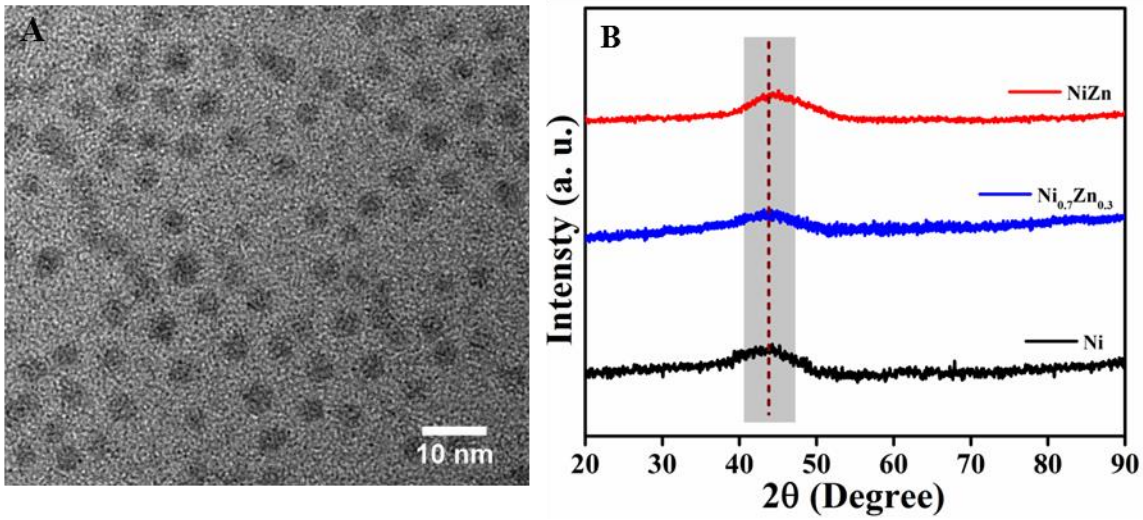

Figure 3.13: (A) TEM micrograph of $Ni_{0.7}Zn_{0.3}$ alloy. (B) XRD patterns of fcc Ni NPs and corresponding fcc $Ni_{0.7}Zn_{0.3}$ and tetragonal NiZn alloys.

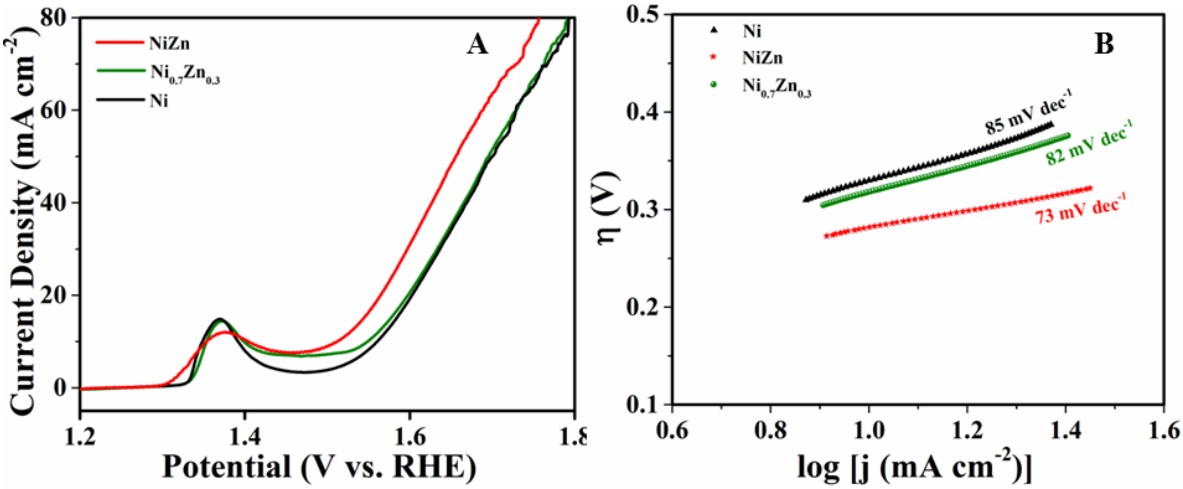

Figure 3.14: (A) LSV curves of Ni, $Ni_{0.7}Zn_{0.3}$ and NiZn at a scan rate of 5 mV s^{-1} in 1.0 M KOH solution and their corresponding (B) Tafel slopes indicate much faster OER kinetics of NiZn intermetallics.

Table 3.1: A summary of overpotentials and Tafel slopes for all the catalysts.

Catalysts	Overpotential (η_{10}) [mV]	Tafel Slope [mV dec^{-1}]
RuO_2	343	92
Ni	332	85
$Ni_{0.7}Zn_{0.3}$	320	82
NiZn	283	73

3.3.3.7 OER Mechanism

In the present system, the diffusion of Zn atoms into the nanocrystalline Ni is the key aspect to enhance the catalytic performances of NiZn alloy. The higher OER activity of the NiZn alloy is associated with the increase in the ECSA together with the intrinsic catalytic activity of Ni as well as the possible synergistic effect between the Ni and Zn metals. The 2p and valence electrons of Ni in case of NiZn alloys shift toward Zn,[38,47,48] resulting in the charge transfer from Ni to Zn and subsequently making the Ni centre slightly positive. Here, Ni is the active center whereas Zn acts as a promoter in NiZn alloy during OER process. Consequently, the OER reaction proceeds very fast via Ni

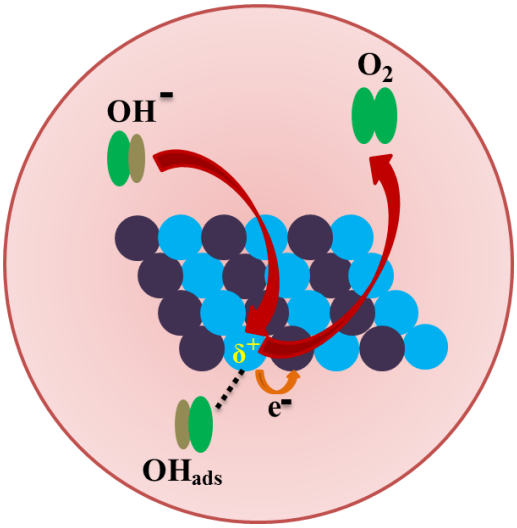

Figure 3.15: Schematic representation of oxygen evolution electrocatalysis in the surface of NiZn alloy. (Ni and Zn centers in NiZn are shown as blue and violet color spheres respectively).

centre in NiZn alloy, as schematically ascribed in Figure 3.15. Basically, upon alloying of Zn into Ni, a modification of the electronic structure of Ni tailored by Zn takes place in the alloy. Furthermore, ordered alloys provide uniform active sites on the same surface plane owing to their compositional and positional order, in addition to the precise control over the structure accompanied by electronic effects.

3.3.3.8 Comparison of Electrocatalytic Activity

Finally, we have compared the electrocatalytic activity of order NiZn alloy with the previously reported Ni-based OER catalysts, as shown in Table 3.2 The as-synthesized NiZn possesses superior electrocatalytic activity towards OER compared to the reported catalysts. In a nutshell, based on the electrocatalytic activity as well as comparison with the expensive conventional electrocatalysts or even several reported electrocatalysts, our overall study demonstrated that intermetallic NiZn NPs can be considered as an effective electrocatalyst for oxygen production.

Table 3.2: OER activity of order NiZn alloy was compared with the reported Ni based electrocatalysts.

Catalysts	Electrolyte	Overpotential (mV) at 10 mA cm^{-2}	Tafel Slope (mV dec^{-1})	References
NiCo LDHs/GC	1.0 M KOH	367	40	49
$NiCo_2O_4$/CNTs		390	68.1	50
NiCo-LDH		335	41	51
$NiCo_2S_4$		337	64	52
Fe-Ni-O_x/GC		286	48	53
NiFe/CN_x		360	59	54
Fe-mCo_3O_4/GC		380	60	55
$Ni_{30}Fe_7Co_{20}Ce_{43}O_x$/GC		410	70	56
NiMo hollow nanorod		310	47	57

NiCo-LDH		420	113	58
NiCoP NPs		360	82	59
$NiCo_2O_4$		360	60	60
NiS@N/S-C		417	48	61
Ni@C-400 NSs		330	145	62
$Ni_xFe_{3-x}O_4$		402	53	63
NiZn		**283**	**73**	**This work**

3.4 Conclusions

In conclusion, an efficient synthesis of ultra-small NiZn intermetallics was demonstrated via thermolysis of corresponding metal precursors in a mixture of hot organic solvents. The present synthetic strategy comprises of chemical conversion of preformed metal NPs into alloys at low temperature via reaction with another metal precursor. The current finding also demonstrates that the Ni NPs act as a precursor to prepare NiZn alloy keeping the morphology intact even during the transformation of metal to the alloy, attributing to a general synthesis pathway to make ultra-small M-Zn intermetallics. The intermetallic NiZn NPs exhibits enhanced electrocatalytic activity and excellent stability towards OER than $Ni_{0.7}Zn_{0.3}$, pure fcc Ni or RuO_2. The present study demonstrates that activity of the alloys upsurges from the composition of the constituents which govern their OER performances. The superior electrocatalytic efficiency of NiZn is ascribed to the modification of the electronic structure of Ni upon incorporation of Zn, together with the atomic scale synergistic effect produced from Ni and Zn in NiZn alloy. Thus, the novelties of our work lie in the controlled fabrication of monodisperse tiny alloys of NiZn having excellent OER activity compared to the expensive conventional as well as several reported electrocatalysts. Our findings also suggest that catalysts with superior activity can be developed by engineering the composition of the constituent metals during fabrication of desired alloyed nanoparticles.

3.5 References

(1) Turner, J. A. Sustainable Hydrogen Production. *Science* **2004**, *305*, 972-974.
(2) Walter, M. G.; Warren, E. L.; McKone, J. R.; Boettcher, S. W.; Mi, Q.; Santori, E. A.; Lewis, N. S. Solar Water Splitting Cells. *Chem. Rev.* **2010**, *110*, 6446-6473.
(3) Tang, C.; Cheng, N.; Pu, Z.; Xing, W.; Sun, X. NiSe Nanowire Film Supported on Nickel Foam: An Efficient and Stable 3D Bifunctional Electrode for Full Water Splitting. *Angew. Chem. Int. Ed.* **2015**, *54*, 9351-9355.
(4) Samanta, A.; Das, S.; Jana, S. Doping of Ni in α-Fe_2O_3 Nanoclews to Boost Oxygen Evolution Electrocatalysis. *ACS Sustainable Chem. Eng.* **2019**, *7*, 12117-12124.
(5) Wang, H.; Lu, Z.; Xu, S.; Kong, D.; Cha, J. J.; Zheng, G.; Hsu, P. C.; Yan, K.; Bradshaw, D.; Prinz, F. B.; Cui, Y. Electrochemical Tuning of Vertically Aligned MoS_2 Nanofilms and Its Application in Improving Hydrogen Evolution Reaction. *Proc. Natl Acad. Sci. U.S.A.* **2013**, *110*, 19701-19706.
(6) Lee, Y.; Suntivich, J.; May, K. J.; Perry, E. E.; Shao-Horn, Y. Synthesis and Activities of Rutile IrO_2 and RuO_2 Nanoparticles for Oxygen Evolution an Acid and Alkaline Solutions. *J. Phys. Chem. Lett.* **2012**, *3*, 399-404.
(7) Concepcion, J. J.; Jurss, J. W.; Brennaman, M. K.; Hoertz, P. G.; Patrocinio, A. O. T.; Iha, N. Y. M.; Templeton, J. L.; Meyer, T. J. Making Oxygen with Ruthenium Complexes. *Acc. Chem. Res.* **2009**, *42*, 1954-1965.
(8) Wang, Y.-J.; Zhao, N.; Fang, B.; Li, H.; Bi, X. T.; Wang, H. Carbon-Supported Pt-Based Alloy Electrocatalysts for the Oxygen Reduction Reaction in Polymer Electrolyte Membrane Fuel Cells: Particle Size, Shape, and Composition Manipulation and Their Impact to Activity. *Chem. Rev.* **2015**, *115*, 3433-3467.
(9) Stamenkovic, V. R.; Mun, B. S.; Arenz, M.; Mayrhofer, K. J. J.; Lucas, C. A.; Wang, G.; Ross, P. N.; Markovic, N. M. Trends in Electrocatalysis on Extended and Nanoscale Pt-Bimetallic Alloy Surfaces. *Nat. Mater.* **2007**, *6*, 241-247.
(10) Shao, M. H.; Sasaki, K.; Adzic, R. R. Pd−Fe Nanoparticles as Electrocatalysts for Oxygen Reduction. *J. Am. Chem. Soc.* **2006**, *128*, 3526-3527.
(11) Lim, B.; Jiang, M.; Camargo, P. H. C.; Cho, E. C.; Tao, J.; Lu, X.; Zhu, Y.; Xia, Y. N. Pd–Pt Bimetallic Nanodendrites with High Activity for Oxygen Reduction. *Science* **2009**, *324*, 1302-1305.
(12) Bu, L.; Guo, S.; Zhang, X.; Shen, X.; Su, D.; Lu, G.; Zhu, X.; Yao, J.; Guo, J.; Huang, X. Surface Engineering of Hierarchical Platinum-Cobalt Nanowires for Efficient Electrocatalysis. *Nat. Commun.* **2016**, *7*, 11850-11859.
(13) Shen, Y.; Zhou, Y.; Wang, D.; Wu, X.; Li, J.; Xi, J. Nickel–Copper Alloy Encapsulated in Graphitic Carbon Shells as Electrocatalysts for Hydrogen Evolution Reaction. *Adv. Energy Mater.* **2018**, *8*, 1701759-1701765.

(14) Yi, Z.; Wang, Z.; Cheng, Y.; Wang, L. Sn-Based Intermetallic Compounds for Li-ion Batteries: Structures, Lithiation Mechanism, and Electrochemical Performances. *Energy Environ. Mater.* **2018**, *1*, 132-147.
(15) Obrovac, M. N.; Chevrier, V. L. Alloy Negative Electrodes for Li-Ion Batteries. *Chem. Rev.* **2014**, *114*, 11444-11502.
(16) Maeda, K.; Teramura, K.; Masuda, H.; Takata, T.; Saito, N.; Inoue, Y.; Domen, K. Efficient Overall Water Splitting under Visible-Light Irradiation on $(Ga_{1-x}Zn_x)(N_{1-x}O_x)$ Dispersed with Rh−Cr Mixed-Oxide Nanoparticles: Effect of Reaction Conditions on Photocatalytic Activity. *J. Phys. Chem. B* **2006**, *110*, 13107-13112.
(17) Jiao, Z.; Zhang, Y.; Ouyang, S.; Yu, H.; Lu, G.; Ye, J.; Bi, Y. BiAg Alloy Nanospheres: A New Photocatalyst for H_2 Evolution from Water Splitting. *ACS Appl. Mater. Interfaces* **2014**, *6*, 19488-19493.
(18) Cai, X.; Wang, A.; Wang, J.; Wang, R.; Zhong, S.; Zhao, Y.; Wu, L.; Chen, J.; Bai, S. Order Engineering on the Lattice of Intermetallic PdCu Co-Catalysts for Boosting the Photocatalytic Conversion of CO_2 into CH_4. *J. Mater. Chem. A* **2018**, *6*, 17444-17456.
(19) Pei, Y.; LaLonde, A. D.; Heinz, N. A.; Snyder, G. J. High Thermoelectric Figure of Merit in PbTe Alloys Demonstrated in PbTe–CdTe. *Adv. Energy Mater.* **2012**, *2*, 670-675.
(20) Takagiwa, Y.; Utada, S.; Kanazawa, I.; Kimura, K. $MoSi_2$-Type Narrow Band Gap Intermetallic Compound $Al_6Re_5Si_4$ as a Thermoelectric Material. *J. Mater. Chem. C* **2015**, *3*, 10422-10429.
(21) Taub, A. I.; Fleischer, R. L. Intermetallic Compounds for High-Temperature Structural Use. *Science* **1989**, *243*, 616-621.
(22) Krenke, T.; Duman, E.; Acet, M.; Wassermann, E. F.; Moya, X.; Manosa, L.; Planes, A. Inverse Magnetocaloric Effect in Ferromagnetic Ni–Mn–Sn Alloys. *Nat. Mater.* **2005**, *4*, 450-454.
(23) Körner, W.; Krugel, G.; Elsässer, C. Theoretical Screening of Intermetallic $ThMn_{12}$-Type Phases for New Hard-Magnetic Compounds with Low Rare Earth Content. *Sci. Rep.* **2016**, *6*, 24686-24694.
(24) Ding, J.; Bu, L.; Guo, S.; Zhao, Z.; Zhu, E.; Huang, Y.; Huang, X. Morphology and Phase Controlled Construction of Pt−Ni Nanostructures for Efficient Electrocatalysis. *Nano Lett.* **2016**, *16*, 2762-2767.
(25) Liu, Y.; Liu, X.; Feng, Q.; He, D.; Zhang, L.; Lian, C.; Shen, R.; Zhao, G.; Ji, Y.; Wang, D.; Zhou, G.; Li, Y. Intermetallic Ni_xM_y (M = Ga and Sn) Nanocrystals: A Non-precious Metal Catalyst for Semi-Hydrogenation of Alkynes. *Adv. Mater.* **2016**, *28*, 4747-4754.

(26) Furukawa, S.; Komatsu, T. Intermetallic Compounds: Promising Inorganic Materials for WellStructured and Electronically Modified Reaction Environments for Efficient Catalysis. *ACS Catal.* **2017**, *7*, 735-765.
(27) Kuttiyiel, K. A.; Sasaki, K.; Su, D.; Wu, L.; Zhu, Y.; Adzic, R. R. Gold-Promoted Structurally Ordered Intermetallic Palladium Cobalt Nanoparticles for the Oxygen Reduction Reaction. *Nat. Commun.* **2014**, *5*, 5185-5192.
(28) Yan, Y.; Du, J. S.; Gilroy, K. D.; Yang, D.; Xia, Y.; Zhang, H. Intermetallic Nanocrystals: Syntheses and Catalytic Applications. *Adv. Mater.* **2017**, *29*, 1605997-1606025.
(29) Wang, D.; Xin, H. L.; Hovden, R.; Wang, H.; Yu, Y.; Muller, D. A.; DiSalvo, F. J.; Abruña, H. D. Structurally Ordered Intermetallic Platinum-Cobalt Core-Shell Nanoparticles with Enhanced Activity and Stability as Oxygen Reduction Electrocatalysts. *Nat. Mater.* **2013**, *12*, 81-87.
(30) Casado-Rivera, E.; Volpe, D. J.; Alden, L.; Lind, C.; Downie, C.; Vazquez-Alvarez, T.; Angelo, A. C.; DiSalvo, F. J.; Abruna, H. D. Electrocatalytic Activity of Ordered Intermetallic Phases for Fuel Cell Applications. *J. Am. Chem. Soc.* **2004**, *126*, 4043-4049.
(31) Vassilev, G.; Gomez-Acebo, T.; Tedenac, J.-C. Thermodynamic Optimization of the Ni-Zn System. *J. Phase Equilib.* **2000**, *21*, 287-301.
(32) Schmetterer, C.; Rajamohan, D.; Ipser, H.; Flandorfer, H. The High-Temperature Phase Equilibria of the Ni–Sn–Zn System: Isothermal Sections. *Intermetallics* **2011**, *19*, 1489-1501.
(33) Jana, S. Advances in Nanoscale Alloys and Intermetallics: Low Temperature Solution Chemistry Synthesis and Application in Catalysis, *Dalton Trans.* **2015**, *44*, 18692–18717.
(34) Wu, L. S.; Dai, H. B.; Wen, X. P.; Wang, P. Ni-Zn Alloy Nanosheets Arrayed on Nickel Foamas a Promising Catalyst for Electrooxidation of Hydrazine. *ChemElectroChem* **2017**, *4*, 1944-1949.
(35) Biesinger, M. C.; Payne, B. P.; Grosvenor, A. P.; Lau, L. W.; Gerson, A. R.; Smart, R. S. C. Resolving Surface Chemical States in XPS Analysis of First Row Transition Metals, Oxides and Hydroxides: Cr, Mn, Fe, Co and Ni. *Appl. Surf. Sci.* **2011**, *257*, 2717-2730.
(36) Yin, G.; Abe, H.; Kodiyath, R.; Ueda, S.; Srinivasan, N.: Yamaguchi, A.; Miyauchi, M. Selective Electro-or Photo-Reduction of Carbon Dioxide to Formic Acid Using a Cu–Zn Alloy Catalyst. *J. Mater. Chem. A* **2017**, *5*, 12113-12119.
(37) Sivagami, I. N.; Prasanna, K.; Santhoshkumar, P.; Jo, Y. N.; Seo, G. Y.; Lee, C. W. Agar Templated Electrodeposition of Binary Zinc-Cobalt Alloy and Formation of Zinc-Cobalt-Carbon Nanocomposite for Application in Secondary Lithium Batteries. *J. Alloys Compd.* **2017**, *697*, 450-460.

(38) Rodriguez, J. A.; Kuhn, M. Interaction of Zinc with Transition-Metal Surfaces: Electronic and Chemical Perturbations Induced by Bimetallic Bonding. *J. Phys. Chem.* **1996**, *100*, 381-389.
(39) Puntes, V. F.; Zanchet, D.; Erdonmez, C. K.; Alivisatos, A. P. Synthesis of hcp-Co Nanodisks. *J. Am. Chem. Soc.* **2002**, *124*, 12874−12880.
(40) Jana, S.; Chang, J. W.; Rioux. R. M. Synthesis and Modeling of Hollow Intermetallic Ni−Zn Nanoparticles. Formed by the Kirkendall Effect. *Nano Lett.* **2013**, *13*, 3618-3625.
(41) Jia, Y.; Zhang, L.; Gao, G.; Chen, H.; Wang, B.; Zhou, J.; Soo, M. T.; Hong, M.; Yan, X.; Qian, G.; Zou, J. A Heterostructure Coupling of Exfoliated Ni–Fe Hydroxide Nanosheet and Defective Graphene as a Bifunctional Electrocatalyst for Overall Water Splitting. *Adv. Mater.* **2017**, *29*, 1700017-1700024.
(42) Xuan, C.; Wang, J.; Xia, W.; Zhu, J.; Peng, Z.; Xia, K.; Xiao, W.; Xin, H. L.; Wang, D. Heteroatom (P, B, or S) Incorporated NiFe-Based Nanocubes as Efficient Electrocatalysts for the Oxygen Evolution Reaction. *J. Mater. Chem. A* **2018**, *6*, 7062-7069.
(43) Yu, M.; Moon, G.; Bill, E.; Tüysüz, H. Optimizing Ni–Fe Oxide Electrocatalysts for Oxygen Evolution Reaction by Using Hard Templating as a Toolbox. *ACS Appl. Energy Mater.* **2019**, *2*, 1199-1209.
(44) McCrory, C. C.; Jung, S.; Peters, J. C.; Jaramillo, T. F. Benchmarking Heterogeneous Electrocatalysts for the Oxygen Evolution Reaction. *J. Am. Chem. Soc.* **2013**, *135*, 16977-16987.
(45) Naghash, A. R.; Etsell, T. H.; Xu, S. XRD and XPS Study of Cu-Ni Interactions on Reduced Copper-Nickel-Aluminum Oxide Solid Solution Catalysts. *Chem. Mater.* **2006**, *18*, 2480-2488.
(46) Guillory II, R. J.; Sikora-Jasinska, M.; Drelich, J. W.; Goldman, J. In Vitro Corrosion and In Vivo Response to Zinc Implants with Electropolished and Anodized Surfaces. *ACS Appl. Mater. Interfaces* **2019**, *11*, 19884-19893.
(47) Rodriguez, J. A. Physical and Chemical Properties of Bimetallic Surfaces. *Surf. Sci. Rep.* **1996**, *24*, 223-287.
(48) Pan, Z.; Wang, R; Chen, J. Deoxygenation of Methyl Laurate as a Model Compound on Ni-Zn Alloy and Intermetallic Compound Catalysts: Geometric and Electronic Effects of Oxophilic Zn. *Appl. Catal., B* **2018**, *224*, 88-100.
(49) Liang, H.; Meng, F.; Cabán-Acevedo, M.; Li, L.; Forticaux, A.; Xiu, L.; Wang, Z.; Jin, S. Hydrothermal Continuous Flow Synthesis and Exfoliation of NiCo Layered Double Hydroxide Nanosheets for Enhanced Oxygen Evolution Catalysis. *Nano Lett.* **2015**, *15*, 1421-1427.

(50) Cheng, H.; Su, Y. Z.; Kuang, P. Y.; Chen, G. F.; Liu, Z. Q. Hierarchical $NiCo_2O_4$ Nanosheet-Decorated Carbon Nanotubes towards Highly Efficient Electrocatalyst for Water Oxidation. *J. Mater. Chem. A* **2015**, *3*, 19314-19321.
(51) Song, F.; Hu, X. Exfoliation of Layered Double Hydroxides for Enhanced Oxygen Evolution Catalysis. *Nat. Commun.* **2014**, *5*, 4477-4485.
(52) Jiang, J.; Yan, C.; Zhao, X.; Luo, H.; Xue, Z.; Mu, T. A PEGylated Deep Eutectic Solvent for Controllable Solvothermal Synthesis of Porous $NiCo_2S_4$ for Efficient Oxygen Evolution Reaction. *Green Chem.* **2017**, *19*, 3023-3031.
(53) Kuai, L.; Geng, J.; Chen, C. Y.; Kan, E. J.; Liu, Y. D.; Wang, Q.; Geng, B. Y. A Reliable Aerosol-Spray-Assisted Approach to Produce and Optimize Amorphous Metal Oxide Catalysts for Electrochemical Water Splitting. *Angew. Chem. Int. Ed.* **2014**, *53*, 7547-7551.
(54) Ci, S.; Mao, S.; Hou, Y.; Cui, S.; Kim, H.; Ren, R.; Wen, Z.; Chen, J. Rational Design of Mesoporous NiFe-Alloy Based Hybrids for Oxygen Conversion Electrocatalysis. *J. Mater. Chem. A* **2015**, *3*, 7986-7993.
(55) Xiao, C.; Lu, X.; Zhao, C. Unusual Synergistic Effects Upon Incorporation of Fe and/or Ni into Mesoporous Co_3O_4 for Enhanced Oxygen Evolution. *Chem. Commun.* **2014**, *50*, 10122-10125.
(56) Haber, J. A.; Cai, Y.; Jung, S.; Xiang, C.; Mitrovic, S.; Jin, J.; Bell, A. T.; Gregoire, J. M. Discovering Ce-Rich Oxygen Evolution Catalysts, from High Throughput Screening to Water Electrolysis. *Energy Environ. Sci.* **2014**, *7*, 682-688.
(57) Tian, J.; Cheng, N.; Liu, Q.; Sun, X.; He, Y.; Asiri, A. M. Self-Supported NiMo Hollow Nanorod Array: An Efficient 3D Bifunctional Catalytic Electrode for Overall Water Splitting. *J. Mater. Chem. A* **2015**, *3*, 20056-20059.
(58) Jiang, J.; Zhang, A.; Li, L.; Ai, L. Nickel-Cobalt Layered Double Hydroxide Nanosheets as High-Performance Electrocatalyst for Oxygen Evolution Reaction. *J. Power Sources* **2015**, *278*, 445-451.
(59) Vigil, J. A.; Lambert, T. N.; Christensen, B. T. Cobalt Phosphide-Based Nanoparticles as Bifunctional Electrocatalysts for Alkaline Water Splitting. *J. Mater. Chem. A* **2016**, *4*, 7549-7554.
(60) Xiao, Y.; Feng, L.; Hu, C.; Fateev, V.; Liu, C.; Xing, W. $NiCo_2O_4$ 3 Dimensional Nanosheet as Effective and Robust Catalyst for Oxygen Evolution Reaction. *RSC Adv.* **2015**, *5*, 61900-61905.
(61) Yang, L.; Gao, M.; Dai, B.; Guo, X.; Liu, Z.; Peng, B. An Efficient NiS@N/S-C Hybrid Oxygen Evolution Electrocatalyst Derived from Metal-Organic Framework. *Electrochim. Acta* **2016**, *191*, 813-820.

(62) Xi, W.; Ren, Z.; Kong, L.; Wu, J.; Du, S.; Zhu, J.; Xue, Y.; Meng, H.; Fu, H. Dual-Valence Nickel Nanosheets Covered with Thin Carbon as Bifunctional Electrocatalysts for Full Water Splitting. *J. Mater. Chem. A* **2016**, *4*, 7297-7304.
(63) Feng, Y.; Wei, J.; Ding, Y. Efficient Photochemical, Thermal, and Electrochemical Water Oxidation Catalyzed by a Porous Iron-Based Oxide Derived Metal-Organic Framework. *J. Phys. Chem. C* **2015**, *120*, 517-526.

****

Chapter 4

Doping of Ni in Iron Oxide Nanoclews to Boost Oxygen Evolution Electrocatalysis

4.1 Introduction

The never ending energy demands provoke to the researchers for the production of clean and renewable energy via water splitting as a substitute to the fossil fuels, resulting in a challenging direction to pursue and subsequently design of efficient and renewable energy conversion systems.[1,2] However, the fabrication of promising water splitting systems is limited from being of practical use to date owing to the sluggish kinetics of the anodic oxygen evolution reaction (OER) that proceeds via a multistep four proton-coupled electron transfer procedure.[2-4] An effective electrocatalyst is therefore the pressing need to diminish the overpotential, which in turn overcomes the kinetic barrier and accelerates the OER reaction. Currently, the most active and widely used OER catalysts are RuO_2 and IrO_2, but their large-scale application is restricted owing to the high cost, scarcity as well as poor stability in alkali electrolytes, in which they oxidized to IrO_3 and RuO_4 respectively and finally dissolved in solution.[1,5,6]

Over the recent years, extensive efforts have been put forward in pursuing and designing noble metal free durable and low-cost OER catalysts as alternatives, including transition metals,[7-9] metal oxides,[2,10-12] phosphides,[13-15] layered double hydroxides,[16-18] metal dichalcogenides,[19-21] heteroatom doped carbon matrix[22-25] and so on. Significantly, among the numerous catalysts, transition metal oxides are one of the important classes of materials which possess different oxidation states and coordination environments,[26-28] resulting in tunable electrocatalytic OER activity together with long-term stability in alkaline condition. Iron based oxides are fascinating materials from both fundamental and technological relevance. They have triggered considerable attention to the researchers on

account of their intriguing properties, abundance in earth, environmentally benign, ease to make, controllable morphology and superb stability.[29-31] Although extensive research work has been performed on the synthesis of numerous iron oxide nanostructures, however, their application is limited by tedious and expensive synthetic procedures. Thus, their widespread application in the varied field is yet to be achieved. Alternatively, iron oxide nanomaterials synthesized through a light-driven solution chemistry approach may be an attractive method due to cost-effectiveness, large-scale production together with mostly ease of preparation.

However, OER activity of pure iron oxide based catalysts is far beyond the expectation as they demonstrate poor conductivity[32-34] and thus needs further improvement. Innovation of materials with new chemical composition always becomes a fascinating way in the cutting edge research in materials science, but tuning of the electronic structure of developed materials is another aspect in altering their chemico-physical properties for optimization of their catalytic activities. Interestingly, doping is an effective and profound way to improve the OER activity of catalysts,[35-37] most probably due to the change in their electronic structure along with improved electrical conductivity upon inclusion of dopants in catalysts.

In this chapter, a unique synthesis route was demonstrated to prepare α-Fe_2O_3 nanoclews using a simple light-driven solution chemistry route without using any template molecule and the as-prepared nanoclews were explored as an OER electrocatalyst. To boost the catalytic activity, Ni was doped in α-Fe_2O_3 nanoclews, resulting in the formation of Ni-Fe_2O_3 with analogous morphology. Elemental mapping indicates uniform distribution of Ni with the basic elements (Fe and O) throughout the nanoclews, providing more exposed catalytic active sites owing to their unique morphology. An outstanding OER activity with an enduring structural and morphological stability of the Ni-Fe_2O_3 nanoclews has been demonstrated in details and compared with the present-day OER catalyst.

4.2 Experimental Section

4.2.1 Synthesis of Fe_2O_3 Nanoclews

The Fe_2O_3 nanoclews were synthesized based on the following route. First, 1.0 mmol of iron (III) chloride was dissolved in a glass vial containing 7.0 ml of Millipore water. Then, NaOH solution (3 wt%; 3.0 mL) was added drop-wise into the iron (III) chloride solution and the whole reaction mixture was stirred well for 10 min. Next, the glass vial was closed tightly and kept for 24 h under the visible light. The reaction temperature was maintained to 90 °C throughout the reaction. Once the reaction was completed, the product was collected by centrifugation. To remove NaOH and unreacted iron (III) chloride if any, the obtained product was washed with Millipore water for several times. After air-drying, the product was collected to carry out the experiments.

4.2.2 Synthesis of Ni Doped Fe_2O_3 Nanoclews

For the synthesis of Ni doped Fe_2O_3 nanoclews (denoted as Ni-Fe_2O_3), first Fe_2O_3 nanoclews (0.1 g) were added in a glass vial containing 0.2 mmol of nickel (II) chloride dissolved in Millipore water (7.0 mL). Then, NaOH solution (3 wt%; 3.0 mL) was added drop-wise into the aforesaid reaction mixture. In a similar fashion, the glass vial containing the mixture solution was kept for 24 h under the visible light as mentioned earlier. The product was obtained via centrifugation after washing with Millipore water. The product was dried in air and used to study the OER performance.

4.2.3. Electrochemical Experiment

All the electrochemical experiments were performed in a conventional three-electrode system of an electrochemical workstation (CHI 660E) at room temperature using Ag/AgCl (saturated KCl solution) as the reference electrode, Pt wire as the counter electrode and glassy carbon (GC) as the working electrode. All potentials were referenced to the reversible hydrogen electrode (RHE) by the equation: *E (vs. RHE) = E (vs. Ag/AgCl) + 0.197 + 0.059 pH*. Typically, 4.0 mg (30 wt% sample in carbon black) of Fe_2O_3 nanoclews was dispersed in the mixed solution containing distilled water (250 μL),

isopropanol (250 μL) and Nafion® solution (1%, 20 μL), followed by sonication for at least 60 min to form a homogeneous mixture. The working electrode was then prepared by drop-casting 20 μL of the mixture solution onto the glassy carbon (GC) electrode with a diameter of 3 mm and dried overnight in air. Before deposition of the catalyst, the GC electrode was polished with 1.0, 0.3 and 0.05 μm alumina slurry successively and washed several times with distilled water. The final loading for all catalysts on the GC electrode is about 0.68 mg cm^{-2}. Linear sweep voltammetry (LSV) with scan rate of 5 mV s^{-1} was conducted in 1.0 M KOH solution. The electrochemical impedance spectroscopy (EIS) was carried out in the frequency range of 0.1 Hz to 100 kHz with an AC amplitude of 0.005 V. Similar procedure was followed for the preparation of working electrode using Ni-Fe_2O_3 and standard RuO_2 catalysts. Based on the following equation, overpotential (η) was calculated for each catalyst: $\eta = E(RHE) - 1.23\ V$.

4.3 Results and Discussion

4.3.1 Characterization of Fe_2O_3 and Ni-Fe_2O_3 Nanoclews

The synthesis of Fe_2O_3 nanostructures was carried out through a light-driven route via decomposition of an aqueous solution of iron (III) chloride under alkaline condition without using any template molecule. We have then prepared Ni-Fe_2O_3 nanostructures to enhance the catalytic performance of Fe_2O_3 nanostructures.

4.3.1.1 FESEM and TEM Analyses of Pristine Fe_2O_3 Nanoclews

The morphology of Fe_2O_3 nanostructures was characterized by field emission scanning electron microscopy (FESEM) and transmission electron microscopy (TEM), presented in Figure 4.1. The FESEM images demonstrated the formation of clew-like morphology of Fe_2O_3 as illustrated in Figure 4.1.A-C. At high magnification, it was observed that the nanoclews are made up of assemblies of tiny nanorods, oriented in a panoramic morphology (Figure 4.1.C). TEM images (Figure 4.1.D,E) also attribute to the formation of clew-like morphology of Fe_2O_3 with size of 150 ± 10 nm. The high resolution TEM

(HRTEM) image presented in Figure 4.1.F, specifies well-resolved lattice fringes with spacing of 0.25 nm owing to the (110) planes of α-Fe_2O_3.

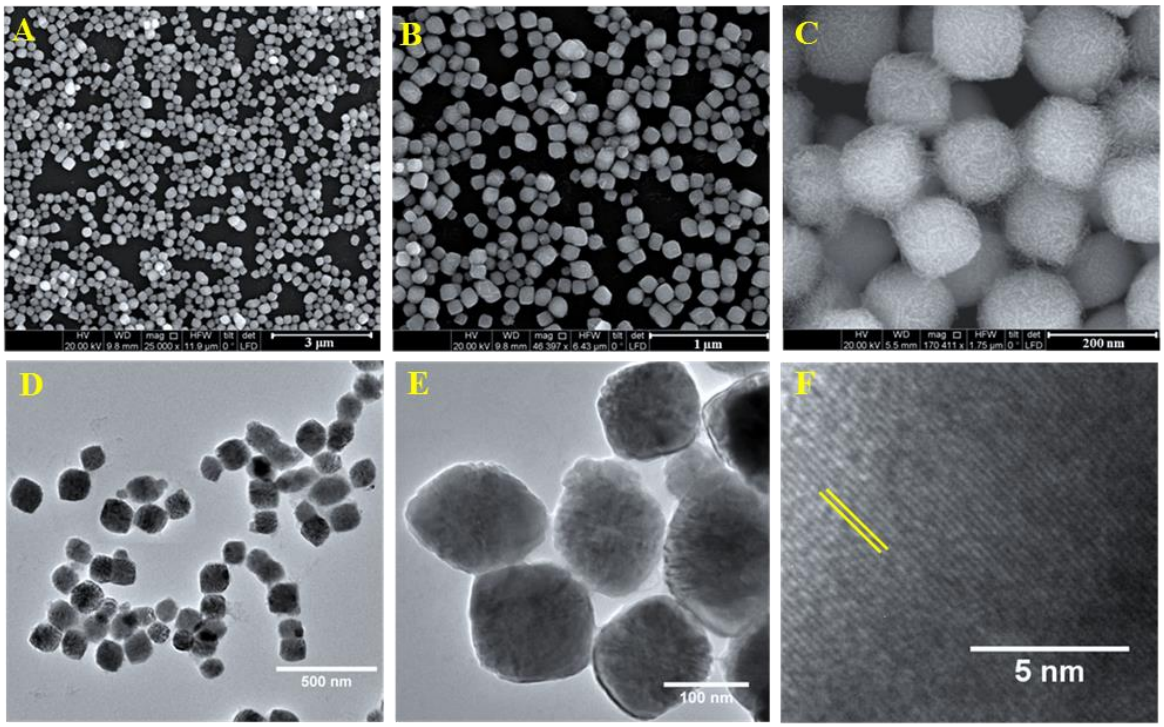

Figure 4.1: (A-C) FESEM and (D,E) TEM images of Fe_2O_3 nanostructures demonstrated the formation of clew-like morphology. (F) HRTEM image represents formation of Fe_2O_3.

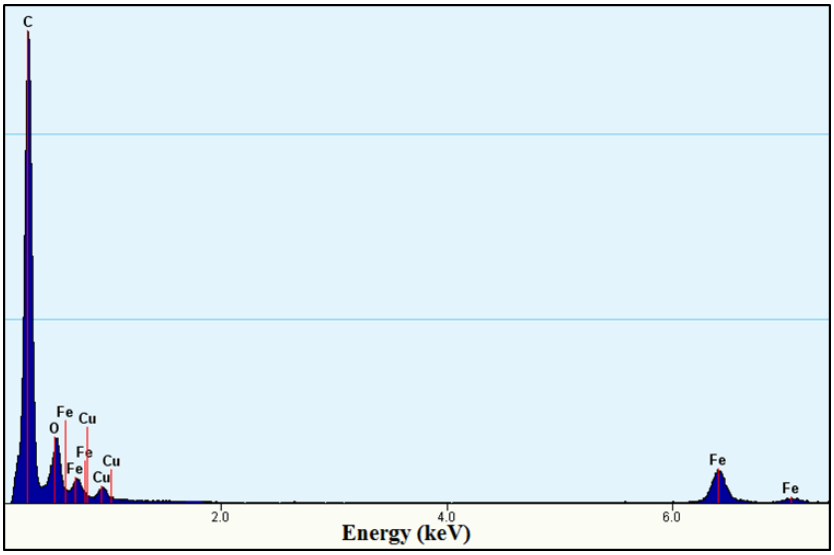

Figure 4.2: EDS spectrum of Fe_2O_3 nanoclews indicates the presence of Fe and O in the nanoclews.

4.3.1.2 EDS Analysis of Fe_2O_3 Nanoclews

The X-ray energy dispersive spectrum (EDS) of Fe_2O_3 nanoclews was presented in Figure 4.2. The spectrum clearly suggested that the nanoclews are composed of Fe and O only.

4.3.1.3 FESEM and TEM Micrographs of Ni-Fe_2O_3 Nanoclews

To analyze the size and morphology after Ni doping, FESEM and TEM analyses were performed, shown in Figure 4.3. FESEM images of the Ni-Fe_2O_3 nanoclews (Figure 4.3.A,B) demonstrate their unaltered morphology or size even after Ni doping. TEM images further ascribed to the formation of clew-like morphology of Ni-Fe_2O_3 with no change in their size (Figure 4.3.C,D).

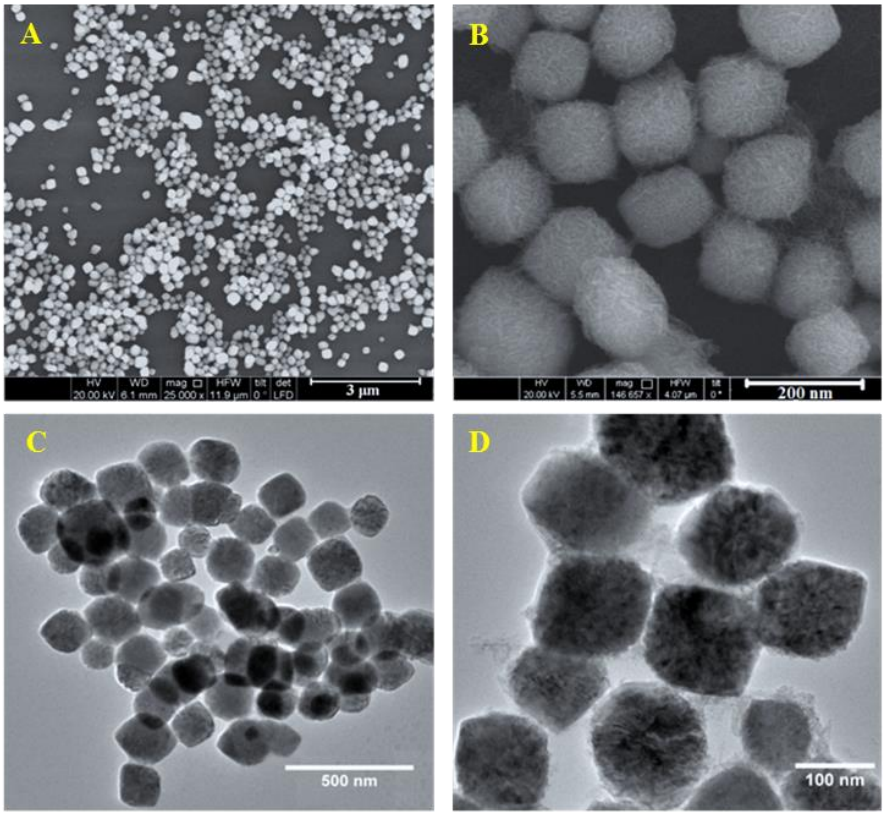

Figure 4.3: (A,B) FESEM and (C,D) TEM images of Ni-Fe_2O_3 nanoclews at different magnifications.

4.3.1.4 EDS and ICP-OES Analyses

EDS spectrum of Ni-Fe_2O_3 nanoclews also demonstrates that the nanoclews are made up of Fe, O, and Ni (Figure 4.4). The concentration of doped Ni in Ni-Fe_2O_3 was assessed to be 7.22 wt% via inductively coupled plasma optical emission spectrometry (ICP-OES) analysis. The elemental composition acquired by EDS analysis indicated that 7.36 wt% Ni was doped in Ni-Fe_2O_3 nanoclews (with an atomic ratio of 1 : 5.7 for Ni to Fe), which is accordance with the ICP-OES analysis.

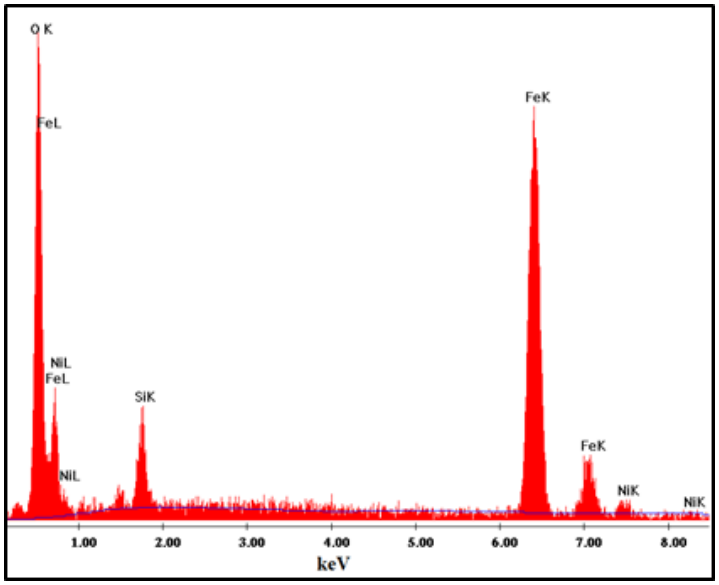

Figure 4.4: EDS spectrum of Ni-Fe_2O_3 nanoclews demonstrates the existence of Ni along with Fe and O in the nanoclews.

4.3.1.5 STEM-EDS Elemental Mapping of Ni-Fe_2O_3 Nanoclews

To directly envisage the Ni-doping in Fe_2O_3 nanoclews, scanning transmission electron microscopy-energy dispersive spectroscopy (STEM-EDS) elemental mapping was carried out. STEM image of Ni-Fe_2O_3 nanoclews is presented in Figure 4.5. The elemental mapping of Ni- Fe_2O_3 nanoclews clearly attributes to the presence of Ni with Fe and O, where Ni is homogeneously distributed throughout the nanoclews. Thus, elemental analysis signifies the uniform doping of Ni within the entire Fe_2O_3 nanoclews.

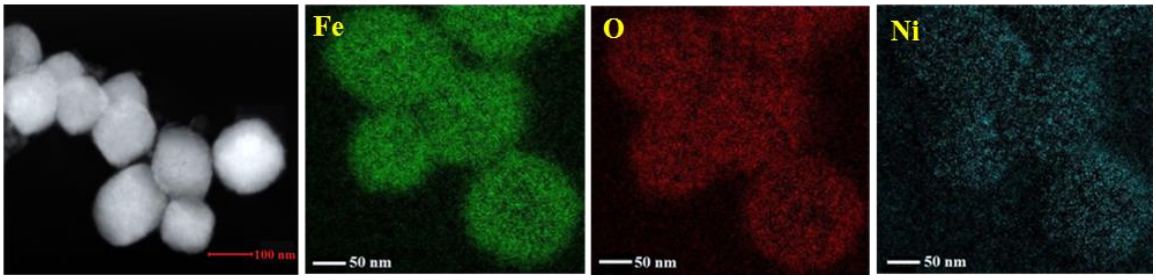

Figure 4.5: STEM image of Ni-Fe_2O_3 nanoclews and their corresponding elemental maps, demonstrating homogeneous distribution of Ni with Fe and O in the nanoclews.

4.3.1.6 XRD Analysis

The crystal structure of Fe_2O_3 nanoclews was characterized by X-ray diffraction (XRD) study. All the diffraction peaks (Figure 4.6) can be assigned to (012), (104), (110), (113), (024) and (116) of α-phase of Fe_2O_3 with a rhombohedral crystal structure (JCPDS No. 33-06664). XRD pattern further authenticates successful synthesis of α-Fe_2O_3 nanoclews, as no signals for iron hydroxides, other oxides or impurities were noticed. Interestingly, XRD pattern of Ni-Fe_2O_3 nanoclews is analogous to that of α-Fe_2O_3 without the presence of any additional phases for Ni. Only a shift of reflections to the lower 2θ angles occurs after doping, suggesting the complete incorporation of Ni atoms into the Fe_2O_3 lattice.

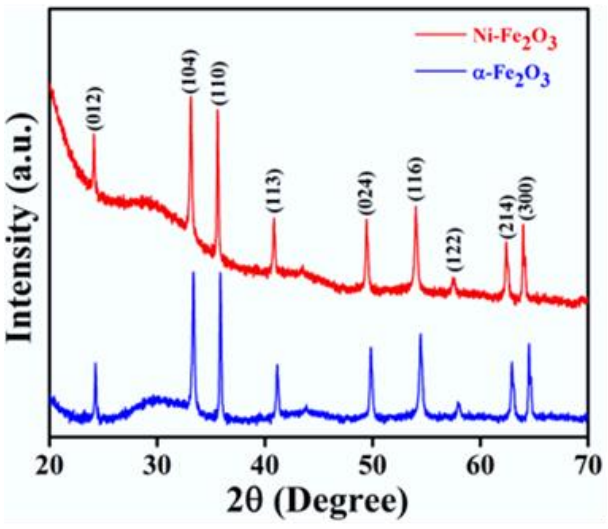

Figure 4.6: XRD pattern of α-Fe_2O_3 and Ni-Fe_2O_3 nanoclews.

4.3.1.7 FTIR Study

Fourier transform infrared (FTIR) spectra indicate the existence of two bands at 3342 and 1643 cm^{-1} for the stretching and bending vibrations of hydroxyl groups or water molecules in both α-Fe_2O_3 and Ni-Fe_2O_3 nanoclews (Figure 4.7). Apart from these bands, two distinct absorption peaks at 574 and 475 cm^{-1} were observed for the Fe-O band vibrations of α-Fe_2O_3,[38,39] which shift to the lower frequency region to 535 and 463 cm^{-1} respectively as a result of Ni doping into the Fe_2O_3 lattice, confirming to the formation of Ni-Fe_2O_3 nanoclews.[39]

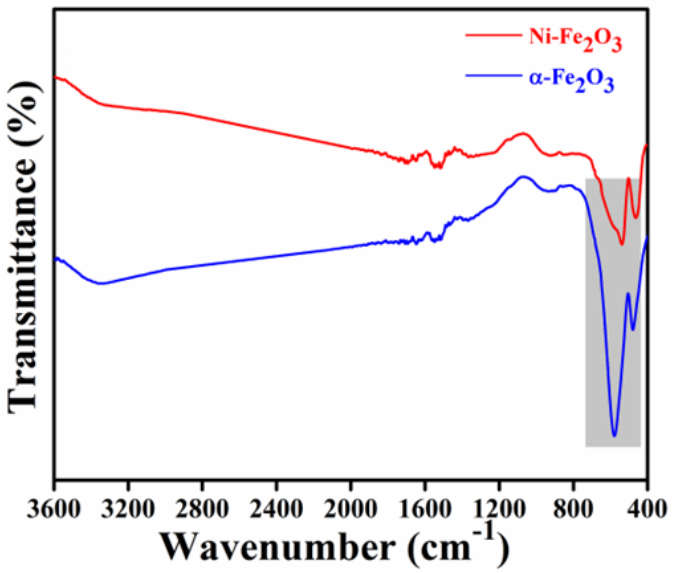

Figure 4.7: FTIR spectra of pristine α-Fe_2O_3 and after Ni doping in α-Fe_2O_3 nanoclews.

4.3.1.8 XPS Analysis

To gain insight into the elemental compositions of the surface as well as valence states of Ni-Fe_2O_3 nanoclews, X-ray photoelectron spectroscopy (XPS) was carried out (Figure 4.8). XPS analysis further confirms the signature of Ni, Fe and O in Ni-Fe_2O_3 nanoclews. In Ni 2p high resolution spectrum (Figure 4.8.A), the main peak at 855.6 eV with a satellite at 861.3 eV accredited to Ni $2p_{3/2}$ and the peak at 873.3 eV with a satellite at 879.2 eV pointed to Ni $2P_{1/2}$, ascribing to the distinctive nickel species, i.e.; Ni^{2+} ion.[40,41]

Likewise, the fine scanned Fe 2p spectrum (Figure 4.8.B) indicates the presence of two peaks for Fe $2p_{3/2}$ and Fe $2p_{1/2}$ with a binding energy difference of 13.8 eV (pink line), attributing to the presence of Fe^{3+}. The electron binding energies of Fe $2p_{3/2}$ at 709.3 and Fe $2p_{1/2}$ at 723.1 eV along with the satellite peaks at 717.7 and 731.1 eV corroborate to the signature of Fe^{3+} as a primary existence form in the nanoclews.[42,43] However, peaks observed at 706.7 and 722.1 eV (blue line) demonstrate the coexistence of a low concentration of Fe^{+2}. The O 1s spectra were deconvoluted into four characteristic peaks at 529.4, 530.4, 531.2 and 531.9 eV respectively (Figure 4.8.C). The observed peaks are due to the oxygen atoms bound to iron (529.4 eV), surface-adsorbed oxygen or hydroxyl groups may be due to substitution of O atoms by hydroxyl groups (530.4 eV), defect sites having low oxygen coordination (531.2 eV), along with physisorbed/chemisorbed molecular water at the surface (531.9 eV) respectively.[9] All the aforesaid experimental analyses and succeeding collective results ascertain the successful doping of Ni into α-Fe_2O_3 nanoclews, ensuing in the formation of Ni-Fe_2O_3, which may find potential application in energy storage and conversion because of their high surface activity.

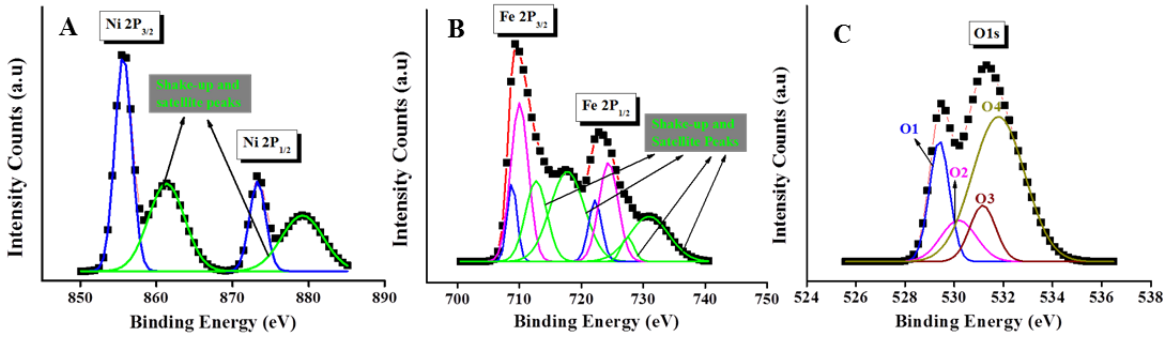

Figure 4.8: XPS analysis for Ni-Fe_2O_3 nanoclews; (A) Ni 2p, (B) Fe 2p and (C) O 1s region of Ni-Fe_2O_3 nanoclews.

4.3.2 OER Activity

Transition metal based nanoclews comprised of assemblies of tiny nanorods are expected to hold rich and tunable electronic properties which may be fascinating to pursue their application as an efficient OER catalyst. The intrinsic catalytic activity of both pristine

Fe_2O_3 and Ni-Fe_2O_3 nanoclews was demonstrated in alkaline solutions (1.0 M KOH) in a standard three-electrode system. The catalytic behavior of the synthesized materials was tested on a deposited ink (~0.68 mg cm^{-2}) containing the sample and carbon black suspended in a mixture of Nafion, isopropanol and water. To assess the performance of synthesized catalyst, we have measured the electrocatalytic activity of a standard OER catalyst, commercial RuO_2 on carbon black with similar loading of ~0.68 mg cm^{-2}.

4.3.2.1 Linear Sweep Voltammetry (LSV) and Electrochemical Impedance Spectroscopy (EIS)

In the present study, Fe_2O_3 nanoclews possess moderate OER efficiency, exhibiting lesser activity than that of commercial RuO_2. Electrocatalytic activity of Fe_2O_3 nanoclews was then tuned by Ni doping. However, upon Ni doping on Fe_2O_3, Ni-Fe_2O_3 nanoclews demonstrate much higher OER activity compare to Fe_2O_3 and even the commercial RuO_2. The required overpotential to achieve the current density of 10 mA cm^{-2} (η_{10}) was estimated from linear sweep voltammetry (LSV) curve (Figure 4.9.A). This is the decisive factor to assess the OER activity of a catalyst. It was found that Ni-Fe_2O_3 shows overpotential of 277 mV which is exceptionally low compare to 440 mV obtained for pristine Fe_2O_3, whereas it is 360 mV for RuO_2 catalyst. Overpotential at different current densities (e.g.; η_{10}, η_{25} and η_{50}) for Ni-Fe_2O_3, pristine Fe_2O_3 and RuO_2 is presented in Figure 4.9.B and Table 1. Likewise, a smaller Tafel slope is the pressing need for a catalyst from practical as well as economical viewpoint. Tafel slope basically determines the OER kinetics and also demonstrates the impact of potential on the steady state current density. Tafel plot was obtained from $\eta = b\ log(j/j_0)$, where η represents the overpotential, b is the Tafel slope, j and j_0 represent current density and exchange current density respectively.[44] The Tafel slope shown in Figure 4.9.C was measured to be 68 mV dec^{-1} for Ni-Fe_2O_3, whereas a higher Tafel slope of 134 mV dec^{-1} was achieved for Fe_2O_3. The lower Tafel slope of Ni-Fe_2O_3 even compared to the state-of-the art RuO_2catalyst (96 mV dec^{-1}) confirms that the doped structure has enhanced ionic and electronic conductivities which facilitate the catalytic process in a better way, accrediting Ni-Fe_2O_3 nanoclews as an efficient electrocatalyst. Overpotential and Tafel slope are summarized for each catalyst in Table 4.1.

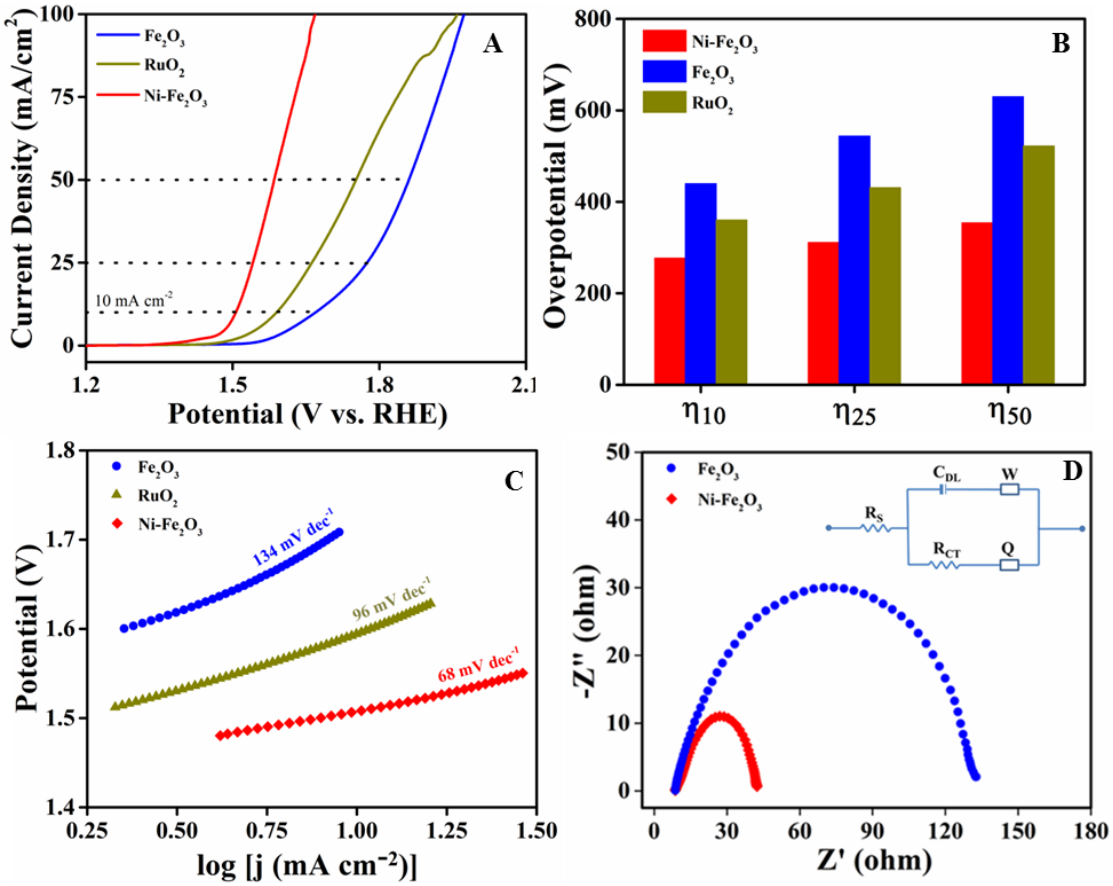

Figure 4.9: Electrochemical activity of Ni-Fe_2O_3 as compared to pristine Fe_2O_3 nanoclews and RuO_2. (A) LSV polarization curves at a scan rate 5 mV s^{-1} and (B) corresponding overpotential required for j = 10 (η_{10}), 25 (η_{25}) and 50 (η_{50}) mA cm^{-2} for Ni-Fe_2O_3, pristine Fe_2O_3 and RuO_2 respectively. (C) Tafel plots of Ni-Fe_2O_3, Fe_2O_3 and RuO_2 respectively. (D) Nyquist plots of OER on Ni-Fe_2O_3 and Fe_2O_3 (AC impedance data were acquired at the potential of 10 mA cm^{-2}).

Table 4.1: Overpotential and Tafel slope for Ni-Fe_2O_3, Fe_2O_3 and RuO_2.

Catalysts	Overpotential (mV)			Tafel slope (mV dec^{-1})
	η_{10}	η_{25}	η_{50}	
RuO_2	360	431	522	96
Fe_2O_3	440	544	630	134
Ni-Fe_2O_3	277	311	354	68

To gain insight into the charge transfer behavior between the catalyst and electrolyte, electrochemical impedance spectroscopy (EIS) was done, since charge transfer is an important feature to evaluate the catalytic property. The EIS were taken at a potential of 10 mA cm^{-2} (η_{10}) for all the catalyst. The Nyquist plot for Fe_2O_3 and Ni-Fe_2O_3 is shown in Figure 4.9.D. Charge transfer resistance (R_{ct}) was evaluated by fitting the acquired impedance data to an equivalent circuit (inset of Figure 4.9.D). In the equivalent circuit, C_{DL} is the double layer capacitance, whereas R_s and R_{ct} are solution resistance and charge transfer resistance respectively. W and Q are Warburg impedance and constant phase element respectively. From the Nyquist plots, it was observed that Ni-Fe_2O_3 has lowest R_{ct} value compared to Fe_2O_3, as doped nanoclews bear the smallest semicircle. Fitting parameters acquired from the EIS data for all the electrocatalysts are illustrated in Table 4.2. The lower R_{ct} of Ni-Fe_2O_3 (26.5 Ω) compared to pristine Fe_2O_3 (118 Ω) demonstrates that a high rate of electron transfer occurred for Ni-Fe_2O_3, which directly relates to the OER process. The faster electron transfer is due to the synergistic effect from the multiple transition metals, resulting in higher electrocatalytic activity of Ni-Fe_2O_3 nanoclews.

Table 4.2: Fitting parameters acquired from the EIS data for both the electrocatalysts during OER.

Electrocatalysts	R_s (Ω cm^2)	R_{ct} (Ω cm^2)	C_{DL} (mF cm^2)	Warburg Impedance (W)	Constant Phase Element (Q)
Fe_2O_3	7.8	118	0.11	0.0008	0.1456
Ni-Fe_2O_3	13.4	26.5	1.7	0.0109	4.0×10^6

4.3.2.2 Electrochemically Active Surface Area (ECSA)

The electrochemically active surface area (ECSA), a pivotal factor in electrochemistry, is related to the activity of a catalyst. ECSA has been calculated for all the catalysts (Figure 4.10) on the basis of scan-rate dependent cyclic voltammetric experiments using Randles-Sevcik equation.[45] The equation is : $i_p = 2.69 \times 10^5 \, n^{3/2} A \, c \, D^{1/2} v^{1/2}$. where, i_p represents

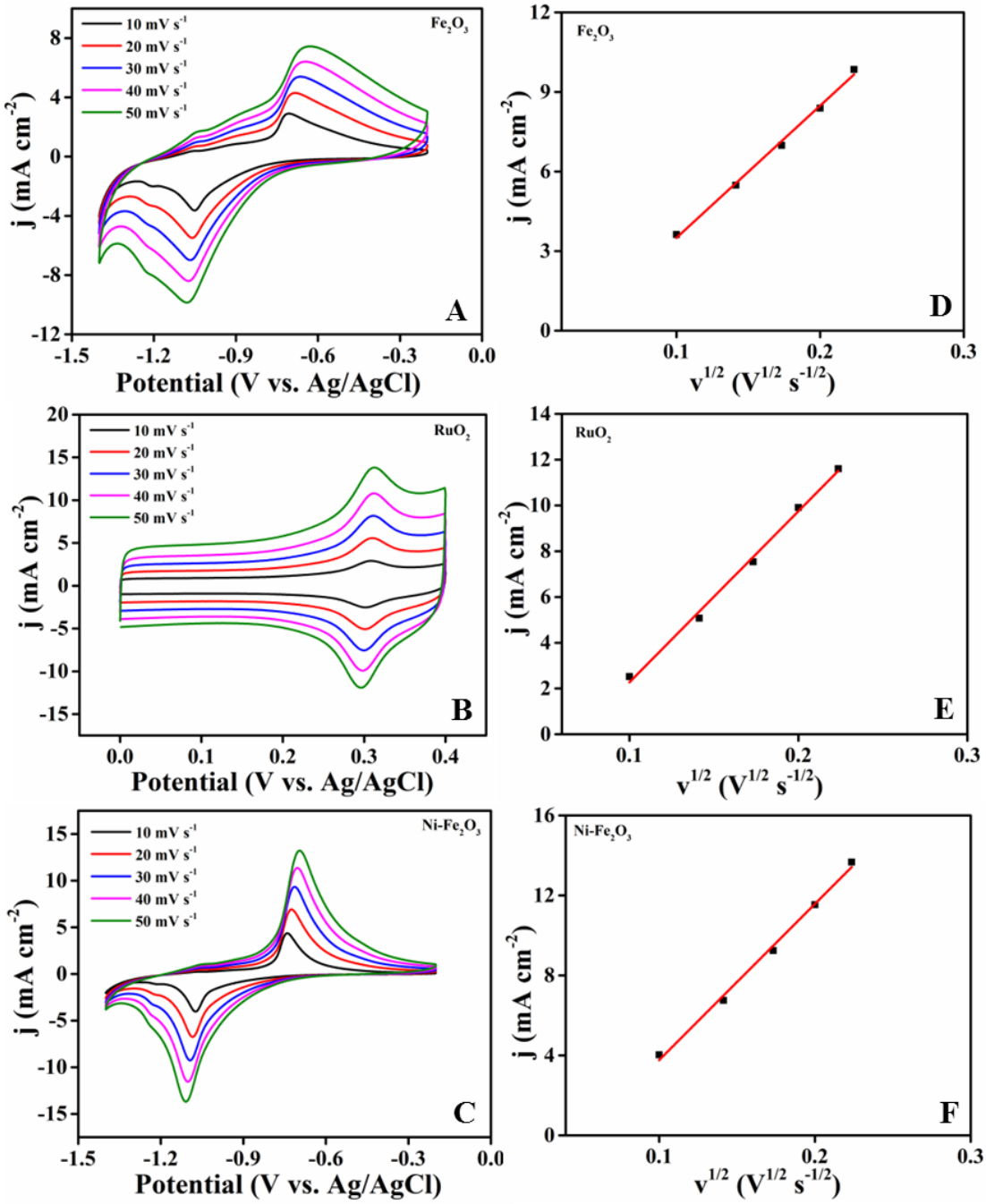

Figure 4.10: Cyclic voltammograms (CVs) of (A) Fe_2O_3, (B) RuO_2 and (C) Ni-Fe_2O_3 at different scan rate. The linear plots of peak current vs. the square root of the scan rate for the estimation of ECSA of (D) Fe_2O_3, (E) RuO_2 and (F) Ni-Fe_2O_3.

the peak current, *n* is the number of transferred electrons (n = 1), *A* indicates ECSA, *c* is the concentration of the electrolyte, *D* is the diffusion coefficient of O_2 in 1.0 M KOH

and it is 1.8×10^{-5} cm^2s^{-1},[46] and v is the potential sweep rate. The ECSA (A) could be determined from the slope of the i_p vs $v^{1/2}$ plot. We have considered the reduction peak for the quantitative determination of ECSA. The ECSA were found to be 0.044, 0.065 and 0.069 cm^2 for Fe_2O_3, RuO_2 and Ni-Fe_2O_3 respectively.

4.3.2.3 Stability Test of Ni-Fe_2O_3 Nanoclews

The stability of the catalysts was further studied at an overpotential of η_{10} for 10 h, since it is another essential criterion in developing a promising OER catalyst. Almost similar current density was noticed even after 10 h (Figure 4.11.A), signifying the outstanding stability and durability of Ni-Fe_2O_3 nanoclews under cycling conditions. The LSV curve of Ni-Fe_2O_3 after continuous OER for 10 h at 10 mA cm^{-2} (Figure 4.11.B) exhibits to the similar onset potential acquired with the fresh as-deposited catalyst.

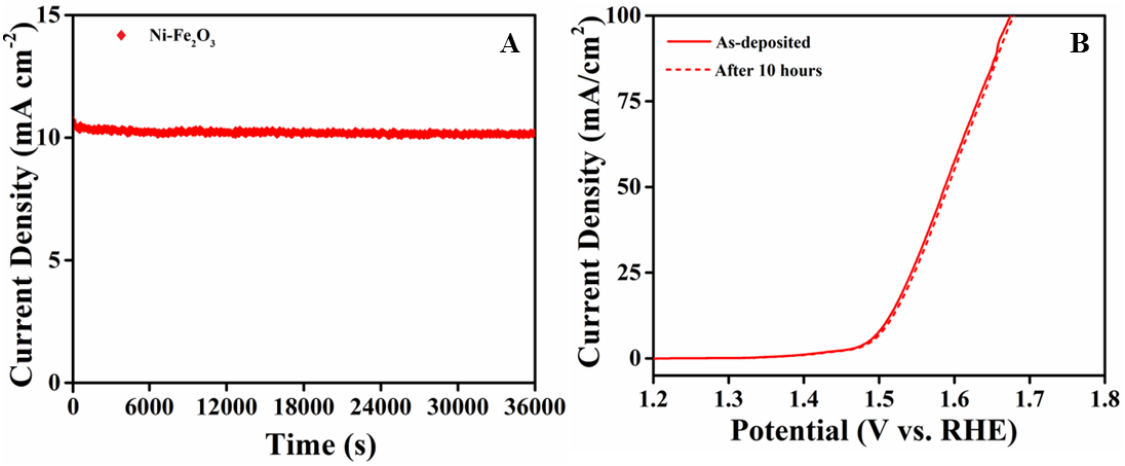

Figure 4.11: (A) i-t curve of Ni-Fe_2O_3 nanoclews at η_{10} potential for 10 h. (B) LSV plots of Ni-Fe_2O_3 nanoclews before and after prolonged OER analysis for 10 h at 10 mA cm^{-2}.

4.3.2.4 Post OER Study

Apart from the electrochemical stability of Ni-Fe_2O_3, FESEM and TEM analyses were also performed after OER study, which demonstrate that there is no alteration in their morphology even under the applied anodic potentials for prolonged time (Figure 4.12). Similarly, we have performed XPS analysis on Ni-Fe_2O_3 after OER process to

demonstrate the chemical change if any, shown in Figure 4.13. XPS spectra of Ni-Fe_2O_3 nanoclews after chronoamperometry indicate the presence of Ni^{2+} along with new peaks for Ni^{3+}, as shown in Figure 4.13.A, ascribing the formation of NiOOH after OER study.[47,48] However, the high resolution XPS spectrum of Fe 2p attributes to the characteristic peaks for Fe^{3+} similar to our earlier observation before electrocatalytic performance, without any alteration of the binding energy (Figure 4.13.B). The deconvolution of O 1s spectrum clearly authenticates different oxygen environments as observed earlier. However, an increase in the intensity of O2 and O4 peaks was seen (Figure 4.13.C) due to surface-adsorbed oxygen or hydroxyl groups and adsorption of molecular water respectively during the prolonged chronoamperometric analysis.[49]

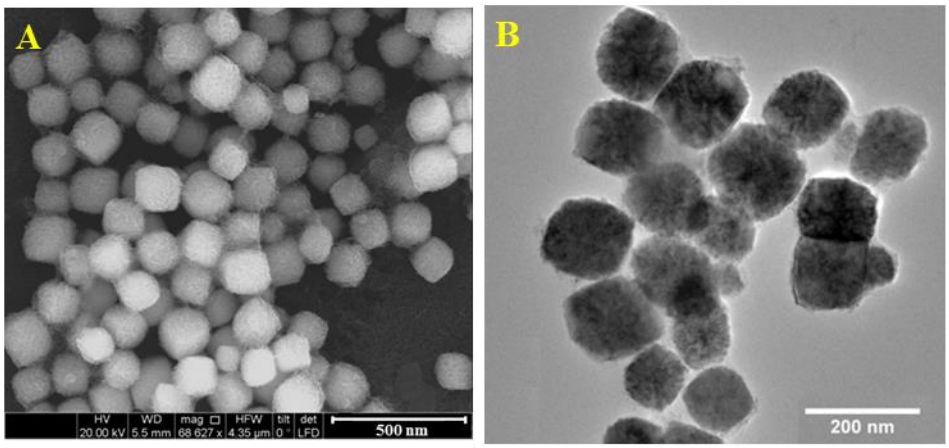

Figure 4.12: (A) FESEM and (B) TEM images of Ni-Fe_2O_3 nanoclews after OER study, representing no alteration of morphology even after prolonged usage.

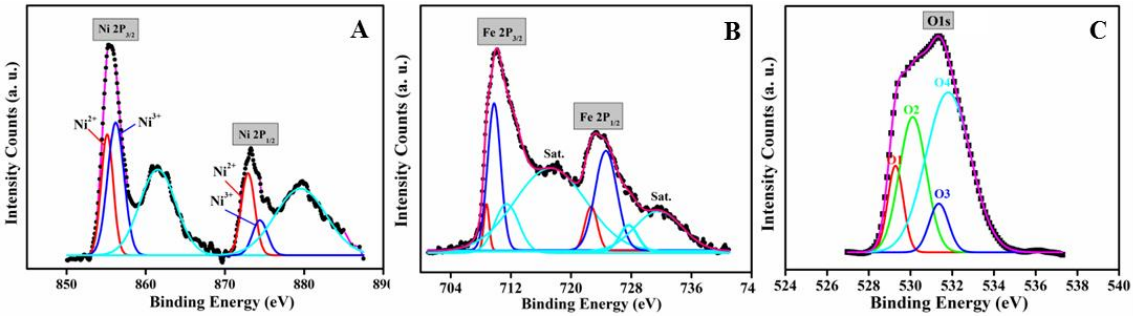

Figure 4.13: XPS spectra of (A) Ni 2p, (B) Fe 2p and (C) O 1s region of Ni-Fe_2O_3 nanoclews after prolonged OER study.

4.3.2.5 Comparison of Electrocatalytic Activity of Ni-Fe_2O_3 Nanoclews

Owing to Ni doping, Ni-Fe_2O_3 nanoclews demonstrate superb electrocatalytic activity. The electrocatalytic activity was compared with previously reported non-noble metal based electrocatalysts as shown in Table 4.3. Ni-Fe_2O_3 exhibits much better electrocatalytic activity compare to the other reported OER catalysts.

Table 4.3: OER activity of Ni-Fe_2O_3 nanoclews was demonstrated in associated with the reported non-noble metal based electrocatalysts.

Catalysts	**Electrolyte**	**Overpotential (mV) at 10 mA cm^{-2}**	**Tafel Slope (mV dec^{-1})**	**References**
CP@FeP	1.0 M KOH	350	64	50
Fe-mCo_3O_4/GC		380	60	51
Co_3O_4/$NiCo_2O_4$/GC		340	88	52
Co_3O_4/graphene		360	67	53
$Co(S_{0.71}Se_{0.29})_2$		283	86	54
CoMn-LDH/GC		324	43	55
CoO/NG/GC		341	71	56
Fe-Ni-Ox/GC		286	48	57
NiCo LDHs/GC		367	40	58
NiFeCr LDH		280	130	59
Co_3O_4/SWNT		580	104	60
Fe-Ni_3S_2/FeNi		282	54	61
CoMnP		330	61	62
$NiCo_2O_4$/CNTs		390	68.1	63
$CoCr_2O_4$/CNT		326	51	64
NiCo-LDH		335	41	65
Ni-Fe_2O_3		**277**	**68**	**Present Work**

4.3.2.6 OER Mechanism

In order to achieve OER electrocatalysts with excellent performances, it is imperative to have exposed active sites to the electrolytes. Owing to the unique clew-like morphology, it provides more exposed catalytic active sites. During OER process, an oxidative transformation occurred on to the surface of the nanoclews, resulting in the formation of in situ-generated oxidized species that may be responsible for the high electrochemical performance. Upon Ni-doping in pristine Fe_2O_3, it improves the activity by enhancing conductivity as well as playing a complementary role during OER. From the microstructural analysis, it was evident that Ni ions are being intercalated into the nanoclews that could effectively transfer electrons at the electrode-electrolyte interface, leading to a superior OER activity. Again, Ni sites with oxygen vacancies are believed to be the most effective in reducing the overpotential during OER process.[34,66] Oxygen vacancies can upsurge the conductivity of the catalyst by delocalizing electrons around the vacancies, leading to an easy electron transfer during OER. Additionally, Ni sites with oxygen vacancies are expected to be more accessible to the OH^- ions, which in turn assist the oxygen evolution. It is important to note that the defect sites having low oxygen coordination are directly associated to the catalyst activity.[67] From the XPS analysis, it was evident that the nanoclews possess defect sites with low oxygen coordination. These evolved oxygen defects on the catalyst surfaces function as charge traps and further assist as an adsorption site, which helps to transfer the charge to the adsorbed species, which in turn helps to enhance the catalytic activity. Thus, the electrochemical analyses of Ni-Fe_2O_3 nanoclews pointed to the formation of an excellent electrocatalyst with high OER activity as well as sustainability under basic medium than that of Fe_2O_3 or even the state-of-the-art RuO_2 catalyst.

4.4 Conclusions

In summary, we demonstrated the facile synthesis of Ni-Fe_2O_3 nanoclews based on a light-aided solution chemistry approach through Ni doping in Fe_2O_3. The exceptional

OER activity with structural and morphological stability of Ni-Fe_2O_3 has been achieved by virtue of their clew-like morphology, comprising of tiny nanorods with uniform distribution of constituent elements. Because of such unique morphology, it provides more exposed active sites and the atomic scale synergistic effect arising from Ni and Fe contributes to a superior intrinsic catalytic activity of Ni-Fe_2O_3 nanoclews. Moreover, Ni sites with oxygen vacancies significantly increase the number of surface active sites followed by reactivity, attributing to the excellent catalytic activity of Ni-Fe_2O_3, leaving behind most of the reported iron oxide based or even state-of-the-art RuO_2 electrocatalysts. The present findings not only provide a general approach to make proficient electrocatalysts using earth-abundant elements but also point to the potential aspects of doping in metal oxides, which in turn tune their energy conversion efficiency.

4.5 References

(1) Suen, N. T.; Hung, S. F.; Quan, Q.; Zhang, N.; Xu, Y. J.; Chen, H. M. Electrocatalysis for the Oxygen Evolution Reaction: Recent Development and Future Perspectives. *Chem. Soc. Rev.* **2017**, *46*, 337-365.

(2) Zhuang, L.; Ge, L.; Yang, Y. S.; Li, M. R.; Jia, Y.; Yao, X. D.; Zhu, Z. H. Ultrathin Iron-Cobalt Oxide Nanosheets with Abundant Oxygen Vacancies for the Oxygen Evolution Reaction. *Adv. Mater.* **2017**, *29*, 1606793-1606799.

(3) Koper, M. Thermodynamic Theory of Multi-Electron Transfer Reactions: Implications for Electrocatalysis. *J. Electroanal. Chem.* **2011**, *660*, 254-260.

(4) Han, L.; Dong, S. J.; Wang, E. Transition-Metal (Co, Ni, and Fe)-Based Electrocatalysts for the Water Oxidation Reaction. *Adv. Mater.* **2016**, *28*, 9266-9291.

(5) Ko¨tz, R.; Neff, H.; Stucki, S. Anodic Iridium Oxide Films XPS-Studies of Oxidation State Changes and. *J. Electrochem. Soc.* **1984**, *131*, 72-77.

(6) Ko¨tz, R.; Lewerenz, H. J.; Stucki, S. XPS Studies of Oxygen Evolution on Ru and RuO_2 Anodes. *J. Electrochem. Soc.* **1983**, *130*, 825-829.

(7) Suntivich, J.; May, K. J.; Gasteiger, H. A.; Goodenough, J. B.; Shao-Horn, Y. A Perovskite Oxide Optimized for Oxygen Evolution Catalysis from Molecular Orbital Principles. *Science* **2011**, *334*, 1383-1385.

(8) Wang, Y.; Liu, D.; Liu, Z.; Xie, C.; Huo, J.; Wang, S. Porous Cobalt–Iron Nitride Nanowires as Excellent Bifunctional Electrocatalysts for Overall Water Splitting. *Chem. Commun.* **2016**, *52*, 12614-12617.

(9) Wu, L. K.; Wu, W. Y.; Xia, J.; Cao, H. Z.; Hou, G. Y.; Tang, Y. P.; Zheng, G. Q. A Nanostructured Nickel–Cobalt Alloy with an Oxide Layer for an Efficient Oxygen Evolution Reaction. *J. Mater. Chem. A* **2017**, *5*, 10669-10677.
(10) Vojvodic, A.; Nørskov, J. K. Optimizing Perovskites for the Water-Splitting Reaction. *Science* **2011**, *334*, 1355-1356.
(11) Li, M.; Xiong, Y.; Liu, X.; Bo, X.; Zhang, Y.; Han, C.; Guo, L. Facile Synthesis of Electrospun MFe_2O_4 (M = Co, Ni, Cu, Mn) Spinel Nanofibers with Excellent Electrocatalytic Properties for Oxygen Evolution and Hydrogen Peroxide Reduction. *Nanoscale* **2015**, *7*, 8920-8930.
(12) Z Lu,.; Wang, H.; Kong, D.; Yan, K.; Hsu, P.-C.; Zheng, G.; Yao, H.; Liang, Z.; Sun, X.; Cui, Y. Electrochemical Tuning of Layered Lithium Transition Metal Oxides for Improvement of Oxygen Evolution Reaction. *Nat. Commun.* **2014**, *5*, 4345-4351.
(13) Kanan, M. W.; Surendranath, Y.; Nocera, D. G. Cobalt–Phosphate Oxygen-Evolving Compound. *Chem. Soc. Rev.* **2009**, *38*, 109-114.
(14) Wasalathanthri, R. N.; Jeffrey, S.; Awni, R. A.; Sun, K.; Giolando, D. M. Electrodeposited Copper−Cobalt−Phosphide: A Stable Bifunctional Catalyst for Both Hydrogen and Oxygen Evolution Reactions. *ACS Sustainable Chem. Eng.* **2019**, *7*, 3092–3100.
(15) X Xiao, X. F.; He, C.-T.; Zhao, S. L.; Li, J.; Lin, W. S.; Yuan, Z. K.; Zhang, Q.; Wang, S. Y.; Dai, L. M.; Yu, D. S. A General Approach to Cobalt-Based Homobimetallic Phosphide Ultrathin Nanosheets for Highly Efficient Oxygen Evolution in Alkaline Media. *Energy Environ. Sci.* **2017**, *10*, 893-899.
(16) Qiao, C.; Zhang, Y.; Zhu, Y.; Cao, C.; Bao, X.; Xu, J. One-Step Synthesis of Zinc–Cobalt Layered Double Hydroxide (Zn–Co-LDH) Nanosheets for High-Efficiency Oxygen Evolution Reaction. *J. Mater. Chem. A* **2015**, *3*, 6878-6883.
(17) Song, F.; Hu, X. Exfoliation of Layered Double Hydroxides for Enhanced Oxygen Evolution Catalysis. *Nat. Commun.* **2014**, *5*, 4477-4485.
(18) Liang, H.; Meng, F.; Cabán-Acevedo, M.; Li, L.; Forticaux, A.; Xiu, L.; Wang, Z.; Jin, S. Hydrothermal Continuous Flow Synthesis and Exfoliation of Nico Layered Double Hydroxide Nanosheets for Enhanced Oxygen Evolution Catalysis. *Nano Lett.* **2015**, *15*, 1421-1427.
(19) Zhang, G.; Liu, H.; Qu, J.; Li, J. Two-Dimensional Layered MoS_2: Rational Design, Properties and Electrochemical Applications. *Energy Environ. Sci.* **2016**, *9*, 1190-1209.
(20) Shi, J.; Wang, X.; Zhang, S.; Xiao, L.; Huan, Y.; Gong, Y.; Zhang, Z.; Li, Y.; Zhou, X.; Hong, M.; Fang, Q. Two-Dimensional Metallic Tantalum Disulfide as a Hydrogen Evolution Catalyst. *Nat. Commun.* **2017**, *8*, 958-966.

(21) Chen, W.; Liu, Y.; Li, Y.; Sun, J.; Qiu, Y.; Liu, C.; Zhou, G.; Cui, Y. In Situ Electrochemically Derived Nanoporous Oxides from Transition Metal Dichalcogenides for Active Oxygen Evolution Catalysts. *Nano Lett.* **2016**, *16*, 7588-7596.
(22) Chen, S.; Duan, J.; Jaroniec, M.; Qiao, S. Z. Three-Dimensional N-Doped Graphene Hydrogel/Nico Double Hydroxide Electrocatalysts for Highly Efficient Oxygen Evolution. *Angew. Chem. Int. Ed.* **2013**, *52*, 13567-13570.
(23) Li, R.; Wei, Z.; Gou, X. Nitrogen and Phosphorus Dual-Doped Graphene/Carbon Nanosheets as Bifunctional Electrocatalysts for Oxygen Reduction and Evolution. *ACS Catal.* **2015**, *5*, 4133-4142.
(24) Chai, G. L.; Qiu, K.; Qiao, M.; Titirici, M. M.; Shang, C.; Guo, Z. Active Sites Engineering Leads to Exceptional ORR and OER Bifunctionality in P, N Co-Doped Graphene Frameworks. *Energy Environ. Sci.* **2017**, *10*, 1186-1195.
(25) Zhou, S.; Liu, N.; Wang, Z.; Zhao, J. Nitrogen-Doped Graphene on Transition Metal Substrates as Efficient Bifunctional Catalysts for Oxygen Reduction and Oxygen Evolution Reactions. *ACS Appl. Mater. Interfaces* **2017**, *9*, 22578-22587.
(26) Jana, S.; Rioux, R. M. Seeded Growth Induced Amorphous to Crystalline Transformation of Niobium Oxide Nanostructures. *Nanoscale* **2012**, *4*, 1782-1788.
(27) Grimaud, A.; Carlton, C. E.; Risch, M.; Hong, W. T.; May, K. J.; Shao-Horn, Y. Oxygen Evolution Activity and Stability of $Ba_6Mn_5O_{16}$, $Sr_4Mn_2CoO_9$, and $Sr_6Co_5O_{15}$: The Influence of Transition Metal Coordination. *J. Phys. Chem. C* **2013**, *117*, 25926–25932.
(28) Das, S.; Samanta, A.; Jana, S. Light-Assisted Synthesis of Hierarchical Flower-Like MnO_2 Nanocomposites with Solar Light Induced Enhanced Photocatalytic Activity. *ACS Sustainable Chem. Eng.* **2017**, *5*, 9086-9094.
(29) Wang, G.; Ling, Y.; Wheeler, D. A.; George, K. E.; Horsley, K.; Heske, C.; Zhang, J. Z.; Li, Y. Facile Synthesis of Highly Photoactive α-Fe_2O_3-Based Films for Water Oxidation. *Nano Lett.* **2011**, *11*, 3503-3509.
(30) Fan, H. M.; You, G. J.; Li, Y.; Zheng, Z.; Tan, H. R.; Shen, Z. X.; Tang, S. H.; Feng, Y. P. Shape-Controlled Synthesis of Single-Crystalline Fe_2O_3 Hollow Nanocrystals and Their Tunable Optical Properties. *J. Phys. Chem. C* **2009**, *113*, 9928-9935.
(31) Das, S.; Jana, S. A Tubular Nanoreactor Directing the Formation of In Situ Iron Oxide Nanorods with Superior Photocatalytic Activity. *Environ. Sci.: Nano* **2017**, *4*, 596-603.
(32) Burke, M. S.; Enman, L. J.; Batchellor, A. S.; Zou, S.; Boettcher, S. W. Oxygen Evolution Reaction Electrocatalysis on Transition Metal Oxides and (Oxy) hydroxides: Activity Trends and Design Principles. *Chem. Mater.* **2015**, *27*, 7549-7558.

(33) Zhang, Y.; Jia, G.; Wang, H.; Ouyang, B.; Rawat, R. S.; Fan, H. J. Ultrathin CNTs@ FeOOH Nanoflake Core/Shell Networks as Efficient Electrocatalysts for the Oxygen Evolution Reaction. *Mater. Chem. Front.* **2017**, *1*, 709-715.
(34) Teng, Y.; Wang, X. D.; Liao, J. F.; Li, W. G.; Chen, H. Y.; Dong, Y. J.; Kuang, D. B. Atomically Thin Defect-Rich Fe–Mn–O Hybrid Nanosheets as High Efficient Electrocatalyst for Water Oxidation. *Adv. Funct. Mater.* **2018**, *28*, 1802463-1802470.
(35) Sun, H.; Chen, G.; Sunarso, J.; Dai, J.; Zhou, W.; Shao, Z.; Molybdenum and Niobium Codoped B-Site-Ordered Double Perovskite Catalyst for Efficient Oxygen Evolution Reaction. *ACS Appl. Mater. Interfaces* **2018**, *10*, 16939-16942.
(36) Fan, J.; Chen, Z.; Shi, H.; Zhao, G. In Situ Grown, Self-Supported Iron–Cobalt–Nickel Alloy Amorphous Oxide Nanosheets with Low Overpotential toward Water Oxidation. *Chem. Commun.* **2016**, *52*, 4290-4293.
(37) Zhao, Z.; Wu, H.; He, H.; Xu, X.; Jin, Y. A High-Performance Binary Ni–Co Hydroxide-based Water Oxidation Electrode with Three-Dimensional Coaxial Nanotube Array Structure. *Adv. Funct. Mater.* **2014**, *24*, 4698-4705.
(38) Song, L.; Zhang, S.; Chen, B.; Ge, J.; Jia, X. A Hydrothermal Method for Preparation of α-Fe_2O_3 Nanotubes and Their Catalytic Performance for Thermal Decomposition of Ammonium Perchlorate. *Colloids Surf. A Physicochem. Eng. Asp.* **2010**, *360*, 1-5.
(39) Lassoued, A.; Lassoued, M. S.; Dkhil, B.; Gadri, A.; Ammar, S. Structural, Optical and Morphological Characterization of Cu-Doped α-Fe_2O_3 Nanoparticles Synthesized through Co-Precipitation Technique. *J. Mol. Struct.* **2017**, *1148*, 276-281.
(40) Cheng, H.; Su, Y. Z.; Kuang, P. Y.; Chen, G. F.; Liu, Z. Q.; Hierarchical $NiCo_2O_4$ Nanosheet-Decorated Carbon Nanotubes towards Highly Efficient Electrocatalyst for Water Oxidation. *J. Mater. Chem. A* **2015**, *3*, 19314-19321.
(41) Yuan, C.; Li, J.; Hou, L.; Zhang, X.; Shen, L.; Lou, X. W. Ultrathin Mesoporous $NiCo_2O_4$ Nanosheets Supported on Ni Foam as Advanced Electrodes for Supercapacitors. *Adv. Funct. Mater.* **2012**, *22*, 4592-4597.
(42) Kim, J. Y.; Youn, D. H.; Kang, K.; Lee, J. S. Highly Conformal Deposition of an Ultrathin FeOOH Layer on a Hematite Nanostructure for Efficient Solar Water Splitting. *Angew. Chem., Int. Ed.* **2016**, *55*, 10854-10858.
(43) Gong, M.; Li, Y.; Wang, H.; Liang, Y.; Wu, J. Z.; Zhou, J.; Wang, J.; Regier, T.; Wei, F.; Dai, H. An Advanced Ni–Fe Layered Double Hydroxide Electrocatalyst for Water Oxidation. *J. Am. Chem. Soc.* **2013**, *135*, 8452-8455.
(44) Xuan, C.; Wang, J.; Xia, W.; Zhu, J.; Peng, Z.; Xia, K.; Xiao, W.; Xin, H. L.; Wang, D. Heteroatom (P, B, or S) Incorporated NiFe-Based Nanocubes as Efficient Electrocatalysts for the Oxygen Evolution Reaction. *J. Mater. Chem. A* **2018**, *6*, 7062-7069.

(45) Dutta, A.; Morstein, C. E.; Rahaman, M.; López, A. C.; Broekmann, P. Beyond Copper in CO_2 Electrolysis: Effective Hydrocarbon Production on Silver-Nanofoam Catalysts. *ACS Catal*. **2018**, *8*, 8357−8368.

(46) Qiao, J.; Xu, L.; Ding, L.; Shi, P.; Zhang, L.; Baker, R.; Zhang, J. Effect of KOH Concentration on the Oxygen Reduction Kinetics Catalyzed by Heat-Treated Co-pyridine/C Electrocatalysts. *Int. J. Electrochem. Sci.* **2013**, *8*, 1189-1208.

(47) Konkena, B.; Masa, J.; Botz, A. J.; Sinev, I.; Xia, W.; Koßmann, J.; Drautz, R.; Muhler, M.; Schuhmann, W. Metallic NiPS3@ NiOOH Core–Shell Heterostructures as Highly Efficient and Stable Electrocatalyst for the Oxygen Evolution Reaction. *ACS Catal.* **2017**, *7*, 229-237.

(48) Song, B.; Li, K.; Yin, Y.; Wu, T.; Dang, L.; Cabán-Acevedo, M.; Han, J.; Gao, T.; Wang, X.; Zhang, Z.; Schmidt, J. R.; Ping, X.; Jin, S. Tuning Mixed Nickel Iron Phosphosulfide Nanosheet Electrocatalysts for Enhanced Hydrogen and Oxygen Evolution. *ACS Catal.*, **2017**, *7*, 8549-8557.

(49) Ye, Y. J.; Zhang, N.; Liu, X. X. Amorphous NiFe (oxy) Hydroxide Nanosheet Integrated Partially Exfoliated Graphite Foil for High Efficiency Oxygen Evolution Reaction. *J. Mater. Chem. A* **2017**, *5*, 24208-24216.

(50) Xiong, D.; Wang, X.; Li, W.; Liu, L. Facile Synthesis of Iron Phosphide Nanorods for Efficient and Durable Electrochemical Oxygen Evolution. *Chem. Commun.* **2016**, *52*, 8711-8714.

(51) Xiao, C. L.; Lu, X. Y. Zhao, C. Unusual Synergistic Effects upon Incorporation of Fe and/or Ni into Mesoporous Co_3O_4 for Enhanced Oxygen Evolution. *Chem. Commun.* **2014**, *50*, 10122-10125.

(52) Hu, H.; Guan, B. Y.; Xia, B. Y.; Lou, X. W. Designed Formation of Co_3O_4/$NiCo_2O_4$ Double-Shelled Nanocages with Enhanced Pseudocapacitive and Electrocatalytic Properties. *J. Am. Chem. Soc.* **2015**, *137*, 5590-5595.

(53) Liang, Y. Y.; Li, Y. G.; Wang, H. L.; Zhou, J. G.; Wang, J.; Regier, T.; Dai, H. J. Co_3O_4 Nanocrystals on Graphene as a Synergistic Catalyst for Oxygen Reduction Reaction. *Nat. Mater.* **2011**, *10*, 780-786.

(54) Fang, L.; Li, W.; Guan, Y.; Feng, Y.; Zhang, H.; Wang, S.; Wang, Y. Tuning Unique Peapod-Like $Co(S_xSe_{1-x})_2$ Nanoparticles for Efficient Overall Water Splitting. *Adv. Funct. Mater.* **2017**, *27*, 1701008-1701016.

(55) Song, F.; Hu, X. L. Ultrathin Cobalt-Manganese Layered Double Hydroxide is an Efficient Oxygen Evolution Catalyst. *J. Am. Chem. Soc.* **2014**, *136*, 16481-16484.

(56) Mao, S.; Wen, Z. H.; Huang, T. Z.; Yang, H.; Chen, J. H. High-performance Bi-Functional Electrocatalysts of 3D Crumpled Graphene-Cobalt Oxide Nanohybrids for Oxygen Reduction and Evolution Reactions. *Energy Environ. Sci.* **2014**, *7*, 609-616.

(57) Kuai, L.; Geng, J.; Chen, C. Y.; Kan, E. J.; Liu, Y. D.; Wang, Q.; Geng, B. Y. A Reliable Aerosol-Spray-Assisted Approach to Produce and Optimize Amorphous Metal Oxide Catalysts for Electrochemical Water Splitting. *Angew. Chem. Int. Ed.* **2014**, *53*, 7547-7551.
(58) Liang, H. F.; Meng, F.; Caban-Acevedo, M.; Li, L. S.; Forticaux, A.; Xiu, L. C.; Wang, Z. C.; Jin, S. Hydrothermal Continuous Flow Synthesis and Exfoliation of NiCo Layered Double Hydroxide Nanosheets for Enhanced Oxygen Evolution Catalysis. *Nano Lett.* **2015**, *15*, 1421-1427.
(59) Yang, Y.; Dang, L.; Shearer, M. J.; Sheng, H.; Li, W.; Chen, J.; Xiao, P.; Zhang, Y.; Hamers, R. J.; Jin, S. Highly Active Trimetallic NiFeCr Layered Double Hydroxide Electrocatalysts for Oxygen Evolution Reaction. *Adv. Energy Mater.* **2018**, *8*, 1703189-1703197.
(60) Wu, J.; Yan, Y.; Yan, X.; Yan, W. S.; Cheng, Q. M.; Xie, Y. Co_3O_4 Nanocrystals on Single-Walled Carbon Nanotubes as a Highly Efficient Oxygen-Evolving Catalyst. *Nano Res.* **2012**, *5*, 521-530.
(61) Yuan, C. Z.; Sun, Z. T.; Jiang, Y. F.; Yang, Z. K.; Jiang, N.; Zhao, Z. W.; Qazi, U. Y.; Zhang, W. H.; Xu, A. W. One-Step In Situ Growth of Iron–Nickel Sulfide Nanosheets on FeNi Alloy Foils: High-Performance and Self-Supported Electrodes for Water Oxidation. *Small* **2017**, *13*, 1604161-1604168.
(62) Li, D.; Baydoun, H.; Verani, C. N.; Brock, S. L. Efficient Water Oxidation Using CoMnP Nanoparticles. *J. Am. Chem. Soc.* **2016**, *138*, 4006-4009.
(63) Cheng, H.; Su, Y. Z.; Kuang, P. Y.; Chen, G. F.; Liu, Z. Q. Hierarchical $NiCo_2O_4$ Nanosheet-Decorated Carbon Nanotubes towards Highly Efficient Electrocatalyst for Water Oxidation. *J. Mater. Chem. A* **2015**, *3*, 19314-19321.
(64) Al-Mamun, M.; Su, X.; Zhang, H.; Yin, H.; Liu, P.; Yang, H.; Wang, D.; Tang, Z.; Wang, Y.; Zhao, H. Strongly Coupled $CoCr_2O_4$/Carbon Nanosheets as High Performance Electrocatalysts for Oxygen Evolution Reaction. *Small* **2016**, *12*, 2866-2871.
(65) Song, F.; Hu, X. Exfoliation of Layered Double Hydroxides for Enhanced Oxygen Evolution Catalysis. *Nat. Commun.* **2014**, *5*, 4477-4485.
(66) Wang, J.; Gan, L.; Zhang, W.; Peng, Y.; Yu, H.; Yan, Q.; Xia, X.; Wang, X. In Situ Formation of Molecular Ni-Fe Active Sites on Heteroatom-Doped Graphene as a Heterogeneous Electrocatalyst toward Oxygen Evolution. *Sci. Adv.* **2018**, *4*, No. eaap7970.
(67) Xiao, H.; Shin, H.; Goddard, W. A. Synergy between Fe and Ni in the Optimal Performance of (Ni,Fe)OOH Catalysts for the Oxygen Evolution Reaction. *Proc. Natl. Acad. Sci. U. S. A.* **2018**, *115*, 5872-5877.

****

Chapter 5

Solution-Processed Nanoscale Metal Doped Iron Oxide (M-Fe_2O_3; M = Mn, Co and Ni) Parallelepipeds for Enhanced Oxygen Evolution

5.1 Introduction

The growing energy demands and subsequent environmental pollution by means of human activity and industrial revolution has encouraged to the researchers in exploring the innovative renewable energy resources together with the fabrication of device for the energy conversion and storage. Consequently, during last few decades' global interest has been directed to the design of sustainable green energy system with high efficiency and stability as an alternative to the fossil fuels.[1-6] Development of less expensive electrocatalyst based on the earth abundant metals is really challenging task to the researchers for catalyzing the electrocatalysis by lowering the energy barrier.

Oxygen evolution reaction (OER) being a multiple electron transfer procedures involves a high activation energy barrier.[7,8] To accelerate the reaction, designing of electrocatalysts having outstanding OER performances is desirable but very much challenging. OER is a half-cell reaction in water electrocatalysis and it is kinetically sluggish reaction involving four electron transfer process.[9-11] Noble metal based electrocatalysts mainly IrO_2 and RuO_2 are considered as very efficient state of the art electrocatalysts for OER but their uses are limited due to their scarceness, high price, and comparatively low stability in alkali electrolytes due to oxidation to IrO_3 and RuO_4 respectively.[12,13] Ideally the desirable catalyst for OER must possesses high activity with low overpotential, good stability and durability along with less expenses and large earth abundance.

Among various electrocatalysts, transition metal-based materials are cost effective, largely available on earth and exhibit different oxidation states, which make them as the

most effective candidates for oxygen evolution reaction. They showed promising electrocatalytic activity in different forms, like oxides,[14-17] (oxy) hydroxide,[18] layered doble hydroxide,[19,20] phosphides,[21,22] dichalcogenides,[23,24] perovskites,[25] metal organic frameworks[26,27] etc. Iron based oxide materials received great attention due to their earth abundance, non-toxicity, superb stability[28,29] but their application in OER as electrocatalyst is limited because of their poor conductivity.[30,31] As the electronic structure and number of active sites play an important role on catalytic performances,[32-35] thus, improvement of their electronic structure and number of active sites are effective way to enhance their conductivity as well as chemico-physical properties for electrocatalysis. There are many approaches to boost the catalytic efficacy of a catalyst, by providing more active sites with large surface area, like incorporation of foreign element or doping,[36,37] defect engineering,[38] designing hybrid materials[39] etc**.** Among them doping is an effective process to boost electrocatalytic activity typically by incorporating another atom into the lattice of metal oxide.[40,41] After doping, dopant can tune the electronic structure of the catalyst by increasing charge carrier density as well as electrical conductivity and further enhance the active sites. There are several methods reported for doping, such as chemical vapor deposition,[42] electro-deposition,[43] spin coating,[44] spray pyrolysis[45] etc. Although researchers have extensively carried out doping by the aforesaid procedures, however to the best of our knowledge, doping of transition metals in metal oxides through low temperature light driven route has not been studied and thus may be an alternative pathway because of its simplicity and effectiveness.

In this chapter, a facile synthesis route was designed to prepare different transition metals doped iron oxide parallelepipeds via a light driven bottom-up chemistry approach deprived of any template molecule. For this purpose, we have successfully prepared iron oxide (Fe_2O_3), Ni doped iron oxide (Ni-Fe_2O_3), Co doped iron oxide (Co-Fe_2O_3) and Mn doped iron oxide (Mn-Fe_2O_3) nanostructures. After detailed characterization, we have explored them as electrocatalyst in basic medium for OER and compared their OER activity. Among all the as-prepared catalysts, Ni-Fe_2O_3 shows highest activity and stability during oxygen production.

5.2 Experimental Section

5.2.1 Synthesis of M-Doped Fe_2O_3 (M = Mn, Co and Ni) and Pristine Fe_2O_3 Nanostructures

Different transition metal doped M-Fe_2O_3 nanostructures have been prepared through a novel procedure based on a low temperature light driven hydrothermal process. First, 1.0 mmol of $FeCl_3$ and 0.1 mmol of $NiCl_2$ were dissolved in 7.5 mL of double distilled water in a beaker. Then, 2.5 mL of NaOH solution (3.0 w/v %) was added to the above solution and the entire solution mixture was sonicated for 30 minutes to make it uniform. Next, the whole solution mixture was transferred into a glass vial and the mouth of the vial was sealed tightly and placed under visible light for 24 hours. The temperature of the system was maintained at 90 °C for entire reaction time. After the completion of the reaction, the precipitated product was collected by centrifugation and washed properly with distilled water. After air-drying, the product was collected for further study and denoted as Ni-Fe_2O_3. Similarly, Co doped Fe_2O_3 (Co-Fe_2O_3) and Mn doped Fe_2O_3 (Mn-Fe_2O_3)

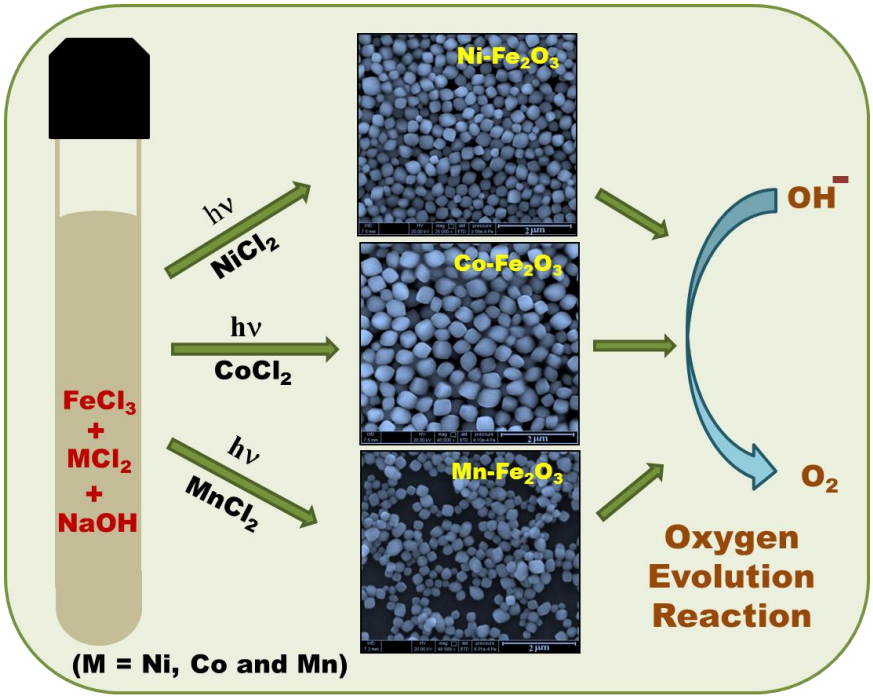

Scheme 5.1: Schematic presentation of the synthesis of nanoscale M-Fe_2O_3 (M = Mn, Co and Ni) parallelepipeds for oxygen production.

nanostructures were synthesized under identical reaction conditions taking $CoCl_2$ and $MnCl_2$ respectively as precursors in place of $NiCl_2$. For the synthesis of pristine Fe_2O_3 nanostructures, only $FeCl_3$ was used, keeping all the reaction conditions unaltered. All the synthesized products were then characterized by different techniques and used them as electrocatalyst for oxygen evolution reaction. Scheme 5.1 represents the synthesis of nanoscale M-Fe_2O_3 (M = Mn, Co and Ni) parallelepipeds for oxygen production.

5.2.2 Electrochemical Experiment

Electrocatalytic activity was investigated using an electrochemical analyzer (CHI 660E instrument) with a standard three electrodes system in 1.0 M KOH solution for OER at room temperature. For this purpose, we have taken glassy carbon electrode as working electrode, alkaline Hg/HgO (1.0 M KOH) as reference electrode and platinum wire as counter electrode. All potentials were converted with respect to the reversible hydrogen electrode (RHE) as following equation, $E\ (vs.\ RHE) = E\ (vs.\ Hg/HgO) + 0.098 + 0.059\ pH$ and overpotential (η) was calculated as $\eta = E\ (vs.\ RHE) - 1.23\ V$. The catalyst ink was prepared using the following process. First, 4.0 mg of Mn-Fe_2O_3 (30 wt% sample in carbon black) was dispersed in a mixture of 0.25 mL double distilled water and 0.25 mL of isopropanol. Then, 20 µL of Nafion solution (1%) was added to the above mixture as a binder and sonicated the solution mixture for 60 minutes to prepare a homogenous solution. Next, 15 µL of the catalyst ink (homogenous solution mixture) was loaded uniformly onto the glassy carbon electrode having diameter 3.0 mm and air dried for overnight. The final catalyst loading is about 54 mg cm^{-2} onto GC electrode. Similar procedures were maintained in making the working electrode for Fe_2O_3, Co-Fe_2O_3 and Ni-Fe_2O_3 as electrocatalysts. The polarization curves were measured at a scan rate of 5 mV s^{-1} in 1.0 M KOH solution. We evaluated the Tafel slopes from the LSV curves by plotting the overpotential against log (current density). Cyclic voltammetry (CV) analysis was performed at varied scan rates to calculate the electrochemically active surface area (ESCA). Chronoamperometry technique was used to check the electrochemical stability of the catalyst. AC impedance was recorded at the frequency range of 0.1 Hz to 100 kHz with an AC amplitude of 5 mV.

5.3 Results and Discussion

5.3.1 Characterization of Pristine Fe_2O_3 and M-Fe_2O_3 (M = Mn, Co and Ni) Nanostructures

5.3.1.1 FESEM and TEM Analyses of Pristine Fe_2O_3 Nanostructures

Field emission scanning electron microscopy (FESEM) and transmission electron microscopy (TEM) analyses were carried out to visualize the size and morphology of the synthesized nanomaterials. We observed the formation of hierarchical parallelepiped-like morphology of pristine Fe_2O_3, having size ~ 340 nm (Figure 5.1). TEM analysis also ascertained the parallelepiped-like morphology of Fe_2O_3 within the nano regime. A closer look to the morphology clearly authenticated that hierarchical parallelepipeds (PPs) were evolved due to assembly of several small nanorods of Fe_2O_3 (Figure 5.1.D).

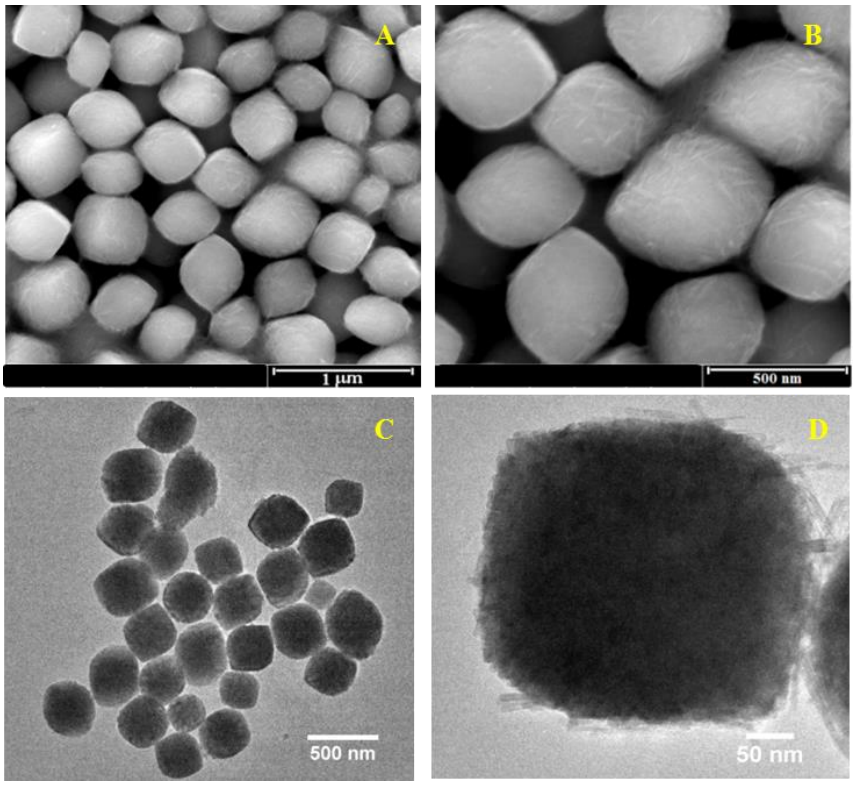

Figure 5.1: (A,B) FESEM and (C,D) TEM micrographs of Fe_2O_3 nanostructures, indicating the formation of hierarchical parallelepiped-like morphology. High magnification TEM micrograph (1D) again corroborated the hierarchical parallelepiped-like morphology of Fe_2O_3 due to assembly of several small nanorods of Fe_2O_3.

5.3.1.2 FESEM and TEM Analyses of Different M-Fe_2O_3 Nanostructures

Likewise, we noticed analogous hierarchical parallelepiped-like morphology for all the synthesized metal doped M-Fe_2O_3 without any alteration in their size or morphology. Figure 5.2 (A-B, D-E, G-H) demonstrated the FESEM images of different M-Fe_2O_3 nanostructures, having parallelepipeds-like morphology. The formation of nanoscale parallelepipeds was further observed from TEM analysis, as shown in Figure 5.2 (C, F, I).

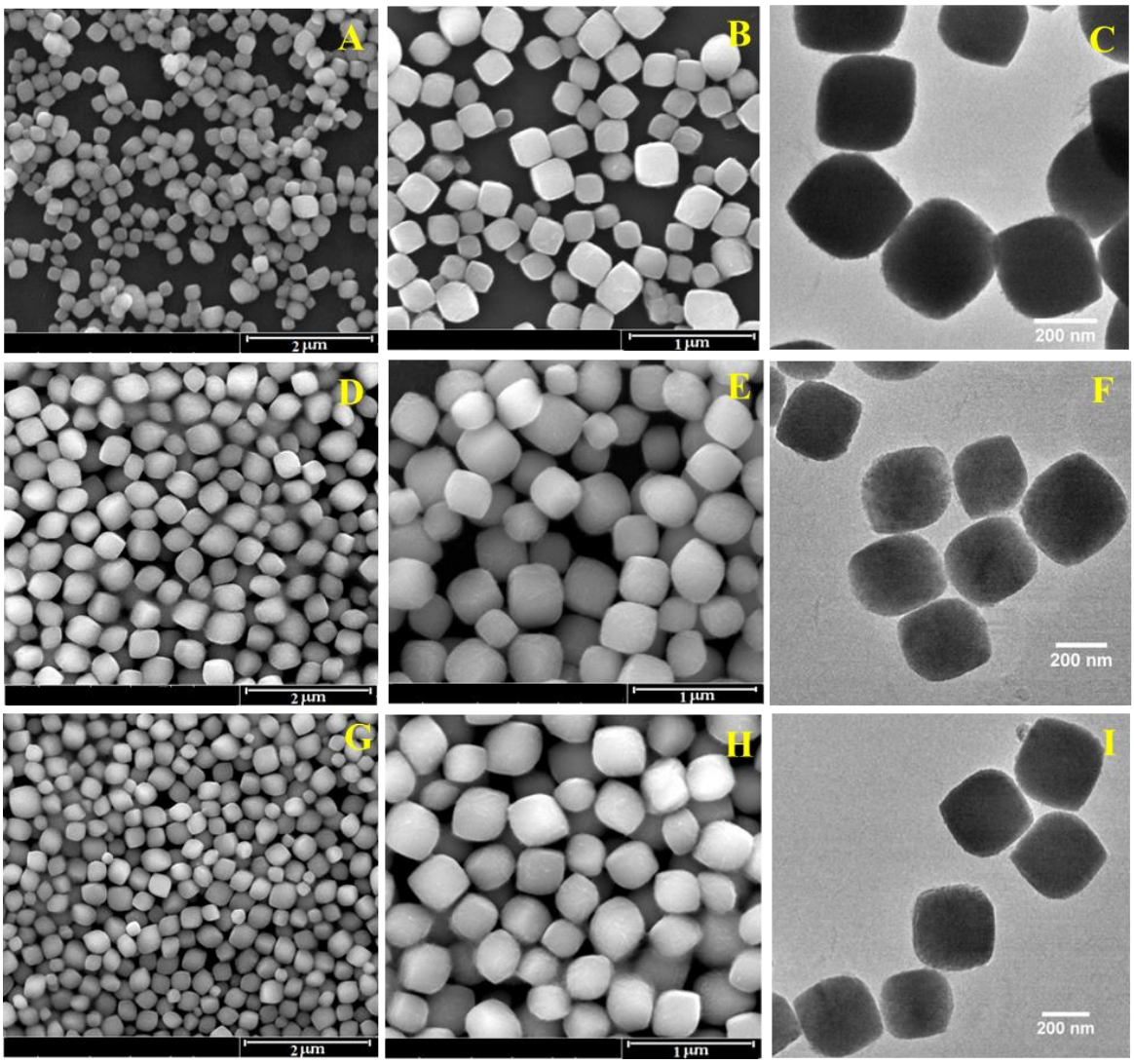

Figure 5.2: FESEM images of (A,B) Mn-Fe_2O_3, (D,E) Co-Fe_2O_3 and (G,H) Ni-Fe_2O_3 nanostructures and their respective TEM images shown in (C) Mn-Fe_2O_3, (F) Co-Fe_2O_3 and (I) Ni-Fe_2O_3, representing the formation of hierarchical parallelepiped-like morphology.

5.3.1.3 EDS and ICP-OES Analyses

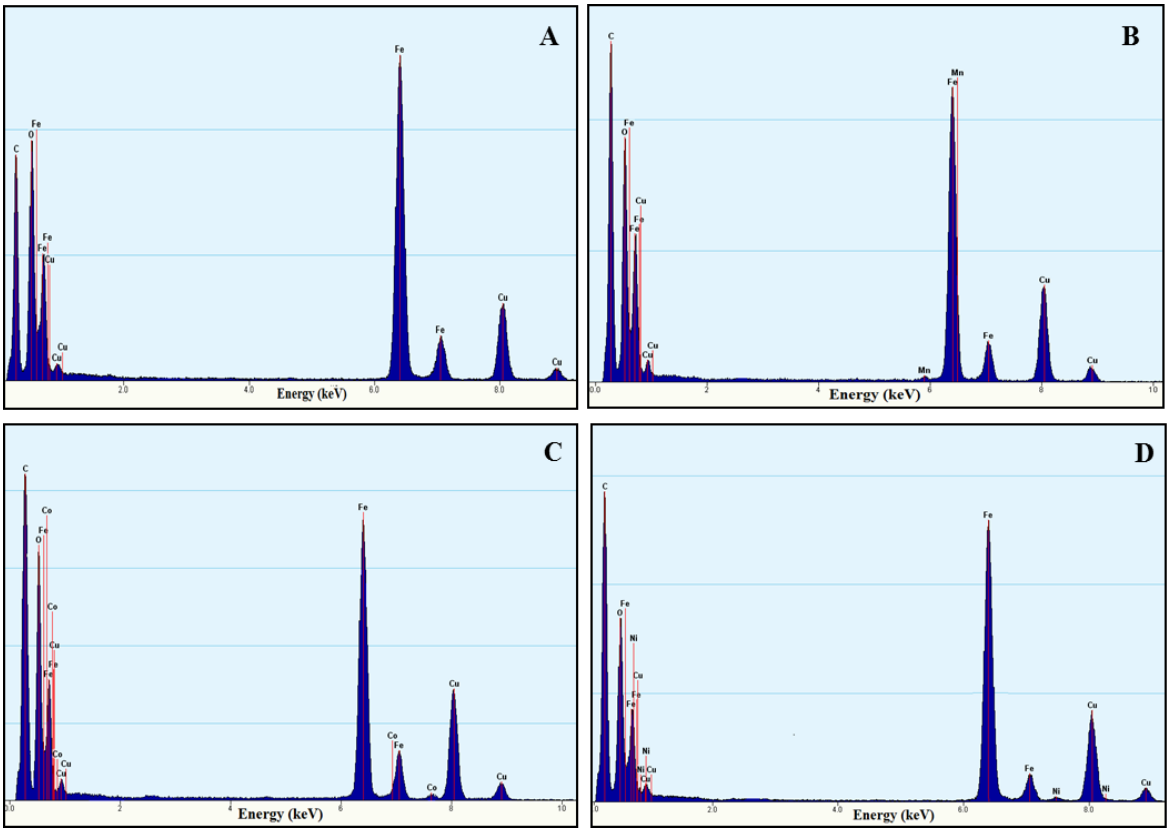

Figure 5.3: EDS spectra of (A) Fe_2O_3 and different M-Fe_2O_3 parallelepipeds namely, (B) Mn-Fe_2O_3, (C) Co-Fe_2O_3 and (D) Ni-Fe_2O_3.

EDS spectrum of Fe_2O_3 parallelepipeds corroborated to the existence of Fe and O, presented in Figure 5.3.A. The presence of each dopant (Mn, Co and Ni) was found along with the basic elements Fe and O in M-Fe_2O_3 PPs from their respective EDS spectrum, Figure 5.3.B-D. The concentration of each doped metal in M-Fe_2O_3 was estimated through inductively coupled plasma optical emission spectrometry (ICP-OES) analysis. The elemental compositions achieved by the EDS analysis were in a good agreement with the data achieved via ICP-OES analysis for all the samples (Table 5.1).

Table 5.1: The elemental compositions acquired by the EDS and ICP-OES analyses for different M-Fe_2O_3 parallelepipeds.

Catalyst	Wt% of dopants (from EDAX analysis)	Wt% of dopants (ICP-OES analysis)
Mn-Fe_2O_3	4.46 (Mn)	4.53 (Mn)
Co-Fe_2O_3	4.51 (Co)	4.39 (Co)
Ni-Fe_2O_3	4.59 (Ni)	4.47 (Ni)

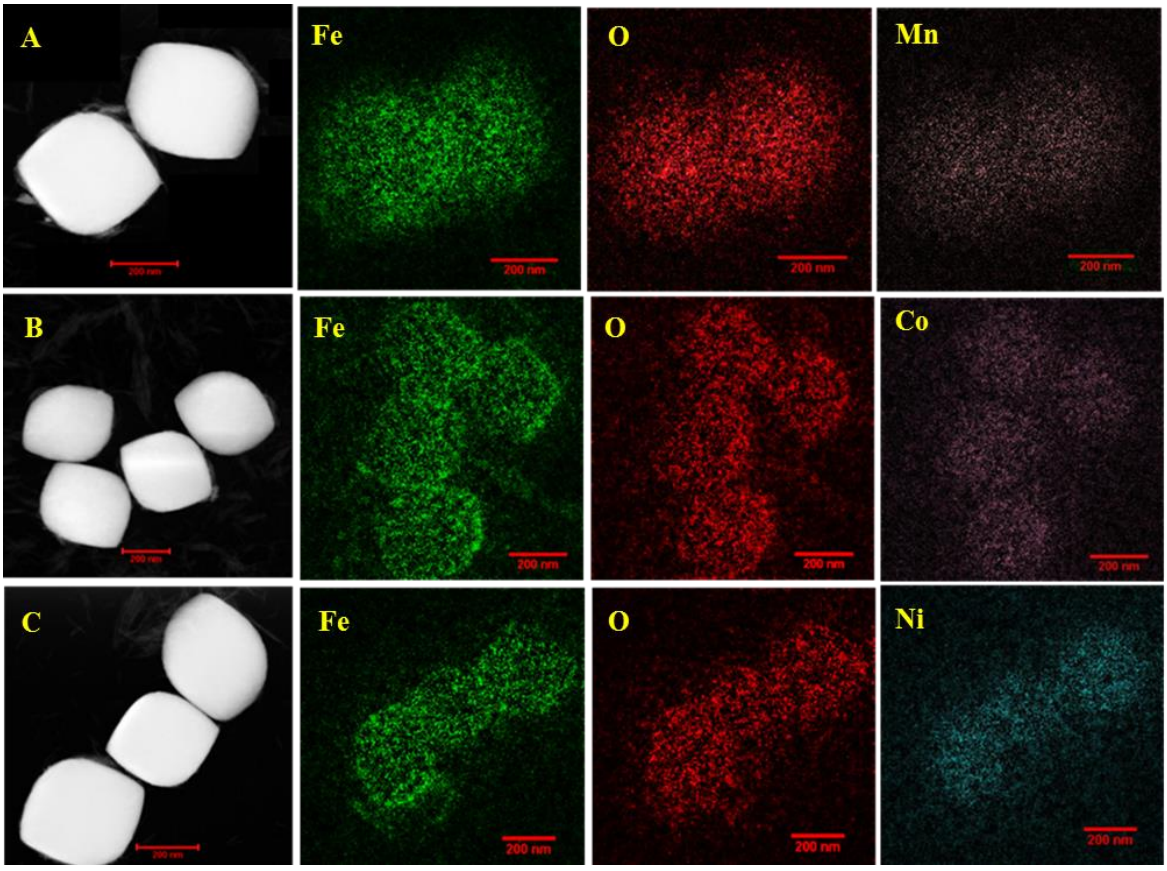

Figure 5.4: STEM images and elemental maps of (A) Mn-Fe_2O_3, (B) Co-Fe_2O_3 and (C) Ni-Fe_2O_3 parallelepipeds, demonstrating uniform distribution of dopant throughout the parallelepiped framework with the constituents Fe and O. (D) STEM image of a bunch of Ni-Fe_2O_3 parallelepipeds. (E) XRD patterns of pristine Fe_2O_3 and all the M-Fe_2O_3 parallelepipeds.

5.3.1.4 STEM-EDS Elemental Mapping Analysis

To visualize the distribution of dopants in M-Fe_2O_3 nanostructures, we performed scanning transmission electron microscopy-energy dispersive spectroscopy (STEM-EDS) elemental mapping on each sample (Figure 5.4). Elemental mapping with color contrast suggested the uniform distribution of dopant together with other constituents all over the parallelepiped nanostructures. The existence of Mn, Co and Ni in Mn-Fe_2O_3, Co-Fe_2O_3 and Ni-Fe_2O_3 respectively was illustrated in Figure 5.4.A-C, indicating that each doped metal was homogeneously distributed throughout the parallelepipeds along with the main elements Fe and O in M-Fe_2O_3 PPs.

5.3.1.5 XRD Study

Figure 5.5 demonstrated the XRD patterns of pristine Fe_2O_3 and M-Fe_2O_3 PPs. The diffraction peaks of the as-obtained Fe_2O_3 PPs could be indexed to the α-phase of Fe_2O_3 with a rhombohedral crystal structure, owing to the presence of (012), (104), (110), (113), (024) and (116) planes (JCPDS No. 33-06664). It was further evident that the XRD patterns of M-Fe_2O_3 PPs remained unaltered and were similar to that of α-Fe_2O_3. No extra peaks were observed for any dopants, however, only the position of the peaks was slightly shifted towards the lower angle, clearly representing the incorporation of the dopants (Mn, Co and Ni) into the Fe_2O_3 lattice.

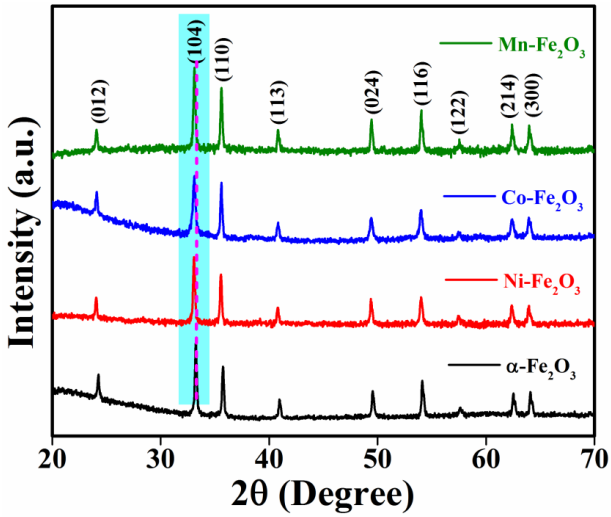

Figure 5.5: XRD patterns of pristine Fe_2O_3 and all the M-Fe_2O_3 PPs.

5.3.1.6 XPS Analysis

X-ray photoelectron spectroscopy (XPS) analysis was carried out to know the valence states and surface chemical compositions of doped structures. XPS analysis performed on M-Fe_2O_3 PPs (Figure 5.6) further authenticated the existence of dopants along with O and Fe in M-Fe_2O_3. The fine spectrum of Mn 2p exhibited two characteristics peaks at 640.9 and 652.4 eV for Mn $2p_{3/2}$ and $Mn2p_{1/2}$ respectively, ascribing to the signature of Mn(II), as shown in Figure 5.6.A.[46,47] The high resolution spectrum of Fe 2p presented in Figure 5.6.B consisted of two peaks at 710.2 and 724.5eV, attributed to the $Fe2p_{3/2}$ and Fe $2p_{1/2}$ respectively, confirming the signature of Fe(III) as the main form present in the nanostructure.[48,49] However, peaks noticed at 709.1 and 722.6 eV revealed the coexistence of a low concentration of Fe(II) in the parallelepipeds. In Figure 5.6.C, the fined scanned O 1s spectrum was deconvoluted into four characteristic peaks, namely O1, O2, O3 and O4. The O1 (529.4 eV) and O2 (530.1 eV) peaks were obtained/observed/achieved owing to the oxygen atoms bound to iron and surface-adsorbed oxygen or oxygen atoms of hydroxyl groups respectively. The O3 (531.2 eV) and O4 (531.9 eV) peaks were appeared for defect sites because of the low oxygen coordination and physisorbed or chemisorbed water molecules over their surfaces respectively.[50] Hence, all XPS results obtained for Mn-Fe_2O_3 indicated successfully doping of Mn into the Fe_2O_3 PPs. Likewise, we have carried out the XPS analysis on Co-Fe_2O_3 as illustrated in Figure 5.6.D-F. In the high resolution spectrum of Co 2p, two individual peaks were observed at 780.7 and 796.7 eV with an energy separation of around 16.0 eV for Co $2p_{3/2}$ and Co $2p_{1/2}$, which was indicative of Co (II).[51,52] Besides Co(II), signature of Fe(III) and O were noticed in Co-Fe_2O_3 and were analogous as found previously in Mn-Fe_2O_3 system. Figure 5.6.G-I described the XPS spectra of Ni-Fe_2O_3. In the high resolution spectrum of Ni 2p, the observed peaks at 855.6 and 873.3 eV ascertained Ni $2p_{3/2}$ and Ni $2p_{1/2}$ respectively, pointing to the presence of Ni(II) in Ni-Fe_2O_3 apart from the existence of Fe(III) and O.[53,54] The aforesaid characterization and subsequent combined results ensured the successful fabrication of M-Fe_2O_3 PPs, which would be explored as an efficient electrocatalyst for energy storage and conversion.

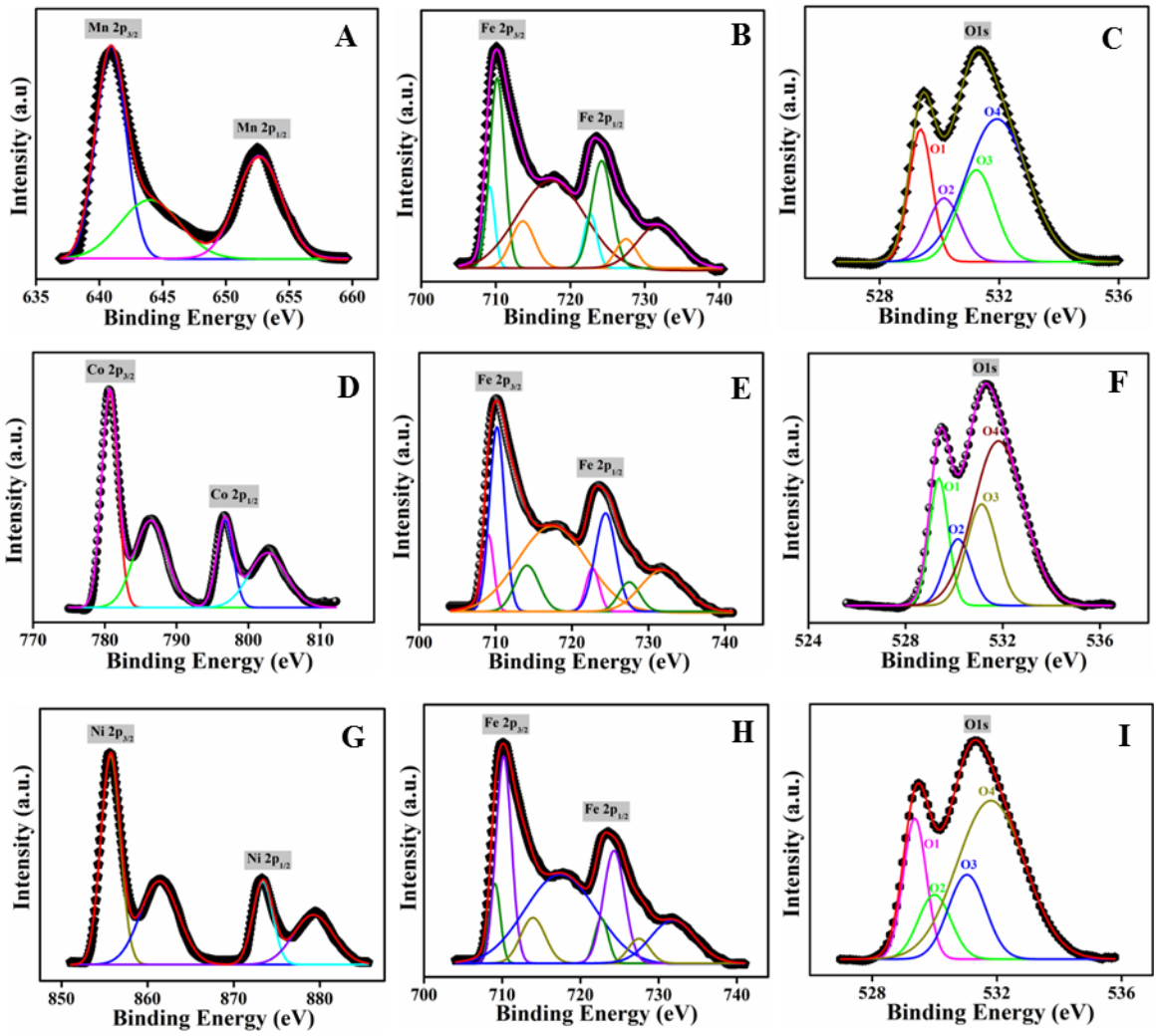

Figure 5.6: High resolution XPS spectra of the constituent elements present in each M-Fe_2O_3 PPs. (A) Mn 2p, (B) Fe 2p, and (C) O 1s for Mn-Fe_2O_3; (D) Co 2p, (E) Fe 2p and (F) O 1s for Co-Fe_2O_3 and (G) Ni 2p (H) Fe 2p (I) O 1s for Ni-Fe_2O_3.

5.3.2 OER Activity

5.3.2.1 Linear Sweep Voltammetry (LSV) and Electrochemical Impedance Spectroscopy (EIS)

To investigate the role of different dopants (Ni, Co, Mn) on the intrinsic property of the iron oxide parallelepipeds, the electrocatalytic activity of M-Fe_2O_3 PPs was studied in basic medium towards oxygen evolution reaction. LSV curves of different catalysts

displayed in Figure 5.7.A, clearly demonstrated that upon incorporation of dopants in Fe_2O_3 the OER activity was enhanced and it's much higher compared to the pristine Fe_2O_3 PPs. It was also observed that Ni-F_2O_3 required least onset potential than that of Co-Fe_2O_3 and Mn-Fe_2O_3. The η_{10} potential illustrated the overpotential needed to reach 10 mA cm^{-2} current density was estimated from LSV curves. The estimated η_{10} value followed the following order: Fe_2O_3 (435 mV) > Mn-Fe_2O_3 (351 mV) > Co-Fe_2O_3 (322 mV) > Ni-F_2O_3 (285 mV). Figure 5.7.B described η_{10} potentials of OER for all the catalysts. It is known to all that Tafel slope is a key parameter to evaluate the catalytic process, which in turn governs the OER kinetics. The smaller Tafel slope pointed to the faster rate of oxygen evolution reaction. Figure 5.7.C depicted the obtained Tafel slopes

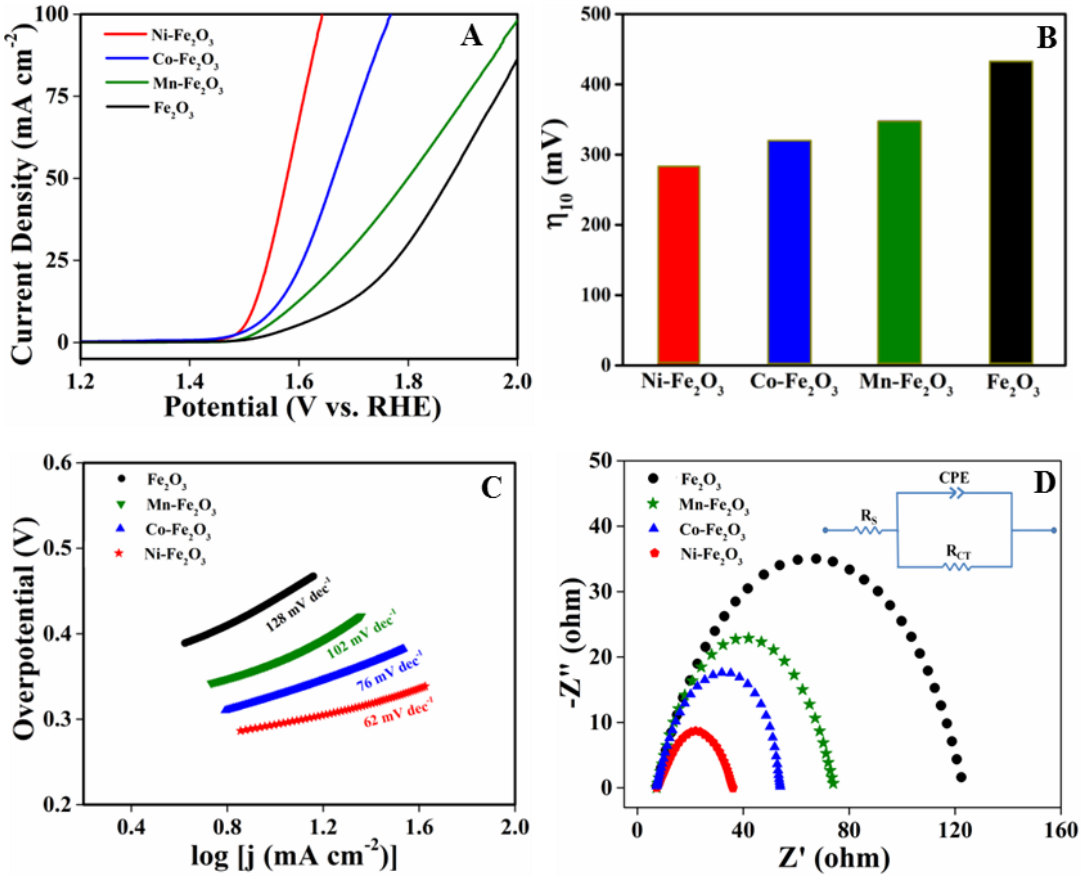

Figure 5.7: (A) Linear sweep voltammetry curves recorded at the scan rate of 5 mV s^{-1} and corresponding (B) η_{10} potential of Ni-Fe_2O_3, Co-Fe_2O_3, Mn-Fe_2O_3 and Fe_2O_3 respectively. (C) Tafel slopes for OER and (D) Nyquist plots for different catalysts (EIS data were recorded at η_{10} potential for all catalysts).

for all the catalysts during OER. Among all the synthesized catalysts, Ni-Fe_2O_3 exhibited lowest Tafel slope compare to pristine Fe_2O_3 or Mn-Fe_2O_3 or even Co-Fe_2O_3, signifying the highest electrocatalytic activity of Ni-Fe_2O_3 catalyst and thus stand out to be the best catalyst. To know about the behavior of charge transfer between the catalyst and electrolyte, we measured the electrochemical impedance spectroscopy (EIS) at a potential of 10 mA cm^{-2} for each catalyst. Figure 5.7.D illustrated the Nyquist plot for all the catalysts and the corresponding simulated equivalent circuit model was displayed in the inset of Figure 5.7.D, where R_S and R_{ct} represent solution resistance and charge transfer resistance respectively and CPE indicates constant phase element. The diameter of the semicircle in Nyquist plot was associated with the charge transfer resistance of the catalyst. The obtained R_{ct} values followed the following sequence: Ni-Fe_2O_3 (28 ohm) < Co-Fe_2O_3 (46 ohm) < Mn-Fe_2O_3 (65 ohm) < Fe_2O_3 (116 ohm). The lower R_{ct} value of Ni-Fe_2O_3 demonstrated faster electron transfer during the OER process, which thus assisted to boost the OER performance. The η_{10} potential, Tafel slope and R_{ct} values of all the catalysts are summarized in Table 5.2.

Table 5.2: η_{10} potential, Tafel slope and R_{CT} for Fe_2O_3, Mn-Fe_2O_3, Co-Fe_2O_3 and Ni-Fe_2O_3 PPs.

Catalysts	**Overpotential (mV) η_{10}**	**Tafel Slope (mV dec^{-1})**	**R_{ct} (ohm)**
Fe_2O_3	435	128	116
Mn-Fe_2O_3	351	102	65
Co-Fe_2O_3	322	76	46
Ni-Fe_2O_3	285	62	28

5.3.2.2 Electrochemically Active Surface Area (ECSA)

Apart from the aforesaid parameters, the electrochemically active surface area (ECSA) is another key factor in electrocatalysis. First, double-layer capacitance (C_{dl}) was calculated for the determination of ECSA, as they are proportional to each other. The ECSA can be

calculated from its C_{dl} according to the following equation; ECSA = C_{dl}/C_s, where C_s is the specific capacitance for a flat standard with 1 cm^{-2} of real surface area. The general value for C_s is between 20 µF cm^{-2} and 60 µF cm^{-2} (generally, 40 µF cm^{-2} is considered as average value of C_s). The C_{dl} was measured by using a simple cyclic voltametric technique. The CVs at different scan rates, ranging from 10 to 50 mV s^{-1}, were presented in Figure 5.8 in the non-faradic region from 1.2 V to 1.3 V vs. RHE. From the slope of the linear plot of half of the capacitive current density differences ($\Delta j = j_{anode} - j_{cathode}$) at 1.25 V i. e.; $\Delta j/2$ vs. the scan rate, C_{dl} can be estimated (Figure 5.9). The estimated C_{dl} values of the catalysts followed the following order: Ni-Fe_2O_3 (3.46 mF cm^{-2}) > Co-Fe_2O_3 (2.57 mF cm^{-2}) > Mn-Fe_2O_3 (1.62 mF cm^{-2}) > Fe_2O_3 (0.58 mF cm^{-2}). The higher C_{dl} value corroborated to the higher ECSA, which could provide more available catalytically active sites to the adsorb hydroxyl ions (OH^-) and thus facilitated the faster oxygen production process. All these outcomes supported that doped structures with more expose active sites offered an improvement of the OER performances.

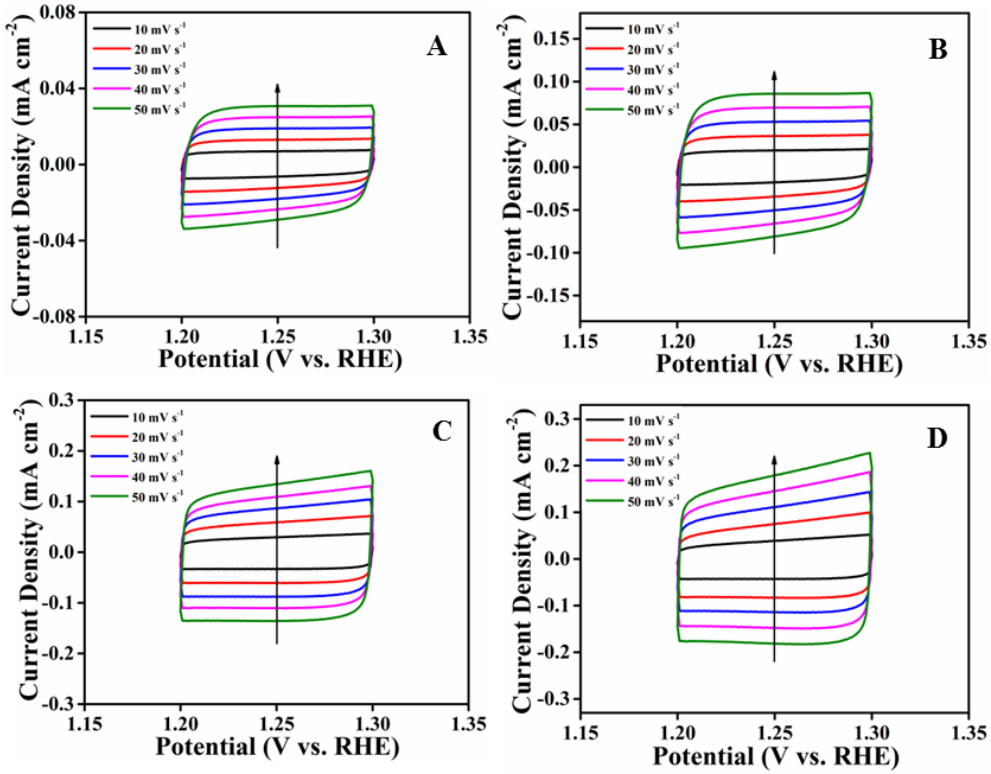

Figure 5.8: Cyclic voltammograms (CVs) at different scan rates in non-faradic region for all the catalyst; (A) Fe_2O_3, (B) Mn-Fe_2O_3, (C) Co-Fe_2O_3 and (D) Ni-Fe_2O_3 PPs.

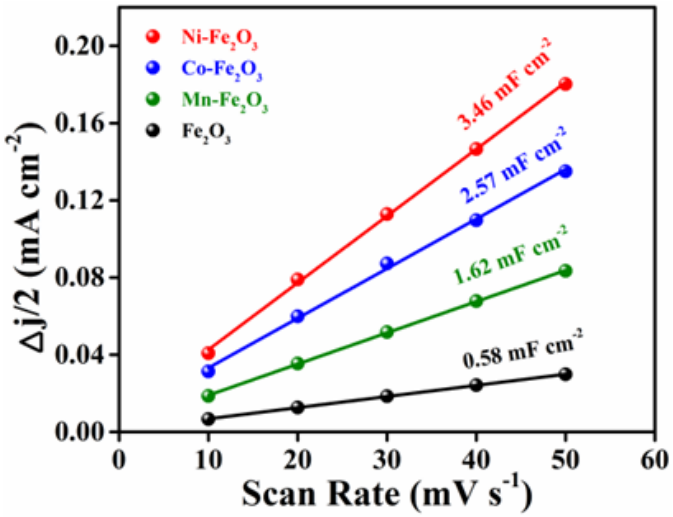

Figure 5.9: The plot of half of the difference in the double-layer charging current densities *(Δj/2)* vs. scan rate of different catalysts for the estimation of C_{dl} values.

5.3.2.3 Stability Test

Additionally, the long-time stability and durability are very important factors for the real field application of an electrocatalyst. To fulfill the aforementioned criteria, chronoamperometric analysis was performed for Ni-Fe_2O_3 PPs as it held the highest electrocatalytic efficiency among all the synthesized catalysts. The analysis carried out at overpotential of η_{10} in 1.0 M KOH, indicated that there was no significant change in the current density even after 16 h, as shown in Figure 5.10.A. Besides chronoamperometric study, LSV curve obtained for Ni-Fe_2O_3 after 16 h of continuous electrocatalytic process further authenticated almost same activity with the as-prepared Ni-Fe_2O_3 catalyst (Figure 5.10.B).

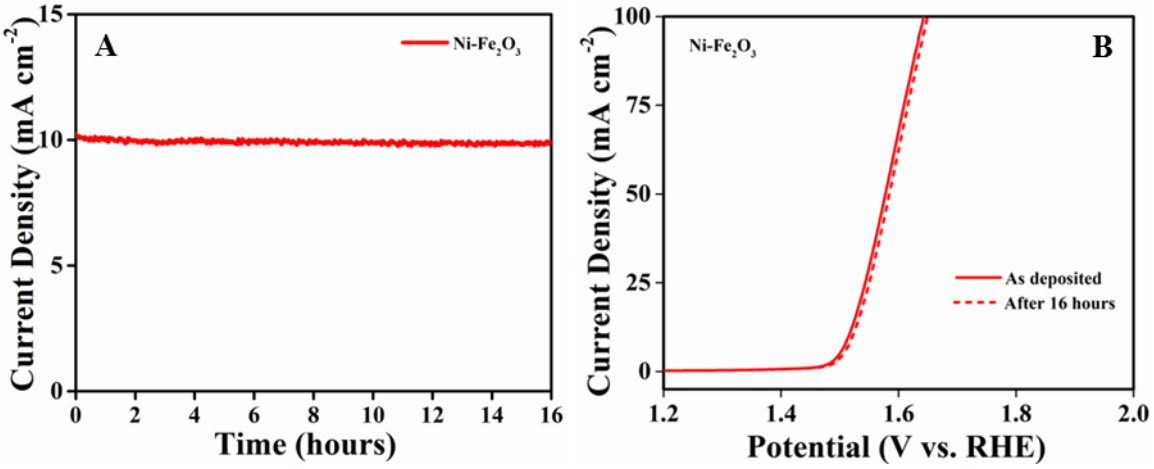

Figure 5.10: (A) i-t curve of Ni-Fe_2O_3 PPs at η_{10} potential for 16 h. (B) LSV plots of Ni-Fe_2O_3 PPs before and after prolonged OER analysis for 16 h at 10 mA cm^{-2}.

5.3.2.4 Post OER Study

FESEM and TEM analyses were also carried out to know the morphological change, if any, for Ni-Fe_2O_3 after electrocatalysis (Figure 5.11). However, all the images specified their intact morphology even after prolonged electrochemical analysis. Although no physical change of the catalyst was found but to understand whether there was any chemical change, XPS analysis was performed after continuous electrocatalytic process. Fe 2p spectrum clearly demonstrated the distinctive peaks for Fe(III) and Fe(II), as shown in Figure 5.12.A. Those peaks were analogous to the observed XPS spectrum of Fe 2p of Ni-Fe_2O_3 before OER study. However, Ni 2p spectrum revealed the appearance of new peaks (Figure 5.12.B) for Ni(III) along with Ni(II), indicating the formation of NiOOH during prolonged electrochemical analysis.[55,56] The O 1s spectrum of the post catalytic sample was presented in Figure 5.12.C. Among the four deconvoluted peaks, intensity of O2 and O4 became higher compare to the peaks obtained for fresh catalysts. The increase in intensity was due to oxygen or hydroxyl groups adsorbed over their surfaces and also surface adsorbed molecular water respectively as a result of continuous electrocatalytic study.[57]

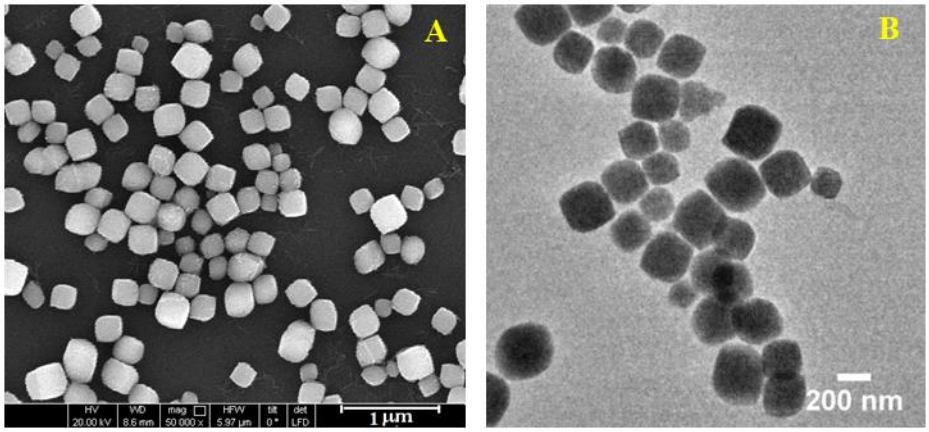

Figure 5.11: (A) FESEM and (B) TEM images of Ni-Fe_2O_3 PPs after OER study, representing no alteration of morphology even after prolonged usage.

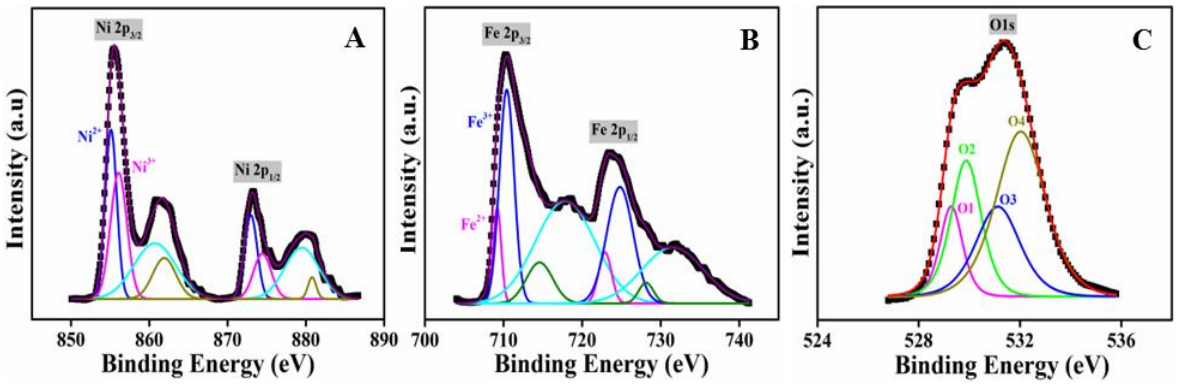

Figure 5.12: XPS spectra of (A) Ni 2p, (B) Fe 2p and (C) O 1s region of Ni-Fe_2O_3 PPs after prolonged OER study.

5.3.2.5 Comparison of Electrocatalytic Activity

Finally, OER activity of all M-Fe_2O_3 parallelepipeds was compared in associated with the electrocatalysts comprised of non-noble metals previously reported in the literature (Table 5.3), which illustrated outstanding catalytic activity of our doped catalysts.

Table 5.3: OER activity of as-obtained M-Fe_2O_3 PPs was compared with the reported non-noble metal based electrocatalysts.

Catalysts	Electrolyte	Overpotential (mV) at 10 mA cm^{-2}	Tafel Slope (mV dec^{-1})	References
$Co_3O_4/NiCo_2O_4$/GC	**1.0 M KOH**	340	88	58
Co_3O_4/graphene		360	67	59
NiCo-LDH		335	41	60
CoMn-LDH/GC		324	43	61
$Co_3O_4/Co_{0.85}Se/Co_9Se_8$		330	91	62
$MoO_2/CoC_2O_4 \cdot 2H_2O$		330	78	63
$CoMoO_4$ nanosheets		312	56	64
CoMnP		330	61	65
NiCoP NPs		360	82	66
NiMo hollow nanorod		310	47	67
Ni@C-400 NSs		330	145	68
$NiCo_2O_4$		360	60	69
$NiCo_2S_4$		337	64	70
$NiCo_2O_4$/CNTs		390	68	71
NiCo-LDH		420	113	72
Mn-Fe_2O_3		**351**	**102**	**This Work**
Co-Fe_2O_3		**322**	**76**	**This Work**
Ni-Fe_2O_3		**285**	**62**	**This Work**

5.3.2.6 OER Mechanism

It is important to note that electrocatalysts should have several exposed active sites to the electrolytes in improving their electrocatalytic efficacy. During electrocatalysis, in situ-generated oxidized species were produced over the catalyst surfaces, which could be

accountable for the higher electrochemical activity by taking part in OER process. Moreover, all these parallelepipeds have several defect sites with low oxygen coordination as evident from XPS study. All these defect sites over the surface of the catalyst play as charge traps and also involve as adsorption sites, where charge transfer occurs to the adsorbed species, resulting in improvement in their electrocatalytic activity.[73] With the aim to achieve excellent electrocatalysts, we have doped several metals in the Fe_2O_3 PPs. It was further pointed out that all the dopants were intercalated into the parallelepipeds and effectively participated in electron transfer process happened at electrode-electrolyte interfaces and subsequently boosted the catalytic activity during OER.[74,75] All the doped M-Fe_2O_3 exhibited enhanced catalytic activity in associated with the pristine Fe_2O_3, owing to the synergistic effect of doped metal together with Fe. It should be noted that the synergistic effect aroused from iron and different dopants would boost the electrocatalytic activity of the catalyst during OER.[76,77] After metal doping, it enhanced the charge carrier density and conductivity of the doped nanostructures and hence attributed to an increase in active sites over the catalysts surfaces. As all the transition metals participate to increase the charge carrier density and conductivity, the surface reaction kinetics is therefore a crucial aspect. The surface metal centers (denoted as M) essentially function as active sites for OER, which then proceeds via formation of a series of intermediates consisting of an M-O bond; like M-OH, M-O, M-OOH, M-OO.[78-81] It is therefore apparent that there is a strong correlation between activity and M-O bond strength, which in fact regulates the OER mechanism. Additionally, Sabatier principle illustrates that intermediate formed due to the interaction between catalyst and adsorbed species should reasonably strong to adsorb the reactants but at the same time it should not be so strong that it impeded desorption of the product from catalyst surfaces. Thus, catalysts with optimal M-O bond strength are considered to be the best catalyst, whereas catalysts having too strong or too weak M-O bonds turn to be the worse catalysts. Interestingly, amongst the different dopants (Ni, Co and Mn), the optimal interaction strength with OH_{ad} has been reported for Ni, which is in consistence with the Sabatier principle.[82] This is further supported by the Carter's calculation reported for doped hematite surfaces.[83] Despite the aforesaid understanding, highest electrocatalytic activity

for oxygen production demonstrated by Ni-Fe_2O_3 is probably due to the higher electronegativity of Ni (1.91) in contrast to Mn (1.55) or Co (1.88).[84] The higher electronegativity of Ni makes it a powerful electron sink and thus adsorbs hydroxyl ions and subsequently promotes the OER process. Moreover, theoretical understanding demonstrated that Ni is the most effective dopant in lowering the overpotential of the subsequent catalyst as Ni holds weak positive charge compare to Fe, facilitating the optimal binding with the adsorbates during OER.[83,85] All parameters all together ascertained that upon doping of non-noble metals in Fe_2O_3, the catalytic activity was enhanced significantly, making the Ni-Fe_2O_3 a best catalyst among them.

5.4 Conclusions

In summary, we have reported a simple low temperature light driven hydrolysis route to prepare pristine as well as different metal doped (M = Mn, Co and Ni) M-Fe_2O_3 parallelepipeds and investigated their OER activity. Our developed route provides an easy way to improve the OER activity of iron oxide parallelepipeds via non-noble metal doping. Among all the prepared parallelepipeds, Ni-Fe_2O_3 exhibits highest catalytic activity and stability in alkaline medium, with an order of activity: Ni-Fe_2O_3>Co-Fe_2O_3>Mn-Fe_2O_3>Fe_2O_3. Upon doing, the resultant doped structures offer an enhanced conductivity and better charge transfer behavior towards OER and thus boosts the electrocatalysis. The synergistic effect of iron and different dopants together with improved electronic structure results superior OER activity of doped structures compare to undoped structure. Hence, our Ni-Fe_2O_3 parallelepipeds demonstrate excellent catalytic activity because of the higher electronegativity of Ni, optimal interaction strength of Ni with OH_{ad} and available exposed active sites, together with the synergistic effect arising from Ni and Fe further boosts the intrinsic catalytic activity for Ni-Fe_2O_3 parallelepipeds. This approach provides a unique way of doping process to make new electrocatalysts with excellent electrocatalytic activity.

5.5 References

(1) Suen, N. T.; Hung, S. F.; Quan, Q.; Zhang, N.; Xu, Y. J.; Chen, H. M. Electrocatalysis for the Oxygen Evolution Reaction; Recent Development and Future Perspectives. *Chem. Soc. Rev.* **2017**, *46*, 337-365.

(2) Maeda, K.; Teremura, K.; Lu, D.; Takata, T.; Saito, N.; Inoue, Y.; Domen, K. Photocatalyst Releasing Hydrogen from Water. *Nature* **2006**, *440*, 295.

(3) McCrory, C. C. L.; Jung, S.; Peters, J. C.; Jaramillo, T. F. Benchmarking Heterogeneous Electrocatalysts for the Oxygen Evolution Reaction. *J. Am. Chem. Soc.* **2013**. 135, 16977-16987.

(4) Kordek, K.; Yin, H.; Rutkowski, P.; Zhao, H. Cobalt-based Composite Films on Electrochemically Activated Carbon Clothes as High Performance Overall Water Splitting Electrodes. *Int. J. Hydrogen Energy* **2019**, *44*, 23-33.

(5) Jia, D.; Gao, H.; Xing, L.; Chen, X.; Dong, W.; Huang, X; Wang, G. 3D Self-Supported Porous NiO@$NiMoO_4$ Core–Shell Nanosheets for Highly Efficient Oxygen Evolution Reaction. *Inorg. Chem.* **2019**, *58*, 6758-6764.

(6) Zhang, B.; Xue, Y.; Jiang, A.; Xue, Z.; Li, Z.; Hao, J. Ionic Liquid as Reaction Medium for Synthesis of Hierarchically Structured One-Dimensional MoO_2 for Efficient Hydrogen Evolution. *ACS Appl. Mater. Interfaces* **2017**, *9*, 7217-7223.

(7) Zhuang, L.; Ge, L.; Yang, Y. S.; Li, M. R.; Jia, Y.; Yao, X. D.; Zhu, Z. H. Ultrathin Iron-Cobalt Oxide Nanosheets with Abundant Oxygen Vacancies for the Oxygen Evolution Reaction. *Adv. Mater.* **2017**, *29*, 1606793-1606799.

(8) Han, L.; Dong, S. J.; Wang, E. Transition-Metal (Co, Ni, and Fe)-Based Electrocatalysts for the Water Oxidation Reaction. *Adv. Mater.* **2016**, *28*, 9266-9291.

(9) Watler, C.; Menezes, P. W.; Orthmann, S.; Schuch, J.; Connor, P.; Kaiser, B.; Lerch, M.; Driess, M. A Molecular Approach to Manganese Nitride Acting as A High Performance electrocatalyst in the Oxygen Evolution Reaction. *Angew. Chem. Int. Ed.* **2018**, *57*, 698-702.

(10) Liu, G.; Li, P.; Zhao, G.; Wang, X.; Kong, J.; Liu, H.; Zhang, H.; Chang, K.; Meng, X.; kuko, T.; Ye, J. Promoting Active Species Generation by Plasmon-Induced Hot Electron Excitation for Efficient Electrocatalytic Oxygen Evolution. *J. Am. Chem. Soc.* **2016**, *138*, 9128-9136.

(11) Zhang, B.; Lui, Y. H.; Gaur, A .P. S.; Chen, B.; Tang, X.; Qi, Z.; Hu, S. Hierarchical FeNiP@ Ultrathin Carbon Nanoflakes as Alkaline Oxygen Evolution and Acidic Hydrogen Evolution Catalyst for Efficient Water Electrolysis and Organic Decomposition. *ACS Appl. Mater. Interfaces* **201**8, *10*, 8739-8748.

(12) Kim, M.; Kim, S.; Song, D.; Oh, S.; Chang, K. J.; Cho, E. Promotion of electrochemical Oxygen Evolution Reaction by Chemical Coupling of Cobalt to Molybdenum Carbide. *Appl. Catal. B: Environ.* **2018**, *220*, 88-97.
(13) Zagalskaya, A.; Alexandrov, V. Mechanistic Study of IrO_2 Dissolution during the Electrocatalytic Oxygen Evolution Reaction. *J. Phys. Chem. Lett*. **2020**, *11*, 2695-2700.
(14) Lu, Z.; Wang, H.; Kong, D.; Yan, K.; Hsu, P. C.; Zheng, G.; Yao, H.; Liang, Z.; Sun, X.; Cui, Y. Electrochemical Tuning of Layered Lithium Transition Metal Oxides for Improvement of Oxygen Evolution Reaction. *Nat. Commun.* **2014**, *5*, 4345-4351.
(15) Grimaud, A.; Diaz-Morales, O.; Han, B.; Hong, W. T.; Lee, Y. -L.; Giordano, L.; Steorzinger, K. A.; Koper, M. T. M.; Shao-Horn, Y. Activating Lattice Oxygen Redox Reactions in Metal Oxides to Catalyse Oxygen Evolution. *Nat. Chem.* **2017**, *9*, 457-465.
(16) Samanta, A.; Das, S.; Jana, S. Doping of Ni in α-Fe_2O_3 Nanoclews to Boost Oxygen Evolution Electrocatalysis. *ACS sustainable Chem. Eng.* **2019**, *7*, 12117-12124.
(17) Men, Y.; Liu, X.; Yang, F.; Ke, F.; Cheng, G.; Luo, W. Carbon Encapsulated Hollow Co_3O_4 Composites Derived from Reduced Graphene Oxide Wrapped Metal–Organic Frameworks with Enhanced Lithium Storage and Water Oxidation Properties. *Inorg. Chem.* **2018**, *57*, 10649-10655.
(18) Batchellor, A. S.; Boettcher, S. W. Pulse-electrodeposited Ni-Fe (Oxy) hydroxide Oxygen Evolution Electrocatalyst with High Geometric and Intrinsic Activities at Large Mass Loading. *ACS Catal.* **2015**, *5*, 6680-6689.
(19) Song, F.; Hu, X. Exfoliation of Layered Double Hydroxides for Enhanced Oxygen Evolution Catalysis. *Nat. Commun.* **2014**, 5, 4477.
(20) Diaz-Morales O.; Ledezma-Yanez, I.; Koper, M. T. M.; Calle-Vallejo, F. Guidelines for the rotational design of Ni-based Double Hydroxide Electrocatalysts for the Oxygen Evolution Reaction. *ACS Catal.* **2015**, *5*, 5380-5387.
(21) Wasalathanthri, R. N.; Jeffrey, S.; Awni, R. A.; Sun, K.; Giolando, D. M. Electrodeposited Copper-Cobalt-Phosphide: A Stable Bifunctional Catalyst for Both Hydrogen and Oxygen Evolution Reactions. *ACS Sustainable Chem. Eng.* **2019**, *7*, 3092-3100.
(22) Menezes, P. W.; Indra, A.; Zaharieva, I.; Watler, C.; Loos, S.; Hoffmann, S.; Schlogl, R.; Dou, H.; Driess, M. Helical Cobalt Borophosphates to Master Durable Overall Water-Splitting. *Energy Environ. Sci.* **2019**, *12*, 988-999.
(23) Chen, W.; Liu, Y.; Li, Y.; Sun, J.; Qui, Y.; Liu, C.; Zhou, G.; Cui, Y. In situ Electrochemically Derived Nanoporous Oxides from Transition Metal Dichalcogenides for Active Oxygen Evolution Catalysts. *Nano. Lett.* **2016**, *16*, 7588-7596.
(24) Zhang, G.; Liu, H.; Qu, J.; Li, J. Two Dimensional Layered MoS_2: Rotational Design, Properties and Electrochemical Application. *Energy Environ. Sci.* **2016**, *9*, 1190-1209.

(25) Bu, Y.; Nam, G.; Kim, S.; Choi, K.; Zhong, Q.; Lee. J.; Qin, Y.; Cho, J.; Kim, G. A Tailored Bifunctional Electrocatalyst: Boosting Oxygen Reduction/Evolution Catalysis via Electron Transfer between N-doped Graphene and Perovskite Oxides. *Small* **2018**, *14*, 1802767.

(26) Ma, T. Y.; Dai, S.; Jaroniec, M.; Qiao, S. Z. Metal-Organic Framework Derived Hybrid Co_3O_4-Carbon Porous Nanowire arrays as Reversible Oxygen Evolution Electrodes. *J. Am. Chem. Soc.* **2014**, *136*, 13925-13931.

(27) Xia, B. Y.; Yan, Y.; Li, N.; Wu, H. B.; Lou, X. W.; Wang, X. A Metal-organic Framework-derived Bifunctional Oxygen Electrocatalyst. *Nat. Energy* **2016**, *1*, 15006.

(28) Wang, G.; Ling, Y.; Wheeler, D. A.; George, K. E.; Horsley, K.; Heske, C.; Zhang, J. Z.; Li, Y. Facile Synthesis of High Photoactive α-Fe_2O_3-based Films for Water Oxidation. *Nano Lett.* **2011**, *11*, 3503-3509.

(29) Das, S.; Jana, S. A Tubular Nanoreactor Directing the formation of in situ Iron Oxide Nanorods with Superior Photocatalytic Activity. *Environ. Sci.: Nano* **2017**, *4*, 596-603.

(30) Burke, M. S.; Enman, L. J.; Batchellor, A. S.; Zou, S.; Boettcher, S. W. Oxygen Evolution Reaction Electrocatalysis on Transition Metal Oxides and (Oxy) hydroxide: Activity Trends and Design Principles. *Chem. Mater.* **2015**, *27*, 7549-7558.

(31) Teng, Y.; Wang, X. D.; Liao, J. F.; Li, W. G.; Chen, H. Y.; Dong, Y. J.; Kuang, D. B. Atomically Thin Defect Rich Fe-Mn-O Hybrid Nanosheets as High Efficient Electrocatalyst for Water Oxidation. *Adv. Funct. Mater.* **2018**, *28*, 1802463-1802470.

(32) Samanta, A.; Das, S.; Jana, S. Ultra-Small Intermetallic NiZn Nanoparticles: A Non-Precious Metal Catalyst for Efficient Electrocatalysis. *Nanoscale Adv.* **2020**, *2*, 417-424.

(33) Das, S.; Samanta, A.; Jana, S. Light-Assisted Synthesis of Hierarchical Flower-Like MnO_2 Nanocomposites with Solar Light Induced Enhanced Photocatalytic Activity. *ACS Sustainable Chem. Eng.* **2017**, *5*, 9086-9094.

(34). Qin, S.; Yao, Y.; Qian, M.; Yang, Q.; Chen, T.; Xu, H.; Zheng, L. Hierarchical Microspheres Composed of Mn-Doped CoP Nanosheets for Enhanced Oxygen Evolution. *ACS Appl. Nano Mater.* **2020**, *3*, 10702-10707.

(35) Jana, S.; Praharaj, S.; Panigrahi, S.; Basu, S.; Pande, S.; Chang, C. -H.; Pal, T. Light-Induced Hydrolysis of Nitriles by Photoproduced α-MnO_2 Nanorods on Polystyrene Beads. *Org. Lett.* **2007**, *9*, 2191-2193.

(36) Moon, G. H.; Yu, M.; Chan, C. K.; Tuysuz, H. Highly Active Cobalt-Based Electrocatalysts with Facile Incorporation of Dopants for the Oxygen Evolution Reaction. *Angew. Chem. Int. Ed.* **2019**, *58*, 3491-3495.

(37) Du, J.; Zou, Z.; Liu, C.; Xu, C. Hierarchical Fe-Doped Ni_3Se_4 Ultrathin Nanosheets as An Efficient Electrocatalyst for Oxygen Evolution Reaction. *Nanoscale* **2018**, *10*, 5163-5170.

(38) Zhang, R.; Zhang R. -C.; Pan, L.; Shen, G. -Q.; Mahmood, N.; Ma, Y. -H.; Shi, Y.; Jia, W.; Wang, L. ; Zhang, X.; Xu, W.; Zou, J. -J. Engineering Cobalt Defects in Cobalt Oxide for Highly Efficient Electrocatalytic Oxygen Evolution. *ACS Catal.* **2018**, *8*, 3803-3811.

(39) Zhuang, Z.; Sheng, W.; Yan, Y. Synthesis of Monodispere Au@Co_3O_4 Core-Shell Nanocrystals and Their Enhanced Catalytic Activity for Oxygen Evolution Reaction. *Adv. Mater.* **2014**, *26*, 3950-395.

(40) Sun, H.; Chen, G.; Sunarso, J.; Dai, J.; Zhou, W.; Shao, Z. Molybdenum and Niobium cododed B-site-ordered double Perovskite catalyst for Efficient Oxygen Evolution Reaction. *ACS Appl. Mater. Interfaces* **2018**, *10*, 16939-16942.

(41) Li, Y. -F.; Selloni, A. Mechanism and Activity of Water Oxidation on Selected Surfaces of Pure and Fe-doped NiOx. *ACS Catal.* **2014**, *4*, 1148-1153.

(42) Park, S.; Kim, H. J.; Lee, C. W.; Song H. J.; Shin, S. S.; Seo, S. W.; Park, H. K.; Lee, S.; Kim. D. W.; Hong, K. S. Sn Self-doped α-Fe_2O_3 Nanobranch Arrays Supported on a Transparent, Conductive SnO_2 Trunk to Improve Photoelectrochemical Water Oxidation. *Int. J. Hydrogen Energy* **2014**, *39*, 16459-16467.

(43) Hu, Y. S.; Kleiman-Shwarsctein, A.; Forman, A. J.; Hazen, D.; Park, J. N.; McFarlang, E. W. Pt-doped α-Fe_2O_3 Thin Films Active for Photoelectrochemical Water Splitting. *Chem. Mater.* **2008**, *20*, 3803-3805.

(44) Frydrych, J.; Machala, L.; Tucek, J.; Siskova, K.; Filip, J.; Pechousek, J.; Safarova, K.; Vondracek, M.; Seo, J. H.; Schneeweiss, O.; Gratzel, M.; Sivula, K.; Zboril, R. Facile Fabrication of Tin-Doped Hematite Photoelectrodes-Effect of Doping on Magnetic Properties and Performance for Light-induced Water Splitting. *J. Mater. Chem.* **2012**, *22*, 23232-23239.

(45) Sartoretti, C. J.; Alexander, B. D.; Solarska, R.; Rutkowska, T. A.; Augustynski, J.; Cerny, R. Photoelectrochemical Oxidation of Water at Transparent Ferric Oxides Film Electrodes. *J. Phys. Chem. B* **2005**, *109*, 13685-13692.

(46) Park, S. A.; Lim, H.; Kim, Y. T. Enhanced Oxygen Reduction Reaction Activity Due to Electronic Effects between Ag and Mn_3O_4 in Alkaline Media. *ACS Catal.* **2015**, *5*, 3995-4002.

(47) Guo, D.; Wu, Z.; An, Y.; Li, X.; Guo, X.; Chu, X.; Sun, C.; Lei, M.; Li, L.; Cao, L.; Li, P. Room Temperature Ferromagnetism in $(Ga_{1-x}Mn_x)_2O_3$ Epitaxial Thin Films. *J. Mater. Chem. C* **2015**, *3*, 1830-1834.

(48) J Wang, J.; Ji, L.; Chen, Z. In Situ Rapid Formation of a Nickel−Iron-Based Electrocatalyst for Water Oxidation. *ACS Catal.* **2016**, *6*, 6987-6992.

(49) Kim, J. Y.; Youn, D. H.; Kang, K.; Lee, J. S. Highly Conformal Deposition of an Ultrathin FeOOH Layer on a Hematite Nanostructure for Efficient Solar Water Splitting. *Angew. Chem. Int. Ed.* **2016**, *55*, 10854-10858.

(50) Wu, L. K.; Wu, W. Y.; Xia, J.; Cao, H. Z.; Hou, G. Y.; Tang, Y. P.; Zheng, G. Q. A Nanostructured Nickel-Cobalt Alloy with an Oxide Layer for an Efficient Oxygen Evolution Reaction. *J. Mater. Chem. A* **2017**, *5*, 10669-10677.
(51) Guan, J.; Ding, C.; Chen, R.; Huang, B.; Zhang, X.; Fan, F.; Zhang, F.; Li, C. CoO_x Nanoparticle Anchored on Sulfonated-Graphite as Efficient Water Oxidation Catalyst. *Chem. Science* **2017**, *8*, 6111-6116.
(52) Zhang, Q.; Duan, Z.; Li, M.; Guan, J. Atomic Cobalt Catalysts for The Oxygen Evolution Reaction. *Chem. Commun.* **2020**, *56*, 794-797.
(53) Cheng, H.; Su, Y. Z.; Kuang, P. Y.; Chen, G. F.; Liu, Z. Q. Hierarchical $NiCo_2O_4$ Nanosheet-Decorated Carbon Nanotubes towards Highly Efficient Electrocatalyst for Water Oxidation. *J. Mater. Chem. A* **2015**, *3*, 19314-19321.
(54) Yuan, C.; Li, J.; Hou, L.; Zhang, X.; Shen, L.; Lou, X. W. Ultrathin Mesoporous $NiCo_2O_4$ Nanosheets Supported on Ni Foam as Advanced Electrodes for Supercapacitors. *Adv. Funct. Mater.* **2012**, *22*, 4592-4597.
(55) Konkena, B.; Masa, J.; Botz, A. J.; Sinev, I.; Xia, W.; Koßmann, J.; Drautz, R.; Muhler, M.; Schuhmann, W. Metallic $NiPS_3$@NiOOH Core−Shell Heterostructures as Highly Efficient and Stable Electrocatalyst for the Oxygen Evolution Reaction. *ACS Catal.* **2017**, *7*, 229-237.
(56) Song, B.; Li, K.; Yin, Y.; Wu, T.; Dang, L.; Cabán-Acevedo, M.; Han, J.; Gao, T.; Wang, X.; Zhang, Z.; Schmidt, J. R.; Xu, P.; Jin, S. Tuning Mixed Nickel Iron Phosphosulfide Nanosheet Electrocatalysts for Enhanced Hydrogen and Oxygen Evolution. *ACS Catal.* **2017**, *7*, 8549-8557.
(57) Ye, Y. J.; Zhang, N.; Liu, X. X. Amorphous NiFe(oxy)hydroxide Nanosheet Integrated Partially Exfoliated Graphite Foil for High Efficiency Oxygen Evolution Reaction. *J. Mater. Chem. A* **2017**, *5*, 24208-24216.
(58) Hu, H.; Guan, B. Y.; Xia, B. Y.; Lou, X. W. Designed Formation of Co_3O_4/$NiCo_2O_4$ Double-Shelled Nanocages with Enhanced Pseudocapacitive and Electrocatalytic Properties. *J. Am. Chem. Soc.* **2015**, *137*, 5590-5595.
(59) Liang, Y. Y.; Li, Y. G.; Wang, H. L.; Zhou, J. G.; Wang, J.; Regier, T.; Dai, H. J. Co_3O_4 Nanocrystals on Graphene as a Synergistic Catalyst for Oxygen Reduction Reaction. *Nat. Mater.* **2011**, *10*, 780-786.
(60) Song, F.; Hu, X. Exfoliation of Layered Double Hydroxides for Enhanced Oxygen Evolution Catalysis. *Nat. Commun.* **2014**, *5*, 4477.
(61) Song, F.; Hu, X. L. Ultrathin Cobalt-Manganese Layered Double Hydroxide Is an Efficient Oxygen Evolution Catalyst. *J. Am. Chem. Soc.* **2014**, *136*, 16481-16484.
(62) Ghosh, S.; Tudu, G.; Mondal, A.; Ganguli, S.; Inta, H. R.; Mahalingam, V. Inception of Co_3O_4 as Microstructural Support to Promote Alkaline Oxygen Evolution Reaction for $Co_{0.85}Se$/Co_9Se_8 Network. *Inorg. Chem.* **2020**, *59*, 17326-17339.

(63) Ghosh, S.; Inta, H. R.; Ganguli, S.; Tudu, G.; Koppisetti, H. V.; Mahalingam, V. MoO_2 as a Propitious "Pore-Forming Additive" for Boosting the Water Oxidation Activity of Cobalt Oxalate Microrods. *J. Phys. Chem. C* **2020**, *124*, 20010-20020.
(64) Yu, M. Q.; Jiang, L. X.; Yang, H. G. Ultrathin Nanosheets Constructed $CoMoO_4$ Porous Flowers with High Activity for Electrocatalytic Oxygen Evolution. *Chem. Commun.* **2015**, *51*, 14361-14364.
(65) Li, D.; Baydoun, H.; Verani, C. N.; Brock, S. L. Efficient Water Oxidation Using CoMnP Nanoparticles. *J. Am. Chem. Soc.* **2016**, *138*, 4006-4009.
(66) Vigil, J. A.; Lambert, T. N.; Christensen, B. T. Cobalt Phosphide-Based Nanoparticles as Bifunctional Electrocatalysts for Alkaline Water Splitting. *J. Mater. Chem. A* **2016**, *4*, 7549-7554.
(67) Tian, J.; Cheng, N.; Liu, Q.; Sun, X.; He, Y.; Asiri, A. M. Self-Supported NiMo Hollow Nanorod Array: An Efficient 3D Bifunctional Catalytic Electrode for Overall Water Splitting. *J. Mater. Chem. A* **2015**, *3*, 20056-20059.
(68) Xi, W.; Ren, Z.; Kong, L.; Wu, J.; Du, S.; Zhu, J.; Xue, Y.; Meng, H.; Fu, H. Dual-Valence Nickel Nanosheets Covered with Thin Carbon as Bifunctional Electrocatalysts for Full Water Splitting. *J. Mater. Chem. A* **2016**, *4*, 7297-7304.
(69) Xiao, Y.; Feng, L.; Hu, C.; Fateev, V.; Liu, C.; Xing, W. $NiCo_2O_4$ 3 Dimensional Nanosheet as Effective and Robust Catalyst for Oxygen Evolution Reaction. *RSC Adv.* **2015**, *5*, 61900-61905.
(70) Jiang, J.; Yan, C.; Zhao, X.; Luo, H.; Xue, Z.; Mu, T. A PEGylated Deep Eutectic Solvent for Controllable Solvothermal Synthesis of Porous $NiCo_2S_4$ for Efficient Oxygen Evolution Reaction. *Green Chem.* **2017**, *19*, 3023-3031.
(71) Cheng, H.; Su, Y. Z.; Kuang, P. Y.; Chen, G. F.; Liu, Z. Q. Hierarchical $NiCo_2O_4$ Nanosheet-Decorated Carbon Nanotubes towards Highly Efficient Electrocatalyst for Water Oxidation. *J. Mater. Chem. A* **2015**, *3*, 19314-19321.
(72) Jiang, J.; Zhang, A.; Li, L.; Ai, L. Nickel-Cobalt Layered Double Hydroxide Nanosheets as High-Performance Electrocatalyst for Oxygen Evolution Reaction. *J. Power Sources* **2015**, *278*, 445-451.
(73) Xiao, H.; Shin, H.; Goddard III, W. A. Synergy between Fe and Ni in the Optimal Performance of (Ni,Fe)OOH Catalysts for the Oxygen Evolution Reaction. *Proc. Natl. Acad. Sci.* **2018**, *115*, 5872-5877.
(74) Wang, J.; Gan, L.; Zhang, W.; Peng, Y.; Yu, H.; Yan, Q.; Xia, X.; Wang, X. In Situ Formation of Molecular Ni-Fe Active Sites on Heteroatom-Doped Graphene as a Heterogeneous Electrocatalyst toward Oxygen Evolution. *Sci. Adv.* **2018**, *4*, eaap7970.
(75) Zou, X.; Su, J.; Silva, R.; Goswami, A.; Sathe, B. R.; Asefa, T. Efficient Oxygen Evolution Reaction Catalyzed by Low-Density Ni-doped Co_3O_4 Nanomaterials Derived from Metal-Embedded Graphitic C_3N_4. *Chem. Commun.* **2013**, *49*, 7522-7524.

(76) Asnavandi, M.; Yin, Y.; Li, Y.; Sun, C.; Zhao, C. Promoting Oxygen Evolution Reactions through Introduction of Oxygen Vacancies to Benchmark NiFe-OOH Catalysts. *ACS Energy Lett.* **2018**, *3*, 1515-1520.
(77) Kong, Q.; Feng, W.; Zhang, Q.; Zhang, P.; Sun, Y.; Yin, Y.; Wang, Q.; Sun, C. Hybrid Amorphous/Crystalline FeNi (Oxy) Hydroxide Nanosheets for Enhanced Oxygen Evolution. *ChemCatChem* **2019**, *11*, 3004-3009.
(78)Rossmeisl, J.; Qu, Z.-W.; Zhu, H.; Kroes, G.-J.; Nørskov, J. K. Electrolysis of Water on Oxide Surfaces. *J. Electroanal. Chem.* **2007**, *607*, 83-89.
(79) Man, I. C.; Su, H. Y.; Calle-Vallejo, F.; Hansen, H. a.; Martínez, J. I.; Inoglu, N. G.; Kitchin, J.; Jaramillo, T. F.; Nørskov, J. K.; Rossmeisl, J. Universality in Oxygen Evolution Electrocatalysis on Oxide Surfaces. *ChemCatChem* **2011**, *3*, 1159-1165.
(80) Burke, M. S.; Enman, L. J.; Batchellor, A. S.; Zou, S.; Boettcher, S. W. Oxygen Evolution Reaction Electrocatalysis on Transition Metal Oxides and (Oxy)hydroxides: Activity Trends and Design Principles. *Chem. Mater.* **2015**, *27*, 7549-7558.
(81) Yin, Y.; Zhang, X.; Sun, C. Transition-Metal-Doped Fe_2O_3 Nanoparticles for Oxygen Evolution Reaction. *Prog. Nat. Sci.: Mater. Int.* **2018**, *28*, 430-436.
(82) Subbaraman, R.; Tripkovic, D.; Chang, K.-C.; Strmcnik, D.; Paulikas, A. P.; Hirunsit, P.; Chan, M.; Greeley, J.; Stamenkovic, V.; Markovic, N. M. Trends in Activity for the Water Electrolyser Reactions on 3d M(Ni,Co,Fe,Mn) Hydr(Oxy)Oxide Catalysts. *Nat. Mater.* **2012**, *11*, 550-557.
(83) Liao, P.; Keith, J. A.; Carter, E. A. Water Oxidation on Pure and Doped Hematite (0001) Surfaces: Prediction of Co and Ni as Effective Dopants for Electrocatalysis. *J. Am. Chem. Soc.* **2012**, *134*, 13296-13309.
(84) Cotton, F. A.; Wilkinson, G.; Murillo, C. A.; Bochmann, M.; Grimes, R. *Advanced Inorganic Chemistry*, John Wiley & Sons, New York, 6th edn, **1999**.
(85) Song, F.; Bai, L.; Moysiadou, A.; Lee, S.; Hu, C.; Liardet, L.; Hu, X. Transition Metal Oxides as Electrocatalysts for the Oxygen Evolution Reaction in Alkaline Solutions: An Application- Inspired Renaissance. *J. Am. Chem. Soc.* **2018**, *140*, 7748-7759.

****

Chapter 6

Exploring Iron Oxyhydroxide Nanorods for Sunlight Driven Photo-Fenton Catalysis

6.1 Introduction

In the 21st Century, environmental pollution has become a great concern to the living systems on the earth due to its adverse consequences. Among the various types of environmental pollutions, water pollution which upsurges with the civilization of the society, is the biggest threat not only to the aquatic lives but also has serious effect onto the human health.[1-5] Such upsurge in water pollution is majorly due to the urban discharges together with industrial effluents, mainly organic dyes immensely utilized in food processing and textile industries.[6] Organic dyes owing to have very complex structure are very harmful due to their toxicity and non-biodegradability.[7,8] Apart from the hazardous effects; they can also hamper the photosynthesis of aquatic plants. Therefore, it is necessary to degrade the organic dyes to minimize their dreadful impact on aqueous environment. Many approaches have been reported to treat dyes in wastewater, including sedimentation,[9] flocculation and coagulation,[10] biodegradation,[11] membrane separation,[12,13] advanced oxidation process[14,15] and adsorption methods.[16,17] Among all the approaches, advanced oxidation method functions as a robust and very effective way to degrade organic dyes. In wastewater treatment, different advanced oxidation processes, such as photocatalysis,[18,19] electrochemical catalysis[20] and Fenton/photo-Fenton process[21,22] have gained considerable attention from the researchers. Fenton and photo-Fenton process are unanimously used procedure/technique to oxidize the organic pollutants by generating the transient species (•OH).[23] In Fenton reaction, •OH radical produced from the decomposition of H_2O_2, played a vital role during the treatment of refractory pollutants.[24,25] Alternatively, iron was cycling between Fe^{2+} and Fe^{3+} under irradiation of light in case of photo-Fenton reaction and H_2O_2 was more

effortlessly transformed to •OH than that of Fenton reaction.[26,27] Therefore, to overcome the short coming of slow dynamics of the conventional Fenton process, photo-Fenton reaction is consider to be a smart way for the degradation of different organic dyes.

To date, there are many catalysts reported for heterogeneous photo-Fenton reactions, however, metal oxides are one of the most explored classes of photocatalytic materials from both the fundamental and technological point of view. Among the various photo-Fenton catalysts, iron-based materials, such as oxides,[28,29] sulfides,[30] carbide,[31] and composite materials[32,33] demonstrate good photocatalytic activity. Iron oxides are non-hazardous, eco-friendly and earth abundant materials and can be prepared in the laboratory easily.[34,35] Thus, development of iron oxide materials for photocatalysis is very simple and cost effective. Earlier studies illustrated that iron oxides are very promising catalysts for heterogeneous Fenton-like processes. β-phase of iron oxyhydroxides (FeOOH), commonly known as akaganeite, has withdrawn enormous interests to the researchers because of their biocompatibility along with abundances in nature. Additionally, they can efficiently harvest visible light in solar spectrum due to their semiconducting property. However, synthesis of such nanomaterials having high photocatalytic activity and stability is very challenging. Although several reports demonstrated the synthesis of β-FeOOH via various routes,[36,37] however, fabrication of β-FeOOH via a simple low temperature light assisted process might be an attractive pathway because of its simplicity and effectiveness.

In this chapter, a simple route was established to synthesize iron oxyhydroxide (β-FeOOH) nanorods without employing any templating agent via a light driven hydrolysis route. After characterization of the synthesized nanorods by different physical techniques, we have explored them as a photo-Fenton catalyst and investigated their photocatalytic activity in presence of H_2O_2 under sunlight. To understand the photocatalytic performance of β-FeOOH nanorods, we have chosen methylene blue (MB) and rhodamine B (RhB) as model refractory pollutants. We have also altered the reaction parameters including pH of the solution and concentration of H_2O_2 to realize the effect

onto their photocatalytic activity. Additionally, excellent photocatalytic efficacy along with structural durability and stability has been discussed for β-FeOOH nanorods.

6.2 Experimental Section

6.2.1 Preparation of Iron Oxyhydroxide Nanorods

The iron oxyhydroxide nanorods (FeOOH NRs) were prepared based on a simple and facile light-assisted hydrothermal technique[38] in absence of any templating molecule. First, 1.0 mmol of iron(III) chloride ($FeCl_3$) and 2.5 mmol of urea were dissolved in 10 mL of Millipore water in a beaker. Then the whole solution mixture was transferred to a glass vial and closed the vial tightly. Afterward, the vial was kept for 24 h under visible light and the reaction temperature of the solution was maintained to 90 °C. Once the reaction was over, the vial was allowed to reach to the room temperature and the product was collected through centrifugation. The obtained product was washed properly by plenty of Millipore water to remove any unreacted urea or $FeCl_3$ if any and then dried in air. After proper air drying, the as-synthesized material was characterized by different techniques and explored as photocatalyst for photo-Fenton reaction, shown in Scheme 1.

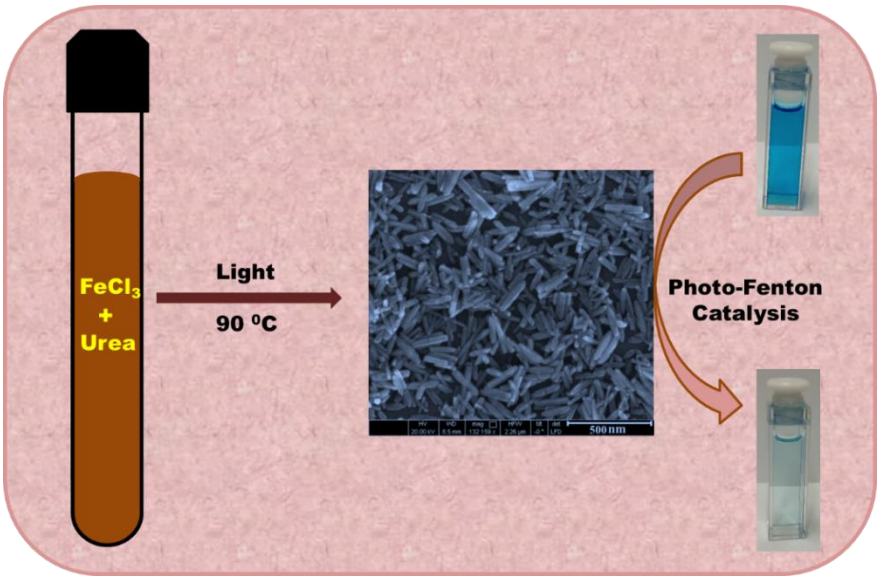

Scheme 6.1: Schematic representation of the synthesis of β-FeOOH nanorods, followed by the exploration as a photocatalyst for photo-Fenton reaction.

6.2.2 Photo-Fenton Reaction

We have examined the photocatalytic activity of β-FeOOH nanorods by measuring the absorbance of the irradiated dye solution during the degradation of the aqueous solution of two different dyes under sun light. All the reactions were performed in a cylindrical reactor vessel (50 mL) and, made of borosilicate glass reactor with a cooling water jacket. During the photocatalysis, we have placed the reactor in solar radiation under stirring condition. The temperature for degradation was upheld to 25 °C throughout the experiment via circulating cold water. The photocatalytic degradation of the aqueous solution of methylene blue (MB) and rhodamine B (RhB) was checked as a function of time by measuring the absorbance of the irradiated solution with the help of UV–vis spectrophotometer. Before exposing the dye to solar light irradiation, the FeOOH NRs having concentration of 0.25 g L^{-1} were added to the aqueous solution of dye (20 mL, 10 mg L^{-1} and pH 3). The reaction mixture was then shaken well and kept in dark for 2 hours to attain an adsorption/desorption equilibrium. After the equilibrium, the initial concentration of the dye (C_0) was measured and then 50 mM of H_2O_2 was added into this reaction solution immediately and subsequently exposed to the solar light irradiation. To calculate the residual dye concentration, 3.0 mL of the dye solution was collected from the glass reactor at a specific time duration and used the solution for absorbance measurement. Before recording the spectrum, the photocatalyst was separated from the reaction solution via centrifugation each time. Once the absorbance spectrum of the dye solution was recorded, it was then transferred back into the reactor. Afterwards, the absorption spectra of solar light exposed MB have been quantitatively evaluated at 664 nm with a definite time interval during the degradation process. Likewise, absorption spectrum for RhB was considered at 554 nm for its degradation study. To check the photocatalytic activity at different pH, the pH of the dye solution was adjusted by using H_2SO_4 and NaOH solution. The % of degradation of dyes was determined as the following: % of degradation = $[(C_0 - C_t)/C_0] \times 100$; where C_0 is initial dye concentration and C_t is concentration of dye after solar light irradiation at a time t.

6.3 Results and Discussion

6.3.1 Characterization of Iron Oxyhydroxide (FeOOH) Nanorods

6.3.1.1 FESEM Images of Iron Oxyhydroxide (FeOOH) Nanorods

Iron oxyhydroxides (FeOOH) are achieved based on a simple light-assisted hydrothermal technique without the presence of any templating molecule, where urea functions as a hydrolyzing agent. The size and shape of the as-prepared FeOOH was visualized by FESEM analysis. Figure 6.1.A-C display FESEM images of FeOOH NRs at different magnifications, which demonstrate the formation of FeOOH nanorods under the present synthetic condition.

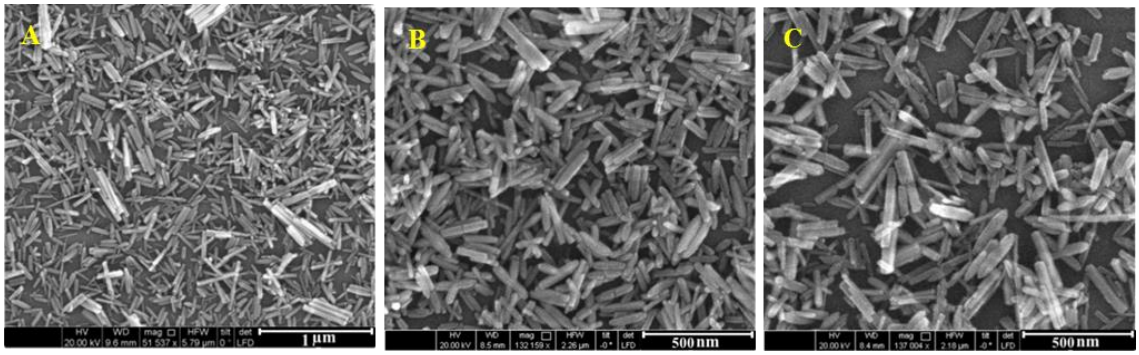

Figure 6.1: (A-C) FESEM micrographs of FeOOH NRs at different magnifications.

6.3.1.2 TEM and EDS Analyses of Iron Oxyhydroxide (FeOOH) Nanorods

We have also performed TEM and HRTEM analyzes of the nanorods. Figure 6.2.A-C represent TEM images of FeOOH NRs, having length ~250 nm and diameter of ~ 40 nm. TEM micrograph of a single FeOOH nanorod is presented in Figure 6.2.C. HRTEM images of this single FeOOH NR at diverse magnifications have been presented in Figure 6.2.D-F. The clear lattice fringes having spacing of 0.53 nm corroborate to the (200) plane of β-FeOOH NR. We have carried out EDS analysis on FeOOH NRs. EDS spectrum of the nanorods was presented in Figure 6.3, which corroborates to the presence of Fe and O in the nanorods.

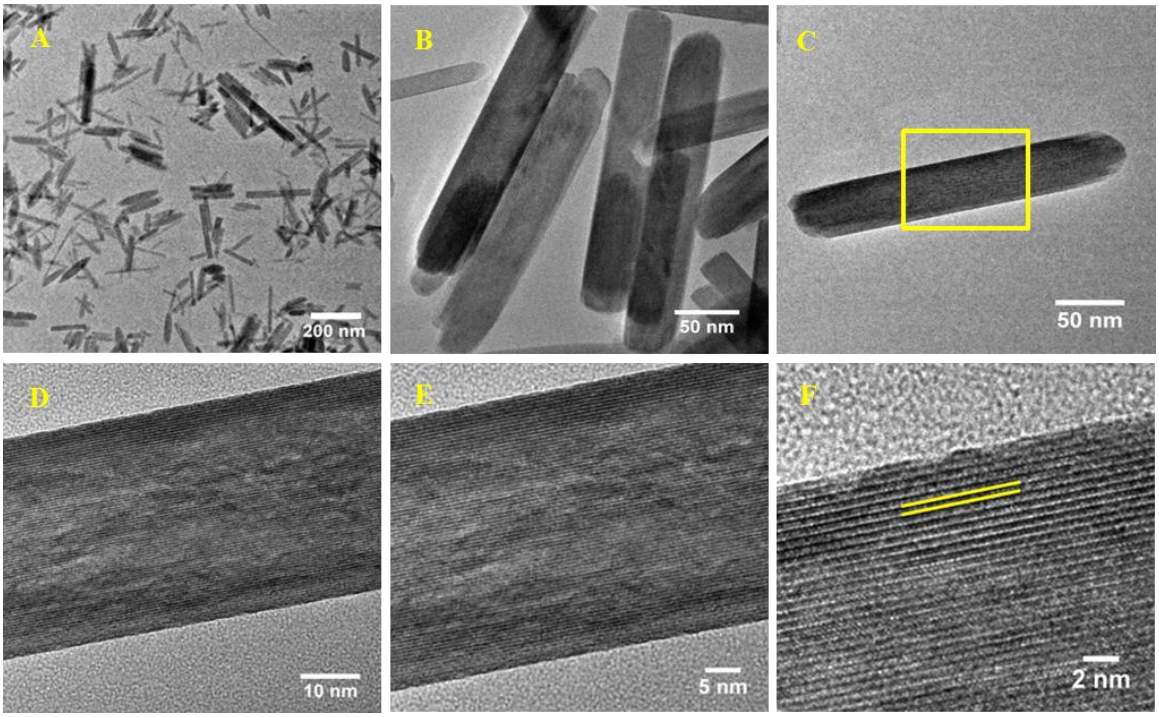

Figure 6.2: (A-C) TEM images of FeOOH NRs at different magnifications. (C) TEM image of a single FeOOH nanorod. (D-F) HRTEM images of FeOOH NRs at diverse magnifications.

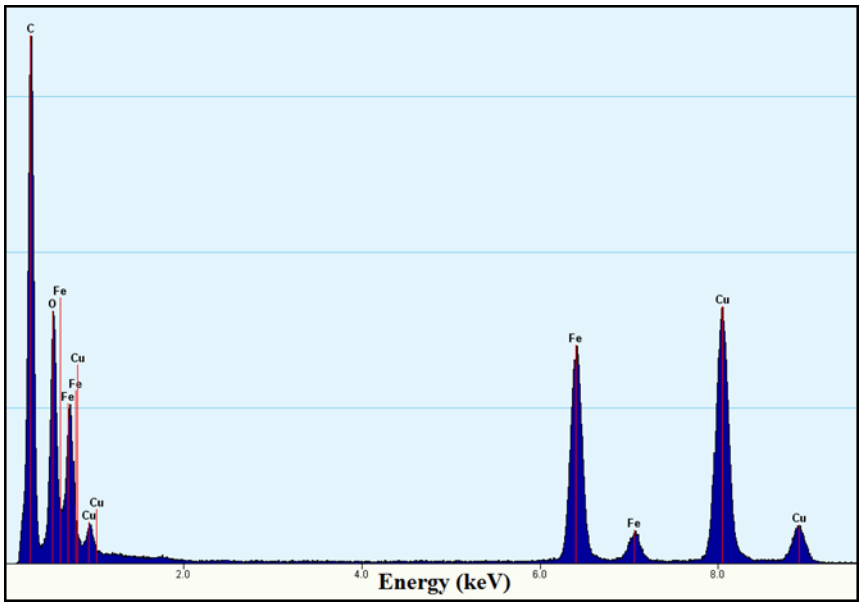

Figure 6.3: EDS spectrum of β-FeOOH nanorods, indicating the presence of Fe and O.

6.3.1.3 XRD Study

The crystal structure of the as-prepared FeOOH NRs was investigated by X-ray diffraction (XRD) analysis (Figure 6.4). All the observed diffraction peaks could be well assigned to the pure tetragonal β-FeOOH phase (JCPDS no. 34-1266). No other characteristics peaks were observed for any kind of impurities. All the sharp peaks observed in the XRD patterns suggest well crystallization of the β-FeOOH NRs.

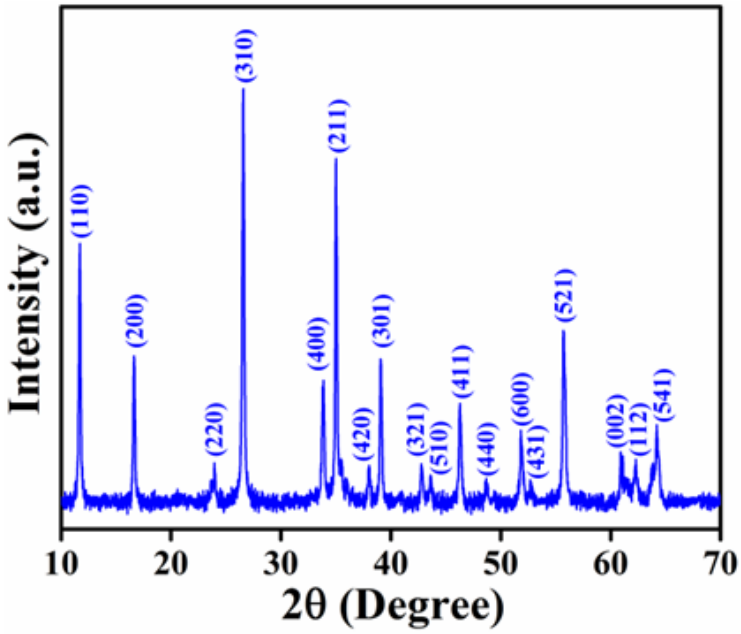

Figure 6.4: XRD pattern of the nanorods, indicating pure tetragonal β-FeOOH phase.

6.3.1.4 FTIR Analysis

FTIR spectrum of β-FeOOH NRs illustrates the presence of several bands at 3380, 1630 and 1390 cm^{-1}, which can be attributed to the O-H stretching vibrations of absorbed water molecules or structural OH groups of NRs (Figure 6.5).[39] Additionally, two more peaks observed at 688 and 846 cm^{-1} are due to Fe-O vibrational modes of β-FeOOH.[40]

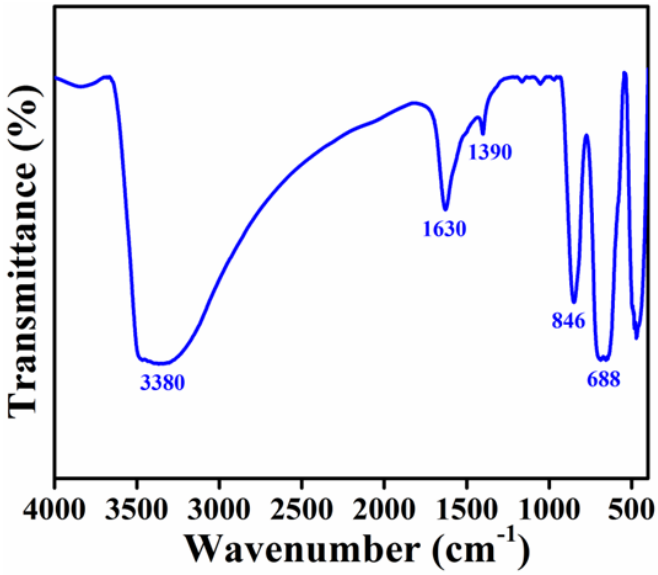

Figure 6.5: FTIR spectrum of β-FeOOH NRs nanorods, indicating the presence of structural OH groups.

6.3.1.5 BET Surface Area Measurement

N_2 adsorption/desorption analysis of the NRs was also carried out at 77 K to evaluate the specific surface area (Figure 6.6). The specific surface area has been found to be 55 m^2g^{-1} for β-FeOOH NRs estimated using Brunauer- Emmett-Teller (BET) method.

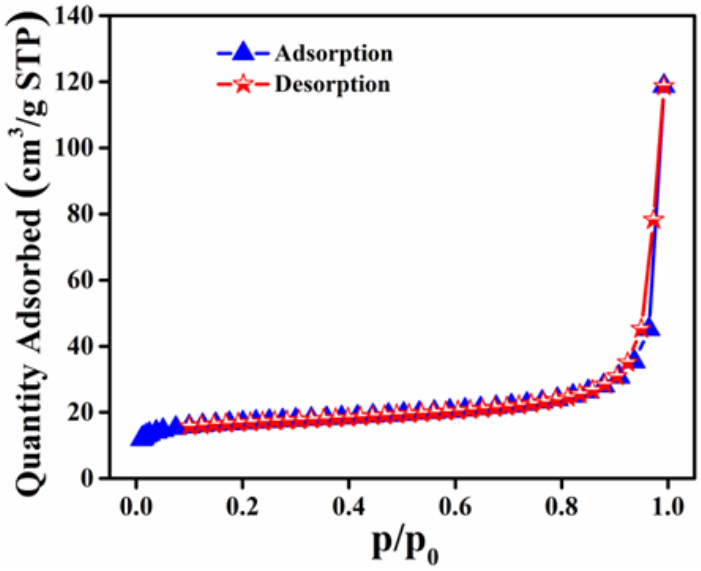

Figure 6.6: Nitrogen adsorption/desorption isotherms of β-FeOOH NRs.

6.3.1.6 UV-visible Diffuse Reflectance Study and Band Gap Calculation

The optical absorption property of β-FeOOH NRs was further established by performing their UV-vis DRS analysis, shown in Figure 6.7.A. The band gap energy (E_g) of β-FeOOH NRs has been estimated according to the following formula:[41,42] $\alpha h\nu = A (h\nu - E_g)^{1/2}$, where α, h, ν, E_g, and A are the absorption coefficient, Planck's constant, light frequency, the band gap energy and a constant respectively. We have then calculated the E_g for β-FeOOH NRs, which has been found to be 2.06 eV (Figure 6.7.B). This is in accordance with the reported result.[43]

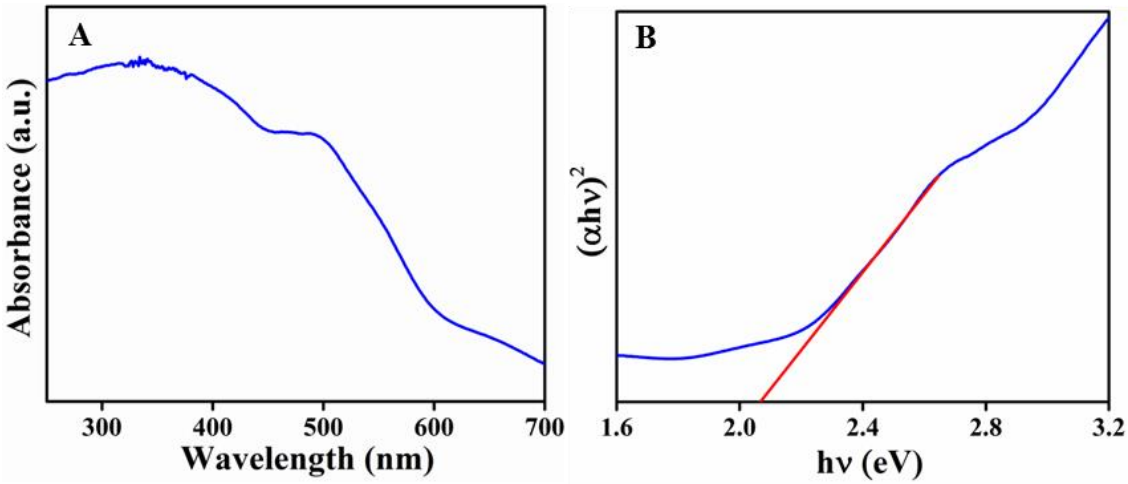

Figure 6.7: (A) UV-vis diffuse-reflectance spectra of the β-FeOOH NRs and (B) Plot of $(\alpha h\nu)^2$ versus hν for the β-FeOOH nanorods to calculate the band gap energy.

6.3.2 Photocatalytic Activity of Iron Oxyhydroxide Nanorods

6.3.2.1 Degradation of Organic Dyes

The photocatalytic efficacy of β-FeOOH NRs towards the degradation of organic dyes was studied under solar light irradiation. For this purpose, we have taken methylene blue (MB) and Rhodamine B (RhB) as model pollutants. After reaching the adsorption-desorption equilibrium, dye solution was irradiated under sunlight in presence of H_2O_2 and the UV-visible absorption spectra of the dye solution was recorded as a function of

irradiated time during the photo degradation process. The time dependent degradation of MB by β-FeOOH NRs at pH 3 is presented in Figure 6.8.A. During the degradation process, the color of MB solution progressively transformed from blue to pale blue and finally became colorless. Keeping the irradiation time unaltered, we also examined photocatalytic efficacy of β-FeOOH NRs in different reaction conditions. We observed that there was almost no degradation of MB in presence of only β-FeOOH NRs under solar light (Figure 6.8.B) but the degradation efficiency of β-FeOOH NRs increased to approximately 100% within 60 min in presence of H_2O_2 under sunlight. However, in presence of both β-FeOOH NRs and H_2O_2 under dark condition, the degradation of MB was estimated to be almost 8%. Similarly, upon exposure of sunlight on RhB solution, the bright red aqueous solution of RhB gradually faded away and finally turned out to be colorless in about 100 min (Figure 6.9). In photo-Fenton reaction, the synergistic effect of sunlight and H_2O_2 facilitates the formation of enormous amount of hydroxyl radicals (•OH) that boost the dye degradation process.

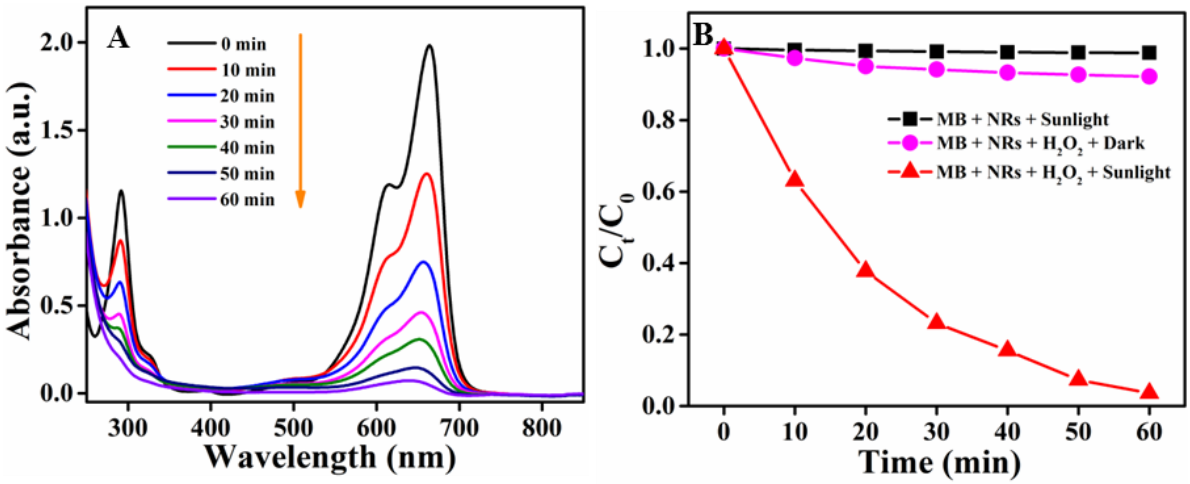

Figure 6.8: (A) Time-dependent UV-vis absorption spectra of aqueous solution of MB during photodegradation using β-FeOOH NRs as catalysts in presence of H_2O_2 under irradiation of sunlight. (B) Degradation efficiency towards MB in different reaction conditions.

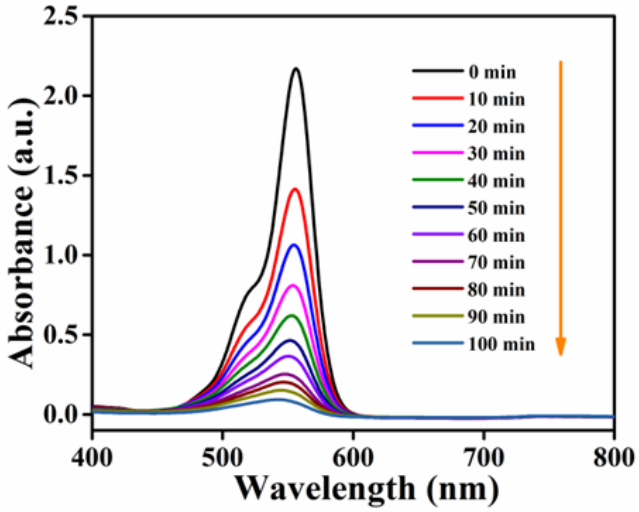

Figure 6.9: Time-dependent UV-visible absorption spectra of RhB in photodegradation process under irradiation of sunlight using β-FeOOH NRs as catalysts in presence of H_2O_2.

6.3.2.2 Kinetics of the Degradation Reaction

Langmuir-Hinshelwood (LH) kinetics is the most frequently used kinetic expression to describe the kinetics of the heterogeneous catalytic processes.[44,45] The expression is given by:

$$r = - dC/dt = k_r K_e C/(1+K_e C) \qquad (1)$$

where, r represents the rate of reaction that changes with time. C is the concentration (mg L^{-1}) of the dye solution which is being degraded, k_r and K_e are the reaction rate constant (mg L^{-1} min^{-1}) and equilibrium constant (L mg^{-1}) for the adsorption of the dye molecules on the catalyst surface respectively. The term $k_r K_e$ is considered as k (min^{-1}). Thus, the equation (1) can be written as:

$$-dC/dt = kC /(1+K_e C) \qquad (2)$$

When the chemical concentration C is a millimolar solution (for small C, $K_e C < 1$), equation (2) can be simplified to an apparent first-order equation.

Then, $-dC/dt = kC$ Or, $-dC/C = kdt$ (3)

Equation (3) can be integrated between the limits: $C = C_0$ at $t = 0$ and $C = C_t$ at $t = t$. The integrated expression is given by: $\ln(C_0/C_t) = kt$. Thus, the kinetics of photo-Fenton reaction using β-FeOOH NRs was further illustrated under solar light irradiation based on the above pseudo-first-order kinetic model: $\ln(C_0/C_t) = kt$;[46] where C_0 was the initial concentration of the dye and C_t was the concentration of dye at the degradation time t, and k was the reaction rate constant. It was observed that the degradation of the dyes followed the pseudo-first-order kinetic model (Figure 6.10) and the corresponding rate constants of the degradation of each dye were evaluated. Degradation time, percentage of degradation and the first-order rate constants for each dye have been shown in Table 6.1.

Table 6.1: The summary of degradation time and percentage of degradation of two different dyes using β-FeOOH NRs under irradiation of sun light with the corresponding rate constant evaluated using pseudo-first-order kinetic model.

Catalyst	Name of Dye	Degradation Time (min)	% of Degradation	First-Order Rate Constant (k, min^{-1})
β-FeOOH NRs	MB	60	97	0.05409
	RhB	100	96	0.02956

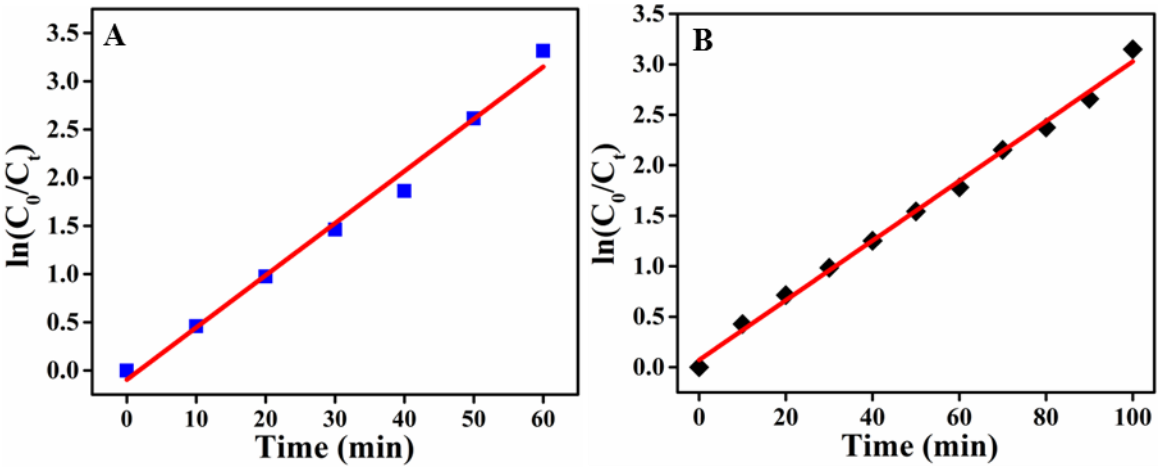

Figure 6.10: Rate of degradation of (A) MB and (B) RhB using β-FeOOH NRs as photocatalyst.

6.3.2.3 Effect of Different Experimental Parameters during the Photo-Fenton Reaction of MB

Generally, in photo-Fenton reaction, catalyst dose, solution pH and concentration of H_2O_2 impart very significant roles. We have optimized each parameter.

6.3.2.3.1 Effect of Catalyst Dosages

In order to estimate the optimum catalyst dose, the degradation reaction was performed by changing the dosages of catalyst. After performing the reaction with different dosages of β-FeOOH NRs, the catalyst dose was optimized and found to be 0.25 g L^{-1} for this photo-Fenton reaction (Figure 6.11). Beyond a certain catalyst dose, excessive amount of catalyst makes reaction solution turbid and blocks light irradiation and thus leading to the decrease in MB degradation efficiency.

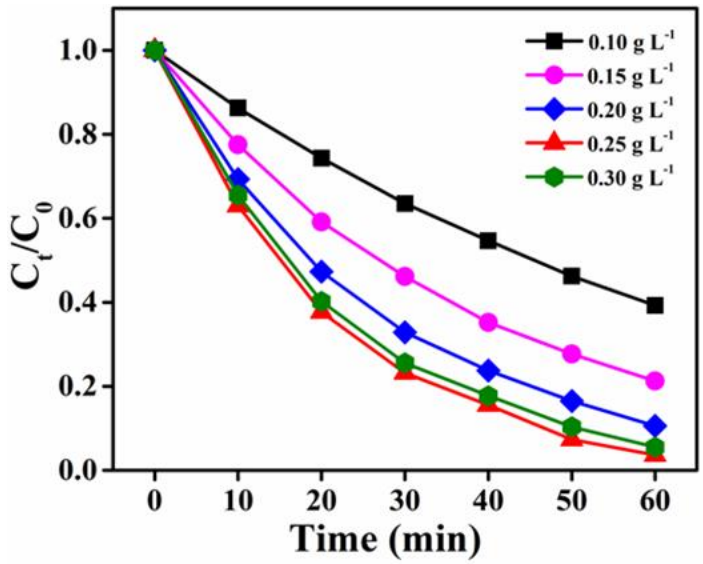

Figure 6.11: Effect of catalyst dose on the degradation efficiency of MB using β-FeOOH NRs.

6.3.2.3.2 Effect of Solution pH

The photocatalytic activity of β-FeOOH NRs was studied against varied pH of the dye solution (Figure 6.12). It was found that the photocatalytic activity decreased with the

increase in pH value. This is probably owing to the formation of small amount of •OH radicals at high solution pH in the course of photo-Fenton process.[47] Moreover, the surface of the catalyst would gradually be deprotonated with increasing solution pH, which in turn lowered the adsorption of MB over NRs surfaces.[48]

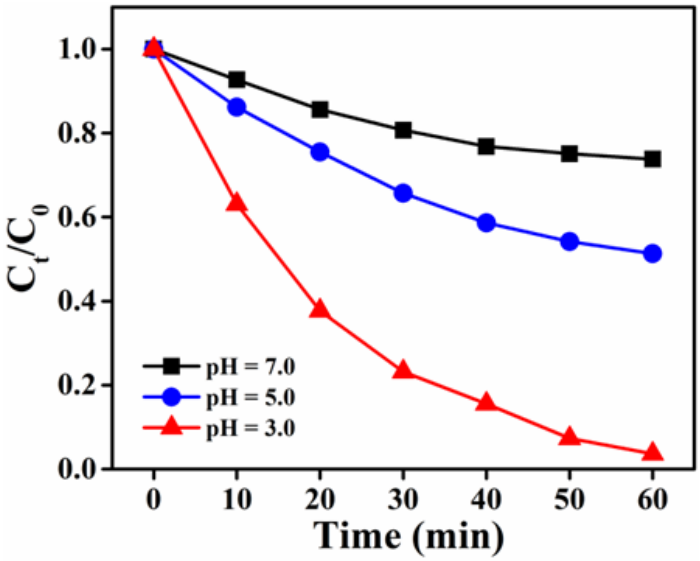

Figure 6.12: Effect of solution pH on the photocatalytic activity of β-FeOOH NRs towards MB degradation.

6.3.2.3.3 Effect of Concentration of H_2O_2

Likewise, the photocatalytic activity of β-FeOOH NRs was evaluated as a function of H_2O_2 concentration, resulting in an increase in degradation rate with increasing H_2O_2 concentration up to 50 mM, as shown in Figure 6.13. Interestingly, the rate of degradation was significantly dropped with further increasing in concentration of H_2O_2 to 70 mM. This is possibly attributed to the scavenging effect of the hydroxyl radicals.[49,50] In presence of excessive H_2O_2, •OH radicals produce hydroperoxyl (•OOH) radicals, which don't participate in the degradation reaction owing to their much lower oxidation capacity.[51]

$$\bullet OH + H_2O_2 \longrightarrow H_2O + \bullet OOH$$

$$\bullet OH + \bullet OOH \longrightarrow H_2O + O_2$$

Basically, these auto-generated •OOH radicals were responsible in lowering the degradation efficacy of a catalyst, as they possessed much lesser oxidation potentials compared to •OH radical.[52] Additionally, excessive H_2O_2 may adsorb over the surface of the catalyst and thus inhibits the adsorption of MB, resulting in decrease in degradation efficacy of the catalyst. Hence, it is necessary to find out the optimal concentration of H_2O_2 to enhance the degradation, beyond which it lowers the degradation efficacy of a catalyst. The threshold concentration of H_2O_2 for this particular degradation reaction was estimated to be 50 mM under mentioned reaction conditions.

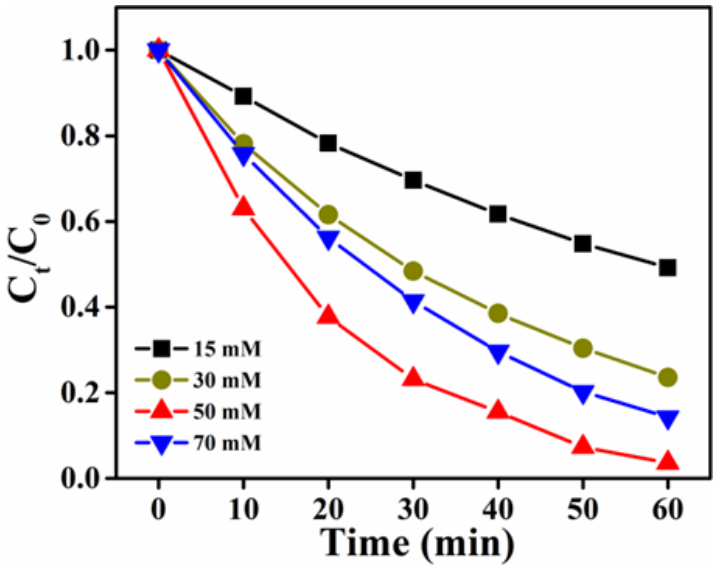

Figure 6.13: Effect of concentration of H_2O_2 on the photocatalytic activity of β-FeOOH NRs towards MB degradation.

6.3.2.4 Recyclability of β-FeOOH NRs

To demonstrate the recyclability of β-FeOOH NRs, they have been used repetitively for dye degradation reaction (Figure 6.14). After every use, the photocatalyst was easily

recovered via centrifugation from the reaction solution and further employed for the next cycle. A reasonably good degradation efficacy of β-FeOOH NRs was noticed even after several usages, further demonstrating the exceptional advantage of utilization of β-FeOOH NRs as photocatalyst from the effective separation and recycling point of view.

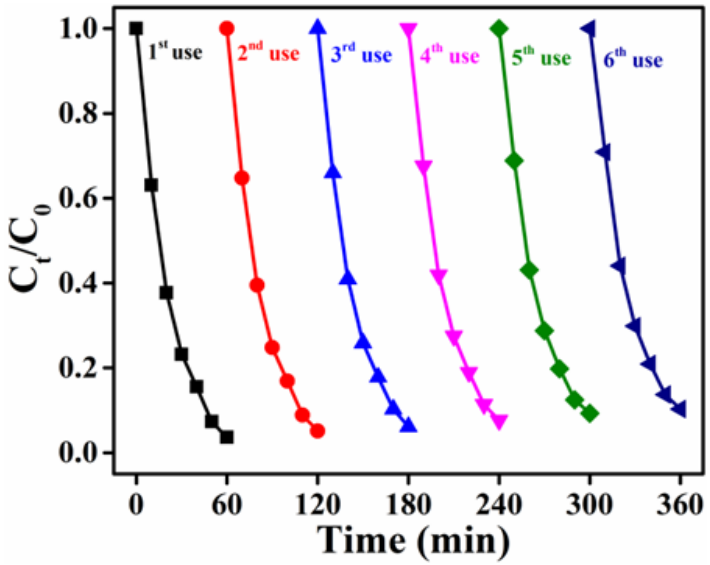

Figure 6.14: Multi-cycles degradation efficacy of β-FeOOH NRs during the degradation of MB under irradiation of sunlight.

6.3.2.5 Characterization of the Catalyst after Photocatalysis

After the end of the photocatalytic reactions, we have performed the FESEM and TEM analysis of the catalyst to check their morphology change if occurs. However, all the micrographs indicate their unaltered morphology even after reuse (Figure 6.15). Apart from these analyses, we have also carried out XRD analysis to specify whether there is any structural change of the NRs. Interestingly, XRD pattern of the NRs after photocatalysis (Figure 6.16) is analogous to the fresh catalysts, with no alternation of their crystal structure, which again demonstrates their excellent durability and stability.

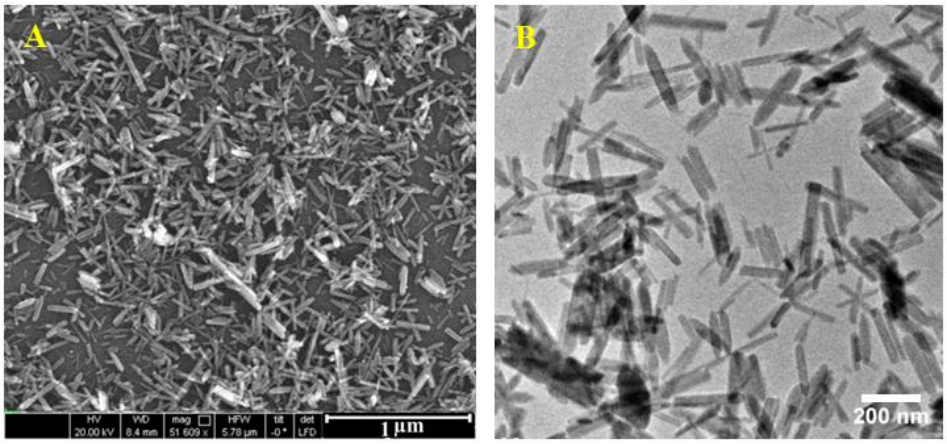

Figure 6.15: (A) FESEM and (B) TEM images of β-FeOOH NRs after photocatalysis.

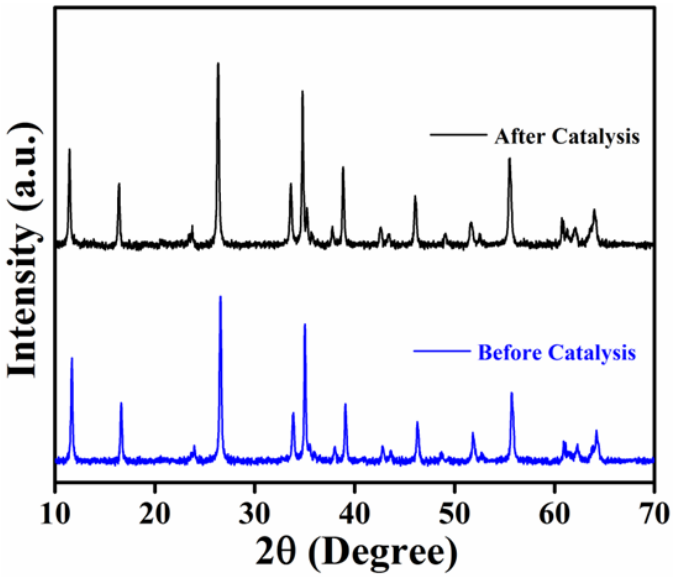

Figure 6.16: XRD patterns of β-FeOOH NRs before and after photocatalysis.

6.3.2.6 Comparison of Catalytic Efficiency of β-FeOOH NRs

Finally, catalytic efficacy of β-FeOOH NRs was compared in associated with the reported oxide based photocatalysts for the dye degradation (presented in Table 6.2), substantiating much higher catalytic performance of the β-FeOOH NRs.

Table 6.2: Comparison of the degradation efficiency of β-FeOOH NRs with other reported oxide based photocatalysts for the degradation of methylene blue.

Catalysts	Irradiation time (min)	Degradation efficiency (%)	References
CeO_2/V_2O_5	300	76.9	53
CeO_2/CuO	300	85.7	53
Bi_2O_3-RGO	240	96	54
Fe-doped CeO_2	180	80	55
$CoFe_2O_4$	140	80	56
RGO/Fe_3O_4	120	96	57
β-MnO_2	120	90.2	58
Ag/Cu_2O	120	96.5	59
RGO/Ag/TiO_2-nanotubes/Ti plates	120	89	60
α-Fe_2O_3/HNTs	120	88	61
$CuFe_2O_4$	80	92.1	62
Si–Al/α-FeOOH	60	72	63
β-FeOOH	**60**	**97**	**Present work**

6.3.2.7 Degradation Mechanism

The dye degradation reaction using β-FeOOH NRs under solar light irradiation proceeds via photo-generated reactive oxygen species (ROS), mainly hydroxyl (•OH) radicals, a superoxide ($\bullet O_2^-$) radicals and holes (h^+).[64,65] Basically, due to irradiation of solar light onto the semiconductor photocatalysts, electrons in valence band (VB) get excited and move to the conduction band (CB), resulting in the formation holes in VB. These photo-generated holes (h^+) and electrons (e^-) function as primary reactive species and take part directly or indirectly in the degradation process through redox reactions.[66] The proposed

dye degradation mechanism using β-FeOOH NRs under solar light irradiation via photo-generated reactive oxygen species is illustrated in Figure 6.17.

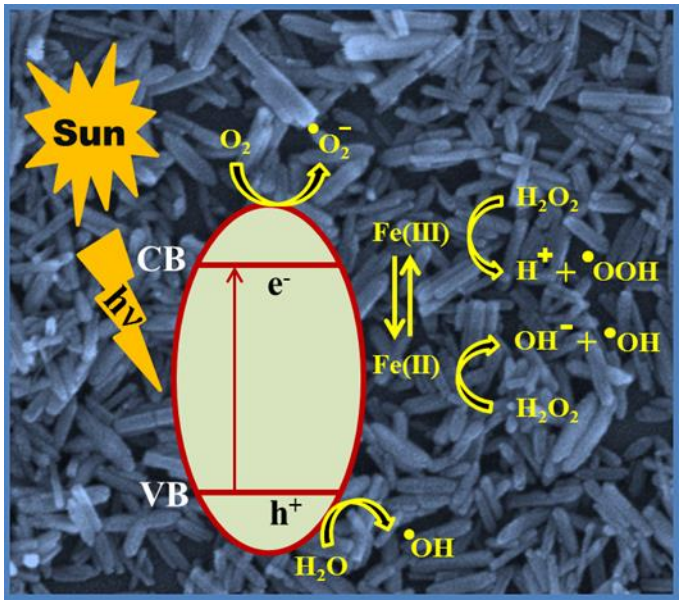

Figure 6.17: The proposed dye degradation mechanism using β-FeOOH NRs under solar light irradiation via photo-generated reactive oxygen species.

The photo-generated h^+ directly acts as an oxidant during the degradation of the pollutant, whereas electrons (e^-) react with O_2 present in the aqueous solution produce $\bullet O_2^-$ radicals. Usually in photo-Fenton reaction, •OH radicals are produced due to the transfer of electrons between Fe(II)/Fe(III) and H_2O_2.[67]

$$Fe(III) + H_2O_2 \longrightarrow Fe(II) + H^+ + \bullet OOH$$

$$Fe(II) + H_2O_2 \longrightarrow Fe(III) + OH^- + \bullet OH$$

These photo-generated •OH radicals take part in dye degradation and are mainly responsible in enhancing the degradation process. To confirm the generation of •OH radicals, we performed the degradation process in presence of tert-butyl alcohol (t-BA), which acts as •OH radical scavenger.[18,68,69] In presence of t-BA, the degradation rate of

MB was drastically reduced (Figure 6.18). Thus, insights into the dye degradation using iron oxides based materials further points to the fundamental significance in understanding the photocatalysis and at the same time extend a broad applicability of naturally-occurring such semiconducting nanomaterials.

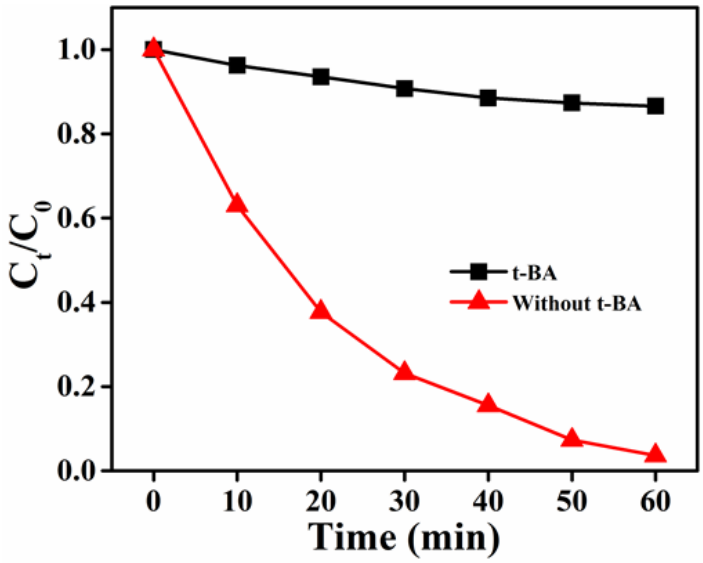

Figure 6.18: Effect of tert-butyl alcohol (t-BA) on the degradation efficiency of β-FeOOH nanorods during MB degradation.

6.4 Conclusions

In summary, we have described a facile route to synthesize iron oxide nanorods without employing any templating agent via a light driven hydrolysis route. After characterization of synthesized nanorods by different physical techniques, the photocatalytic activity of as-synthesized β-FeOOH nanorods was explored as a photo-Fenton catalyst under sunlight. Methylene blue (MB) and rhodamine B (RhB) were chosen as model refractory pollutants to demonstrate the photocatalytic performance of β-FeOOH nanorods. The effect of pH of the solution together with concentration of H_2O_2 on their photocatalytic activity has also been demonstrated. The overall dye degradation under solar light irradiation using β-FeOOH NRs proceeds via photo-generated reactive oxygen species. Our approach thus points to an excellent photo-catalytic activity of β-FeOOH nanorods

during the photo-Fenton reaction. This work offers an environmentally friendly and cost-effective way in developing highly active photocatalytic nanomaterials to combat with environmental pollutants.

6.5 References

(1) Hoffmann, M. R.; Martin, S. T.; Choi, W.; Bahnemann, D. W. Environmental Applications of Semiconductor Photocatalysis. *Chem. Rev.* **1995**, *95*, 69−96.
(2) Schwarzenbach, R. P.; Egli, T.; Hofstetter, T. B.; Von Gunten, U.; Wehrli, B. Global Water Pollution and Human Health. *Annu. Rev. Environ. Resour.* **2010**, *35*, 109−136.
(3) Sires, I.; Brillas, E. Remediation of Water Pollution Caused by Pharmaceutical Residues Based on Electrochemical Separation and Degradation Technologies: A Review. *Environ. Int.* **2012**, *40*, 212−229.
(4) Qian, J.; Gao, X.; Pan, B. Nanoconfinement-Mediated Water Treatment: From Fundamental to Application. *Environ. Sci. Technol.* **2020**, *54*, 8509-8526.
(5) Dong, S.; Feng, J.; Fan, M.; Pi, Y.; Hu, L.; Han, X.; Liu, M.; Sun, J.; Sun, J. Recent Developments in Heterogeneous Photocatalytic Water Treatment using Visible Light-Responsive Photocatalysts: A Review. *RSC Adv.* **2015**, *5*, 14610-14630.
(6) Mills, A.; Davies, R. H.; Worsley, D. Water Purification by Semiconductor Photocatalysis. *Chem. Soc. Rev.* **1993**, *22*, 417−425.
(7) Grau, P. Textile Industry Wastewater Treatment. *Water Sci. Technol.* **1991**, *24*, 97−103.
(8) Sanjini, N. S.; Velmathi, S. Photocatalytic Degradation of Rhodamine B by Mesoporous Ti-KIT-6 under UV Light and Solar Light Irradiation. *J. Porous Mater.* **2015**, *22*, 1549−1558.
(9) Weber, E. J.; Adams, R. L. Chemical- and Sediment-Mediated Reduction of the Azo Dye Disperse Blue 79. *Environ. Sci. Technol.* **1995**, *29*, 1163−1170.
(10) Steplin, S. S. P.; Radhika, N.; Borang, O.; Lydia, I. S.; Merlin, J. P. Visible Light Driven Photodegradation of Rhodamine B using Cysteine Capped ZnO/GO Nanocomposite as Photocatalyst. *J. Mater. Sci.: Mater. Electron.* **2017**, *28*, 6722−6730.
(11) Guo, J.; Yuan, S.; Jiang, W.; Yue, H.; Cui, Z.; Liang, B. Adsorption and Photocatalytic Degradation Behaviors of Rhodamine Dyes on Surface-Fluorinated TiO_2 under Visible Irradiation. *RSC Adv.* **2016**, *6*, 4090−4100.
(12) Zhao, R.; Wang, Y.; Li, X.; Sun, B.; Wang, C. Synthesis of β-Cyclodextrin-Based Electrospun Nanofiber Membranes for Highly Efficient Adsorption and Separation of Methylene Blue. *ACS Appl. Mater. Interfaces* **2015**, *7*, 26649−26657.

(13) Luan, J.; Hou, P. X.; Liu, C.; Shi, C.; Li, G. X.; Cheng, H. M. Efficient Adsorption of Organic Dyes on a Flexible Single-Wall Carbon Nanotube Film. *J. Mater. Chem. A* **2016**, *4*, 1191−1194.

(14) Song, S.; Wang, Y.; Shen, H.; Zhang, J.; Mo, H.; Xie, J.; Zhou, N.; Shen, J. Ultrasmall Graphene Oxide Modified with Fe_3O_4 Nanoparticles as a Fenton-Like Agent for Methylene Blue Degradation. *ACS Appl. Nano Mater.* **2019**, *2*, 7074−7084.

(15) Ismael, M.; Wu, Y. A Facile Synthesis Method for Fabrication of $LaFeO_3/gC_3N_4$ Nanocomposite as Efficient Visible-Light-Driven Photocatalyst for Photodegradation of RhB and 4-CP. *New J. Chem.* **2019**, *43*, 13783−13793.

(16) Kimling, M. C.; Chen, D.; Caruso, R. A. Temperature-Induced Modulation of Mesopore Size in Hierarchically Porous Amorphous TiO_2/ZrO_2 Beads for Improved Dye Adsorption Capacity. *J. Mater. Chem. A* **2015**, *3*, 3768−3776.

(17) Huang, L.; He, M.; Chen, B.; Cheng, Q.; Hu, B. Facile Green Synthesis of Magnetic Porous Organic Polymers for Rapid Removal and Separation of Methylene Blue. *ACS Sustainable Chem. Eng.* **2017**, *5*, 4050−4055.

(18) Das, S.; Samanta, A.; Jana, S. Light-Assisted Synthesis of Hierarchical Flower-Like MnO_2 Nanocomposites with Solar Light Induced Enhanced Photocatalytic Activity. *ACS Sustainable Chem. Eng.* **2017**, *5*, 9086−9094.

(19) Yu, C. L.; Li, G.; Kumar, S.; Yang, K.; Jin, R. C. Phase Transformation Synthesis of Novel Ag_2O/Ag_2CO_3 Heterostructures with High Visible Light Efficiency in Photocatalytic Degradation of Pollutants. *Adv. Mater.* **2014**, *26*, 892−898.

(20) Yang, Y.; Li, J. X.; Wang, H.; Song, X. K.; Wang, T. H.; He, B. Q.; Liang, X. P.; Ngo, H. H. An Electrocatalytic Membrane Reactor with Self-Cleaning Function for Industrial Wastewater Treatment. *Angew. Chem. Int. Ed.* **2011**, *50*, 2148−2150.

(21) Tusar, N. N.; Maucec, D.; Rangus, M.; Arcon, I.; Mazaj, M.; Cotman, M.; Pintar, A.; Kaucic, V. Manganese Functionalized Silicate Nanoparticles as a Fenton-type Catalyst for Water Purification by Advanced Oxidation Processes (AOP). *Adv. Funct. Mater.* **2012**, *22*, 820−826.

(22) Vu, T. A.; Le, G. H.; Dao, C. D.; Dang, L. Q.; Nguyen, K. T.; Dang, P. T.; Tran, H. T.; Duong, Q. T.; Nguyen, T. V.; Lee, G. D. Isomorphous Substitution of Cr by Fe in MIL-101 Framework and Its Application as a Novel Heterogeneous Photo-Fenton Catalyst for Reactive Dye Degradation. *RSC Adv.* **2014**, *4*, 41185−41194.

(23) Zhang, Y.; Zhang, N.; Wang, T.; Huang, H.; Chen, Y.; Li, Z.; Zou, Z. Heterogeneous Degradation of Organic Contaminants in the Photo-Fenton Reaction Employing Pure Cubic β-Fe_2O_3. *Appl. Catal. B* **2019**, *245*, 410−419.

(24) Yang, Y.; Pignatello, J. J.; Ma, J.; Mitch, W. A. Comparison of Halide Impacts on the Efficiency of Contaminant Degradation by Sulfate and Hydroxyl Radical-Based Advanced Oxidation Processes (AOPs). *Environ. Sci. Technol.* **2014**, *48*, 2344−2351.

(25) Zhang, C.; Ou, Y.; Lei, W. X.; Wan, L. S.; Ji, J.; Xu, Z. K. $CuSO_4/H_2O_2$-Induced Rapid Deposition of Polydopamine Coatings with High Uniformity and Enhanced Stability. *Angew. Chem. Int. Ed.* **2016**, *55*, 3054−3057.
(26) Liu, Y. Y.; Jin, W.; Zhao, Y. P.; Zhang, G. S.; Zhang, W. Enhanced Catalytic Degradation of Methylene Blue by α-Fe_2O_3/Graphene Oxide via Heterogeneous Photo-Fenton Reactions. *Appl. Catal. B* **2017**, *206*, 642−652.
(27) Qian, X.; Ren, M.; Zhu, Y.; Yue, D.; Han, Y.; Jia, J.; Zhao, Y. Visible Light Assisted Heterogeneous Fenton-Like Degradation of Organic Pollutant via α-FeOOH/Mesoporous Carbon Composites. *Environ. Sci. Technol.* **2017**, *51*, 3993−4000.
(28) Tian, H.; Peng, J.; Du, Q.; Hui, X. H.; He, H. One-pot sustainable synthesis of Magnetic MIL-100 (Fe) with Novel Fe_3O_4 Morphology and Its Application in Heterogeneous Degradation. *Dalton Trans.* **2018**, *47*, 3417−3424.
(29) Wang, X.; Wang, J. Q.; Cui, Z. T.; Wang, S. G.; Cao, M. H. Facet Effect of α-Fe_2O_3 Crystals on Photocatalytic Performance in the Photo-Fenton Reaction. *RSC Adv.* **2014**, *4*, 34387−34394.
(30) Chen, H.; Zhang, Z. L.; Yang, Z. L.; Yang, Q.; Li, B.; Bai, Z. Y. Heterogeneous Fenton-like Catalytic Degradation of 2, 4-Dichlorophenoxyacetic Acid in Water with FeS. *Chem. Eng. J.* **2015**, *273*, 481−489.
(31) Huang, X.; Niu, Y.; Hu, W. Fe/Fe_3C Nanoparticles Loaded on Fe/N-Doped Graphene as an Efficient Heterogeneous Fenton Catalyst for Degradation of Organic Pollutants. *Colloids Surf. A Physicochem. Eng. Asp.* **2017**, *518*, 145−150.
(32) Shi, W.; Du, D.; Shen, B.; Cui, C. F.; Lu, L. J.; Wang, L. Z.; Zhang, J. L. Synthesis of Yolk-Shell Structured Fe_3O_4@void@CdS Nanoparticles: A General and Effective Structure Design for Photo-Fenton Reaction. *ACS Appl. Mater. Interfaces* **2016**, *8*, 20831−20838.
(33) Liu, Y. Y.; Jin, W.; Zhao, Y. P.; Zhang, G. S.; Zhang, W. Enhanced Catalytic Degradation of Methylene Blue by α-Fe_2O_3/Graphene Oxide via Heterogeneous Photo-Fenton Reactions. *Appl. Catal. B* **2017**, *206*, 642−652.
(34) Samanta, A.; Das, S.; Jana, S. Doping of Ni in α-Fe_2O_3 Nanoclews to Boost Oxygen Evolution Electrocatalysis. *ACS Sustainable Chem. Eng.* **2019**, *7*, 12117−12124.
(35) Samanta, A.; Jana, S. Ni-, Co-, and Mn-Doped Fe_2O_3 Nano-Parallelepipeds for Oxygen Evolution. *ACS Appl. Nano Mater.* **2021**, *4*, 5131–5140.
(36) He, L.; Tan, C.; Sheng, C.; Chen, Y.; Yu, F.; Chen, Y. A β-FeOOH/MXene Sandwich for High-Performance Anodes in Lithium-Ion Batteries. *Dalton Trans.* **2020**, *49*, 9268−9273.
(37) Wang, C.; Yang, X.; Zheng, M.; Xu, Y. Synthesis of β-FeOOH Nanorods Adhered to Pine-Biomass Carbon as A Low-Cost Anode Material for Li-Ion Batteries. *J. Alloys Compd.* **2019**, *794*, 569−575.

(38) Samanta, A.; Das, S.; Jana, S. Exploring β-FeOOH Nanorods as an Efficient Adsorbent for Arsenic and Organic Dyes. *ChemistrySelect* **2018**, *3*, 2467−2473.
(39) Wei, C.; Nan, Z. Effects of Experimental Conditions on One-Dimensional Single-Crystal Nanostructure of β-FeOOH. *Mater. Chem. Phys.* **2011**, *127*, 220−226.
(40) Mao, Y.; Jiang, W.; Xuan, S.; Fang, Q.; Leung, K. C. F.; Ong, B. S.; Wang, S.; Gong, X. Rod-Like β-FeOOH@Poly(Dopamine)-Au-Poly(Dopamine) Nanocatalysts with Improved Recyclable Activities. *Dalton Trans.* **2015**, *44*, 9538−9544.
(41) Jana, S.; Pande, S.; Sinha, A. K.; Sarkar, S.; Pradhan, M.; Basu, M.; Saha, S.; Pal, T. A Green Chemistry Approach for the Synthesis of Flower-Like Ag-Doped MnO_2 Nanostructures Probed by Surface-Enhanced Raman Spectroscopy. *J. Phys. Chem. C* **2009**, *113*, 1386−1392.
(42) Sultana, S.; Mansingh, S.; Parida, K. M. Rational Design of Light Induced Self Healed Fe Based Oxygen Vacancy Rich CeO_2 (CeO_2NS-FeOOH/Fe_2O_3) Nanostructure Materials for Photocatalytic Water Oxidation and Cr(VI) Reduction. *J. Mater. Chem. A* **2018**, *6*, 11377−11389.
(43) Xu, Z.; Yu, Y.; Fang, D.; Xu, J.; Liang, J.; Zhou, L. Microwave-Ultrasound Assisted Synthesis of β-FeOOH and Its Catalytic Property in a Photo-Fenton-Like Process. *Ultrason. Sonochem.* **2015**, *27*, 287−295.
(44) Mahamallik, P.; Pal, A. Photo-Fenton Process in a Co (II)-Adsorbed Micellar Soft-Template on an Alumina Support for Rapid Methylene Blue Degradation. *RSC Adv.* **2016**, *6*, 100876-100890.
(45) Konstantinou, I. K.; Albanis, T. A. Photocatalytic Transformation of Pesticides in Aqueous Titanium Dioxide Suspensions using Artificial and Solar Light: Intermediates and Degradation Pathways. *Appl. Catal. B* **2003**, *42*, 319-335.
(46) Das, S.; Jana, S.; A Tubular Nanoreactor Directing the Formation of In Situ Iron Oxide Nanorods with Superior Photocatalytic Activity. *Environ. Sci.: Nano* **2017**, *4*, 596−603.
(47) Zhang, C.; Yang, H. C.; Wan, L. S.; Liang, H. Q.; Li, H.; Xu, Z. K. Polydopamine-Coated Porous Substrates as a Platform for Mineralized β‑FeOOH Nanorods with Photocatalysis under Sunlight. *ACS Appl. Mater. Interfaces* **2015**, *7*, 11567−11574.
(48) Xu, Z.; Liang, J.; Zhou, L. Photo-Fenton-Like Degradation of Azo Dye Methyl Orange using Synthetic Ammonium and Hydronium Jarosite. *J. Alloys Compd.* **2013**, *546*, 112−118.
(49) Feng, J. Y.; Hu, X. J.; Yue, P. L.; Zhu, H. Y.; Lu, G. Q. Degradation of Azo-Dye Orange II by a Photoassisted Fenton Reaction Using a Novel Composite of Iron Oxide and SilicateNanoparticles as a Catalyst. *Ind. Eng. Chem. Res.* **2003**, *42*, 2058−2066.

(50) Zhao, Y. P.; Hu, J. Y.; Jin, W. Transformation of Oxidation Products and Reduction of Estrogenic Activity of 17β-Estradiol by a Heterogeneous Photo-Fenton Reaction. *Environ. Sci. Technol.* **2008**, *42*, 5277−5284.

(51) Ahmed, Y.; Yaakob, Z.; Akhtara, P. Degradation and Mineralization of Methylene Blue Using a Heterogeneous Photo-Fenton Catalyst under Visible and Solar Light Irradiation. *Catal. Sci. Technol*. **2016**, *6*, 1222−1232.

(52) Cheng, M.; Liu, Y.; Huang, D.; Lai, C.; Zeng, G.; Huang, J.; Liu, Z.; Zhang, C.; Zhou, C.; Qin, L.; Xiong, W. Prussian Blue Analogue Derived Magnetic Cu-Fe Oxide as a Recyclable Photo-Fenton Catalyst for the Efficient Removal of Sulfamethazine at Near Neutral pH Values. *Chem. Eng. J.* **2019**, *362*, 865−876.

(53) Saravanan, R.; Joicy, S.; Gupta, V.; Narayanan, V.; Stephen, A. Visible Light Induced Degradation of Methylene Blue using CeO_2/V_2O_5 and CeO_2/CuO Catalysts. *Mater. Sci. Eng., C* **2013**, *33*, 4725−4731.

(54) Liu, X.; Pan, L.; Lv, T.; Sun, Z.; Sun, C. Q. Visible Light Photocatalytic Degradation of Dyes by Bismuth Oxide-Reduced Graphene Oxide Composites Prepared via Microwave-Assisted Method. *J. Colloid Interface Sci.* **2013**, *408*, 145−150.

(55) Sabari Arul, N.; Mangalaraj, D.; In Han, J. Enhanced Photocatalytic Property of Self-Assembled Fe-Doped CeO_2 Hierarchical Nanostructures. *Mater. Lett.* **2015**, *145*, 189−192.

(56) Kalam, A.; Al-Sehemi, A. G.; Assiri, M.; Du, G.; Ahmad, T.; Ahmad, I.; Pannipara, M. Modified Solvothermal Synthesis of Cobalt Ferrite ($CoFe_2O_4$) Magnetic Nanoparticles Photocatalysts for Degradation of Methylene Blue with H_2O_2/Visible Light. *Results Phys.* **2018**, *8*, 1046−1053.

(57) Jiang, X.; Li, L.; Cui, Y.; Cui, F. New Branch on Old Tree: Green-Synthesized RGO/Fe_3O_4 Composite as a Photo-Fenton Catalyst for Rapid Decomposition of Methylene Blue. *Ceram. Int.* **2017**, *43*, 14361−14368.

(58) Cheng, G.; Yu, L.; Lin, T.; Yang, R.; Sun, M.; Lan, B.; Yang, L.; Deng, F. A Facile One-Pot Hydrothermal Synthesis of β-MnO_2 Nanopincers and Their Catalytic Degradation of Methylene Blue. *J. Solid State Chem.* **2014**, *217*, 57−63.

(59) Sun, Y.; Cai, L.; Liu, X.; Cui, Z.; Rao, P. Tailoring Heterostructures of Ag/Cu_2O Hybrids for Enhanced Photocatalytic Degradationdegradation. *J. Phys. Chem. Solids* **2017**, *111*, 75−81.

(60) Faraji, M.; Mohaghegh, N. Ag/TiO_2-Nanotube Plates Coated with Reduced Graphene Oxide as Photocatalysts. *Surf. Coat. Technol.* **2016**, *288*, 144−150.

(61) Das, S.: Jana, S. A Tubular Nanoreactor Directing the Formation of In Situ Iron Oxide Nanorods with Superior Photocatalytic Activity. *Environ. Sci.: Nano* **2017**, *4*, 596−603.

(62) Guo, X.; Wang, K.; Xu, Y. Tartaric Acid Enhanced $CuFe_2O_4$-Catalyzed Heterogeneous Photo-Fenton-Like Degradation of Methylene Blue. *Mater. Sci. Eng., B* **2019**, *245*, 75−84.
(63) Yuan, B.; Xu, J.; Li, X.; Fu, M. L. Preparation of Si–Al/α-FeOOH Catalyst from an Iron-Containing Waste and Surface-Catalytic Oxidation of Methylene Blue at Neutral pH Value in the Presence of H_2O_2. *Chem. Eng. J.* **2013**, *226*, 181−188.
(64) Nosaka, Y.; Nosaka, A. Y. Generation and Detection of Reactive Oxygen Species in Photocatalysis. *Chem. Rev.* **2017**, *117*, 11302−11336.
(65) Chen, C.; Ma, W.; Zhao, J. Semiconductor-Mediated Photodegradation of Pollutants under Visible-Light Irradiation. *Chem. Soc. Rev.* **2010**, *39*, 4206−4219.
(66) Banerjee, S.; Pillai, S. C.; Falaras, P.; O'shea, K. E.; Byrne, J. A.; Dionysiou, D. D. New Insights into the Mechanism of Visible Light Photocatalysis. *J. Phys. Chem. Lett.* **2014**, *5*, 2543−2554.
(67) Hartmann, M.; Kullmann, S.; Keller, H. Wastewater Treatment with Heterogeneous Fenton-Type Catalysts Based on Porous Materials. *J. Mater. Chem.* **2010**, *20*, 9002-9017.
(68) Guo, T.; Jiang, L.; Wang, K.; Li, Y.; Huang, H.; Wu, X.; Zhang, G., Efficient Persulfate Activation by Hematite Nanocrystals for Degradation of Organic Pollutants under Visible Light Irradiation: Facet-Dependent Catalytic Performance and Degradation Mechanism. *Appl. Catal. B* **2021**, *286*, 119883.
(69) Huang, H.; Guo, T.; Wang, K.; Li, Y.; Zhang, G. Efficient Activation of Persulfate by a Magnetic Recyclable Rape Straw Biochar Catalyst for the Degradation of Tetracycline Hydrochloride in Water. *Sci. Total Environ.* **2021**, *758*, 143957.

****

Chapter 7

Synthesis of Novel MnO_2/Ag Flowery Nanocomposites with Excellent Photocatalytic Activity

7.1 Introduction

With the fast growth of industrial advances and urbanization, together with the massive rise of population, water pollution has become a serious threat to the mankind and thus the pressing need is to access clean water sources world-wide. One of the main sources of the water pollution is the existence of diverse organic compounds, which are mainly discharged from various industries, like food processing, textiles, leather, pharmaceutical, and plastic.[1-4] Being very toxic and non-biodegradable, these organic pollutants have adverse influence on the aquatic environment and also on human lives.[5,6] Hence, it is a pressing necessity to develop an effective but at the same time inexpensive wastewater treatment technology to reduce their environmental effect.[7]Among the various wastewater treatment technologies, advanced oxidation process has been received a great attention amongst researchers owing to its strong oxidation ability together with high efficacy.[8-10] However, designing of a photocatalyst having high efficacy using semiconductor materials emerges as a promising approach in advanced oxidation process. Likewise, it is also important to design green and sustainable way for waste water treatment. To meet this requirement, the sun light driven photocatalysis is an ideal and cost-effective way by utilizing the renewable and endless solar energy for the degradation of toxic pollutants via low temperature approach.

Over the past years, metal oxides being a family of semiconductor have received immense attention worldwide as photocatalysts for environmental remediation.[11-14] In photocatalysis, upon irradiation of light, photocatalyst gets activated and subsequently facilitates the kinetics of the reaction but itself remains unchanged. Basically, the photodegradation process takes place via redox reaction prompted by the photoproduced

electrons and holes in a photocatalyst.[15,16] Hence, the photocatalytic efficiency of any semiconductor entirely relies on the light absorption and subsequent charge separation efficacy.

Among the different oxide based materials, manganese oxides have been considered as one of the miscellaneous classes of materials from the technological and fundamental point of view. They exhibit potential applications in the field of environmental purification,[17,18] catalysis,[19-23] adsorption,[24-26] sensing,[27,28] supercapacitors,[29-31] lithium-air batteries[32,33] etc. Nanoscale manganese dioxide (MnO_2) appears as a non-stoichiometric compound with various polymorphic forms, including α-MnO_2, [34,35] β-MnO_2,[36,37] γ-MnO_2,[38 39] δ-MnO_2,[40,41] and ε-MnO_2,[42,43] which are observed as a result of the arrangement of the basic structural octahedral [MnO_6] unit in MnO_2 in diverse ways. MnO_2 having structural flexibility along with strong oxidation ability, serves as a promising photocatalyst to degrade the organic pollutants in wastewater and has withdrawn a great attention because of its high abundance, inexpensiveness, and environmental-friendly in nature. However, the photocatalytic efficacy of MnO_2 sometimes gets restricted owing to the faster recombination of photoproduced excitons (electron-hole pairs). To address this issues, loading of noble metals onto MnO_2 is the most possible way in enhancing the photocatalytic efficiency, since they participate in the process by conducting the electrons as well as preventing the recombination rate of electron-hole pairs. Thus, immobilized nanostructures facilitate the charge transfer via trapping the photogenerated charge carriers, which in turn enhances the photocatalytic rate by lowering the possibility of the rate of recombination of the photoproduced excitons. In comparison to the diverse noble metals (Ag, Au, Pd, and Pt), Ag has been considered to be the most promising dopant owing to its good conductivity, low-cost and nontoxic nature.

In this chapter, a facile and effective route was developed to fabricate flowery MnO_2 and MnO_2/Ag nanocomposites (NCs) for the exploration as photocatalysts towards the degradation of organic dye under the irradiation of natural solar light. From the photocatalytic experiments, it was observed that MnO_2/Ag NCs exhibit much better

photocatalytic performance compared to the pristine MnO_2 NCs. Moreover, repetitive experiments were carried out to establish the reusability and followed by stability of the catalyst. The detail mechanism of the degradation process was illustrated in presence of several scavengers as well as additional supplementary oxygen source, signifying the generation of reactive oxygen species during photocatalysis.

7.2 Experimental Section

7.2.1 Surface Functionalization of Halloysite Nanotubes (HNTS)

For the preparation of MnO_2 nanocomposites (NCs), first we functionalized the surface of the halloysite nanotubes (HNTs) by grafting reaction with an organosilane (scheme 7.1).[44] Organosilane grafted halloysite nanotubes were synthesized according to the following procedure. The grafting reaction was carried out under nitrogen atmosphere using standard air free techniques. A total of 3.0 g of HNTs was taken in a 50 mL three-necked round-bottom flask containing 15.0 mL of toluene. Afterward, the reaction flux was fixed with a rubber septum, condenser, thermocouple adaptor, and additional quartz sheath in which a thermocouple was inserted. The reaction mixture was deaerated for 30 min under nitrogen at room temperature, followed by heated with a heating mantle. Then, 1.5 mL of (3-aminopropyl) triethoxysilane was injected into the reaction flask at 60 °C under stirring condition and refluxed for 20 h. Finally, the as-synthesized product was collected through filtration and washed several times with toluene and ethanol, respectively. The obtained product was dried at 100 °C overnight under vacuum. Amine functionalized HNTs were abbreviated as FHNTs and were used as a support material to grow the MnO_2 nanoflowers over it.

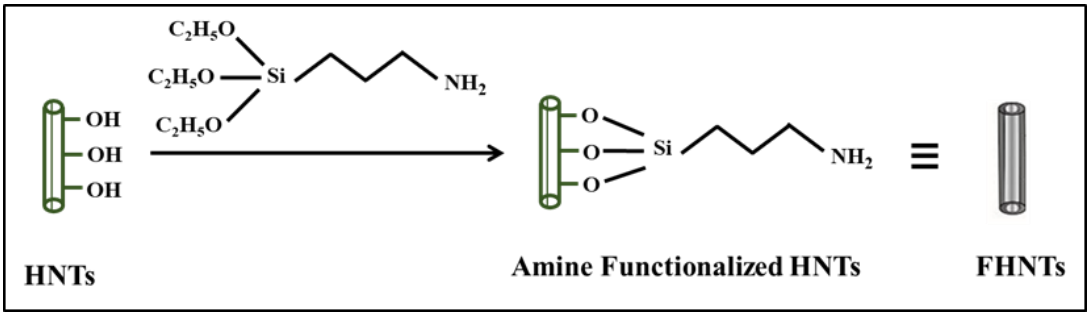

Scheme 7.1: Schematic presentation of the functionalization of the surface of the halloysite nanotubes (HNTs) through grafting of an aminosilane leading to the formation of amine functionalized HNTs (FHNTs).

7.2.2 Synthesis of MnO_2 Nanocomposites

After functionalization of HNTs with the aminosilane, MnO_2 nanoflowers were grown over FHNTs. For this purpose, first 2.0 mmol of $KMnO_4$ was taken in a beaker and dissolved it properly in 15.0 mL of Millipore water by sonication. Then, 0.2 g of FHNTs were added to the above solution. Next, the whole mixture was transferred to a vial and 3 wt% NaOH solution (6.0 mL) was added into the above vial drop-wise. After completion addition of NaOH solution, the whole mixture was shaken well by a vortexer for 15 min. Then, the mouth of the vial was sealed tightly and placed in a water bath for 10 h at 100 °C. Once the reaction was completed, the product was collected easily via filtration process and washed properly using Millipore water. The prepared product was air dried for one day and designated as MnO_2 NCs which were used for the preparation of MnO_2/Ag nanocomposites.

7.2.3 Synthesis of MnO_2/Ag Nanocomposites

MnO_2/Ag nanocomposites (NCs) were prepared via the following method. First, 0.5 g aforesaid MnO_2 NCs was taken in a beaker and then 15 mL $AgNO_3$ (5×10^{-3} M) solution was added into the beaker. After that the whole solution mixture was stirred well on a magnetic stirrer for 8 h to immobilize Ag^+ ions over the flowery NCs. Once the MnO_2

NCs got saturated with Ag^+ ions, the product was collected through simple filtration and washed properly with Millipore water in order to eliminate the unadsorbed Ag^+ ions. Next, the silver ion Ag^+ ions adsorbed MnO_2 NCs were dispersed in a beaker by adding 12 mL of Millipore water under stirring condition and reduced using aqueous solution of $NaBH_4$ (ice cold) to make MnO_2/Ag NCs. After the reduction, the synthesized MnO_2/Ag NCs were washed by Millipore water and collected through filtration. After air-drying, the obtained product was explored as photocatalyst and compared the photocatalytic activity with the pristine MnO_2 NCs.

7.2.4 Photocatalytic Experiment

The photocatalytic efficiency of flowery MnO_2 and MnO_2/Ag NCs was studied for the degradation of methylene blue (MB) dye under natural solar light. All the reactions were executed in a cylindrical borosilicate glass reactor containing a cooling water jacket. For the period of the photocatalysis, the reactor was placed under solar irradiation. The temperature of the dye solution was kept to 25 °C during the degradation experiment by the circulation of cold water. The photocatalytic degradation of dye solution was evaluated with time by measuring the absorbance of the irradiated solution using a UV–vis spectrophotometer. Before exposing the dye solution under solar light, catalysts having concentration of 0.25 g L^{-1} were added to the aqueous solution of dye (20 mL, 0.03mM). Next, the whole solution was shaken well and kept in dark for 6 h to attain an adsorption-desorption equilibrium. After that, the initial concentration of the dye solution (C_0) was measured. Once initial concentration was measured, the dye solution was then exposed to the solar light. To calculate the residual dye concentration, 3.0 mL of the dye solution was taken from the reactor at specific time intervals and used for the absorbance measurement. Before recording the spectrum, the photocatalyst was separated from the reaction solution via centrifugation each time. Once the absorbance spectrum of the dye solution was recorded, it was then transferred again into the glass reactor. Absorption spectra of solar light irradiated dye have been quantitatively evaluated with a certain time interval during the photocatalytic process. The % of degradation of dye was determined

as the following: % of degradation = $[(C_0 - C_t)/C_0] \times 100$; where, C_0 is initial dye concentration and C_t is concentration of dye after solar light irradiation at time t. In order to check the stability and reusability of the catalyst, after each run the catalyst was collected by centrifugation and dried it before using in the next run. To get the information regarding the active species produced during the photodegradation process and their role in the photocatalysis, several experiments for the trapping of free radicals were performed using appropriate quenchers, like, tert-butyl alcohol (t-BA), sodium azide and triethanolamine (TEA) respectively.

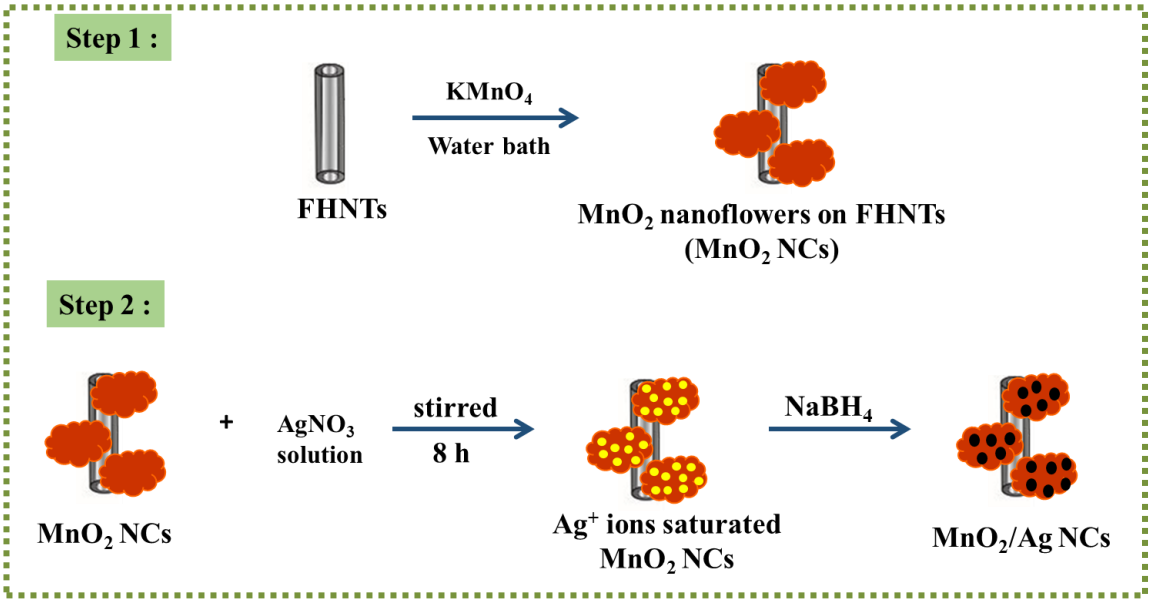

Scheme 7.2: Schematic presentation of the fabrication process of flowery MnO_2 and MnO_2/Ag NCs.

7.3 Results and Discussion

The fabrication process to achieve flowery MnO_2 and MnO_2/Ag NCs has been schematically presented in scheme 7.2. In the first step, MnO_2 nanoflowers were grown over the surfaces of amine functionalized HNTs (FHNTs) taking $KMnO_4$ as precursor, resulting in the formation of MnO_2 NCs. In the second step, MnO_2 NCs were kept emerged in aqueous solution of $AgNO_3$ and then Ag^+ ions loaded MnO_2 NCs were

reduced by ice-cold solution of $NaBH_4$, which in turn produced MnO_2/Ag NCs. Basically, MnO_2 NCs possess negative ζ-potentials of – 39.5 mV, which facilitates the immobilization of positively charged Ag^+ ions over their flowery surfaces through the electrostatic interaction. After subsequent reduction of Ag^+ ions loaded MnO_2 NCs results in the successful fabrication of MnO_2/Ag NCs.

7.3.1 Characterization of MnO_2 NCs

7.3.1.1 Time Dependent Growth of MnO_2 NCs

Time dependent growth of MnO_2 NCs presented in Figure 7.1 clearly indicates the formation of MnO_2 flowery nanostructures over the surface of FHNTs. The morphology of the prepared MnO_2 nanostructures was characterized by field emission scanning electron microscopy (FESEM). All the FESEM images further illustrate the step-wise growth of MnO_2 nanoflowers on FHNTs as the reaction progress. Figure 7.2.A-C represent the FESEM images of MnO_2 nanostructures at different magnifications. These images indicate hierarchical flower-like morphology of MnO_2 nanostructures.

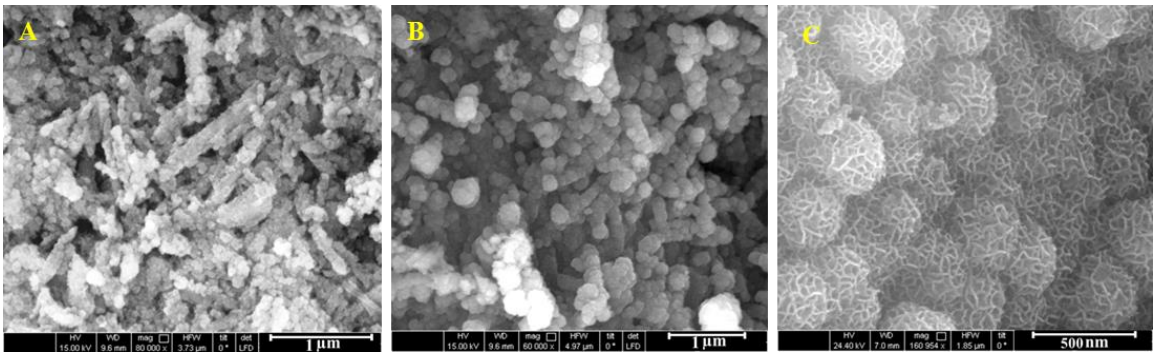

Figure 7.1: Time dependent growth of MnO_2 NCs over the surface of FHNTs, clearly indicates the formation of MnO_2 flowery nanostructures. FESEM images of the intermediates during the formation of flower-like MnO_2 NCs at different reaction times, (A) 2 h, (B) 5 h and (C) 10 h.

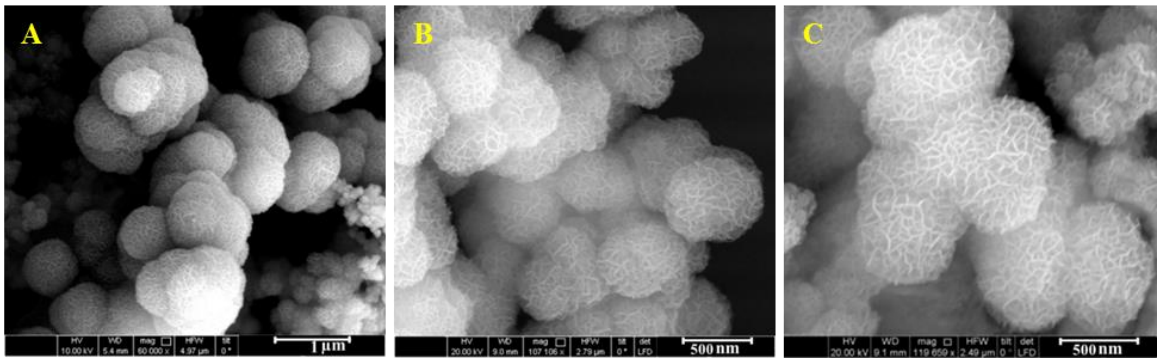

Figure 7.2: (A-C) FESEM images of MnO_2 NCs at various magnifications, indicating flowery morphology of MnO_2 fabricated over the surfaces of FHNTs.

7.3.1.2 TEM Analysis

Transmission electron microscopy (TEM) micrographs of MnO_2 nanostructures at various magnifications have also been authenticated the fabrication of MnO_2 nanoflowers, which are comprised of the assemble of several wrinkly thin interconnected nanosheets (Figure 7.3.A-C). This as-synthesized MnO_2 NCs was then taken as a support material to prepare MnO_2/Ag NCs.

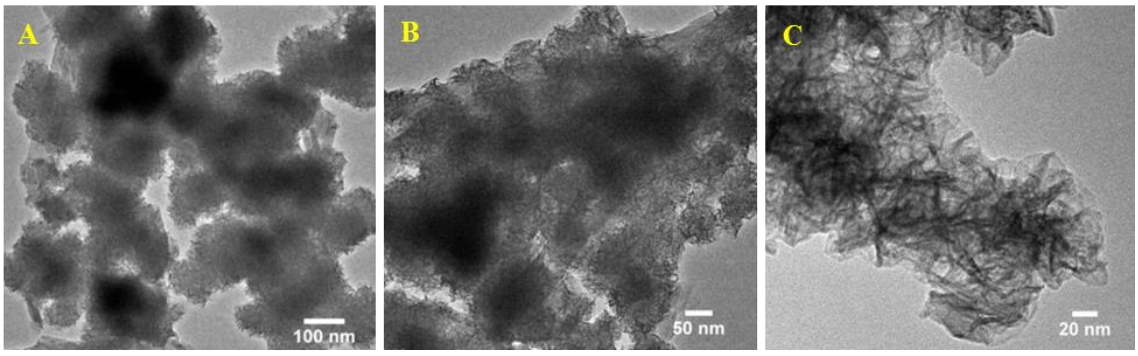

Figure 7.3: (A-C) TEM micrographs of flowery MnO_2 NCs revealing that the nanostructures are comprised of the assemble of several wrinkly thin interconnected nanosheets.

7.3.1.3 EDS Analysis

The energy dispersive X-ray spectroscopy (EDS) analysis of MnO_2 has also been carried out to know the presence of different elements in the NCs. The EDS spectrum of MnO_2 NCs (Figure 7.4) demonstrates the presence of Mn and O along with Si and Al obtained from the clay nanotubes, HNTs.

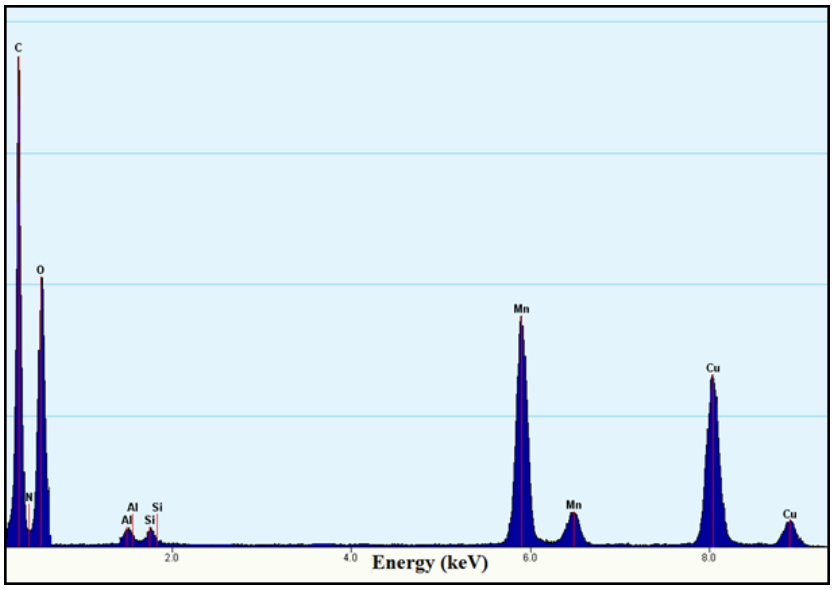

Figure 7.4: EDS spectrum of MnO_2 NCs.

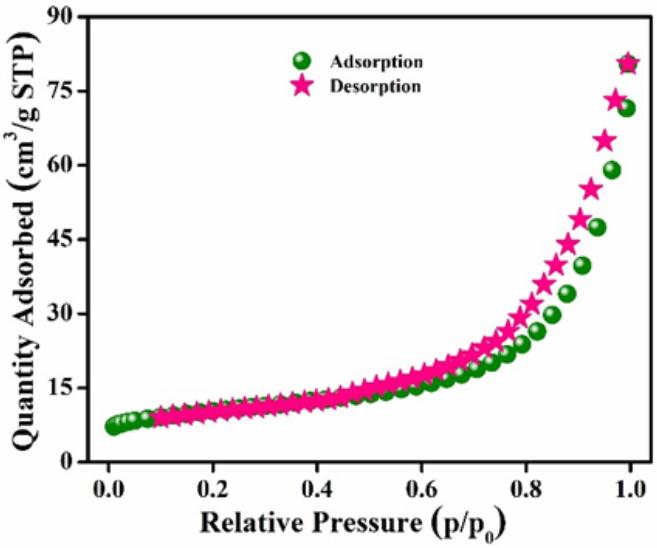

Figure 7.5: The nitrogen adsorption-desorption isotherms of MnO_2 NCs.

7.3.1.4 BET Surface Area Measurement

N_2 adsorption-desorption study was performed at 77 K for the estimation of the specific surface area of the synthesized NCs (Figure 7.5) using the Brunauer-Emmett-Teller (BET) method. The specific surface area has been found to be 34 m^2 g^{-1} for the MnO_2 NCs.

7.3.1.5 UV-visible Diffuse Reflectance Study

The DRS spectrum of the MnO_2 (Figure 7.6.A) displays an absorption band in the range of 270-430 nm. The band gap energy (E_g) was also estimated according to the Tauc's equation: [45,46] $\alpha h\nu = A\,(h\nu - E_g)^{1/2}$, where α, h, ν, E_g, and A are the absorption coefficient, Planck's constant, light frequency, the band gap energy and a constant respectively. From the Tauc's plots, the band gaps have been found to be 2.03 eV for MnO_2 NCs (Figure 7.6.B).

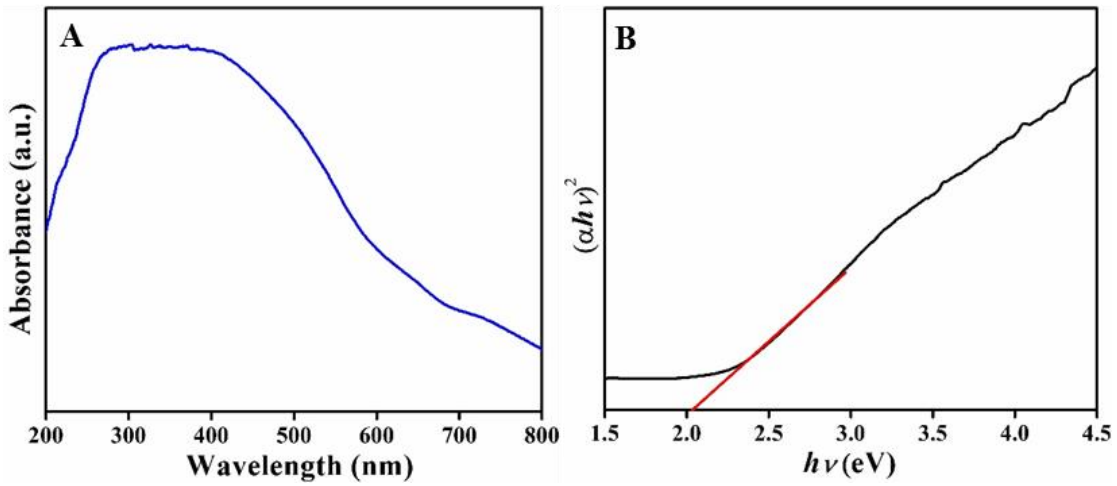

Figure 7.6: (A) UV-vis diffuse-reflectance spectra of MnO_2 NCs and (B) corresponding plot of $(\alpha h\nu)^2$ versus $h\nu$ to determine the band gap energy.

7.3.2 Characterization of MnO_2/Ag NCs

7.3.2.1 TEM Analysis

The TEM images of MnO_2/Ag NCs shown in Figure 7.7 at various magnifications, clearly illustrates that Ag nanoparticles (NPs) are loaded over the surface of MnO_2 nanoflowers. High resolution TEM (HRTEM) micrograph presented in Figure 7.7.D attributes to the formation of Ag NPs having size of around 10 nm.

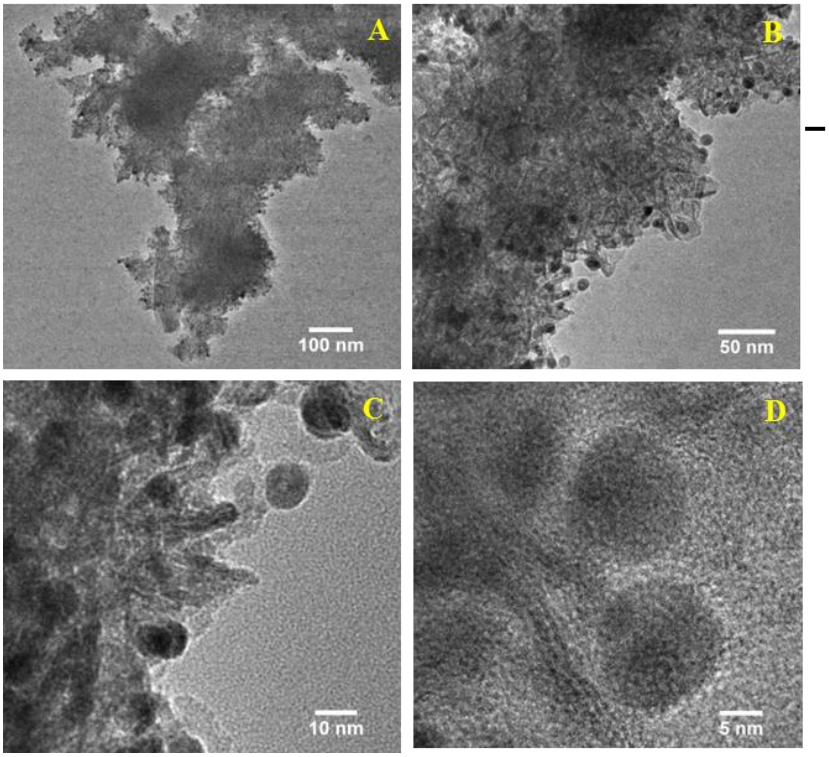

Figure 7.7: (A-C) TEM micrographs of MnO_2/Ag NCs at varied magnifications and (D) HRTEM image of MnO_2/Ag NCs. All images demonstrating the fruitful fabrication of MnO_2/Ag NCs.

7.3.2.2 EDS Spectrum and ICP-OES Analysis

In case of EDS spectrum of MnO_2/Ag NCs, new signals are achieved for Ag (~4.0 wt%) together with the previously observed peaks for pristine MnO_2 (Figure 7.8), further

signifying the fruitful fabrication of MnO_2/Ag NCs. This was further verified by ICP-OES analysis.

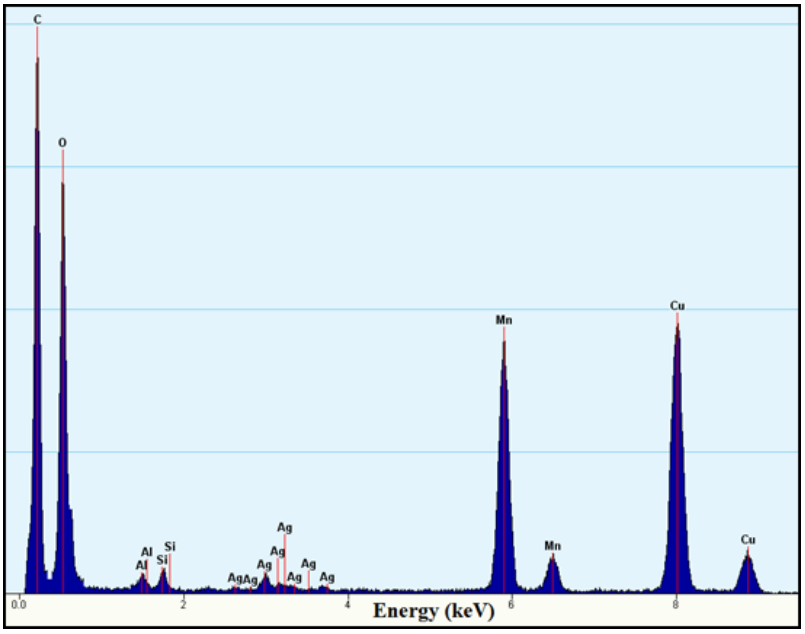

Figure 7.8: EDS spectrum of MnO_2/Ag NCs. In EDS spectrum of MnO_2/Ag NCs, new signals are observed for Ag together with the previously observed peaks for pristine MnO_2.

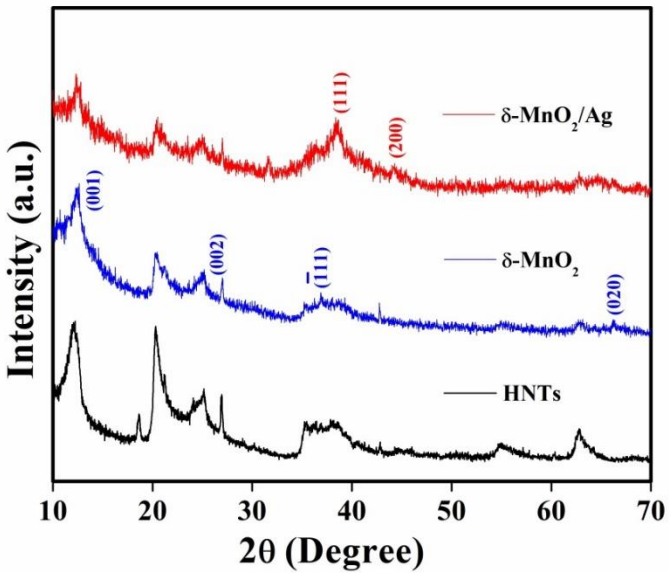

Figure 7.9: XRD patterns of HNTs, δ-MnO_2 and δ-MnO_2/Ag NCs.

7.3.2.3 XRD Study

The peaks observed in the X-ray diffraction (XRD) pattern of MnO_2 NCs (Figure 7.9) can be assigned to the presence of (001), (002), ($\bar{1}11$) and (020) planes of δ-MnO_2 phase, suggesting the successful growth of pure monoclinic δ-MnO_2 over FHNTs surfaces.[24] From the XRD pattern of MnO_2/Ag NCs illustrated in Figure 7.9, we have seen the peaks for Ag NPs having (111) and (200) planes along with MnO_2, representing the loading of Ag NPs over the surfaces of MnO_2 flowery NCs.

7.3.2.4 BET Surface Area Measurement

N_2 adsorption-desorption study was also performed at 77 K for the estimation of the specific surface area of the MnO_2/Ag NCs NCs (Figure 7.10) using the Brunauer-Emmett-Teller (BET) method. The specific surface area has been found to be 29 m^2 g^{-1} for the MnO_2/Ag NCs.

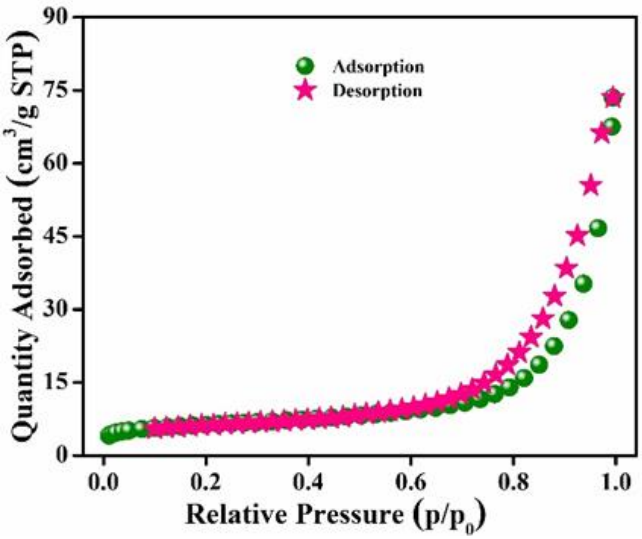

Figure 7.10: The nitrogen adsorption-desorption isotherms MnO_2/Ag NCs.

7.3.2.5 UV-visible Diffuse Reflectance Study

The band gap energy of semiconductor materials is a significant parameter for acquiring the information about their photocatalytic degradation efficacy. The DRS spectrum of the

MnO_2/Ag NCs (Figure 7.11.A) displays with a wide absorption band over 270-550 nm region. The band gap energy (E_g) was also estimated according to the aforesaid Tauc's equation. From the Tauc's plots, the band gap has been found to be 1.78 eV for MnO_2/Ag NCs (Figure 7.11.B). The above result ascertains that loading of Ag onto MnO_2 can efficiently moderate the optical properties of MnO_2 flowery NCs by improving the light absorption efficiency towards wide range of light spectrum.

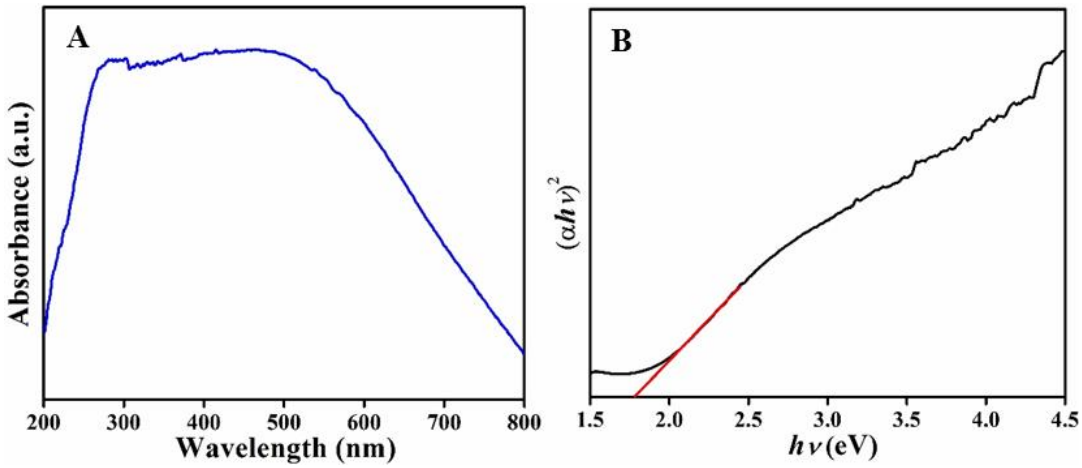

Figure 7.11: (A) UV-vis diffuse-reflectance spectra of MnO_2/Ag NCs and (B) corresponding plot of $(\alpha h\nu)^2$ versus $h\nu$ for the determination of the band gap energy.

7.3.3 Photocatalytic Activity

7.3.3.1 Degradation of Organic Dye

The photocatalytic efficacy of MnO_2 and MnO_2/Ag NCs was investigated towards the degradation of aqueous solution of an organic dye, namely methylene blue (MB) under the irradiation of natural solar light. Time-dependent UV-vis absorption spectra of aqueous solution of MB during photodegradation under solar light using MnO_2 and MnO_2/Ag NCs as catalysts are presented in Figure 7.12. After the addition of the catalyst during the photo-degradation process, the blue color of MB solution gradually changed to pale blue and finally became colorless. Figure 7.13 demonstrates the degradation efficiency for MB solution using both the synthesized catalysts in presence of solar light,

indicating much faster degradation efficiency of MnO_2/Ag NCs in associated to MnO_2 NCs under the identical experimental conditions. We observed that the time required to degrade the dye solution was around 70 min for MnO_2 NCs explored as catalyst, whereas the degradation time was reduced to 40 min when MnO_2/Ag NCs were employed as catalyst. After 40 min, almost 79% of MB solution was degraded by MnO_2 NCs, while it was enhanced significantly to 97% by exploring MnO_2/Ag NCs as photocatalyst, thus demonstrating the exceptional effectiveness of a metal loaded transition metal oxide catalyst than that of the pristine metal oxide catalyst.

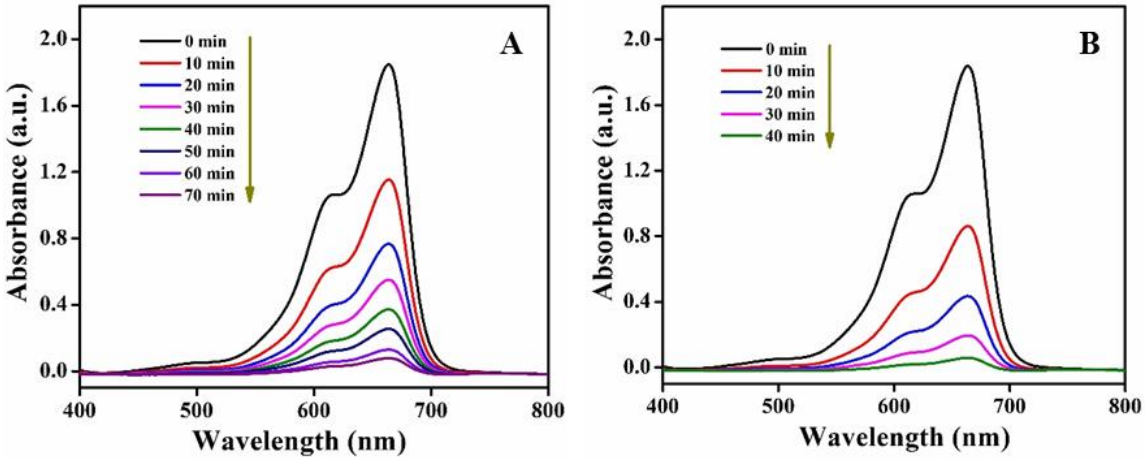

Figure 7.12: Time-dependent UV-vis absorption spectra of MB aqueous solution using (A) MnO_2 and (B) MnO_2/Ag NCs as catalysts.

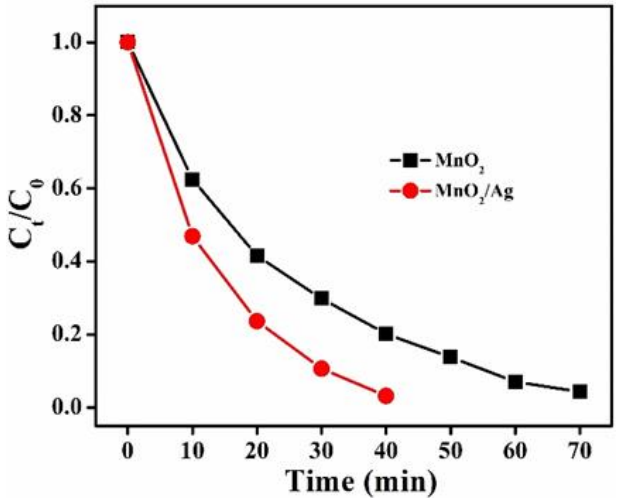

Figure 7.13: Degradation efficiency towards MB for two catalysts.

7.3.3.2 Kinetics of the Degradation Reaction

The kinetics of the photodegradation reaction was further illustrated based on the pseudo-first-order kinetic model: [47,48] $ln(C_0/C_t) = kt$, where C_0 was the initial concentration of the dye and C_t was the concentration of dye at the degradation time t. k was the reaction rate constant. From the slope of the plot of $ln(C_0/C_t)$ vs. t, the degradation rate constants were evaluated for both the catalysts for the degradation of MB solution (Figure 7.14). Degradation time, percentage of degradation, and the first-order rate constants for each catalyst have been presented in Table 7.1. All the parameters clearly substantiate that the degradation of MB using MnO_2/Ag NCs upon irradiation of sun light proceeds much faster compared to pristine MnO_2 NCs.

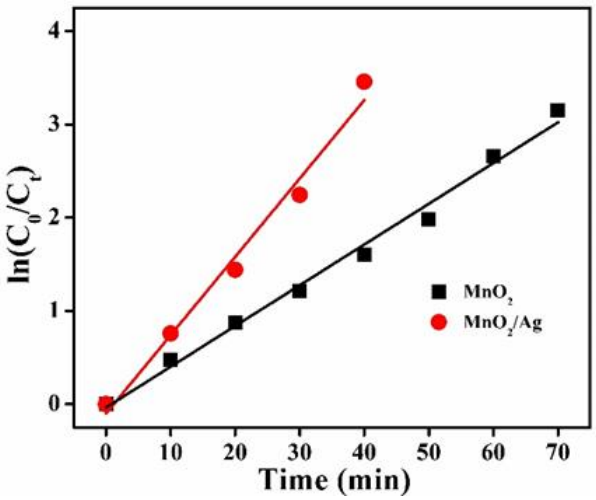

Figure 7.14: Plot of $ln(C_0/C_t)$ *vs.* t to calculate the rate constant of degradation process.

Table 7.1: Summary of the degradation time, percentage of degradation, and the first-order rate constants for MB degradation using MnO_2 and MnO_2/Ag NCs as catalysts under irradiation of sun light.

Catalyst	Degradation Time (min)	% of Degradation	First-Order Rate Constant (k, min^{-1})
MnO_2	70	96	0.04367
MnO_2/Ag	40	97	0.08398

7.3.3.3 Recyclability of MnO_2/Ag NCs

To have an understanding on the reusability of the photocatalyst, the photocatalytic study was carried out with six consecutive cycles for MnO_2/Ag NCs with irradiation of solar light as presented in Figure 7.15. The results demonstrated that the MnO_2/Ag NCs showed almost unaltered photocatalytic activity even after multi-cycle usages.

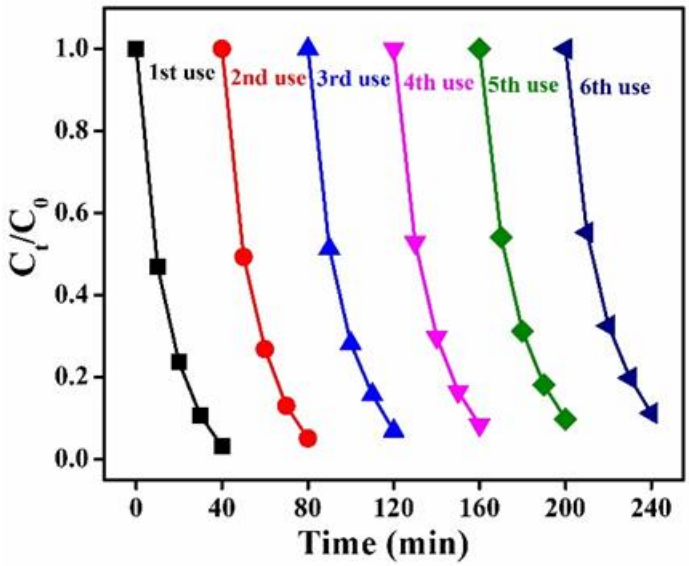

Figure 7.15: Multi-cycles degradation efficacy of MnO_2/Ag NCs for the degradation of MB with irradiation of solar light.

7.3.3.4 Study after Photocatalysis

We also performed the TEM and XRD analyses on MnO_2/Ag NCs after photocatalysis to check their morphology and structural change if any. The TEM images (Figure 7.16) of MnO_2/Ag NCs after photocatalysis indicated there is no alternation of their morphology even after photocatalytic study. XRD analysis also corroborated to their unaltered diffraction pattern even after prolonged photocatalytic study (Figure 7.17). All these results therefore ascertain their exceptional stability and sustainability as a photocatalyst under natural sunlight irradiation.

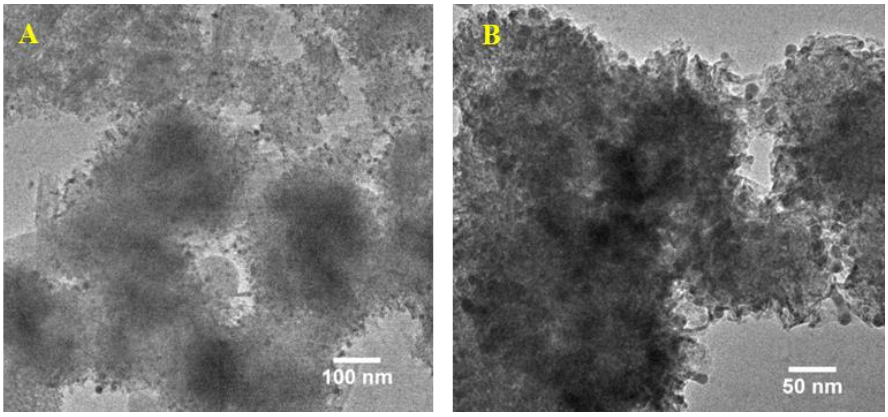

Figure 7.16: TEM micrographs of MnO_2/Ag NCs after photocatalysis.

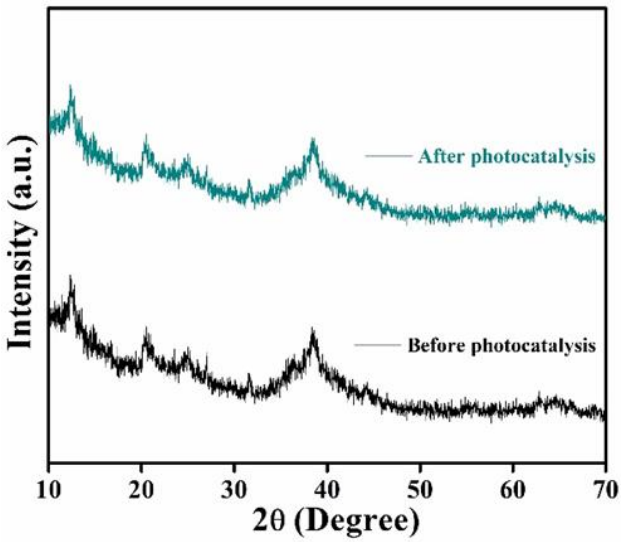

Figure 7.17: XRD patterns of MnO_2/Ag NCs before and after photocatalysis.

7.3.3.5 Degradation Mechanism

To have an insight into the formation and subsequent role of photo-produced reactive oxygen species (ROS) in the photodegradation process, a series of experiments were carried out in presence of several scavengers and a supplementary oxygen source upon unaltered experimental conditions (Figure 7.18). In presence of the supplementary oxygen source, namely H_2O_2, the degradation rate of MB was notably increased,

suggesting the probable generation of ROS upon irradiation of sunlight and subsequently boosting the degradation rate of the dye. Likewise, we have chosen several scavengers in order to trap the photo-produced ROS during the degradation reaction. For the trapping experiment, different scavengers including triethanolamine (TEA), sodium azide and tert-butyl alcohol (t-BA) were used to trap the various photo-produced ROS, like holes (h^+), super oxide radical anion ($\bullet O_2^-$) and hydroxyl radical (•OH). As we anticipated, the degradation rate was significantly reduced after the addition of aforesaid scavenges, since they trapped the photo-produced ROS during degradation process. Hence, this trapping experiment clearly suggests that the degradation of dye under irradiation of light proceeds via the formation of photo-generated reactive oxygen species.

Typically, the photo-degradation occurs via a series of reactions due to the formation of the ROS as follows:[49,50]

$$\text{Photocatalyst} + h\nu \longrightarrow h^+ + e^-$$

$$h^+ + H_2O \longrightarrow \bullet OH$$

$$e^- + O_2 \longrightarrow \bullet O_2^-$$

$$\bullet O_2^- + H_2O \longrightarrow \bullet OH + \bullet OOH$$

$$\text{Dye} + (h^+, \bullet O_2^-, \bullet OH) \longrightarrow \text{Degradation product}$$

Basically, upon shining of light on the as-prepared catalyst, the electrons (e^-) of valence band (VB) get excited and move to the conduction band (CB), which subsequently produces photo-generated holes (h^+) at the VB. These photo-generated h^+ and electrons e^- participate directly or indirectly in the degradation process through redox reactions. The photo-generated h^+ generally reacts with hydroxide anion (OH^-) or water molecule produces hydroxyl radical (•OH), whereas the photo-excited e^- reduces the dissolved O_2 to form superoxide radical anions ($\bullet O_2^-$), which further produced •OOH and •OH. All these photo-generated h^+, $\bullet O_2^-$ and •OH radicals are considered as main reactive species to oxidize the dye.

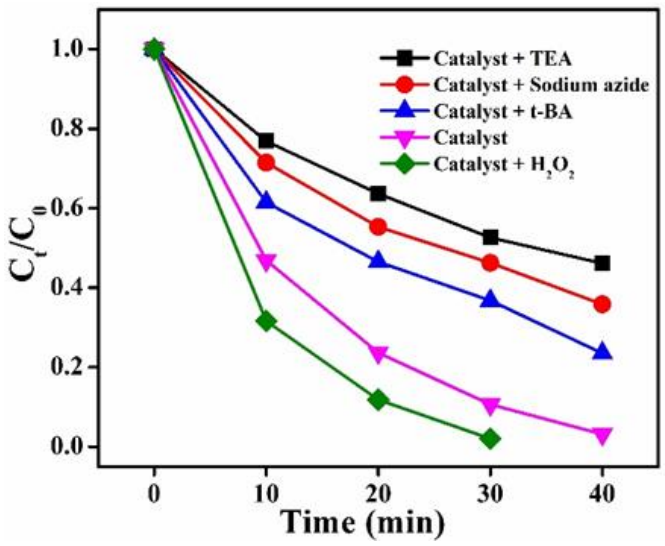

Figure 7.18: Effects of H_2O_2 and different scavengers on the MB degradation using MnO_2/Ag NCs under solar light irradiation.

Interestingly, the photocatalytic activity of MnO_2 nanoflowers was enhanced remarkably after immobilization of Ag NPs over their surfaces. This is as a result of improved light absorption efficiency towards wide range of light spectrum by MnO_2/Ag NCs. Figure 7.19 schematically depicts the probable degradation mechanism towards organic dye upon irradiation of light on MnO_2/Ag NCs, which proceeds via photo-generated reactive oxygen species. Generally, pure semiconductor nanomaterials possess low photocatalytic activity owing to their narrow absorption spectrum together with weak charge separation efficacy and fast recombination of photo-generated excitons. The photocatalytic performances of such semiconductor nanomaterials can be tuned by combing a suitable metal NPs, resulting in the formation of hybrid nanocomposites that demonstrate enhanced catalytic activity.[51,52] This is because of the relatively lower Fermi energy level (E_F) of metal compared to the conduction band edge present in the semiconductor nanomaterials, enabling them to store the photo-generated electrons coming from the CB and subsequently facilitate the charge separation capability followed by increased catalytic activity. Thus, immobilization of Ag NPs over the surface of MnO_2 NCs

enhanced the charge separation capability by delaying the recombination of the charge carriers produced in MnO_2. In a nutshell, the notable improvement in the photocatalytic efficiency of flowery MnO_2/Ag NCs compared to the pristine MnO_2 NCs may be ascribed to the enhanced charge separation capability, which in turn enhances the photocatalytic rate by lowering the possibility of the recombination of the photoproduced excitons.

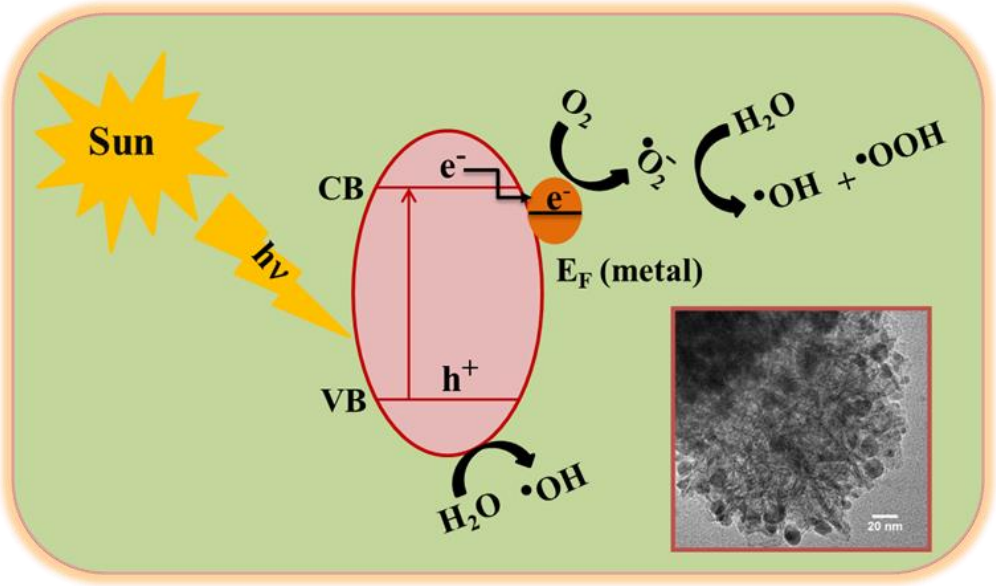

Figure 7.19: Schematic presentation of the probable degradation mechanism towards organic dye upon irradiation of solar light using MnO_2/Ag NCs, which proceeds via photo-generated reactive oxygen species.

7.3.3.6 Comparison of Catalytic Efficiency

A comparison on the degradation efficiency of the NCs towards MB in associated to the reported several MnO_2 based photocatalysts was presented in Table 7.2. They exhibit better degradation performances under renewable sun light irradiation compare to other reported catalysts.

Table 7.2: Comparison of the degradation efficiency of MnO_2/Ag NCs with the other reported MnO_2 based catalysts for the degradation of methylene blue.

Catalysts	Irradiation Time (min)	Degradation Efficiency (%)	References
δ-MnO_2/ montmorillonite	700	92	53
Cu doped MnO_2@diatomite	240	96.2	54
Fe_3O_4@polydopamine-MnO_2	240	97.36	55
MnO_2/Fe_3O_4	180	98.2	56
Polyaniline-modified MnO_2 composite	120	94	57
MnO_2/TiO_2 nanocomposite	120	90	58
β-MnO_2	120	90.2	59
Fe/M-MnO_2	120	94.8	60
MnO_2/CH-FP	90	95.6	61
MnO_2/$BiVO_4$/GNP	60	76	62
Mn_3O_4-MnO_2 composite	60	93.5	63
MnO_2 NCs	**70**	**96**	**Present Work**
MnO_2/Ag NCs	**40**	**97**	**Present Work**

7.4 Conclusions

In summary, we have demonstrated an efficient and simple approach to boost the photocatalytic efficacy of our synthesized flowery MnO_2 NCs by loading the Ag NPs onto their surfaces, which in turn produces MnO_2/Ag NCs. The detail study on the degradation mechanism in presence of several scavengers as well as additional supplementary oxygen source ascertains the generation of reactive oxygen species (•OH, h^+, and $•O_2^-$) during photocatalysis, which participate in the degradation process. A

comparison of their photocatalytic performances towards the degradation of organic dye under renewable sunlight indicates much better photocatalytic efficacy of MnO_2/Ag NCs in associated to the pristine MnO_2 NCs. Such improvement of the photocatalytic effectiveness of flowery MnO_2/Ag NCs could be attributed to the efficient separation of the photoproduced electron-hole pairs and thus prevents the recombination rate of photogenerated electron-hole pairs. Hence, our present approach demonstrates a facile and unique way to fabricate metal oxide/noble metal nanocomposites to boost the photocatalytic activity of the pristine metal oxide, which further offers an attractive route in the field of waste water treatment under renewable solar light because of their excellent degradation efficacy.

7.5 References

(1) Mills, A.; Davies, R. H.; Worsley, D. Water Purification by Semiconductor Photocatalysis. *Chem. Soc. Rev.* **1993**, *22*, 417-425.

(2) Li, M.; Wang, X.; Porter, C. J.; Cheng, W.; Zhang, X.; Wang, L.; Elimelech, M. Concentration and Recovery of Dyes from Textile Wastewater using a Self-Standing, Support-Free Forward Osmosis Membrane. *Environ. Sci. Technol.* **2019**, *53*, 3078-3086.

(3) Zhou, Y.; Lu, J.; Zhou, Y.; Liu, Y. Recent Advances for Dyes Removal Using Novel Adsorbents: A Review. *Environ. Pollut.* **2019**, *252*, 352-365.

(4) Routoula, E.; Patwardhan, S. V. Degradation of Anthraquinone Dyes from Effluents: A Review Focusing on Enzymatic Dye Degradation with Industrial Potential. *Environ. Sci. Technol.* **2020**, *54*, 647-664.

(5) Wu, Z.; Yuan, X.; Zhang, J.; Wang, H.; Jiang, L.; Zeng, G. Photocatalytic Decontamination of Wastewater Containing Organic Dyes by Metal-Organic Frameworks and Their Derivatives. *ChemCatChem* **2017**, *9*, 41-64.

(6) Grau, P. Textile Industry Wastewater Treatment. *Water Sci. Technol.* **1991**, *24*, 97-103.

(7) Kubacka, A.; Fernandez-Garcia, M.; Colon, G. Advanced Nanoarchitectures for Solar Photocatalytic Applications. *Chem. Rev.* **2012**, *112*, 1555-1614.

(8) Yu, C. L.; Li, G.; Kumar, S.; Yang, K.; Jin, R. C. Phase Transformation Synthesis of Novel Ag_2O/Ag_2CO_3 Heterostructures with High Visible Light Efficiency in Photocatalytic Degradation of Pollutants. *Adv. Mater.* **2014**, *26*, 892-898.

(9) Yang, Q.; Ma, Y.; Chen, F.; Yao, F.; Sun, J.; Wang, S.; Yi, K.; Hou, L.; Li, X.; Wang, D. Recent Advances in Photo-Activated Sulfate Radical-Advanced Oxidation Process (SR-AOP) for Refractory Organic Pollutants Removal in Water. *Chem. Eng. J.* **2019**, *378*, 122149.

(10) Nidheesh, P. V. Graphene-Based Materials Supported Advanced Oxidation Processes for Water and Wastewater Treatment: A Review. *Environ. Sci. Pollut. Res.* **2017**, *24*, 27047-27069.

(11) Li, Y.; Jiang, J.; Fang, Y.; Cao, Z.; Chen, D.; Li, N.; Xu, Q.; Lu, J. TiO_2 Nanoparticles Anchored onto the Metal-Organic Framework NH_2-MIL-88B(Fe) as an Adsorptive Photocatalyst with Enhanced Fenton-like Degradation of Organic Pollutants under Visible Light Irradiation. *ACS Sustainable Chem. Eng.* **2018**, *6*, 16186-16197.

(12) Babar, S.; Gavade, N.; Shinde, H.; Mahajan, P.; Lee, K. H.; Mane, N.; Deshmukh, A.; Garadkar, K.; Bhuse, V. Evolution of Waste Iron Rust Into Magnetically Separable g-C_3N_4-Fe_2O_3 Photocatalyst: An Efficient and Economical Waste Management Approach. *ACS Appl. Nano Mater.* **2018**, *1*, 4682-4694.

(13) Shi, H.; Zhao, T.; Zhang, Y.; Tan, H.; Shen, W.; Wang, W.; Li, Y.; Wang, E. Pt/POMs/TiO_2 Composite Nanofibers with an Enhanced Visible-Light Photocatalytic Performance for Environmental Remediation. *Dalton Trans.* **2019**, *48*, 13353-13359.

(14) Cai, J.; Huang, J.; Lai, Y. 3D Au-Decorated $BiMoO_6$ Nanosheet/TiO_2 nanotube Array Heterostructure with Enhanced UV and Visible-Light Photocatalytic Activity. *J. Mater. Chem. A* **2017**, *5*, 16412-16421.

(15) Hoffmann, M. R.; Martin, S. T.; Choi, W. Y.; Bahnemann, D. W. Environmental Applications of Semiconductor Photocatalysis. *Chem. Rev.* **1995**, *95*, 69-96.

(16) Rauf, M. A.; Ashraf, S. S. Fundamental Principles and Application of Heterogeneous Photocatalytic Degradation of Dyes in Solution. *Chem. Eng. J.* **2009**, *151*, 10-18.

(17) Yang, R.; Fan, Y.; Ye, R.; Tang, Y.; Cao, X.; Yin, Z.; Zeng, Z. MnO_2-Based Materials for Environmental Applications. *Adv. Mater.* **2021**, *33*, 2004862.

(18) Fei, J. B.; Cui, Y.; Yan, X. H.; Qi, W.; Yang, Y.; Wang, K. W.; He, Q.; Li, J. B. Controlled Preparation of MnO_2 Hierarchical Hollow Nanostructures and Their Application in Water Treatment. *Adv. Mater.* **2008**, *20*, 452-456.

(19) Cheng, F.; Su, Y.; Liang, J.; Tao, Z.; Chen, J. MnO_2-Based Nanostructures as Catalysts for Electrochemical Oxygen Reduction in Alkaline Media. *Chem. Mater.* **2010**, *22*, 898-905.

(20) Lu, L.; Tian, H.; He, J.; Yang, Q. Graphene-MnO_2 Hybrid Nanostructure as a New Catalyst for Formaldehyde Oxidation. *J. Phys. Chem. C* **2016**, *120*, 23660-23668.

(21) Das, S.; Samanta, A.; Jana, S. Light-Assisted Synthesis of Hierarchical Flower-Like MnO_2 Nanocomposites with Solar Light Induced Enhanced Photocatalytic Activity. *ACS Sustainable Chem. Eng.* **2017**, *5*, 9086-9094.
(22) Chen, B.; Wu, B.; Yu, L.; Crocker, M.; Shi, C. Investigation into the Catalytic Roles of Various Oxygen Species Over Different Crystal Phases of MnO_2 for C_6H_6 and HCHO Oxidation. *ACS Catal.* **2020**, *10*, 6176-6187.
(23) Yuan, W.; Shen, P. K. Controllable Synthesis of Graphene Supported MnO_2 Nanowires via Self-Assembly for Enhanced Water Oxidation in both Alkaline and Neutral Solutions. *J. Mater. Chem. A* **2014**, *2*, 123-129.
(24) Das, S.; Samanta, A.; Kole, K.; Gangopadhyay, G.; Jana, S. MnO_2 Flowery Nanocomposites for Efficient and Fast Removal of Mercury (II) from Aqueous Solution: A Facile Strategy and Mechanistic Interpretation. *Dalton Trans.* **2020**, *49*, 6790-6800.
(25) Zhao, T.; Yao, Y.; Wang, M.; Chen, R.; Yu, Y.; Wu, F.; Zhang, C. Preparation of MnO_2-Modified Graphite Sorbents from Spent Li-Ion Batteries for the Treatment of Water Contaminated by Lead, Cadmium, and Silver. *ACS Appl. Mater. Interfaces* **2017**, *9*, 25369-25376.
(26) Liu, J.; Ge, X.; Ye, X.; Wang, G.; Zhang, H.; Zhou, H.; Zhang, Y.; Zhao, H. 3D Graphene/δ-MnO_2 Aerogels for Highly Efficient and Reversible Removal of Heavy Metal Ions. *J. Mater. Chem. A* **2016**, *4*, 1970-1979.
(27) Xia, C.; Ning, W.; Lin, G. Facile Synthesis of Novel MnO_2 Hierarchical Nanostructures and Their Application to Nitrite Sensing. *Sens. Actuators B Chem.* **2009**, *137*, 710-714.
(28) Xiao, T.; Sun, J.; Zhao, J.; Wang, S.; Liu, G.; Yang, X. FRET Effect between Fluorescent Polydopamine Nanoparticles and MnO_2 Nanosheets and Its Application for Sensitive Sensing of Alkaline Phosphatase. *ACS Appl. Mater. Interfaces* **2018**, *10*, 6560-6569.
(29) Zhang, X.; Yu, P.; Zhang, H.; Zhang, D.; Sun, X.; Ma, Y. Rapid Hydrothermal Synthesis of Hierarchical Nanostructures Assembled from Ultrathin Birnessite-Type MnO_2 Nanosheets for Supercapacitor Applications. *Electrochim. Acta* **2013**, *89*, 523-529.
(30) Yu, Z.; Duong, B.; Abbitt, D.; Thomas, J. Highly Ordered MnO_2 Nanopillars for Enhanced Supercapacitor Performance. *Adv. Mater.* **2013**, *25*, 3302-3306.
(31) Jaidev, J. R.; Mishra, A. K.; Ramaprabhu, S. Polyaniline-MnO_2 Nanotube Hybrid Nanocomposite as Supercapacitor Electrode Material in Acidic Electrolyte. *J. Mater. Chem.* **2011**, *21*, 17601-17605.
(32) Hu, Y.; Zhang, T.; Cheng, F.; Zhao, Q.; Han, X.; Chen, J. Recycling Application of Li-MnO_2 Batteries as Rechargeable Lithium-Air Batteries. *Angew. Chem. Int. Ed.* **2015**, *127*, 4412-4417.

(33) Truong, T. T.; Liu, Y.; Ren, Y.; Trahey, L.; Sun, Y. Morphological and Crystalline Evolution of Nanostructured MnO_2 and Its Application in Lithium-Air Batteries. *ACS Nano* **2012**, *6*, 8067-8077.

(34) Su, X.; Yang, X.; Yu, L.; Cheng, G.; Zhang, H.; Lin, T.; Zhao, F. H. A Facile One-Pot Hydrothermal Synthesis of Branched α-MnO_2 Nanorods for Supercapacitor Application. *CrystEngComm* **2015**, *17*, 5970-5977.

(35) Su, D.; Ahn, H. J.; Wang, G. Hydrothermal Synthesis of α-MnO_2 and β-MnO_2 Nanorods as High Capacity Cathode Materials for Sodium Ion Batteries. *J. Mater. Chem. A* **2013**, *1*, 4845-4850.

(36) Jana, S.; Basu, S.; Pande, S.; Ghosh, S. K.; Pal, T. Shape-Selective Synthesis, Magnetic Properties, and Catalytic Activity of Single Crystalline β-MnO_2 Nanoparticles. *J. Phys. Chem. C* **2007**, *111*, 16272-16277.

(37) Jana, S.; Pande, S.; Sinha, A. K.; Pal, T. Synthesis of Superparamagnetic β-MnO_2 Organosol: a Photocatalyst for the Oxidative Phenol Coupling Reaction. *Inorg. Chem.* **2008**, *47*, 5558-5560.

(38) Ni, L.; Wu, Z.; Zhao, G.; Sun, C.; Zhou, C.; Gong, X.; Diao, G. Core-Shell Structure and Interaction Mechanism of γ-MnO_2 Coated Sulfur for Improved Lithium-Sulfur Batteries. *Small* **2017**, *13*, 1603466.

(39) Zeng, X.; Cheng, G.; Liu, Q.; Yu, W.; Yang, R.; Wu, H.; Li, Y.; Sun, M.; Zhang, C.; Yu, L. Novel Ordered Mesoporous γ-MnO2 Catalyst for High-Performance Catalytic Oxidation of Toluene and o-Xylene. *Ind. Eng. Chem. Res.* **2019**, *58*, 13926-13934.

(40) Zhang, J.; Luan, Y.; Lyu, Z.; Wang, L.; Xu, L.; Yuan, K.; Pan, F.; Lai, M.; Liu, Z.; Chen, W. Synthesis of Hierarchical Porous δ-MnO_2 Nanoboxes as an Efficient Catalyst for Rechargeable Li-O_2 Battery. *Nanoscale* **2015**, *7*, 14881-14888.

(41) Zhong, X.; Lu, Z.; Liang, W.; Guo, X.; Hu, B. The Fabrication of 3D Hierarchical Flower-Like δ-MnO_2@COF Nanocomposites for the Efficient and Ultra-Fast Removal of UO_2^{2+} Ions from Aqueous Solution. *Environ. Sci.: Nano* **2020**, *7*, 3303-3317.

(42) He, G.; Duan, Y.; Song, L.; Zhang, X. Doping Strategy to Boost Electromagnetic Property and Gigahertz Tunable Electromagnetic Attenuation of Hetero-Structured Manganese Dioxide. *Dalton Trans.* **2019**, *48*, 2407-2421.

(43) Jiang, Y.; Yuan, L.; Wang, X.; Zhang, W.; Liu, J.; Wu, X.; Huang, K.; Li, Y.; Liu, Z.; Feng, S. Jahn-Teller Disproportionation Induced Exfoliation of Unit-Cell Scale ϵ-MnO_2. *Angew. Chem. Int. Ed.* **2020**, *132*, 22848-22855.

(44) Jana, S.; Das, S.; Ghosh, C.; Maity, A.; Pradhan, M. Halloysite Nanotubes Capturing Isotope Selective Atmospheric CO_2. *Sci. Rep.* **2015**, *5*, 8711.

(45) Sultana, S.; Mansingh, S.; Parida, K. M. Rational Design of Light Induced Self Healed Fe Based Oxygen Vacancy Rich CeO_2 (CeO_2NS-FeOOH/Fe_2O_3) Nanostructure

Materials for Photocatalytic Water Oxidation and Cr(VI) Reduction. *J. Mater. Chem. A* **2018**, *6*, 11377-11389.

(46) Jana, S.; Pande, S.; Sinha, A. K.; Sarkar, S.; Pradhan, M.; Basu, M.; Saha, S.; Pal, T. A Green Chemistry Approach for the Synthesis of Flower-Like Ag-Doped MnO_2 Nanostructures Probed by Surface-Enhanced Raman Spectroscopy. *J. Phys. Chem. C* **2009**, *113*, 1386-1392.

(47) Mahmoodi, N. M.; Arami, M.; Limaee, N. Y.; Tabrizi, N. S. Kinetics of Heterogeneous Photocatalytic Degradation of Reactive Dyes in an Immobilized TiO_2 Photocatalytic Reactor. *J. Colloid Interface Sci.* **2006**, *295*, 159-164.

(48) Das, S.; Jana, S.; A Tubular Nanoreactor Directing the Formation of In Situ Iron Oxide Nanorods with Superior Photocatalytic Activity. *Environ. Sci.: Nano* **2017**, *4*, 596-603.

(49) Banerjee, S.; Pillai, S. C.; Falaras, P.; O'shea, K. E.; Byrne, J. A.; Dionysiou, D. D. New Insights into the Mechanism of Visible Light Photocatalysis. *J. Phys. Chem. Lett.* **2014**, *5*, 2543-2554.

(50) He, W.; Kim, H. K.; Wamer, W. G.; Melka, D.; Callahan, J. H.; Yin, J. J. Photogenerated Charge Carriers and Reactive Oxygen Species in ZnO/Au Hybrid Nanostructures with Enhanced Photocatalytic and Antibacterial Activity. *J. Am. Chem. Soc.* **2014**, *136*, 750-757.

(51) Liu, X.; Iocozzia, J.; Wang, Y.; Cui, X.; Chen, Y.; Zhao, S.; Li, Z.; Lin, Z. Noble Metal-Metal Oxide Nanohybrids with Tailored Nanostructures for Efficient Solar Energy Conversion, Photocatalysis and Environmental Remediation. *Energy Environ. Sci.* **2017**, *10*, 402-434.

(52) Kochuveedu, S. T.; Jang, Y. H.; Kim, D. H. A Study on the Mechanism for the Interaction of Light with Noble Metal-Metal Oxide Semiconductor Nanostructures for Various Photophysical Applications. *Chem. Soc. Rev.* **2013**, *42*, 8467-8493.

(53) Zhu, M. X.; Wang, Z.; Xu, S. H.; Li, T. Decolorization of Methylene Blue by δ-MnO_2-Coated Montmorillonite Complexes: Emphasizing Redox Reactivity of Mn-Oxide Coatings. *J. Hazard. Mater.* **2010**, *181*, 57-64.

(54) Xiao, Y.; Huo, W.; Yin, S.; Jiang, D.; Zhang, Y.; Zhang, Z.; Liu, X.; Dong, F.; Wang, J.; Li, G.; Hu, X. One-Step Hydrothermal Synthesis of Cu-doped MnO_2 Coated Diatomite for Degradation of Methylene Blue in Fenton-Like System. *J. Colloid Interface Sci.* **2019**, *556*, 466-475.

(55) Pan, X.; Cheng, S.; Su, T.; Zuo, G.; Zhao, W.; Qi, X.; Wei, W.; Dong, W. Fenton-Like Catalyst Fe_3O_4@Polydopamine-MnO_2 for Enhancing Removal of Methylene Blue in Wastewater. *Colloids and Surfaces B: Biointerfaces* **2019**, *181*, 226-233.

(56) Zhang, L.; Lian, J.; Wu, L.; Duan, Z.; Jiang, J.; Zhao, L. Synthesis of a Thin-Layer MnO_2 Nanosheet-Coated Fe_3O_4 Nanocomposite as a Magnetically Separable Photocatalyst. *Langmuir* **2014**, *30*, 7006-7013.
(57) Xu, H.; Zhang, J.; Chen, Y.; Lu, H.; Zhuang, J.; Li, J. Synthesis of Polyaniline-Modified MnO_2 Composite Nanorods and Their Photocatalytic Application. *Mater. Lett.* **2014**, *117*, 21-23.
(58) Xue, M.; Huang, L.; Wang, J. Q.; Wang, Y.; Gao, L.; Zhu, J. H.; Zou, Z. G. The Direct Synthesis of Mesoporous Structured MnO_2/TiO_2 Nanocomposite: A Novel Visible-Light Active Photocatalyst with Large Pore Size. *Nanotechnology* **2008**, *19*, 185604.
(59) Cheng, G.; Yu, L.; Lin, T.; Yang, R.; Sun, M.; Lan, B.; Yang, L.; Deng, F. A Facile One-Pot Hydrothermal Synthesis of β-MnO_2 Nanopincers and Their Catalytic Degradation of Methylene Blue. *J. Solid State Chem.* **2014**, *217*, 57-63.
(60) Huang, R.; Liu, Y.; Chen, Z.; Pan, D.; Li, Z.; Wu, M.; Shek, C. H.; Wu, C. L.; Lai, J. K. Fe-Species-Loaded Mesoporous MnO_2 Superstructural Requirements for Enhanced Catalysis. *ACS Appl. Mater. Interfaces* **2015**, *7*, 3949-3959.
(61) Yang, J.; Ao, Z.; Wu, H.; Zhang, S. Immobilization of Chitosan-Templated MnO_2 Nanoparticles onto Filter Paper by Redox Method as a Retrievable Fenton-Like Dip Catalyst. *Chemosphere* **2021**, *268*, 128835.
(62) Trzciński, K.; Szkoda, M.; Sawczak, M.; Karczewski, J.; Lisowska-Oleksiak, A. Visible Light Activity of Pulsed Layer Deposited $BiVO_4/MnO_2$ Films Decorated with Gold Nanoparticles: The Evidence for Hydroxyl Radicals Formation. *Appl. Surf. Sci.* **2016**, *385*, 199-208.
(63) Zhao, J.; Nan, J.; Zhao, Z.; Li, N.; Liu, J.; Cui, F. Energy-Efficient Fabrication of a Novel Multivalence Mn_3O_4-MnO_2 Heterojunction for Dye Degradation Under Visible Light Irradiation. *Appl. Catal. B Environ.* **2017**, *202*, 509-517.

****

Chapter 8

Conclusion and Future Scope of the Study

8.1 Conclusion

The overall research findings are summarized here. First, an efficient synthesis of ultra-small Ni and NiZn NPs were demonstrated via thermolysis of corresponding metal precursors in a mixture of hot organic solvents. The developed synthetic strategy comprised of chemical conversion of preformed metal NPs into alloys at low temperature via reaction with another metal precursor. The current study also demonstrated that the Ni NPs acted as a precursor to prepare NiZn alloy keeping the morphology intact even during the transformation from metal to alloy. The intermetallic NiZn NPs exhibited enhanced electrocatalytic activity and excellent stability towards OER than $Ni_{0.7}Zn_{0.3}$, pure Ni NPs or RuO_2. It was also established that activity of the alloys upsurged from the composition of the constituents that governed their OER performances. The superior electrocatalytic efficiency of NiZn was ascribed to the modification of the electronic

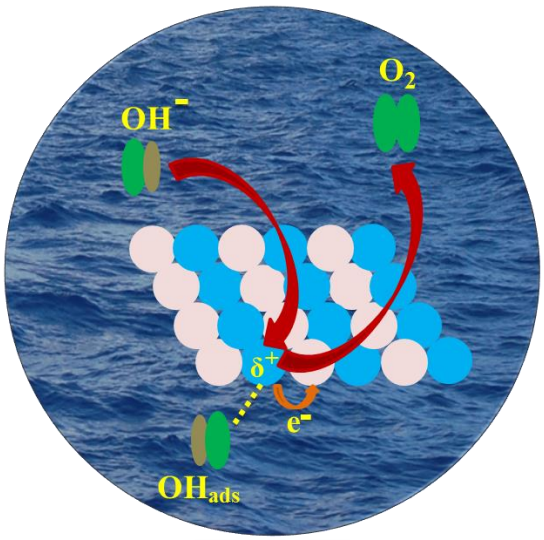

Scheme 8.1: *Ultra-small monodisperse intermetallic NiZn nanoparticles synthesized via low temperature solution chemistry route demonstrated enhanced electrocatalytic activity toward oxygen evolution reaction.*

structure of Ni upon incorporation of Zn, together with the atomic scale synergistic effect produced from Ni and Zn in NiZn alloy (Scheme 8.1). Thus, the novelty of our work lies in the controlled fabrication of monodisperse tiny alloys of NiZn having excellent OER activity compared to the expensive conventional as well as several reported electrocatalysts. Our findings also suggest that catalysts with superior activity can be developed by engineering the composition of the constituent metals during fabrication of desired alloyed nanoparticles.

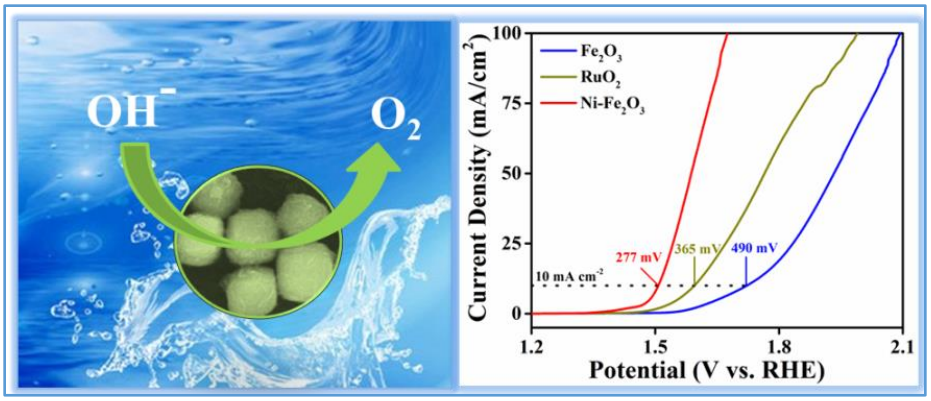

Scheme 8.2: *Ni-doped Fe_2O_3 nanoclews were synthesized with the aid of a light-assisted solution chemistry route, possessing enhanced electrocatalytic activity toward the oxygen evolution reaction.*

Next, a simple light-driven solution chemistry route was demonstrated for the synthesis of α-Fe_2O_3 nanoclews without using any template molecule and explored them as an OER electrocatalyst. To boost the catalytic activity, Ni was doped in α-Fe_2O_3 nanoclews, resulting in the formation of Ni-Fe_2O_3 with analogous morphology. The exceptional OER activity with structural and morphological stability of Ni-Fe_2O_3 was achieved by virtue of their clew-like morphology, comprising of tiny nanorods with uniform distribution of constituent elements. Because of such unique morphology, it provided more exposed active sites and the atomic scale synergistic effect arising from Ni and Fe contributed to a superior intrinsic catalytic activity of Ni-Fe_2O_3 nanoclews (Scheme 8.2). Moreover, Ni sites with oxygen vacancies significantly increased the number of surface-active sites followed by reactivity, attributing to the excellent catalytic activity of Ni-Fe_2O_3 and thus

leaving behind most of the reported iron oxide based or even state-of-the-art RuO_2 electrocatalysts. The present findings not only provide a general approach to make proficient electrocatalysts using earth-abundant elements but also point to the potential aspects of doping in metal oxides, which in turn tune their energy conversion efficiency.

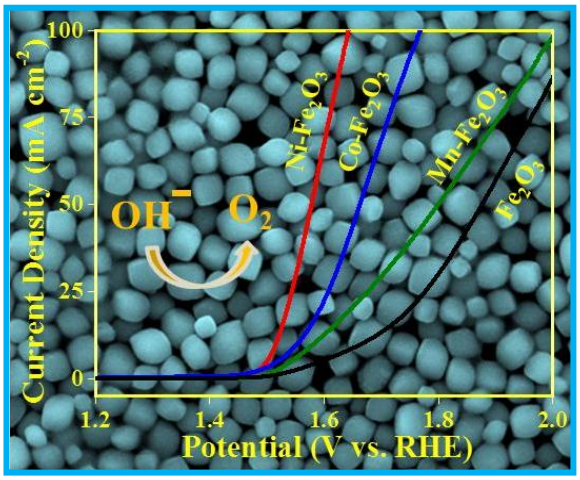

Scheme 8.3: *Developing a facile synthesis route to achieve hierarchical parallelepiped-like morphology of M- doped Fe_2O_3 via a light driven bottom-up chemistry approach to boost oxygen evolution reaction*.

Then, a unique synthesis route was designed to prepare different transition metals doped iron oxide parallelepipeds via a light driven bottom-up chemistry approach deprived of any template molecule. Our developed route provided an easy way to improve the OER activity of iron oxide parallelepipeds via non-noble metal doping. Among all the prepared parallelepipeds, Ni-Fe_2O_3 exhibited highest catalytic activity and stability in alkaline medium, with an order of activity: Ni-Fe_2O_3>Co-Fe_2O_3>Mn-Fe_2O_3>Fe_2O_3 (Scheme 8.3). Upon doing, the resultant doped structures offered an enhanced conductivity and better charge transfer behaviour towards OER and thus boosting the electrocatalysis. The synergistic effect of iron and different dopants together with improved electronic structure resulted in superior OER activity of doped structures compare to the undoped structure. Hence, our Ni-Fe_2O_3 parallelepipeds demonstrated excellent catalytic activity

because of the higher electronegativity of Ni, optimal interaction strength of Ni with OH_{ad} and available exposed active sites, together with the synergistic effect arising from Ni and Fe further enhanced the intrinsic catalytic activity for Ni-Fe_2O_3 parallelepipeds. The present synthetic approach thus provides a unique way of doping process to make new electrocatalysts with excellent electrocatalytic activity.

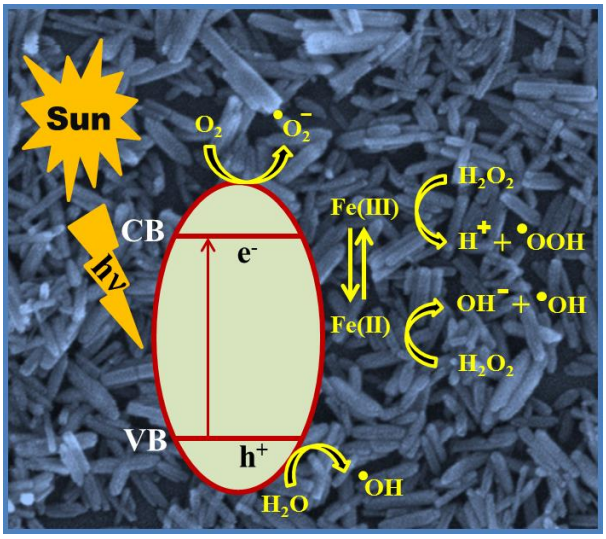

Scheme 8.4: *Synthesis of β-FeOOH nanorods through a light driven solution chemistry pathway in absence of any templating agent, demonstrating excellent photocatalytic efficacy and sustainability under solar light irradiation.*

Afterwards, a very facile route was illustrated to synthesize iron oxyhydroxide nanorods without employing any templating agent via a light driven hydrolysis route. After characterization of synthesized nanorods by different physical techniques, the photocatalytic activity of as-synthesized β-FeOOH nanorods was explored as a photo-Fenton catalyst under sunlight for the degradation of organic dyes (Scheme 8.4). The effect of pH of the solution, catalyst dosages and concentration of H_2O_2 were studied during the degradation process. The overall dye degradation under solar light irradiation using β-FeOOH NRs proceeded via photo-generated reactive oxygen species. Photocatalytic efficacy of β-FeOOH NRs was compared in associated with the reported

oxide based photocatalysts for the dye degradation, substantiating much higher catalytic performance of the β-FeOOH NRs. This work offers an environmentally friendly and cost-effective way in developing highly active photocatalytic nanomaterials to combat with environmental pollutants.

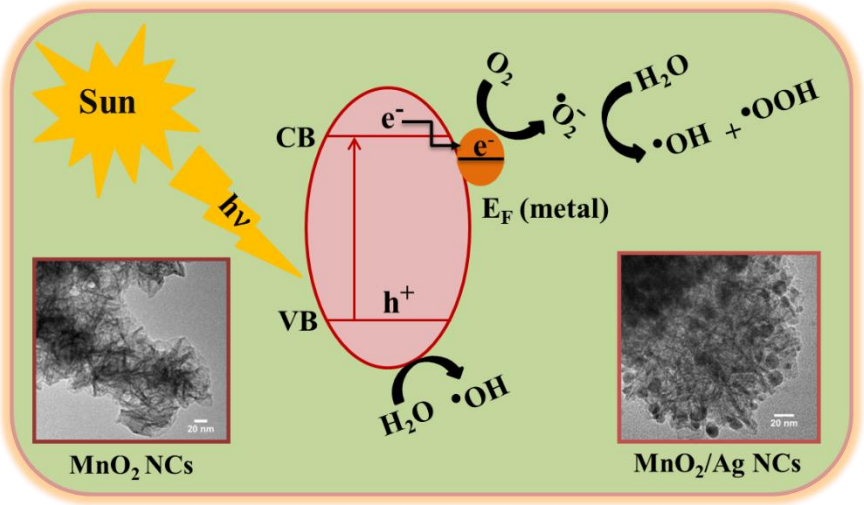

Scheme 8.5: *An efficient and facile approach was developed to boost the solar light driven photocatalytic efficacy of pristine flowery MnO_2 nanocomposites through immobilization of Ag nanoparticles onto their surfaces, which in turn produces MnO_2/Ag nanocomposites.*

At the end of the thesis, a simple route was established to prepare hierarchical MnO_2 and MnO_2/Ag NCs over the surface of HNTs. The photocatalytic activity of both MnO_2 and MnO_2/Ag NCs was studied under natural sunlight irradiation for the degradation of methylene blue dye (Scheme 8.5). It was found that MnO_2/Ag NCs showed better photocatalytic activity compare to pristine MnO_2 NCs. Such improvement of the photocatalytic efficiency of flowery MnO_2/Ag NCs could be attributed to the efficient separation of the photoproduced electron-hole pairs and thus prevented the recombination rate of photogenerated electron-hole pairs. The detail study on the degradation mechanism in presence of several scavengers as well as additional supplementary oxygen source ascertained the generation of reactive oxygen species during photocatalysis, which participated in the degradation process. Thus, the present approach demonstrates a facile

and unique way to fabricate metal oxide/noble metal NCs to boost the photocatalytic activity of the pristine metal oxide, which further offers an attractive route in the practical applications of heterogeneous catalysts for environmental remediation through wastewater treatment in a greener approach.

8.2 Future Scope of the Study

- Alloy based catalysts with superior activity can be developed by engineering the composition of the constituent metals during fabrication of the desired nanoscale uniform alloys.

- The modification of the electronic structure of metal oxides by different dopants may be an effective pathway to design novel electrocatalysts with enhanced electrocatalytic activity for oxygen evolution reaction.

- Design and synthesis of various nanoscale metal oxides with specific shape, size and morphology can be carried out to be utilized as nanocatalysts for the development of sustainable and challenging ways in natural sunlight driven photocatalysis.

- Fabrication of metal oxide/noble metal nanocomposites can be a unique way to boost the photocatalytic activity of the pristine metal oxide, which further offers an attractive route in the field of waste water treatment due to their excellent degradation efficacy.

****